MASSIVE BLACK HOLES AND DISK GALAXIES IN A HIERARCHICAL UNIVERSE

Dissertation

zur

Erlangung der naturwissenschaftlichen Doktorwürde
(Dr. sc. nat.)

vorgelegt der

Mathematisch-naturwissenschaftlichen Fakultät

der

Universität Zürich

von

Simone Callegari

aus

Italien

Promotionskomitee

Prof. Dr. Lucio Mayer (Vorsitz, Leitung der Dissertation)
Prof. Dr. Ben Moore
Prof. Dr. Monica Colpi

Zürich, 2011

Summary

In the current ΛCDM cosmological theory, galaxy evolution is thought to proceed through mergers and accretion of other galaxies. Accumulating evidence in the last decades has shown that massive black holes (MBHs) from 10^6 to above 10^9 $M_\odot$ reside at the centers of massive galaxies, in the local and distant Universe, and couples of MBHs have been observed in systems made of two merging galaxies. This suggests that the evolution of galaxies and MBHs is linked: during the assembly of a galaxy, multiple MBHs may end up in its nucleus. A nuclear MBH binary would give rise to many key astrophysical phenomena, and its coalescence is expected to be source of a loud burst of gravitational waves. However, even if there is consensus about the existence of a link between galaxies and MBHs, a clear physical scenario of their joint formation and evolution is still missing.

In this thesis, the topic of the coevolution of galaxies and MBHs, introduced in chapter 1, is addressed from three different perspectives, through high-resolution numerical simulations.

In chapter 2, we explore the orbital decay and mass accretion of MBHs in galaxy mergers. This has been traditionally studied mostly in the idealized case of equal-mass mergers, using coarser resolution, and *assuming* that the MBHs would become a close pair, reaching sub-kiloparsec distances. For the first time, we put constraints on the efficiency of the formation of MBH pairs in cosmologically relevant unequal-mass mergers. We find that MBH pair formation is very sensitive to the properties of the galaxies and their orbit: mergers with high gas content and more equal masses produce MBH pairs more efficiently. We also find that the conditions that favor the pairing enhance mass accretion onto the smaller MBH, which may even exceed in luminosity the larger MBH. Based on this tendency towards equalizing the masses of close MBH pairs, we deduce strong implications for their observability and demographics.

In chapter 3, we propose a new model for the formation of MBHs: strong dynamical instabilities occurring in major galaxy mergers in the early Universe can form gas clouds of almost a billion solar masses in the center of the merger remnant. Inside such clouds, further instabilities can lead to the birth of a $> 10^5$ $M_\odot$ MBH “seed”, avoiding many issues encountered by other scenarios. We predict that MBH seed formation through this mechanism is inefficient in low-mass galaxies and at low redshifts.

In chapter 4, we present the most successful simulations so far of the formation of a galaxy like our Milky Way, and many physical and numerical issues are discussed. With these simulations, we open the way for a fully cosmological study of how a population of MBHs may have formed and evolved in the history of our Galaxy.

Kurzzusammenfassung

Im momentan gültigen kosmologischen Weltmodell, dem ΛCDM Modell, geht man davon aus, dass die Galaxienentwicklung durch die Verschmelzung von Galaxien oder die Akkretion anderer Galaxien vonstatten geht. Im Laufe der letzten Jahrzehnte haben sich die Beweise dafür verdichtet, dass masseree iche Schwarze Löcher im Bereich von 10^6 bis 10^9 Sonnenmassen sich im Zentrum von massereichen Galaxien befinden – sowohl im lokalen als auch im fernen Universum. Weiterhin wurden Paare Schwarzer Löcher in gerade verschmelzenden Galaxien beobachtet. Somit ist es naheliegend, dass die Entwicklung von Galaxien und Schwarzen Löchern im Zusammenhang stehen: Während der Entstehung der Galaxie können sich mehrere Schwarze Löcher in ihrem Zentrum anlagern. Ein Paar Schwarzer Löcher im Kern würde eine Reihe wichtiger astrophysikalischer Phänomene mit sich bringen und die Verschmelzung der beiden Schwarzen Löcher würde zu einer intensiven Emission von Graviatationswellen führen. Doch selbst wenn es einen Konsens bezüglich der Existens eines Zusammenhanges zwischen Schwarzen Löchern und Galaxien gibt, die Modellierung der astrophysikalischen Prozesse, die bei ihrer gemeinsamen Bildung und Entwicklung eine Rolle spielen, ist eine komplexe Aufgabe und ein endgültiges physikalisches Modell ist noch ausstehend.

In dieser Arbeit wird die Koevolution von Galaxien und massereichen Schwarzen Löchern zuerst in Kapitel 1 vorgestellt und dann im Weiteren unter Nutzung hochauflösender numerischer Simulationen von drei verschiedenen Gesichtspunkten aus beleuchtet.

Im Kapitel 2 betrachten wir die Schrumpfung der Umlaufbahnen und die Massenakkretion massereicher Schwarzer Löcher bei der Galaxienverschmelzung. Traditionell wurde dies meist im idealisierten Fall der Verschmelzungen zweier gleichschwerer Galaxien betrachtet. Zudem lagen den bisherigen Studien weniger gut aufgelöste Simulationen zu Grunde es wurde *angenommen*, dass die massereichen Schwarzen Löcher ein Paar mit einem Abstand von weniger als einem Kiloparsec bilden. Wir können erstmals die Effizienz der Bildung von Paaren Schwarzer Löcher im kosmologisch relevanten Fall der der Verschmelzung verschieden schwerer Galaxien einschränken. Es zeigt sich das die Bildung von Paaren Schwarzer Löcher sehr empfindlich gegenüber den Eigenschaften der verschmelzenden Galaxien und deren Orbit ist. Verschmelzungen mit höherem Gasanteil und ähnlicheren Massen führen zu einer effizienteren Bildung von Paaren Schwarzer Löcher. Wir haben auch herausgefunden, dass die selben Bedingungen, die die Paarung begünstigen, die Massenakkretion auf das leichtere Schwarze Loch verstärken, welches dadurch eine höhere Leuchtkraft als sein schwereres Gegenstück erreichen kann. Basierend auf dieser Tendenz zu einer Angleichung der Massen von Paaren Schwarzer Löcher können wir Schlüsse auf ihre Beobachtbarkeit und Verteilung im Universum ziehen.

Im Kapitel 3 stellen wir ein neues Modell für die Bildung massiver Schwarzer Löcher vor: starke dynamische Instabilitäten die während der Verschmelzung von Galaxien im frühen Universum auftreten, können zur Bildung von Gaswolken von nahezu einer Milliarde Sonnenmassen in der Mitte des Verschmelzungsgebietes führen. In diesen Wolken, können weitere Instabilitäten dann zur Bildung eines Keims für ein Schwarzes Loch von Sonnenmassen führen, womit viele Probleme alternativer Szenarien umgangen werden. Unser Modell sagt jedoch voraus, dass die Keimbildung in massearmen Galaxien und bei niedrigen Rotverschiebungen ineffizient ist.

In Kapitel 4 präsentieren wir die bis dato erfolgreichsten Simulationen zur Bildung von Galaxien vom Typ unserer Milchstrasse. Wir diskutieren relevante physikalische und numerische Probleme, und eröffnen damit einen neuen Weg zu einer kosmologischen Betrachtung der Entstehung und Entwicklung Schwarzer Löcher in der Geschichte unserer Galaxie.

Contents

1

Introduction

This work aims at exploring, through numerical simulations, some astrophysical aspects of the joint evolution and formation of two classes of objects: massive black holes (MBHs) and galaxies, in particular late-type disk galaxies.

In this chapter, we present the broad context for this study: we first introduce MBHs, their relevance for astrophysics and fundamental physics, their connection to the galaxy population, as well as the unsolved problem of their formation, in §1.1. The code used for the simulations is presented in §1.2, while the rest of this thesis is outlined in §1.3.

1.1 Massive Black Holes and their host galaxies

Here we give a brief overview of observational evidence for the existence of MBHs (§1.1.1); of the connections between the MBH and galaxy populations (§1.1.2); of the physical implications of such connection (§1.1.3); and of the issue of how MBHs may have formed in the early Universe (§1.1.4).

1.1.1 Observational evidence for MBHs

The idea of MBHs with masses from 10^6 to above 10^9 $M_\odot$ being the engines of high-energy phenomena taking place in the very centers of distant and nearby galaxies was for the first time suggested by Salpeter (1964), Zel'Dovich (1964) and then by Lynden-Bell (1969). The high efficiency of energy extraction from matter accreting onto a compact object was recognized as the most likely explanation for such phenomena, which fall in the broad category of *Active Galactic Nuclei* (hereafter, AGN). The observations that prompted this idea started with Seyfert (1943), who found in some spiral galaxies nuclear emission lines that were broadened “presumably by Doppler motion, by amounts varying up to $8500\,\mathrm{km\,s^{-1}}$”.

Seyfert also observed that “the maximum width of the Balmer emission lines seems to increase with the absolute magnitude of the nucleus and with the ratio of the light in the nucleus to the total light of the nebula” and such broad lines were observed to be typical only of spiral galaxies (which would be now classified as *Seyfert I* galaxies) with a strong nuclear emission[1]. Two decades later, Schmidt (1963) published the discovery of 3C 273: “a star-like object with large redshift” – the first of the many Quasars (also called QSOs) that would be found in the next decades. Among these are the bright QSO J114816.64+525150.3 at a cosmological redshift $z = 6.43$ (Fan et al. 2003) and ULAS J1120+0641 at $z = 7.08$ (Mortlock et al. 2011), two extremely massive compact objects shining less than 1 Gyr after the Big Bang according to standard Lambda Cold Dark Matter (ΛCDM) cosmology.

In the more than 60 years since the discovery of AGNs, much effort has been dedicated to confirming their theoretical explanation, i.e. to proving that MBHs do inhabit the centers of galaxies. The best confirmation of such scenario would be to observe strong-gravity effects (as predicted by General Relativity) close to the black hole's event horizon. However, they occur at small scales compared to current observational limits: the horizon of a black hole of mass $M_{\rm BH}$, depending on its spin, is located between the two extremes

$$\frac{GM_{\rm BH}}{c^2} \leq R_g \leq \frac{2GM_{\rm BH}}{c^2}$$

where of course G is the gravitational constant and c the speed of light. For example, the horizon of a non-rotating (“Schwarzschild”) black hole is a sphere of radius

$$R_g = \frac{2GM_{\rm BH}}{c^2} \approx 10^{-7} \left(\frac{M_{\rm BH}}{10^6\ {\rm M}_\odot} \right) \ {\rm pc}\,.$$

Nonetheless, the MBH can significantly affect, through its gravitational influence, objects at much larger distances – roughly out to a distance known as its *radius of influence*. It is defined as

$$R_i \equiv GM_{\rm BH}/\sigma_*^2\,,$$

where σ_* is the stellar velocity dispersion at the center of the host galaxy, measuring the depth of the galaxy's potential well. Trajectories of stars and gas clouds in the central region of a galaxy can then indicate the presence of a “point mass” component in the gravitational potential, which could be the dynamical fingerprint of a MBH. This has originated different techniques aimed at estimating masses of MBHs (or, more precisely, of large gravitational masses confined within small radii):

- **dynamical methods:** while in the center of our Galaxy stars can be individually

---

[1] Such spectral features are now thought to come from the “Broad Line Region”, or BLR. This name indicates a complex of ionized clouds orbiting ~ 100 light days away from the active MBH. They are identified through broad (typically ≥ 2000 km s^{-1}) emission lines corresponding to high ionization states.

resolved and followed over time (see below), in other galaxies the stellar kinematics within the influence radius of a central MBH is measured using high-resolution spectroscopy. Stellar-dynamical estimates of black hole masses are the most precise and direct, despite the uncertainties associated with their theoretical modeling (for a review of this method and its successes, see Kormendy 2004). The drawback of this method is that it is very time-consuming, and can only be applied to nearby galaxies.

- **reverberation mapping and virial techniques:** Blandford & McKee (1982) pointed out that any variation in the ionizing emission from the central engine of an AGN would cause a variation both in the continuum (emitted closest to the MBH) and in the emission lines produced in the BLR. Such variation would bear a time delay between continuum and lines, due to the time it takes for the ionizing photons to travel between the central source and the BLR. The MBH mass can then be estimated through virial arguments combining the time delay with the width of the spectral emission lines. Interestingly, Kaspi et al. (2000) found that the radius of the BLR scales with the continuum luminosity at 510 nm: $r_{BLR} \propto L_{510}^{0.7}$. This relation provides a quick (though less reliable) way to estimate BLR sizes, since the luminosity can be obtained in a single observation (“single-epoch” detection). Similar relations have been found at other wavelengths, and can be used to estimate BH masses up to intermediate-high redshifts (Vestergaard 2002).

Still, the best proof of the existence of a MBH so far comes from the observations of the nucleus of our own Milky Way. Performing infrared observations using interferometry and adaptive optics, Genzel et al. (1997, 2000) and Ghez et al. (2005) have followed the proper motions of a small cluster of stars around Sgr A*, the compact radio source at the center of the Milky Way. The stars orbit at distances of a few 100 AU from Sgr A*, with orbital periods as short as a few years. Modelling of such orbits requires the existence of an enclosed mass so high and compact that the most plausible explanation seems to be the presence of a MBH: the most recent estimates of the MBH yield $\sim 4 \times 10^6$ M$_\odot$. In this scenario, the radio emission from Sgr A* would come from gas falling into the event horizon (e.g., Genzel & Karas 2007).

1.1.2 The “cosmic connection” between MBHs and galaxies

In the last couple of decades, when stellar-dynamical measurements of MBH masses became available, correlations between MBHs and properties of their host galaxies were found. Magorrian & al. (1998) show the mass of the central object is ~ 0.006 times the mass of the bulge of its host galaxy. Ferrarese & Merritt (2000) and Gebhardt & al. (2000) found that the MBH mass is related also to the stellar velocity dispersion σ_* of the host, approximately as $M_{\rm BH} \propto \sigma_*^4$ and with a scatter smaller than the one observed for the $M_{\rm BH} - M_{\rm bulge}$ relation. A lot of effort has been invested in measuring the precise slope and scatter of these relations (e.g. Tremaine et al. 2002; Marconi & Hunt 2003; Gültekin et al. 2009), and their evolution with time (e.g., Decarli et al. 2010) as they could yield important clues to the physical origin of the relation itself.

Over the years, the idea of some physical coupling between MBH and galaxy evolution strengthened as other scaling relations were found – such as that between the black hole mass and the Sersic index[2] of the galaxy density profile (Graham et al. 2001), or even between the black hole mass and the mass of the host dark matter halo (Ferrarese 2002). More and more often such scaling relations, after being calibrated via the techniques mentioned in §1.1.1, are used alongside those as an alternative method for estimating MBH masses in large samples of galaxies. As an example, Fig. 1.1 shows various estimates of the local black hole mass function in the most recent compilation of Shankar (2009) as derived in particular from the $M_{\rm BH} - M_{\rm bulge}$ and $M_{\rm BH} - \sigma_*$: from a wide census of bulge masses, luminosities or velocity dispersion it is, in fact, possible to estimate the corresponding central MBH masses. The integral of this mass function is the total present MBH mass density, which is now estimated to be $\rho_{\rm BH} \sim 4 \times 10^5$ $M_\odot$ Mpc^{-3} (see Graham & Driver 2007, for a recent discussion on different black hole mass-density estimates). Soltan (1982) combined the local black hole mass density with the AGN luminosity function (integrated over time) and estimated that most of the mass in present-day MBHs must have been accreted in phases of bright activity. Following this so-called "Soltan argument", many groups have analyzed the evolution of the AGN luminosity function to also impose limits on the *radiative efficiency* ϵ_r (see also §1.2.3), finding that, across cosmic time, $\epsilon_r \sim 0.1$ (e.g., Yu & Tremaine 2002; Merloni et al. 2004; Shankar et al. 2004).

For a long time now it has been known that the number density of quasars is higher at higher redshifts than today, with a peak at $z \sim 2$–3. An analogous trend is found for the density of star formation (SF) as a function of cosmic time. The striking similarity between these two global trends (see Fig. 1.2) is taken as an additional indication of how the growth of galaxies and MBHs is connected. Moreover, AGNs with high X-ray luminosities are more common at higher redshift with respect to their low-luminosity counterparts (e.g., Hasinger et al. 2005); recently, the same conclusions have been obtained also with optical data (Croom et al. 2009). This suggests that the more massive BHs were already in place (and accreting at a higher rate) at high redshift, and since then the accretion activity has shifted to smaller objects. This is a puzzle in itself (see §1.1.4), to which a possible solution will be proposed in chapter 3.

---

[2] The *Sersic index* n indicates the steepness of the density profile of a galaxy, usually expressed as: $I(R) \propto e^{-R^{1/n}}$, where $I(R)$ is the surface brightness, or projected density profile, as a function of the cylindrical radial distance R (de Vaucouleurs 1948; Sersic 1968).

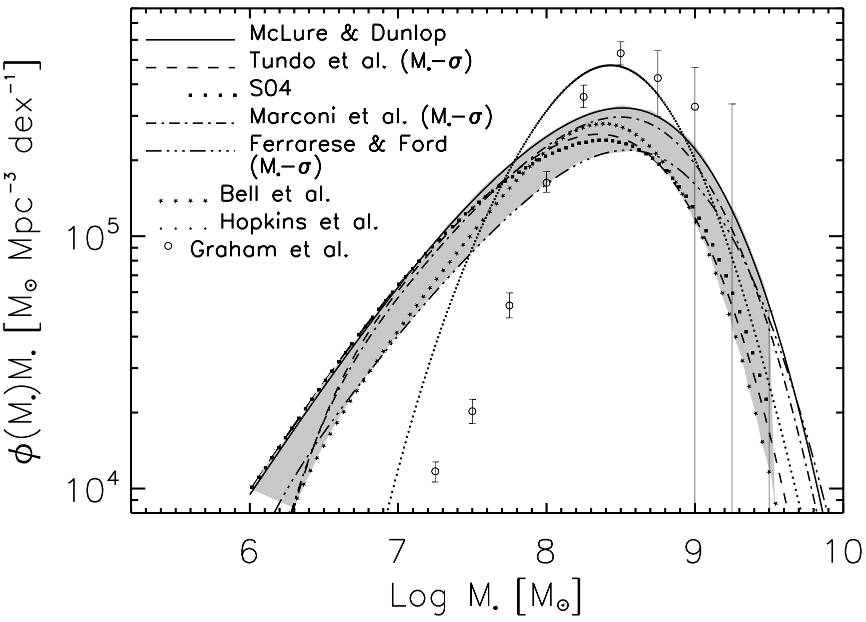

Figure 1.1: Various estimates of the present-day MBH mass function, with some theoretical models overlayed, taken from Shankar (2009).

The standard theoretical framework for these observations is based on the ΛCDM structure formation model, according to which objects of small mass form first from fluctuations of the density field, and then grow by accretion and mergers, in a “hierarchical” or “bottom-up” fashion (White & Rees 1978; White et al. 1991). In this context, galaxy mergers are thought to play a primary role in triggering star formation and shaping galaxy morphologies. Numerical simulations have shown that galactic spheroids can arise from the merger of two disk galaxies (e.g., Barnes 1988; Hernquist 1992; Springel & Hernquist 2005). They have also shown that, in gas-rich mergers, starbursts occur as gas is funnelled by gravitational torques toward the nuclei of the merging galaxies (Negroponte & White 1983; Barnes & Hernquist 1991; Mihos & Hernquist 1996), where it may also fuel AGNs. For this reason, gas-rich galaxy mergers have been considered as the natural link explaining the correlations between MBHs and their host bulges. Kauffmann & Haehnelt (2000) analyzed the evolution of the black hole population in a cosmological context, assuming that galaxy mergers were the main mechanism responsible for efficient black hole growth; they were able to reproduce some of the main properties of the black hole and quasar population, demonstrating the viability of this basic assumption. In the following years, more work has been done in this direction (e.g., Wyithe & Loeb 2002; Volonteri et al. 2003; Granato et al. 2004; Bonoli et al. 2009, among others). On the physical side, it is known that the energy released by an accreting MBH can exceed the binding energy of the host galaxy; however, how (and how much) the emitted energy can couple with the MBH’s surroundings is still debated. Silk & Rees (1998) first proposed that a wind from a black

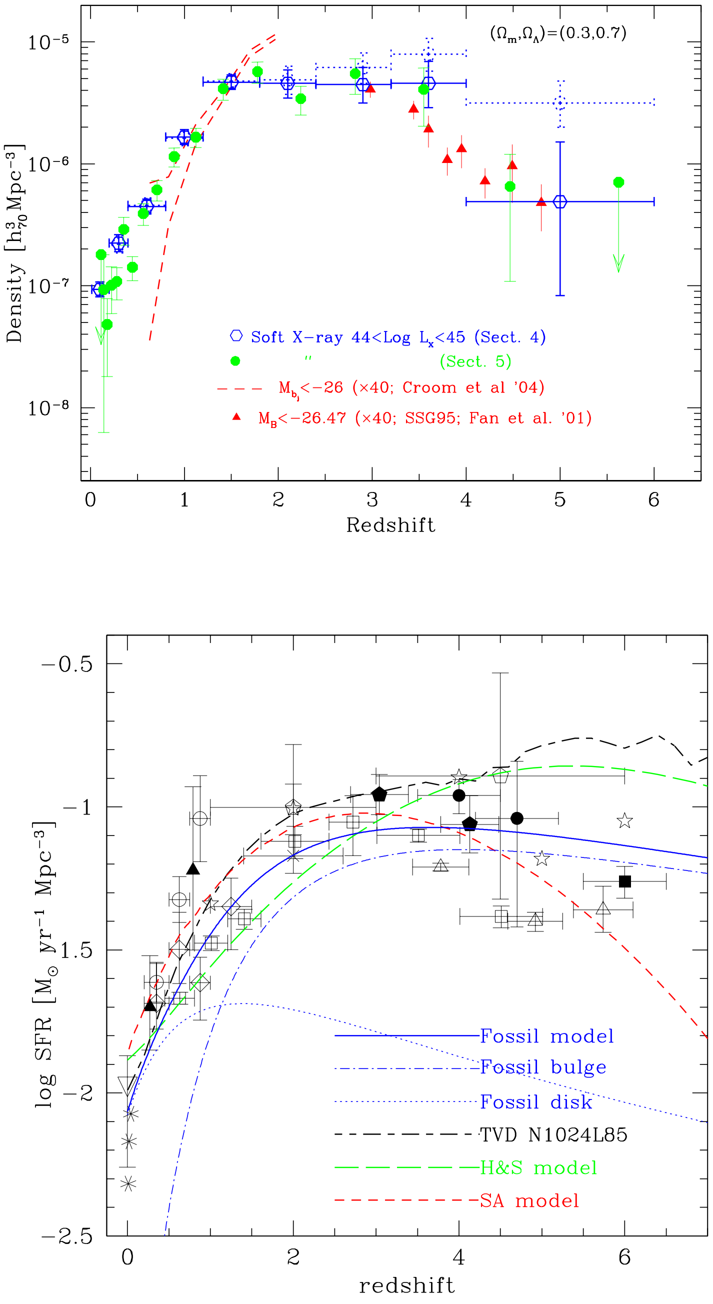

Figure 1.2: *Upper panel*: Redshift evolution of the AGN luminosity density from the X-ray luminosity function plus other data, taken from (Hasinger et al. 2005). *Lower panel*: Compilation of data points of star formation rate density as a function of cosmic redshift, from Nagamine et al. (2006), with some theoretical models overlayed as different lines.

hole in a "quasar phase" could mechanically couple with the surrounding gas, halting star formation, regulating the growth of the black hole itself and possibly explaining the scaling relation between the black hole and the host galaxy stellar mass. Such self-regulated MBH growth has also been included in hydrodynamical simulations of galaxy mergers, successfully obtaining the $M_{\rm BH} - \sigma_*$ relation in the merger remnants by assuming, through a sub-resolution numerical “recipe”, that a fraction of the radiative luminosity from the accreting central black hole is able to heat the surrounding gas (Di Matteo et al. 2005; Springel et al. 2005), as formalized in §1.2.3. From this initial idea, many more scenarios for such correlations have been proposed (e.g., Granato et al. 2004; Escala 2007).

There is also more direct observational confirmation of this general picture. Sanders et al. (1988) first suggested a connection between QSOs and starburst galaxies with signatures of recent mergers. Morphologically-disturbed galaxies with a young stellar population seem indeed to be the typical hosts of AGN with high mass accretion rates (e.g., Sánchez et al. 2004; Jahnke et al. 2004; Bennert et al. 2008), whereas it has been observed that low-luminosity AGN seem to be hosted by galaxies that do not necessarily show signs of recent merger activity (e.g., Kauffmann et al. 2003; Silverman et al. 2008). While galaxy mergers seem then to be responsible for triggering the activity of very bright AGNs as the “AGN feedback” scenario assumes, low-luminosity AGN are possibly triggered by other mechanisms, such as stellar winds from supernovae explosions or bars produced in galactic disks by gravitational instabilities (e.g., Jogee 2006; Ciotti & Ostriker 2007), although this division between “external” and “internal” triggers might be not as simple as environment and minor galaxy interactions complicate the picture (Strand et al. 2008; Barth et al. 2008; Georgakakis et al. 2009). The topic of minor mergers will be addressed in chapter 2.

1.1.3 MBH pairs and binaries

The idea of the *coevolution* of MBHs and galaxies which spans their cosmic history has an intriguing implication (among many), first envisioned by Begelman, Blandford, & Rees (1980). This is the key idea: if indeed galaxies harbor MBHs at their centers, and if galaxies do grow via mergers, then the presence of a MBH binary in the nucleus of a galaxy during its assembly seems to be an unavoidable outcome.

In support to this idea, three classes of objects have been looked for in the sky: *dual*, *binary* and *offset* (or *recoiling*) AGNs. Dual AGNs are defined as two MBHs that are simultaneously shining during a galaxy interaction, seen when they are still at ≥ 100 pc separation. There are now very compelling observations of such systems, e.g. the bright double X-ray nucleus in the starbursting NGC 6240 (as observed by Komossa et al. 2003) and Mrk 463 (Bianchi et al. 2008), and the double radio source in 3C 75 in Abell 400 (Hudson et al. 2006). A similar case in a system undergoing less dramatic interaction may be the galaxy with multiple nuclei NGC 3341 (Barth et al. 2008). On the other hand, no clear-cut observational cases for binary or kinematically and/or spatially offset AGNs have been published yet, although some compelling evidence exists, mainly from spectral or light-curve features. For example, the BL Lac OJ 287 shows a periodic variation consistent with the modulation of nuclear emission due to a binary MBH system (Valtonen et al. 2008), while VLBI observations of the galaxy 0402+379 revealed two compact nuclear radio sources at a projected separation of only 7 pc. The quest for other systems of this kind continues.

On the theoretical side, the phases that two MBHs could go through as they get closer and closer as consequence of a galaxy merger were outlined already in Begelman et al. (1980), and are usually divided as follows (see the in-depth review by Colpi & Dotti (2009)).

Dynamical friction

The collective response of a gravitating system to the movement of a massive object inside of it (called *dynamical friction*) exerts a drag that, in the Chandrasekhar (1943) original formulation, can be expressed as:

$$\vec{F}_{\rm DF} = -4\pi G^2 \ln\Lambda M^2 \rho_{\rm bkg} \left[{\rm erf}\left(\frac{V}{\sqrt{2}\sigma}\right) - \left(\sqrt{\frac{2}{\pi}}\frac{V}{\sigma}\right) e^{-V^2/2\sigma^2} \right] \frac{\vec{V}}{V^3}\,, \tag{1.1}$$

where $\rho_{\rm bkg}$ is the "background" density through which the object is moving (e.g., the dark halo of a massive galaxy for a satellite, but a similar formula applies to gaseous backgrounds – see Ostriker 1999), $\vec{V}$ is the relative velocity between object and background, σ is the 1D background velocity dispersion, $\ln\Lambda$ is the so-called "Coulomb logarithm" (see one of the references for its meaning), and M is the mass of the object being decelerated. The "object" in our case may be, depending on the circumstance or the time during the merger, one of the two galaxies (if much smaller than the other), a stellar cusp wth MBH at its center, or the "naked" MBH itself. The situation is much more complex in reality, especially during the first phases of near equal-mass mergers, where there is no clearly defined "background" and global instabilities play a major role; nonetheless, even in this case, once the system has settled after the first violent phase, dynamical friction still acts on the MBHs inside the remnant.

As an analytical example, in a singular isothermal sphere of density profile $\rho(r) \propto r^{-2}$, the sinking time needed for an object of mass M to reach the center from a certain distance is

$$\tau_{\rm DF} \approx 0.5 \left(\frac{5}{\ln(M_{\rm encl}/M)}\right) \left(\frac{r_{\rm cir}}{300\ {\rm pc}}\right)^2 \left(\frac{V_{\rm cir}}{141\ {\rm km\ s^{-1}}}\right) \left(\frac{10^6\ M_\odot}{M}\right) \epsilon^{0.4}\,{\rm Gyr}\,,$$

where $r_{\rm cir}$ and $V_{\rm cir}$ are the initial radius and velocity of the circular orbit with the same energy as the actual orbit, ϵ is the ratio between the actual orbital angular momentum and $M r_{\rm cir} V_{\rm cir}$, and $M_{\rm encl}$ is the background mass enclosed within $r_{\rm cir}$. The formula above can be taken to be representative of the general scalings of $\tau_{\rm DF}$ in a generic background: roughly speaking, $\tau_{\rm DF} \propto r/M$. Such timescale marks the transition from *dual MBHs* to a

MBH pair, and may constitute the first – though not widely acknowledged in literature so far – bottleneck in MBH orbital decay (chapter 2).

Hardening

The phase of dynamical friction-driven orbital shrinking continues until the background mass enclosed within the relative orbit of the two MBHs is equal to the total mass of the MBHs themselves. Then, they enter a second stage called *binary hardening* (see the extensive review by Merritt & Milosavljević 2005), and at this point, different processes may kick in depending on the nature of the "background" (i.e. the nucleus of the merger remnant).

In predominantly collisionless backgrounds (dominated by stars and/or dark matter), scattering off the binary by single stars or other compact objects becomes the main process by which energy and angular momentum are extracted from the MBH pair. Whether this mechanism alone is able to bring the MBHs close enough to initiate the next sinking stage is still a matter of debate. In fact, as stars are ejected, less and less stars with orbits suitable for ejection can be found by the MBHs, which may eventually stall at some separation, or at least slow down significantly (Milosavljević & Merritt 2003). Triaxial backgrounds with chaotic orbital structure or two-body relaxation of the stellar distribution may ease this problem (references in Merritt & Milosavljević 2005).

If the background is gas-dominated because of the formation of a nuclear disk during the merger, orbital decay can be very quick even down to less than 1 pc, as shown for massive circumnuclear disks formed through major mergers (Mayer et al. 2007), and a wealth of physical mechanisms affecting MBH pairs orbiting in such disks has been investigated both numerically (e.g., Escala et al. 2004, 2005; Dotti et al. 2006, 2007) and with analytic or hybrid approaches (e.g., Lodato et al. 2009; Cuadra et al. 2009).

Here it will suffice to note that, both in collisionless and in collisional enviroments, it is uncertain if there is always a mechanism able to bring the two MBHs to closer and closer separations in galactic nuclei; though the general consensus in very recent years seems to be that possible solutions are many, the issue of inefficient orbital shrinking in this regime has become famous as the *"final parsec problem"*.

Radiation of gravitational waves and recoil

Assuming that the final parsec problem is overcome, when the binary MBH reaches a separation of $\sim 10^4\ R_g$, emission of gravitational waves (GW) becomes the dominant mechanism of energy loss, which happens on progressively shorter timescales (Peters 1964) as the

MBHs approach coalescence. Such events are expected to be the loudest sources of gravitational waves in the Universe, and will hopefully be the target of future GW detection experiments. GW emission from these systems is a very rich testing ground for fundamental physics, from strong-field general relativity, to the *no-hair* theorem, etc. Moreover, as the two horizons coalesce into a single MBH (an event that is 10^{12} orders of magnitude smaller than the initial scale of a galaxy merger), anisotropic GW emission imparts a “kick” to the newly formed black hole, with speeds that can be up to > 1000 km s^{-1} (González et al. 2007; Herrmann et al. 2007; Campanelli et al. 2007; Baker et al. 2008). With such high recoil velocities, a kicked MBH could even leave the host galaxy, with dramatic effects on the occupation fraction of today’s galaxy nuclei. We will touch upon this problem in §2.2.3.

1.1.4 MBH seed formation

The local demographics of MBHs overviewed in §1.1.2 suggests not only that their evolution is linked to that of their host galaxies, but also that MBH formation is a generic feature of galaxy formation, at least above a certain mass scale. Accretion onto the black holes may be linked to galaxy mergers and in general to the production of stellar mass in the Universe, but the *seeding* of MBHs must happen through yet unknown mechanisms at very early epochs, early enough to explain the high-z QSOs we mentioned earlier.

The most widely considered hypothesis is that the first generation of metal-free stars (called Population III stars) leaves behind a population of remnants with very heavy masses, providing initial seed black holes of 10–100 M$_\odot$ (e.g., Madau & Rees 2001; Volonteri, Haardt, & Madau 2003). Growing these seeds to match the observed abundance of high-z QSOs requires long periods of Eddington-limited or super-Eddington growth (Volonteri & Rees 2005). However, as will be discussed in §3.1, recent numerical simulations show that, since these seeds are left most likely within bubbles of hot and rarified gas, their accretion rates should be much lower than required (Johnson & Bromm 2007; Pelupessy et al. 2007; Alvarez et al. 2009).

Alternative theories of MBH formation aim at the production of $\sim 10^5$ M$_\odot$ seeds, so that the constraints on their subsequent accretion rates would not be so stringent. This can be accomplished by the direct collapse of dense gas clouds (see Haehnelt & Rees 1993; Umemura et al. 1993; Loeb & Rasio 1994; Eisenstein & Loeb 1995). In this case, the main difficulty to overcome is getting rid of the angular momentum of the gas. A bias towards seed formation in low-angular momentum halos has been proposed as solution (Eisenstein & Loeb 1995; Koushiappas et al. 2004). Alternatively, central inflows in protogalactic disks can be achieved with various kinds of dynamical instabilities (e.g., Shlosman et al. 1990; Lodato & Natarajan 2006). However, current models require quite idealized conditions such as metal-free gas, to prevent cooling and star formation from consuming the gas reservoir on timescales shorter than those of the inflow (Omukai et al. 2008; Regan & Haehnelt 2009; Bromm & Loeb 2003).

Given these theoretical difficulties, how those first MBHs came into place is still an unsolved problem. We will discuss further these difficulties and propose a somewhat novel solution in chapter 3.

1.2 The GASOLINE code

1.2.1 Basics of the code

All the simulations presented in the next chapters have been performed with GASOLINE (Wadsley et al. 2004), an N-body / SPH code.

GASOLINE computes gravitational forces using an N-body tree-code (Barnes & Hut 1986) that employs multipole expansions to approximate the long-range gravitational forces. First, a tree is built with each node storing its multipole moments. Each node is then recursively divided into smaller subvolumes until the final leaf nodes are reached, containing a maximum number of particles. In this way, starting from the root node and moving level by level toward the leaves of the tree, a progressively more detailed representation of the underlying mass distribution is obtained. When computing the force of gravity acting on an "active" particle, the tree walk is halted (a node is not opened further) whenever the apparent size of the node at the distance of the active particle is less than some tolerance angle. Therefore, in calculating the force on each particle, a multipole representation of the more distant particles is used, leading to an $O(N \log N)$ method. "Computational locality" thus translates directly to spatial locality and leads to a natural domain decomposition. Time integration of the equations of motion is carried out using a multi-step "leapfrog" method, which is a second-order symplectic integrator requiring only one costly force evaluation per timestep and only one copy of the physical state of the system.

SPH is a technique that uses particles to integrate fluid elements representing gas (Gingold & Monaghan 1977; Monaghan 1992), which effectively behave as Lagrangian sampling points of the fluid. Sampling is done via a smoothing kernel with compact support $w(r,h)$, where r is the distance from the particle and h is an adaptive smoothing length, containing always a fixed number of closest "neighbors". The physical quantities of the fluid are estimated via a kernel-weighted average that uses a symmetrization of $w(r,h)$ (Hernquist & Katz 1989),

$$W_{ij} = \frac{1}{2} w\left(\frac{|\vec{r}_i - \vec{r}_j|}{h_i}\right) + \frac{1}{2} w\left(\frac{|\vec{r}_i - \vec{r}_j|}{h_j}\right),$$

where $|\vec{r}_i - \vec{r}_j|$ is the distance between two particles. As an example, the density at the position of the i^{th} gas particle is evaluated from its N neighbors of masses m_j as

$$\rho_i = \sum_{j=1}^{n} m_j W_{ij} \, .$$

The specific internal energy of the gas is integrated using the asymmetric formulation. With this formulation the total energy is conserved exactly (unless physical dissipation due to cooling processes is included) and entropy is closely conserved away from shocks, which makes it similar to alternative entropy integration approaches (Springel & Hernquist 2002). Dissipation in shocks is modeled using the quadratic term of the standard Monaghan artificial viscosity (Price & Monaghan 2004). The Balsara correction term is used to reduce unwanted shear viscosity (Balsara 1995).

1.2.2 Star formation and supernovae

Star formation occurs on much smaller scales than those resolved in the simulations presented here. Therefore, in the simulations where SF is included, it is treated with a "subgrid" phenomenological approach. Gas particles become eligible for SF if their density exceeds a certain density threshold (usually indicated as a number density $n_{\rm SF}$) and their temperature is below some maximum $T_{\rm SF}$. If these conditions are satisfied, the SF rate at that point in the fluid is given by

$$d\rho_*/dt = \epsilon_{\rm SF}\, \rho_{\rm gas}/t_{\rm dyn} \propto \rho_{\rm gas}^{1.5} \, , \tag{1.2}$$

where ρ_* and $\rho_{\rm gas}$ are the stellar and gas densities, and $t_{\rm dyn}$ is the local dynamical time of the gas. In this way, a Schmidt law is enforced locally (Schmidt 1959; Kennicutt 1998).

Each star particle is created stochastically, with a mass equal to 30% of the original gas particles mass, and the gas particle that spawns the new star has its own mass reduced accordingly. A star particle represents a simple stellar population with its own age, metallicity, and a Kroupa (2001) initial stellar mass function (IMF). Each supernova type II (SN) contained within this stellar population deposits metals and a net energy of $\epsilon_{\rm SN} \times 10^{51}$ erg (in the form of heat) into the nearest neighbor gas particles when exploding. The heated gas has its cooling shut off until the end of the snowplow phase of the SN blastwave, which is set by the local gas density and temperature and by the total energy injected $E_{\rm SN}$. The whole numerical prescription is described in detail in Stinson et al. (2006). The energy injected by many SNe adds up to create larger hot bubbles and longer shutoff times. For example, at the typical ISM conditions at threshold found in Eris (4), this translates into regions of size $R_E \sim 30 E_{51}^{0.32}$ pc heated by individual SNe and having their cooling shut off

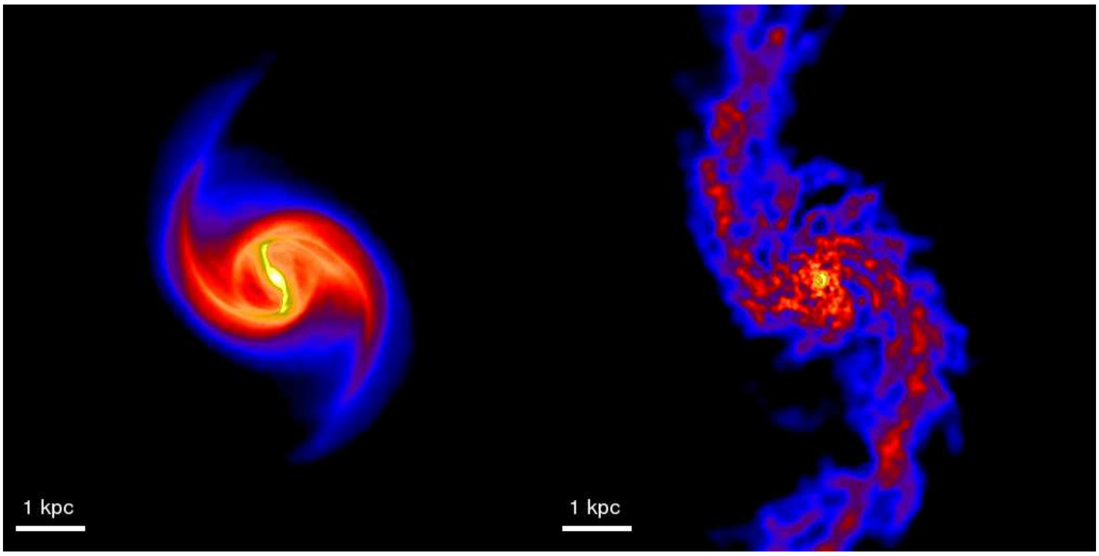

Figure 1.3: Gas density maps of the satellite at first pericenter in a 1:10 merger (chapter 2) with temperature floor and not SF (*left panel*) and with SF plus SN "blastwave" feedback (*right panel*). Images are 8 kpc on a side.

for a timescale $t_E \sim 5 \times 10^5 E_{51}^{0.31}$ yr, where $E_{51} \equiv E_{\rm SN}/10^{51}$ ergs.

In simulations of the previous generation (e.g., Kazantzidis et al. 2005), the effect of feedback was mimicked by imposing a temperature "floor" below which gas would not cool, at temperatures $\sim 2 \times 10^4$ K. Fig. 1.3 shows how the SN "blastwave" feedback prescription results in striking qualitative differences in galaxy morphology, producing an inhomogeneous structure of the simulated interstellar medium (ISM), which more closely resembles observed galaxies.

1.2.3 Black hole accretion and feedback

Similarly to SF, a sub-resolution recipe is employed also to model accretion onto MBHs, following Springel et al. (2005). The accretion rate $\dot{M}_{\rm BH}$ is estimated from the density ρ_g, sound speed c_s and relative velocity V of the gas within a smoothing length from the MBH, via a Bondi-Hoyle-Lyttleton type formula (Bondi 1952),

$$\dot{M}_{\rm Bondi} \equiv \lambda 4\pi G^2 M_{\rm BH}^2 \frac{\rho_g}{(V^2 + c_s^2)^{3/2}} \,. \tag{1.3}$$

This formula is derived as solution for the accretion rate onto a MBH inside an infinite gaseous medium, whose equation of state determines the value of the parameter λ. In our case, this parameter is simply a normalization factor with no direct physical meaning, and will be set to $\lambda = 1$. Strictly speaking, Eq. 1.3 could only apply to scales below the influence radius R_i where the gravity of the black hole dominates, and would in any case neglect the effect of angular momentum; it is therefore best viewed as a simple estimate of the infall rate of gas into an unresolved “accretion region” around the MBH, where the real physics of accretion takes place. This issue will be discussed in more detail on p. 42.

A fraction $\epsilon_r = 0.1$ of the mass-energy budget $\dot{M}_{\rm BH}c^2$ is assumed to be radiated away, following the “Soltan argument”, while a fraction $(1-\epsilon_r) = 0.9$ is added to the mass of the MBH from its neighboring gas particles. Such radiation efficiency leads to an additional constraint to the MBH accretion rate which we impose in the simulations. In fact, assuming a spherically symmetric accretion flow, there is a limiting luminosity which cannot be exceeded, as it corresponds to the luminosity whose radiation pressure onto the (ionized) gas exactly balances the gravitational pull by the MBH. This luminosity is known as the *Eddington limit* (Eddington 1916), and it yields a maximum accretion rate of

$$\dot{M}_{\rm Edd} \equiv \frac{1}{\epsilon_r c^2}\frac{4\pi c G M_{\rm BH}\mu_e m_p}{\sigma_T} \tag{1.4}$$

where σ_T is the Thomson cross-section, m_p the proton mass, and μ_e the mean molecular weight per electron. $\dot{M}_{\rm BH}$ is then given by Eq. 1.3 whenever it is lower than $\dot{M}_{\rm Edd}$, otherwise we enforce $\dot{M}_{\rm BH} = \dot{M}_{\rm Edd}$.

We note here (as it will be useful in the following) that this limit for spherical accretion leads to a natural minimum e-folding timescale for MBH mass growth. It is known as the *Salpeter time* (see a nice review in Shapiro 2005), and it is given by

$$\tau \equiv \frac{M_{\rm BH}c^2}{\epsilon_r \dot{M}_{\rm Edd}c^2} \approx 0.45\mu_e^{-1}\,{\rm Gyr}\,. \tag{1.5}$$

Of the radiated luminosity, a fraction $\epsilon_{\rm fb}$ couples to the surrounding gas as a heating source, enforcing thermal AGN feedback. This last parameter is unconstrained at the moment, except for numerical simulations where it is usually chosen to match the observed normalization of the MBH scaling relations (Springel et al. 2005). Our choice will be discussed in §2.3.2.

1.3 Outline of the thesis

In this thesis, the topic of coevolution of MBHs and galaxies will be addressed from different perspectives, all relying on numerical simulations to shed light on the complex interplay of different dynamical processes.

In chapter 2, the interplay between galaxy mergers and MBH evolution is explored in non-cosmological simulations, with focus first on the efficiency with which black hole binaries can be produced, and then on a newly found correlation between the pairing efficiency and the final mass ratio of the MBH pair.

In chapter 3, a new scenario for the formation of MBH seeds, relying on high-z galaxy mergers, is presented.

In chapter 4, we describe a set of cosmological simulations that produced the most realistic Milky Way-type galaxy to date, the ideal candidate for exploring the evolution of MBHs in a galaxy with its full cosmological context.

In the Appendix, we will present work on a somewhat different subject: morphological transformations of dwarf galaxies interacting with Milky Way-sized hosts.

2

Massive Black Hole pairs in minor mergers of disk galaxies

In this chapter, we examine the dynamics of MBHs during mergers of disk galaxies, with focus on the orbital sinking (§2.2) and on the mass growth (§2.3) of the black holes in mergers of unequal-mass ratio.[1] The key role of gas dynamics and star formation will be highlighted, in particular concerning the efficency of orbital decay of the MBHs, and its connection to variations in their mass ratio during the merger.

2.1 Context

It has been argued in chapter 1 how the ubiquity of MBHs at the centers of galactic spheroids, together with the "bottom–up" nature of galaxy formation in ΛCDM cosmology, suggests that the presence of two or more MBHs in the remnant of a galaxy merger will be almost inevitable during galaxy assembly. The correlations between MBH masses and properties of their host spheroids suggest the existence of fundamental physical mechanisms that link MBH assembly and galaxy formation, and which may connect the properties of galaxy mergers with the resulting MBH binaries. The study of the dynamics of MBHs during galaxy mergers, then, appears to be fundamental to understand the link betweenn the cosmological assembly of galaxies and that of MBHs.

In the following, we will define two MBHs a *"MBH pair"* whenever the merger brings them to sub-kiloparsec separations. Through the physical processes outlined in §1.1.3,

---

[1] Results presented in this chapter have appeared in:
Callegari, Mayer, Kazantzidis, Colpi, Governato, Quinn, & Wadsley (2009),
Callegari, Kazantzidis, Mayer, Colpi, Bellovary, Quinn, & Wadsley (2011),
Guedes, Madau, Mayer, & Callegari (2011b).

such pairs may undergo further orbital decay, become bound binaries, and eventually coalesce via the emission of gravitational waves, which will hopefully be one of the main targets of the next generation of gravitational wave detectors such as the new incarnation of the Laser Interferometer Space Antenna (LISA) mission (Vecchio 2004). MBH orbital sinking has been shown to proceed quickly when both compact objects are hosted by steep stellar cusps approaching each other from close distances (Milosavljević & Merritt 2001), or when embedded in a massive circumnuclear gaseous disk under appropriate thermodynamic conditions (Mayer et al. 2007), but whether the large-scale merger can lead the MBHs to such a favorable configuration is still a matter of debate. Previous studies found that, following a galaxy merger, the relative distance of the MBHs in the remnant is very sensitive to the structure of the merging galaxies and to their initial orbit (Governato et al. 1994). Kazantzidis et al. (2005) showed that pairing is efficient in equal-mass disk galaxy mergers (with and without gas) with cosmologically relevant orbits, while the presence of a dissipative component seemed to be necessary for the pairing of MBHs in 1:4 mergers. Other studies (e.g., Springel et al. 2005; Johansson et al. 2009) focused on the effect of energetic feedback from black hole accretion onto the surrounding galaxy, but were not designed to follow the orbital evolution of MBHs. Moreover, substantially less effort has been devoted to examining the fate of MBHs in minor mergers (but see Boylan-Kolchin & Ma 2007), which are much more frequent in ΛCDM cosmologies than nearly equal-mass mergers (Lacey & Cole 1993; Fakhouri & Ma 2008). Investigating the necessary conditions for MBH pair formation in this regime is of primary importance for the search of gravitational waves and for MBH demographics. In 2.2.1 we describe the set of N-body/SPH simulations that we ran for this purpose, in 2.2.2 we report their results on the efficiency of the MBH pairing process, and in 2.2.3 we discuss some implications for recoiling black holes.

In addition to the orbital decay of the MBHs, another key issue in this context is accretion onto the black holes, if both galaxies and MBHs are expected to “grow” throughout cosmic history as hypothesized by standard models of MBH seed formation (see chapter 3). Many numerical studies have focused on the connection between galaxy mergers and MBH growth, specifically in relation to the MBH final mass, scaling relations and phenomenology of quasars (e.g., Di Matteo et al. 2005; Hopkins et al. 2005; Boylan-Kolchin & Ma 2007; Younger et al. 2008; Johansson et al. 2009). However, much less attention has been devoted to investigating the orbital decay and evolution of both MBHs *during* mergers, particularly in the unequal-mass regime which comprises the vast majority of such events. As argued in the following, the formation of unequal-mass MBH pairs at sub-kpc scales is sensitive to the details of the gas dynamics during the merger (confirming the earlier findings of Kazantzidis et al. (2005)). In 2.3 it is shown that the same is true for the accretion onto the MBHs and the evolution of their mass ratio, which is a fundamental parameter driving their subsequent evolution on nuclear scales (e.g., Dotti et al. 2007; Lodato et al. 2009). In

2.3.1 we describe the simulations of minor mergers of disk galaxies used for this part of the study, and in 2.3.2 we discuss in detail the mass evolution of MBHs throughout the pairing process.

2.2 Formation of close MBH pairs

2.2.1 The simulations

The simulations discussed in this whole chapter are a set of mergers between two disk galaxies with varying orbits and gas contents. All galaxy models were initialized as three-component systems following the method outlined in Hernquist (1993). They comprise a Hernquist spherical stellar bulge (Hernquist 1990), an exponential disk with a gas mass fraction $f_{\rm g}$, and an adiabatically contracted dark matter halo (Blumenthal et al. 1986) with an initial NFW profile (Navarro et al. 1996). A collisionless particle representing the MBH was added at the center of each galaxy.

The primary galaxy model at $z = 0$ has morphological parameters consistent with a Milky Way-like galaxy, with a virial velocity $V_{\rm vir} = 145$ km/s and a halo concentration parameter $c = 12$ (Bullock et al. 2001), a disk mass fraction $M_d = 0.04 M_{\rm vir}$, and a bulge mass fraction $M_b = 0.008 M_{\rm vir}$. The mass of its central MBH is $M_{\rm BH} = 3 \times 10^6$ $\rm M_\odot$. The disk scale height and the bulge scale radius are $z_0 = 0.1 R_d$ and $a = 0.2 R_d$ respectively, R_d being the exponential disk scale length. R_d is determined self-consistently for each model from m_d and the spin parameter of the dark halo $\lambda = 0.04$ (Vitvitska et al. 2002), following Mo, Mao, & White (1998) (MMW hereafter) which yields disk galaxies lying on the Tully-Fisher relation. Satellite galaxies were initialized with the same relations between structural parameters, and with the mass in each component scaled down by q.

We also performed merger simulations with initial conditions rescaled to $z = 3$ keeping $V_{\rm vir}$ fixed as expected for the progenitors of our $z = 0$ models (Li et al. 2007). Following MMW, all masses, positions and softening lengths were rescaled by a factor $H(z = 3)/H_0$, i.e. the ratio between the Hubble constant at $z = 3$ and its present-day value for a ΛCDM "concordance" cosmology ($H_0 = 70$ km s^{-1} Mpc^{-1}, $\Omega_{\rm m} = 0.3$, $\Omega_\Lambda = 0.7$). The halo concentration $c = 3$ was again chosen according to Bullock et al. (2001). Considering high-redshift mergers is crucial for two main reasons. First, the merger rate increases with look-back time, and a large fraction of the gravitational wave signal from coalescences of MBH binaries is predicted to originate from this cosmic epoch at the corresponding mass scale (Sesana et al. 2005; Volonteri et al. 2003). Moreover, mergers of very unequal-mass galaxies would take of the order of a Hubble time to completion if performed with typical $z = 0$

q	SF	f_g	z	BH final distance[a]	notes
0.25	no	0	0	2 – 4 kpc	-
0.25	yes	0.1	0	200 pc	-
0.1	no	0	3	1 – 6 kpc	-
0.1	no	0	3	1 – 5 kpc	high-res
0.1	yes	0.1	3	400 pc	-
0.1	yes	0.3	3	70 pc	-
0.1	yes	0.3	3	~3 kpc	retrograde

Table 2.1: Summary of simulations discussed in 2.2. All simulations are coplanar.
[a] When possible, estimates of pericenter and apocenter of the orbit of the lighter MBHs inside the merger remnant are given.

orbits, while the smaller orbital times and larger densities expected for high-z mergers makes them more suitable candidates to harbor MBH pairs.

The merger orbital parameters were chosen to be representative of merging halos in cosmological simulations (Benson 2005): the baricenters of the two galaxies were placed at a distance equal to the sum of their virial radii and set on parabolic orbits with pericentric distances of 20% the virial radius of the most massive halo. All mergers considered in this section are coplanar and prograde, except for one retrograde case. The MBHs in these simulations fall in the typical range of masses whose coalescences would have been detectable with the now “old” LISA design (Sesana et al. 2005).

We ran collisionless (“*dry*”, with $f_g = 0$) and gasdynamical mergers with the same gas fraction in the primary and secondary galaxies, either $f_g = 0.1$ or 0.3. In gasdynamical runs, atomic gas cooling and star formation (§1.2.2) were allowed, with $n_{\rm SF} = 0.1$ atoms cm^{-3} and $T_{\rm SF} = 2 \times 10^4$ K. A summary of this first set of simulations is presented in Table 2.1. In each galaxy (except for a very high-resolution test, see 2.2.2), we employed 10^6 particles for the halo, and, initially, 2×10^5 star particles and 10^5 gas particles, when included. The force softening was 100 pc in our reference model, scaled down by $q^{1/3}$ in the satellites, and by $H(z)/H_0$ in high-z runs, yielding a force resolution of $\sim$ 20 pc in the satellite galaxy for $q = 0.1$ at $z = 3$. With such a high particle number, the masses of star particles in the satellite is an order of magnitude lower than $M_{\rm BH}$, ensuring that MBH dynamics is not affected by spurious two-body collisions. In what follows, we define two MBHs as a “pair” if their relative orbit shrinks down to a separation equal to twice the softening. From these distances, a MBH binary may form in $\sim$ 1 Myr (e.g., Mayer et al. 2007).

2.2.2 Orbital evolution

Here we discuss first the relatively simpler case of collisionless mergers, and then analyze the role of gas in determining the fate of the two MBHs.

Collisionless mergers

In collisionless runs, the satellite is not able to dissipate energy gained through tidal shocks at pericentric passages (as discussed e.g. in Gnedin et al. (1999); Taffoni et al. (2003)). For $q = 0.25$, dynamical friction on the dark matter halo of the more massive galaxy is efficient, and the satellite sinks down to a few ~ 10 kpc from the center after 3 orbits. At that point the central density of the satellite has decreased considerably because of tidal heating (Kazantzidis et al. 2004). Its innermost region is then tidally disrupted, leaving the small MBH at a distance of a few kiloparsecs. The dynamical friction timescale has now greatly increased, because the mass of the small "naked" MBH is orders of magnitude lower than that of the satellite's core that once surrounded it. No pair is formed, and the smaller MBH is left wandering a few kiloparsecs away from the center of the remnant (Fig. 2.1). Note that, in this regime, the dynamical friction of the MBH is poorly modelled by the simulation, because the dark matter component is still dynamically important at kiloparsec distances from the center of the remnant: even at high resolution, the mass of the dark matter particles of the primary galaxy is comparable with that of the MBH. However, the dynamical friction timescale needed for the "naked" MBH to reach the center of the remnant can be estimated applying Chandrasekhar's formula locally, and it turns out to be longer than a Hubble time. Hence we conclude that the two MBHs will not form a pair.

In the $q = 0.1$ case, dynamical friction is rather ineffective even before satellite disruption: the sinking timescale is longer than a Hubble time for a $z = 0$ merger, owing to the low initial mass of the satellite and to mass loss due to tidal stripping (Colpi et al. 1999). However, since mergers are much more common at higher redshift, when orbital times are shorter by a factor $H(z)/H_0$, we performed $q = 0.1$ mergers starting with conditions expected at $z = 3$, an epoch at which these MBH pairs are predicted to be most typical in standard scenarios of MBH evolution (Volonteri et al. 2003). This is completed in ~ 2.5 Gyr. Similarly to the $q = 0.25$ case, a wandering MBH is left at several kiloparsecs from the center of the primary (Fig. 2.1). In order to check that the tidal disruption of the core was not affected by numerical heating, we ran the same merger with a 5 times higher mass resolution in the stellar component of both galaxies, and correspondingly higher force resolution; no significant difference in the MBH orbit was found (Table 2.1). Therefore, even in this $z = 3$ case the two MBHs do not form a pair.

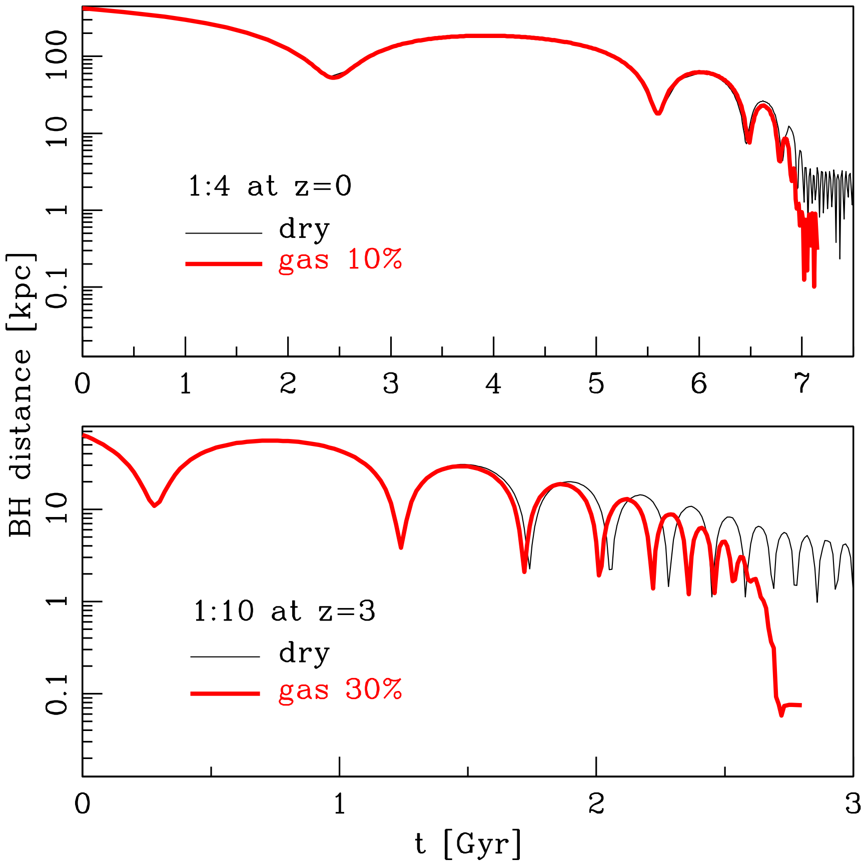

Figure 2.1: Separation of the MBHs as a function of time in four of our prograde merger simulations. *Upper panel*: MBH distance in $q = 0.25$ mergers; the thin and thick lines refer to the dry and wet cases, respectively. *Lower panel*: MBH distance for $q = 0.1$, $z = 3$; the thin and thick line refer to the dry and $f_g = 0.3$ cases, respectively.

Dissipational mergers with star formation

The presence of a star-forming gaseous component crucially affects the orbital decay of the MBH via its dynamical response to tidal forces and torques.

The orbits of dry and wet $q = 0.25$ mergers differ only after the first couple of orbits (~ 6 Gyr, see Fig. 2.1). At second pericenter, tidal forces excite a strong bar instability in the satellite. Dissipation in the gas and torques exerted by the stellar bar onto the gas drive a gaseous inflow toward the center of the satellite (Fig. 2.2), increasing the central star formation rate by a factor of 3. Thus, the potential well of the satellite deepens, ensuring resilience of its central part to tidal stripping and shocks even when it plunges near the center of the primary. As a consequence, the small MBH continues to sink quickly, because it remains embedded in the massive core of the satellite. A pair of MBHs is formed in this case at odds with the collisionless case, confirming previous results obtained with a different modelling of SF and feedback (Kazantzidis et al. 2005).

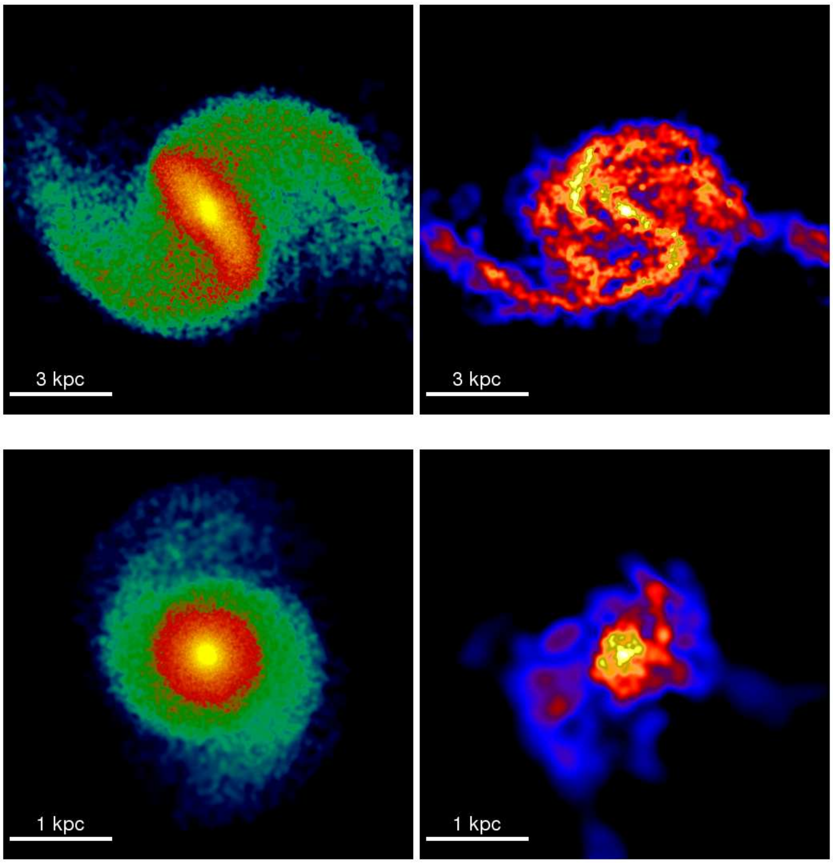

Figure 2.2: The images show the color-coded density of stars (*left columns*) and gas (*right columns*) of the satellites. *Upper panel*: the wet 1:4 case at $t = 5.75$ Gyr (marked in red on the curve); each image is 12 kpc on a side, and colors code the range $10^{-2} - 1\ \mathrm{M}_\odot\ \mathrm{pc}^{-3}$ for stars, and $10^{-3} - 10^{-1}\ \mathrm{M}_\odot\ \mathrm{pc}^{-3}$ for the gas. *Lower panel*: density maps at $t = 1.35$ Gyr for the 1:10 $f_g = 0.3$ case; images are 4 kpc on a side (color coding as in upper panel).

In $q = 0.1$, $z = 3$ wet mergers, both $f_\mathrm{g} = 0.1$ and 0.3 were employed; the latter should be a more realistic assumption, since disk galaxies at $z = 3$ are believed to have a higher gas mass fraction (e.g., Franx et al. 2008). In this mass range, star formation and supernovae feedback affect the structure of the ISM in the disks quite dramatically (see also Governato et al. 2007, 2010). The disks develop a clumpy and irregular multi-phase structure, and turbulent velocities of the gas become a significant fraction (~30%) of the circular velocity in this mass range ($V_\mathrm{vir} = 64$ km s^{-1}). Star formation in the center of the satellite is enhanced compared to the same model evolved in isolation, even though the *total* star formation integrated over the whole galaxy is unchanged (Fig. 2.3). Contrary to the higher-mass case of the 1:4 merger, the concentrated star formation and the turbulent motions of the gas stabilize the disks against bar instability (see Fig. 2.2). In the absence of bar-driven torques, the strong gaseous inflow seen for higher-mass objects ($q = 0.25$) does not happen for $q = 0.1$. Yet, compressive tides (Renaud et al. 2009) drive some gas towards the center, explaining the enhanced central star formation (Fig. 2.3). During the first three orbits, the $f_g = 0.1$ case preserves its initial central density owing to the mild mass inflow, rather than lowering it as in the collisionless case, while the $f_{\rm g} = 0.3$ satellite develops an even steeper *stellar* cusp. Once the satellite goes through the second pericentric passage, its ISM is prone to ram pressure stripping by the gas disk of the primary galaxy. The ram pressure stripping radius $R_{\rm ram}$, outside which the satellite is not able to retain gas, can be expressed as

$$R_{\rm ram} = \frac{2\pi P_{\rm ram}}{\rho_{\rm g,sat}(R_{\rm ram})\, g(R_{\rm ram})}$$

for edge-on collisions (Marcolini et al. 2003), where $\rho_{\rm g,sat}(R)$ is the gas density profile and $g(R)$ the gravitational acceleration due to the satellite's self-gravity. The ram pressure $P_{\rm ram} \approx \rho_{\rm ext} V^2$ depends on the gas density $\rho_{\rm ext}$ in the primary, and on the relative velocity V between the two galaxies. Contrary to a test run we conducted without SF, in which a large amount of gas was funnelled by torques toward the region inside $R_{\rm ram}$ (see Fig. 1.3 on p. 13), the turbulent and clumpy ISM offers a large effective area to ram pressure, particularly in these lower-mass satellites. Nearly 90% of the gas is swept away when they first enter the disk of the primary, while what remains is stripped during the next orbit: at $t = 2$ Gyr, the satellites in all three 1:10 cases have lost all their gas content, even in their central region. The analytical estimate of $R_{\rm ram}$ corroborates the numerical result.

From this moment onward, the satellite with initial $f_{\rm g} = 0.3$ is a *cuspy, gas-poor object*, subject to dynamical friction in the stellar and gaseous background. Its sinking is relatively quick because the steeper stellar density profile implies a larger bound mass, enhancing dynamical friction relative to the dry merger case. Moreover, its response to tidal shocks is more adiabatic (Gnedin et al. 1999), preserving it from tidal disruption. On the contrary, the satellite of the $f_{\rm g} = 0.1$ run undergoes a slower decay because of its smaller bound mass. It then experiences a higher number of tidal shocks at pericentric passages which further decrease its density, until its complete disruption. As a consequence, the $f_{\rm g} = 0.3$ merger leaves the lighter MBH at 70 pc from the more massive one (Fig. 2.1, Tab. 2.1) in a gas-rich environment, where the dynamical friction timescale for the MBH to sink to the center, based on Chandrasekhar's formula, is very short (< 1 Gyr). Instead, in the $f_{\rm g} = 0.1$ case the final distance of the MBHs is ~ 400 pc; at such separations the dynamical friction timescale is of a few billion years. Hence the pairing will occur within one Hubble time in both cases, but will be considerably faster (thus retaining its temporal association with the galaxy merger itself) in the $f_{\rm g} = 0.3$ case.

The merger dynamics is less favorable to MBH pairing in the retrograde case (Fig. 2.4), where the orbital angular momentum has opposite sign relative to the angular momenta of the two galaxies. This result is expected also on theoretical grounds: in fact, in this configuration, the satellite's velocity with respect to the "background" primary galaxy (whose halo is also rotating according to its λ) is much higher than in the prograde case, and even

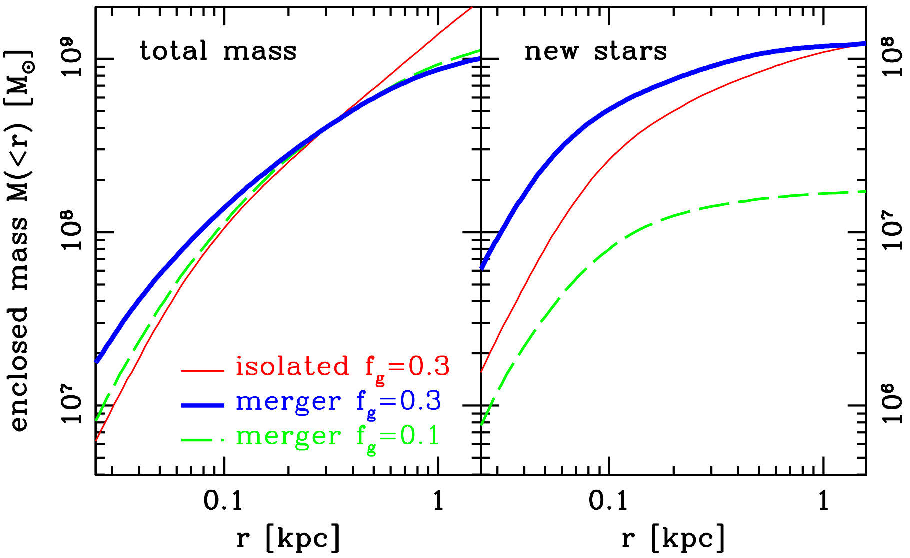

Figure 2.3: Cumulative bound mass profiles of $z = 3$, $q = 0.1$ satellites. Thin red lines refer to the $f_g = 0.3$ satellite in isolation, thick blue lines to the $f_g = 0.3$ merging satellite, and dashed green lines to the merging $f_g = 0.1$. All data refer to the third apocenter, or equivalent time in isolation ($t = 1.8$ Gyr). *Left panel*: total bound mass profiles. The more gas-rich satellite develops a higher concentration during the merger, compared to the other cases. Tidal truncation and gas removal cause a factor of ~ 2 difference in mass at 2 kpc between isolation and merging cases. *Right panel*: bound mass in stars formed after the start of the simulation. The total amount of stars formed depends roughly only on the initial f_g, but SF is more localized in the center during the merger because of tidal forces. The more gas-rich merging satellite undergoes the strongest central SF burst, developing a higher central density.

more so around pericenters, where the primary disk, which contributes significantly to the drag, also rotates in the opposite direction. Since for high relative speed dynamical friction decreases roughly as the inverse square of the speed, the orbital decay of the satellite is much slower[2]. As a consequence, the satellite undergoes many more tidal shocks at pericentric passages, and is disrupted by tidal heating before sinking to distances < 1 kpc. Not unlike the prograde collisionless case, its MBH is thus deposited at large radii from the center of the merger remnant, where the dynamical friction timescale is much longer than a Hubble time.

2.2.3 Gravitational recoils in the merger remnants

Assuming that the timescale for orbital sinking of a MBH pair is short enough, the two black holes should reach separations where energy loss via emission of gravitational waves becomes important. In this regime, the orbit shrinks very quickly until the two event hori-

---

[2] Ram pressure stripping is also more effective in this case, but since all gas is stripped from the satellite even in the prograde merger, this effect does not add anything to the picture here presented.

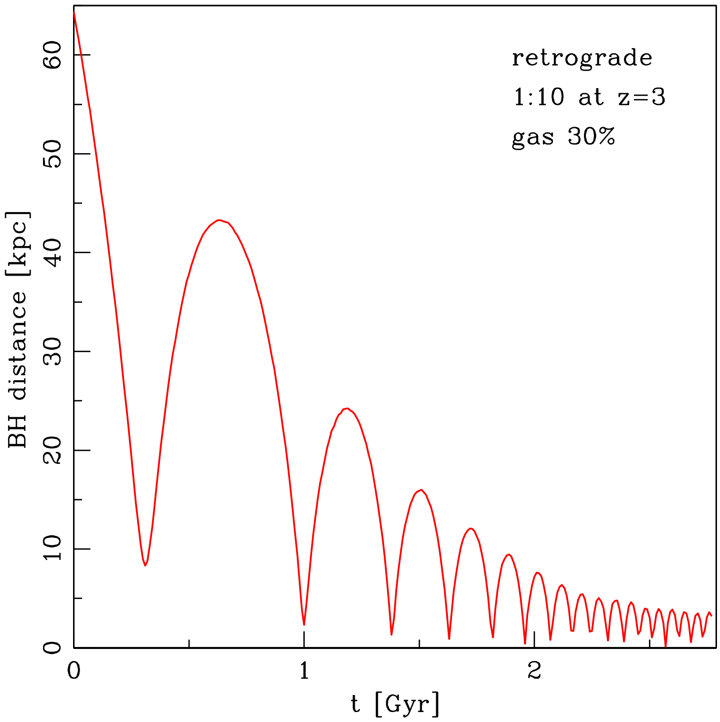

Figure 2.4: Separation of the MBHs as a function of time in the 1:10 retrograde merger with $f_g = 0.3$, up to the time of complete satellite disruption.

zons are eventually expected to merge. Asymmetries in the configuration of the coalescing binary during the very last stages of the inspiral cause the beaming of gravitational wave radiation in a preferred direction. To conserve linear momentum, the remnant hole recoils in the direction opposite to the radiative flux (Peres 1962; Bekenstein 1973; Fitchett & Detweiler 1984). The recoil or “kick" velocity, $V_{\rm kick}$, depends on the binary mass ratio and on the magnitude and direction of their spins, and does not depend on the total mass of the binary. Recent advances in numerical relativity (Pretorius 2005; Campanelli et al. 2006) have allowed several groups (Baker et al. 2006; Herrmann et al. 2007; González et al. 2007) to estimate the resulting recoil velocities as a function of mass ratio and spin (Baker et al. 2008; Campanelli et al. 2007). These studies show kick velocities in the range from ~ 100 km s^{-1} to a maximum speed of 3750 km s^{-1}, obtained for equal-mass maximally-spinning black holes with anti-aligned spin vectors in the orbital plane of the binary (Campanelli et al. 2007).

When $V_{\rm kick}$ is lower than the escape speed of the host, the MBH will wander through the galaxy in an orbit that depends on the detailed characteristics of the host potential. Fig. 2.5 shows the circular velocity profiles (which measure the depth of the potential well) in two of the final states of the mergers in §2.2.2, and an analogous 1:1 merger taken from Mayer et al. (2007). As discussed above, the most important difference between the

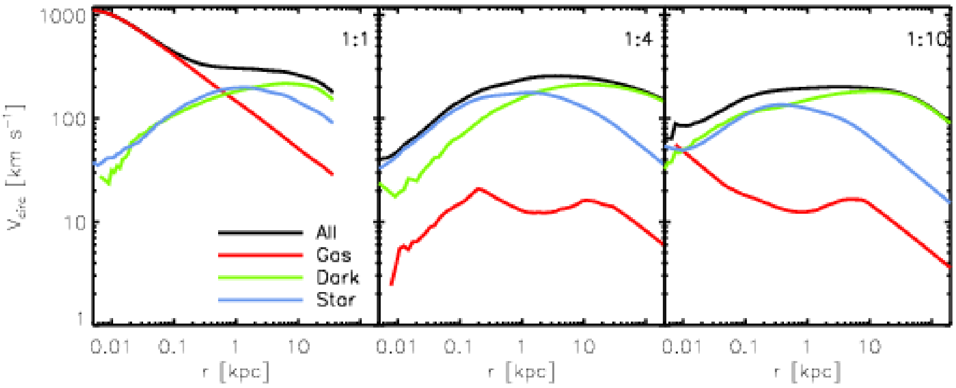

Figure 2.5: Rotation curves of three different merger remnants. *Left panel*: remnant from a higher resolution 1:1 merger from Mayer et al. (2007) between two galaxies analogous to our reference model in §2.2.1, with $f_g = 0.1$ at $z = 0$. *Middle panel*: remnant of the 1:4 merger with $f_g = 0.1$ at $z = 0$. *Right panel*: remnant of the 1:10 merger with $f_g = 0.3$ at $z = 3$. The colors represent the circular velocity profiles of the gas (*red*), stars (*blue*), dark matter (*green*), and total (*black*), respectively.

major and the minor mergers is that gaseous inflows are weak enough to be converted into stars on the timescale of the merger. Moreover, bar-driven torques are much weaker in minor mergers.[3] Therefore, we expect the MBH return time in minor mergers to be largely determined by dynamical friction against the stars and the dark matter. In addition, the lower central densities imply a lower escape speed, so we expect that black holes with a given kick velocity will travel larger distances in this case compared to a major merger. The escape speeds from the center in the perpendicular ($\theta = 90°$) and parallel ($\theta = 0°$) directions to the angular momentum vector of the gaseous disk are $v_e^{\perp} = 520\,\mathrm{km\,s^{-1}}$ and $v_e^{\parallel} = 490\,\mathrm{km\,s^{-1}}$ in the 1:4 merger, respectively, and $v_e^{\perp} = 490\,\mathrm{km\,s^{-1}}$ and $v_e^{\parallel} = 450\,\mathrm{km\,s^{-1}}$ in the 1:10 merger.

In Guedes et al. (2011b), an analytical scheme aimed at integrating the orbits of recoiling MBHs inside N-body/SPH merger remnants was developed. The equation of motion of the MBH was studied under the action of a conservative force $\vec{\nabla}\Phi$ and a damping frictional term:

$$\frac{d\vec{v}}{dt} = -\vec{\nabla}\Phi + \vec{f}_{\rm DF}\,,$$

where the total gravitational potential is $\Phi = \Phi_{\rm gas} + \Phi_{\rm stars} + \Phi_{\rm dark}$. Such formalism was tuned by comparing with a small set of actual numerical experiments in which the MBH pair in the remnant was replaced with a single black hole subject to different velocity kicks.

Fig. 2.6 shows the first apocenter distance $R_{\rm max}$ after the kick, estimated from the semi-analytical approach, for MBHs recoiling in the 1:1 ($z = 0$), 1:4 ($z = 0$), and 1:10 ($z = 3$)

---

[3] This is especially true in the primary galaxy, which is only weakly destabilized by the secondary – a phenomenon which will be analyzed in §2.3.2 in relation to accretion onto the MBHs.

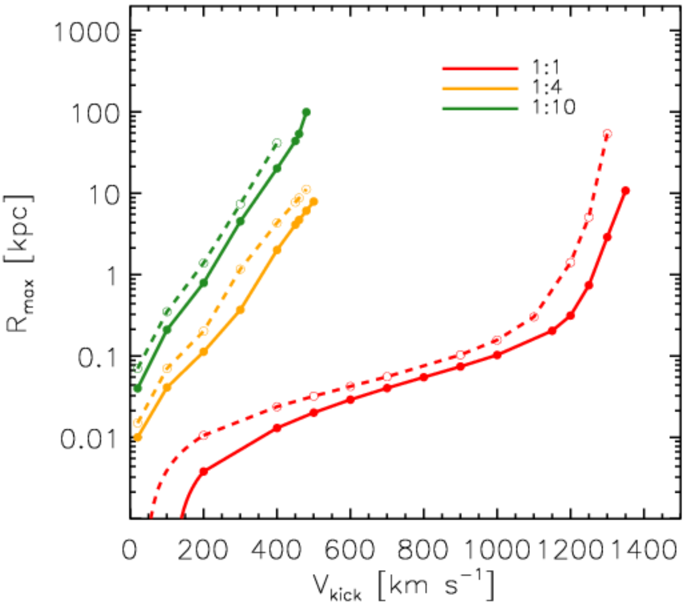

Figure 2.6: First apocenter distance of recoiling MBHs as a function of kick velocity. *Red:* 1:1 merger remnant. *Orange:* 1:4. *Green:* 1:10. *Solid curves:* MBHs recoiling in a direction perpendicular to the disk angular momentum vector. *Dashed curves:* MBHs recoiling in a direction parallel to the disk angular momentum vector.

merger remnants along a direction that is either parallel or perpendicular to the disk angular momentum vector. In the 1 : 4 merger remnant, a kick of $V_{\rm kick} = 500\,{\rm km\,s^{-1}}$ perpendicular to the disk can displace the hole by $R_{\rm max} \sim 10$ kpc. The same initial speed yields a maximal separation of $R_{\rm max} = 100$ kpc in the 1 : 10 case at $z = 3$, reflecting the much shallower potential well of this remnant. The detailed modelling, including an in-depth analysis of the observability of such MBHs as kinematically or spatially offset AGNs, can be found in Guedes et al. (2011b).

2.3 Growth of the MBHs

2.3.1 The simulations

In this second set of simulations, our reference galaxy model is the $z = 3$ progenitor of the Milky Way-type disk galaxy described in 2.2.1. Such a progenitor is constructed assuming a constant $V_{\rm vir} = 145$ km s^{-1} between redshift 0 and 3 (Li et al. 2007), and rescaling the mass and size of the $z = 0$ model by the ratio $[H(z = 3)/H_0] = 0.224$ of the Hubble constant at $z = 3$ over its present-day value (Mo et al. 1998) for a ΛCDM concordance cosmology ($H_0 =$ 70 km s^{-1} Mpc^{-1}, $\Omega_{\rm m} = 0.3$, $\Omega_\Lambda = 0.7$). Our choice for the galaxy masses in conjunction with the assumption that the MBHs follow the $M_{\rm BH} - M_{\rm bulge}$ relation (Häring & Rix 2004)

f_g primary	f_g satellite	θ [a]	notes
0.3	0.3	0°	reference run
0.3	0.5	0°	1.7×10^5 SPH particles in the satellite[b]
0.1	0.1	0°	-
0.3	0.3	20°	-
0.3	0.3	45°	-
0.3	0.3	0°	small pericenter (0.8 kpc)

Table 2.2: Summary of MBH growth simulations (all $z = 3$ 1:10 mergers) of §2.3.

[a] The orbital plane and satellite disk are inclined by an angle θ with respect to the disk of the primary galaxy.

[b] This number has been chosen in order to have the same ratio of gas particle mass to MBH mass in both primary and satellite galaxies, as happens for all other simulations here discussed.

result in MBH masses of 6×10^4 M$_\odot$ and 6×10^5 M$_\odot$ for the satellite and primary MBH respectively, with an initial MBH mass ratio $q = q_{\rm gal}$.

Also in this part of the work, the N-body realizations consist of 10^6 particles in the dark matter halo and 2×10^5 stellar particles in each galaxy. In addition, each galaxy is initialized with 10^5 gas particles in the disk, except for one case (see Table 2.2). We adopted a force resolution of 45 pc for both the dark matter and baryonic particles of the larger galaxy, while for the satellite galaxy we used 20 pc.

Following the procedure outlined in §2.2.1, we choose merger orbital parameters that are common for merging halos in cosmological simulations. All simulations start with the baricenters of the two galaxies at a distance equal to the sum of their virial radii. Their orbit is initially parabolic, with pericentric distance $R_{\rm p} = 8$ kpc, equal to 20% of the primary galaxy's virial radius, except for one case with a 10 times smaller pericenter. We also vary gas fractions and orbital inclinations, noting that only prograde encounters were considered for this part of the work: as retrograde mergers seem to efficiently suppress pairing for typical orbits (see discussion above), we dedicated our computational time to cases which should be more relevant to actual MBH close pairs.

A summary of the simulations presented in this section can be found in Table 2.2. Here we employ both the SF + SN feedback and the MBH accretion sub-grid recipes (§1.2). The AGN feedback efficiency $\epsilon_{\rm fb} = 0.005$ is tuned so that the constraints related to our initial galaxy models can be satisfied (§2.3.2). In principle, the feedback efficiency depends both on the employed sub-grid model for the interstellar medium and the numerical resolution. For these reasons, our specific choice differs from a number of earlier studies (e.g., Springel et al. 2005).

Since the simulations are halted at satellite disruption, the orbital decay of its MBH is determined by the well-resolved drag forces acting on its host galaxy; therefore, we do

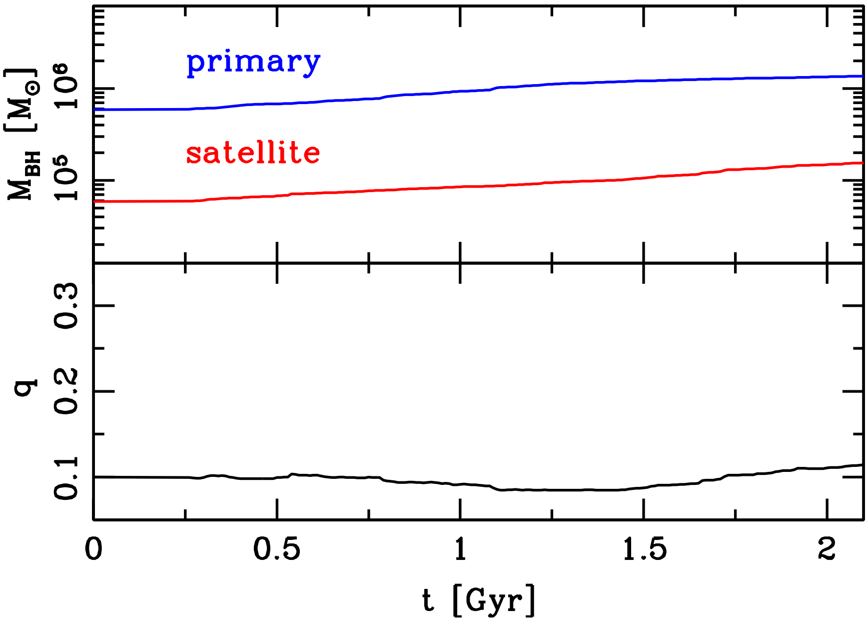

Figure 2.7: Mass growth of the MBHs in the primary (blue) and secondary (red) galaxies *in isolation* for the reference 1:10 run with $f_g = 0.3$. The y axis scales are as in Fig. 2.8.

not include a sub-resolution Bondi drag term, as employed recently by, e.g., Younger et al. (2008). Analogously, we do not employ any other numerical recipe that forces MBH orbital decay, because our aim is to study the growth of MBHs *in relation to the efficiency of close MBH pair formation*. In particular, the black holes were not repositioned at the local minimum of the gravitational potential at each time-step (e.g., Johansson et al. 2009).

2.3.2 Large-scale dynamics of MBH accretion

We will first discuss our reference simulation, where the gas fraction in both disks of the primary and satellite galaxy is $f_g = 0.3$. Then, this reference case will be compared with the other merger simulations of different gas fraction and orbital parameters summarized in Table 2.2.

Reference simulation: coplanar merger with $f_g = 0.3$

In order to assess the effects of the merger on the mass growth of the MBHs, we first performed simulations of the primary and satellite galaxies evolved *in isolation* including our accretion recipe. For these tests, we chose the $f_g = 0.3$ galaxy models of our reference simulation. In these simulations, the mass ratio of the two MBHs in the isolated galaxies does not deviate significantly or systematically from the initial $q = 0.1$ (the maximum fluctuation around this value is $\sim 10\%$) over a period of more than 2 Gyr, equivalent to $\sim$ 10–20 dynamical times (Fig. 2.7). Therefore, we satisfy our working hypothesis that, in

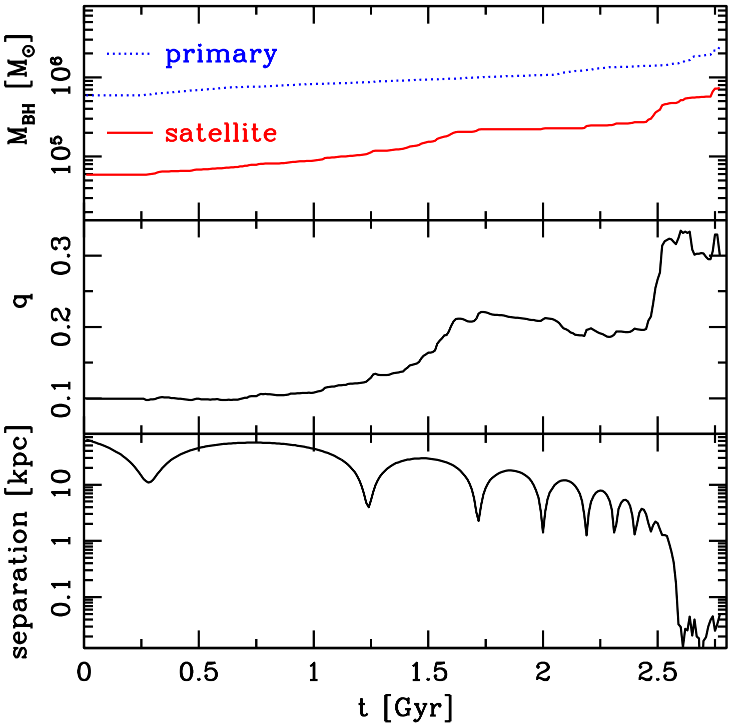

Figure 2.8: Coplanar merger with a disk gas fraction of $f_g = 0.3$ in both galaxies. *Upper panel*: Evolution of the mass of the MBH, M_{BH}, in the primary (dotted line) and satellite galaxy (solid line) as a function of time. *Middle panel*: Evolution of the mass ratio q of the two MBHs as a function of time. *Lower panel*: Orbital decay of the two MBHs as a function of time.

equilibrium conditions, the q of the black holes corresponds to the galaxy mass ratio – a constraint that follows from our initial choice of $M_{BH} - M_{bulge}$ and galaxy morphology. In addition, these tests provide a measure of the MBH "quiescent" accretion: mass-doubling timescales of the MBHs evolved in isolation are ~ 2 Gyr, i.e. comparable to the typical duration of one of the mergers presented below. This result indicates that any larger MBH growth or large variation of q during the merger does not stem from secular evolution in the galaxy models or from numerical effects, but rather should be attributed to the galaxy encounter itself.

Fig. 2.8 presents the mass evolution of the two MBHs, the evolution of their mass ratio, and their relative separation as a function of time in the reference merger. By the end of the merger ($t \sim 2.6$ Gyr), owing to dynamical friction, the two MBHs have formed a close pair in the nucleus of the remnant at a separation comparable to the adopted force resolution. This finding confirms the results in §2.2 and suggests that gas accretion onto the MBHs and associated feedback is not critical for pair formation in this case. The primary MBH grows quiescently throughout most of the merger, while the secondary increases its mass tenfold by the time the pair forms. The corresponding increase in the mass ratio of the two

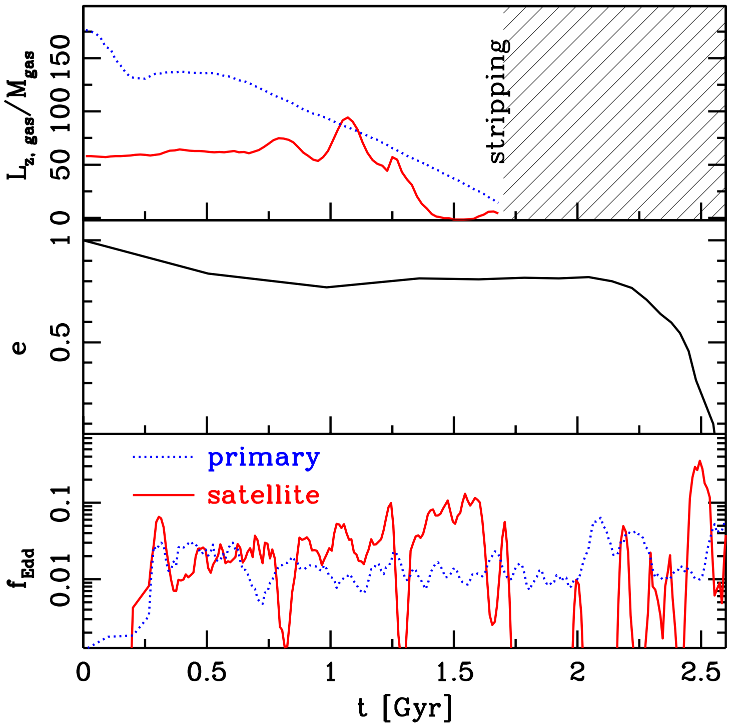

Figure 2.9: Evolution of properties related to the coplanar merger with $f_g = 0.3$ in both galaxies. *Upper panel*: Gas specific angular momentum in the direction of the disk rotation axis in the primary (dotted line) and companion galaxy (solid line) (see text for details). *Middle panel*: Orbital eccentricity of the satellite MBH inside the disk of the primary. *Lower panel*: Eddington ratios, $f_{\rm Edd}$, of the mass accretion rates onto the primary (dotted line) and secondary MBH (solid line).

MBHs, q, occurs in two distinct episodes, whose physical origin is elucidated in Fig. 2.9.

The upper panel of Fig. 2.9 shows the evolution of the gas specific angular momentum in the direction of the disk rotation axis, $L_{z,\rm gas}/M_{\rm gas}$, as a function of time for both galaxies. For this calculation, the gas particles that contribute to the baryonic mass within the central 5 softening lengths of each galaxy right before the third pericentric passage ($t = 1.7$ Gyr) were traced back in time. This figure shows that most of the gas in the nuclear region of the satellite at this stage has lost its specific angular momentum on a relatively short timescale. The reason for the angular momentum loss are the strong tidal torques that occur near the second pericentric passage ($t = 1.2$ Gyr) and are induced by the gravitational interaction with the primary galaxy. As a result, a ~ 0.5 Gyr long accretion episode with a corresponding increase of q is observed. As shown in the lower panel of the same figure, the accretion rate $\dot{M}$ onto the satellite MBH is 10% of the Eddington limit $\dot{M}_{\rm Edd}$ (Eq. 1.4) during this phase. On the other hand, the gas that is funnelled near the center of the primary galaxy has been experiencing a nearly steady loss of specific angular momentum over a very long timescale (Fig.2.9). This indicates that angular momentum loss in the

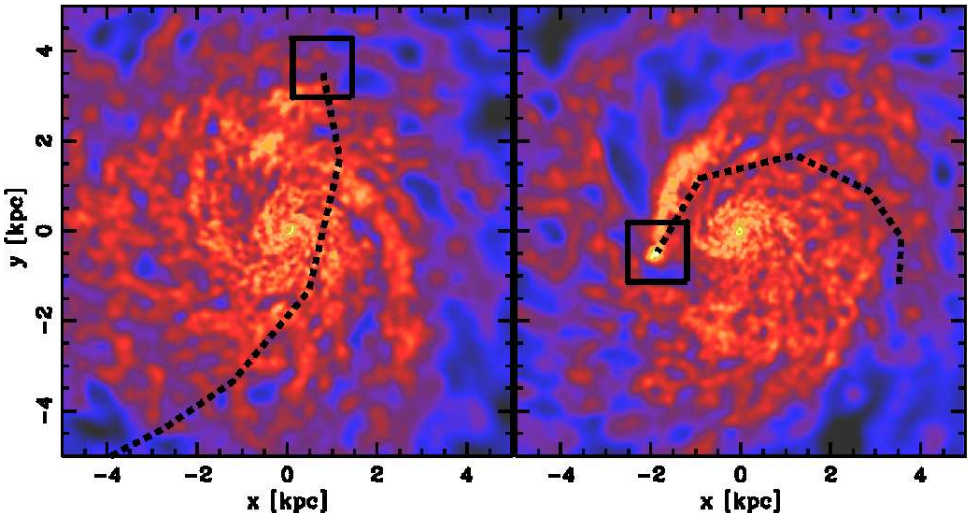

Figure 2.10: Gas density maps at $t = 2.33$ (*left panel*) and $t = 2.48$ Gyr (*right panel*), which correspond to just before and after the orbit of the secondary MBH circularizes inside the disk of the primary. The time span between these two snapshots corresponds roughly to two orbits of the satellite. The maps show the inner 5 kpc of the primary. Density is projected onto the $x - y$ plane and is color-coded on a logarithmic scale with brighter colors corresponding to regions of higher gas density. The black dashed line marks the trajectory of the satellite MBH and the square indicates the region around it. The satellite does not appear in the left panel, as ram pressure has stripped its entire gas content. On the contrary, the position of the satellite in the right panel is evidently traced by the overdensity and wake excited in the primary disk.

case of the primary galaxy is not caused by tidal torques arising from the interaction with the satellite, which would occur at pericentric passages and become stronger as the merger progresses. Rather, it is induced by secular evolution (i.e. spiral arms) which redistributes angular momentum throughout the disk. Indeed, the effect of initial transient spiral arms is evident during the first ~ 200 Myr. This agrees with the fact that mass growth of the primary MBH is essentially unchanged between the merger and the evolution in isolation.

As discussed above, around the third pericentric passage ram pressure exerted by the ISM of the primary galaxy strips all the gas from the satellite down to our force resolution. As a result, the satellite is now devoid of gas (as shown in left panel of Fig. 2.10), and accretion onto the smaller MBH is suddenly halted. A period of slowly decreasing q follows. During this phase ($t > 2$ Gyr), the more massive MBH continues to accrete gas from its host, experiencing an increase in its Eddington ratio $f_{\rm Edd} \equiv \dot{M}_{\rm BH}/\dot{M}_{\rm Edd}$ as the satellite galaxy is now orbiting close enough to excite stronger gas inflows in the primary disk.

The mass of the satellite MBH sharply increases again (with an associated second increase in q) at kiloparsec-scale separations. At this stage, the secondary MBH orbits inside the gaseous disk of the primary. The mass increase coincides with a sudden drop in the orbital eccentricity of the satellite MBH, as shown in the middle panel of Fig. 2.9. This drop

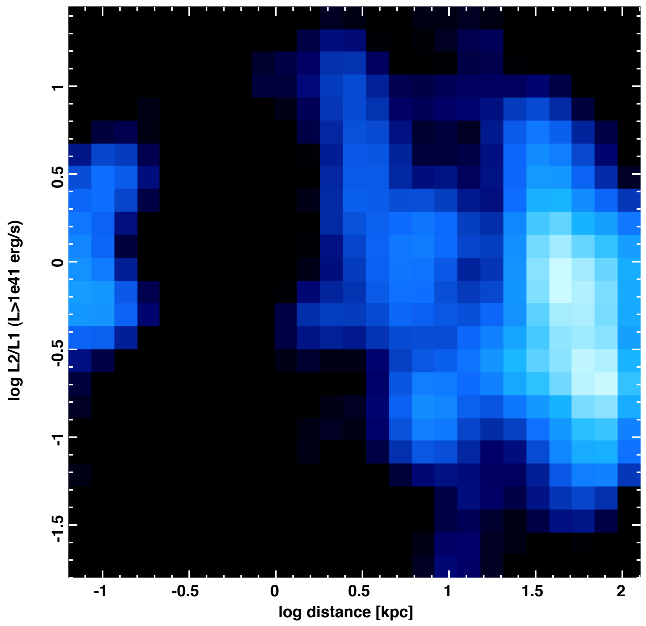

Figure 2.11: Probability density of observing a certain ratio of MBH luminosities vs. 3-dimensional separation, for the $f_g = 0.3$ 1:10 merger at $z = 3$. Here $L1$ is the luminosity of the primary MBH and $L2$ that of the satellite. No effects of inclination and/or obscuration have been added.

in eccentricity is caused by dynamical friction acting on the satellite along its prograde coplanar orbit in the high-density region of the primary disk. Such orbital circularization is analogous to that found for MBHs in circumnuclear disks (Dotti et al. 2009). Thus, the satellite MBH and its host stellar cusp are now moving with a low relative velocity with respect to the disk of the primary. As a consequence, they are able to collect surrounding gas with low angular momentum in the reference frame of the satellite, creating an overdensity (right panel of Fig. 2.10) from which material is efficiently accreted by the satellite MBH up to a peak $f_{\rm Edd} \sim 0.3$. On the other hand, accretion onto the primary MBH still relies on angular momentum transport by instabilities in the disk. Such instabilities, triggered by the sinking satellite, are stronger than at earlier times, but still not able to sustain high $f_{\rm Edd}$.

By the time the satellite is disrupted reaching the nuclear region of the merger remnant and the two MBHs form a close pair, the combination of strong tidal torques and orbital circularization acting on the companion galaxy has caused the MBH mass ratio to increase from $1:10$ to $1:3$, bringing it into a regime of “major” mass ratio.

This physical picture leads to a peculiar pattern of observability of double AGN activity for this merger (Fig. 2.11). The probability to detect both MBHs as active is highest around the apocenters of the first few orbits, where the system spends most of its time; because of the enhanced accretion in the satellite in this stage, the distribution of $q_L \equiv L_{\rm satellite}/L_{\rm primary}$ peaks at ratios larger than 0.1, which would be the value that correctly represents the merger mass ratio and the initial MBH q. At intermediate distances (pericentric passages), where tides are stronger, there is some probability to even observe the secondary MBH as more luminous. At separations of ~ 1 kpc, the observability drops as the MBHs enter the regime of fast decay when the orbit circularizes. There is a last window of detectability at roughly equal luminosities as the two MBH come close to our force resolution and the secondary is now embedded in the gaseous overdensity. Overall, the patterns in the observability of a dual AGN is complex, and does not reflect directly the mass ratio of the merger that triggered MBH accretion. An exploration of this phenomenon in a wider series of simulations is on its way (van Wassenhove et al., in prep.).

The role of gas fraction

Fig. 2.12 compares the evolution of the mass ratio of the MBHs q as a function of time in three mergers with different disk gas fractions, $f_{\rm g}$ (see Table 2.2). All of these mergers are on prograde, coplanar orbits. Again, we follow the evolution of the interacting systems up to completion of the orbital decay (satellite disruption). This figure shows that the first phase of increase in q, caused by dynamical destabilization of the satellite, happens in all three cases: due to the fact that inclination and orbit are fixed in these mergers, the torques acting on the satellites have the same strength. Interestingly, the highest value of q reached in the first stage traces roughly the amount of gas available for MBH fuelling. After this phase, in all the mergers we considered ram pressure is effective in removing gas from the satellite galaxy, once the two galaxy disks come into contact. When this happens, accretion onto the secondary MBH is halted.

Fig. 2.12 shows that the initial $f_{\rm g}$ does cause significant differences in the evolution of q also during the second stage of the mergers. Indeed, the second phase of strong accretion onto the satellite MBH is absent in the merger with the smallest gas fraction ($f_{\rm g} = 0.1$). As discussed earlier, mass growth during this phase becomes efficient only when the secondary MBH moves inside the gas disk of the primary galaxy and its orbit circularizes. Instead, in the case of $f_{\rm g} = 0.1$ the satellite does not sink below ~ 400 pc before being tidally disrupted, because it has not experienced strong gas inflows steepening its potential well during the first orbits (§2.2.2). At such large distances, the MBH orbit is still mildly eccentric, and the background density is not high enough to allow for the formation of an overdensity that could trigger the second accretion episode. As a consequence, the MBH mass ratio at the time of satellite disruption is 1:6, close to its initial value, and the naked satellite MBH will still take a few billion years to sink to the center of the remnant via dynamical friction.

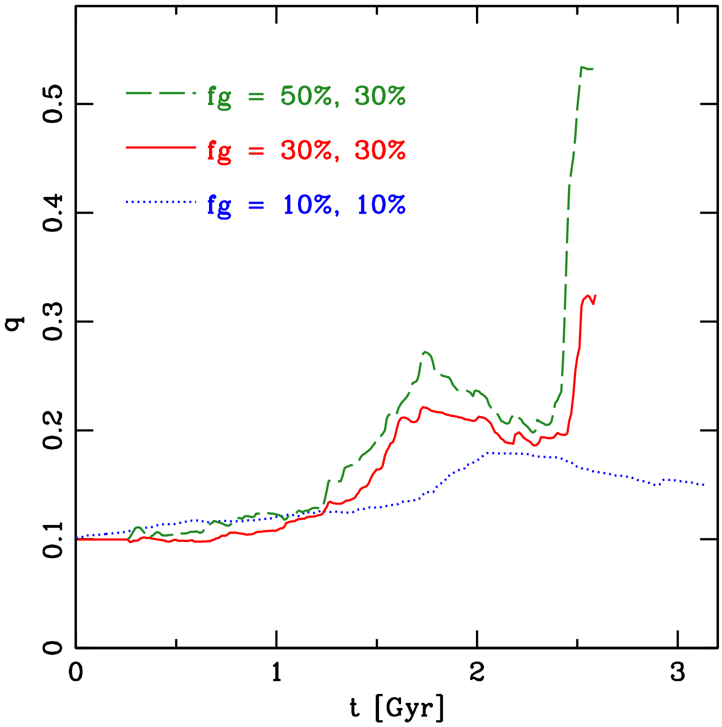

Figure 2.12: Evolution of the mass ratio q of the two MBHs as a function of time in coplanar mergers with different gas fractions f_g. Dotted (blue) and solid (red) lines show results for the mergers with gas fractions $f_g = 0.1$ and $f_g = 0.3$, respectively, in both galaxies. The dashed (green) line corresponds to a merger where the initial gas fractions are $f_g = 0.3$ in the primary and $f_g = 0.5$ in the satellite galaxy.

We now focus on the merger where the initial gas fraction in the primary and companion galaxies is equal to $f_g = 0.3$ and $f_g = 0.5$, respectively. Fig. 2.12 shows that this case is characterized by a much larger final increase in q compared to our reference case, where the initial gas fraction was equal to $f_g = 0.3$ in both galaxies. Bearing in mind that the only difference between the two initial conditions is the satellite f_g, and that the satellite gas has already been entirely stripped by ram pressure at this late stage, this interesting result can be explained as an effect of the different structure of the surviving satellite core and the different mass growth of its MBH. In fact, a larger initial gas fraction allows the satellite to build a denser stellar core via star formation in response to tidal perturbations during the first two orbits. Consequently, the nuclear region of the satellite is denser and more massive. It is therefore more efficient at collecting gas from the disk of the primary and it is subject to an enhanced sinking. As a result, the orbit of the secondary MBH undergoes circularization in a denser region of the primary disk, and is able to accrete more gas. Moreover, by the time the secondary MBH enters the disk of the primary, it is ~ 60% more massive compared to the case of $f_g = 0.3$. This difference in mass naturally enhances its accretion rate, which scales as $\propto M_{\rm BH}^2$ (as it is always below $M_{\rm Edd}$). At the end of this

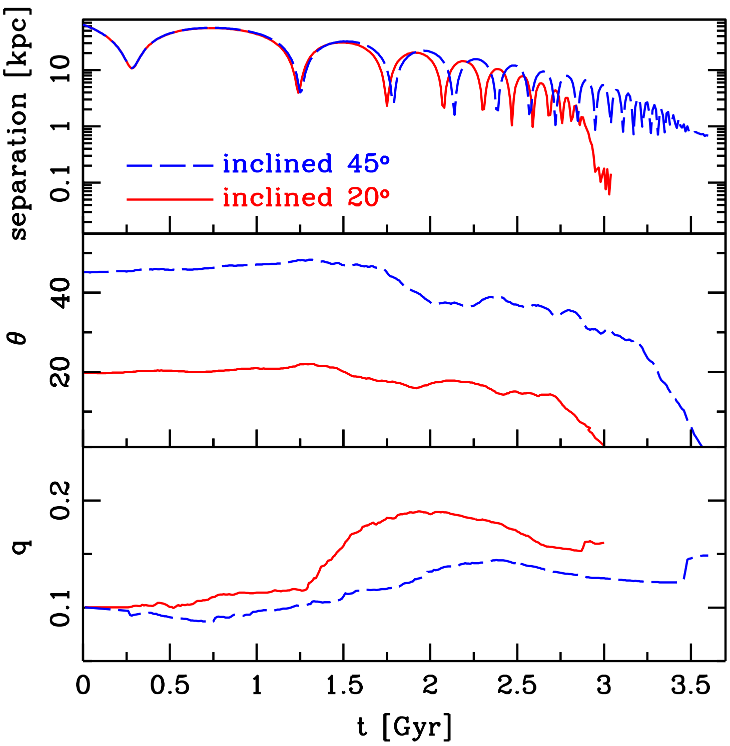

Figure 2.13: The evolution of orbital parameters as a function of time is shown for the inclined runs: the continuous (red) line shows data for the merger with 20° inclination, the dashed (blue) line for the one at 45°. *Upper panel*: MBH separation. As expected, sinking is more effective for more coplanar orbits. *Middle panel*: angle θ between the orbital plane of the two MBHs and the plane of the primary galaxy's disk. Orbit dragging onto the disk plane can be seen in both cases, once the satellite's orbit reaches the disk-dominated region of the primary galaxy. *Lower panel*: Mass ratio of the MBHs.

merger, the satellite MBH has sunk down to the center of the remnant, where a close MBH pair is formed at scales ~ 30 pc, comparable to our force resolution. The mass ratio of the pair at this point is the highest among all our simulations: $q = 0.5$.

The role of orbital parameters

As shown above, the evolution of the MBH mass ratio depends on processes (especially ram pressure stripping of gas and orbit circularization) that may be sensitive to the initial orbit of the merger itself. Here we discuss results from three simulations addressing the dependence on orbital parameters. In all of them, the gas fraction in the two galaxies was equal to that of the reference case, $f_g = 0.3$.

Upper panel of Fig. 2.13 shows the evolution of the MBH orbital separation in two merger simulations where the orbital plane and satellite disk were inclined with respect to the plane of the primary disk, by 20° in one case, and 45° in the other. Torques acting on the satellite during the early phases of the merger are weaker for higher inclinations

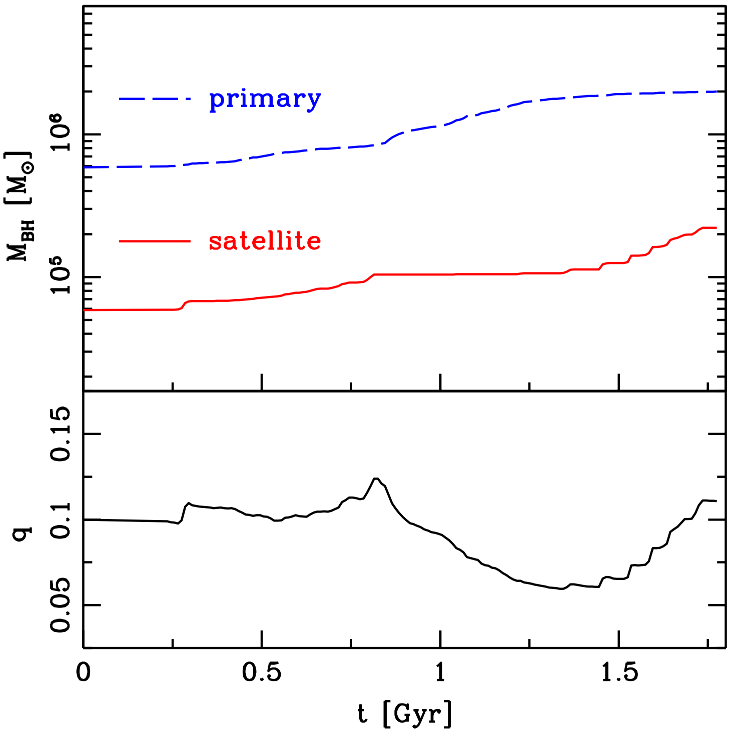

Figure 2.14: MBH evolution in the $f_g = 0.3$ merger with 0° inclination and small pericenter. *Upper panel*: mass accretion of the MBHs. The growth of the satellite MBH stops at second passage ($t = 0.8$ Gyr), earlier than in the other cases, as ram pressure stripping of the satellite gas is more efficient at smaller separations. The primary MBH, on the other hand, starts a period of enhanced accretion after the second orbit, as the perturbations excited onto the primary galaxy are correspondingly stronger. *Lower panel*: evolution of the MBH mass ratio q.

(Barnes & Hernquist 1996), and for this reason the increase in mass ratio q during the first three orbits is milder than in the coplanar case with the same gas fraction (Fig. 2.13, lower panel). Moreover, a higher inclination corresponds to a slower orbital decay; in fact, the satellite spends only a small fraction of each orbit in the high density, co-rotating baryonic region of the primary galaxy, where dynamical friction is most efficient. The orbit is eventually dragged down to the plane of the primary disk (Quinn & Goodman 1986) (see middle panel of Fig. 2.13). However, since such drag takes a number of orbits to cause significant alignment, the circularization effect – which can only happen when orbiting for most of the time inside the primary disk – is delayed compared to the coplanar case. For this reason, the satellite undergoes a larger number of tidal shocks and is eventually disrupted, precluding a second episode of substantial accretion onto the satellite MBH. For low initial inclination ($\theta = 20°$), the drag is effective enough to bring the MBH down to a separation of ~ 120 pc before the satellite is disrupted. If the inclination is higher ($\theta = 45°$), the satellite is disrupted leaving the MBH at ~ 700 pc distance, where the dynamical friction of the naked MBH is of a few billion years.

Finally, we turn to the merger starting on a parabolic orbit with very small pericenter (0.8 kpc). The MBH masses and q as a function of time in this case are shown in Fig. 2.14. During the first orbits, the satellite in this merger is subject to stronger tidal torques than in the reference case, but MBH accretion is weaker. Because of the small distance (corresponding to a high $\rho_{\rm ext}$) and high relative V at pericenters, ram pressure stripping is effective since the very first passage: the satellite MBH is starved early and is unable to accrete a substantial amount of mass. For the same reason, MBH growth in the satellite is halted completely already at second pericenter ($t \sim 1.8$ Gyr). On the contrary, the primary MBH experiences enhanced accretion: in fact, the close passages of the satellite excite stronger instabilities in the primary disk, funnelling gas towards its nucleus. For this reason, at intermediate times during the merger, the mass ratio drops down to $1:20$. Analogously to the reference run, a second phase of accretion onto the satellite MBH occurs, in this case only raising q back to its starting value. However, MBH sinking does not proceed any further: as a consequence of the strong tidal shocks experienced by the satellite at the very close pericentric passages, the satellite is disrupted leaving its MBH at a distance of 1 kpc. At these separations, the estimated timescale for orbital sinking of the naked MBH is longer than a Hubble time.

2.4 Discussion

The results presented in §2.2 show that the formation of a MBH pair in unequal-mass mergers of disk galaxies is very sensitive to the details of the physical processes involved. Applying the standard dynamical friction formula (Eq. 1.1) to the naked MBHs in our merger remnants, we estimate the timescale for bringing them down to the nuclear region (< 30 pc) to be up to a few billion years for separations up to ~ 1 kpc, and comparable to or longer than a Hubble time for larger separations. Thanks to a combination of stellar-dynamical (e.g., Milosavljević & Merritt 2001) and gas-dynamical (e.g., Gould & Rix 2000; Escala et al. 2005; Dotti et al. 2007) processes, a satellite MBH that sinks down to our current force resolution limit may decay further and form a Keplerian binary together with the primary MBH.

None of the collisionless cases we studied led to MBH pairing: tidal shocks progressively lower the density in the satellite until it dissolves, leaving a wandering MBH in the remnant. The inclusion of gas dynamics and SF changes significantly the outcome of the merger. For higher mass ratios ($q = 0.25$) at $z = 0$, bar instabilities funnel gas to the center of the satellite, steepening its potential well and allowing its survival to tidal disruption down to the center of the primary. Therefore, in this case the presence of a dissipative component is necessary and sufficient to pair the MBHs at ~ 200 pc scales, creating favorable conditions for the formation of a binary. The smaller satellites here considered ($q = 0.1$, $z = 3$) are more strongly affected by both internal SF and the gasdynamical interaction between their ISM and that of the primary galaxy. Torques in the early stages of the merger are funnelling the gas to the center less efficiently, due to the absence of a stellar bar and the stabilizing effect of turbulence. As a result, ram pressure strips away all of the ISM of the satellite. If satellites develop a higher central stellar density by rapidly converting their gas into stars before ram pressure removes it, they can retain enough bound mass to ensure the pairing of the two MBHs. Gas-rich satellites ($f_{\rm g} = 0.3$) undergo a stronger burst of SF during the first orbits, and therefore meet this requirement better than $f_{\rm g} = 0.1$ satellites. Yet in both cases the central density of the cusp remains high enough to permit its survival, allowing the pairing of the two MBHs within a Hubble time.

The pairing of the two MBHs takes less than 1 Gyr in the gas rich systems that should be common at $z = 3$. Therefore, if the $M_{\rm BH} - M_{\rm bulge}$ relation approximately holds at $z = 3$ as in the local Universe, the galaxies here considered should lead to the formation of representative MBH pairs at such cosmic epochs (Volonteri et al. 2003). These pairs are also expected to contribute significantly to the high-z gravitational wave signal. Since we show that gas-dynamical processes allow such an efficient pairing of the MBHs, our results strengthen the case for MBH coalescence events. On the other hand, we show that the timing between galaxy mergers and mergers of their MBHs is sensitive to the gaseous content of the merging galaxies. Hence, MBH coalescence events may not necessarily trace galaxy mergers reliably without more sophisticate modelling.

We note that the orbital evolution of the MBH pairs, in the dynamical range considered here, has only a weak dependence on the masses of the two MBHs. As shown in Fig. 2.3, the stellar mass enclosed inside two softening lengths from the center of our galaxy models (hence close to our resolution limit) already exceeds $M_{\rm BH}$ by more than an order of magnitude. This is the effective mass that determines how quickly the MBHs will sink. Therefore, lowering $M_{\rm BH}$ or increasing it by up to an order of magnitude would have no effect on sinking timescales *before* the disruption of the satellite. Instead, *after* disruption, the analytic estimate for the dynamical friction timescale of the naked MBH would change linearly with $M_{\rm BH}$. Similarly, if nuclear star clusters with masses $\sim 10\ M_{\rm BH}$ (Wehner & Harris 2006; Ferrarese et al. 2006) were present around the MBHs, their sinking timescales would still be longer than a Hubble time in our dry mergers, where the final MBH separation exceeds 1 kpc, while the pairing would now occur in less than a billion years in *all* our wet mergers. Hence, either a larger $M_{\rm BH}$ or the presence of a nuclear star cluster would enhance even further the difference between dry and wet mergers.

The outcomes of the simulations presented in §2.3 are summarized in Fig. 2.15, where the mass ratio q of the MBHs is plotted against their separation at the time of satellite

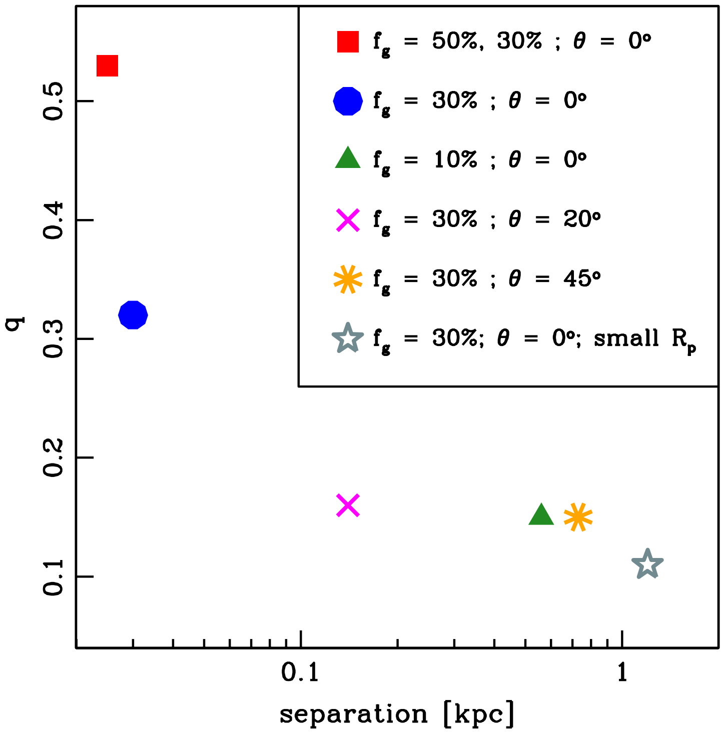

Figure 2.15: The different symbols show the separation of the two MBHs and the corresponding MBH mass ratio q at the time of satellite disruption for all the 1:10 mergers discussed here, labelled according to their initial gas fractions $f_{\rm g}$, orbital inclination θ and initial pericenter $R_{\rm p}$.

disruption. In addition to the dynamics that favor larger galaxy mass ratios in the production of MBH pairs, we showed that the physical processes that facilitate the MBH orbital decay correspond to a stronger accumulation of gaseous mass in the central region of the satellite, compared to the isolated, equilibrium galaxy models. In turn, such gas density enhancement corresponds, in our modelling of black hole accretion, to an increase in the MBH mass ratio compared to its "starting" value. Mergers that may most promptly produce MBH binaries are also those that tend to enhance the MBHs q, with respect to what inferred from the galaxy (bulge) mass ratio $q_{\rm gal}$.

Such increase in MBH q happens in two distinct phases, whose occurrence and relative importance depend on the details of the merger process itself. Specifically, in the initial stages of the encounter, the stronger tidal perturbations experienced by the satellite galaxy, compared to those of the primary, cause an enhanced mass growth of its MBH. In addition, in the last stages of the encounter, the orbit of the secondary MBH may circularize inside the disk of the primary. As a result, its ability to accrete gas and grow in mass relative to that of the primary MBH can be further amplified. Such circularization and associated increase in the accretion rate has been previously reported in small-scale simulations of MBH pairs embedded in a common nuclear disk (Dotti et al. 2009). These processes lead to a complex phenomenology of double AGN activity even for a relatively idealized case as our "reference" 1:10 merger (Fig. 2.11). We note that the amount of gas left around the satellite MBH by ram pressure stripping might be underestimated: in fact, our simulations do not resolve the accretion disk around the MBHs, nor the cold molecular phase in the nuclear region of the satellite; both of these would be less susceptible to ram pressure stripping (e.g., Quilis et al. 2000) and could remain bound to the satellite while the rest of its ISM is lost. In this case, the growth of the secondary MBH may not stop completely and the mass ratios may become even larger.

A cautionary remark concerns the fact that MBH accretion has been modelled assuming the Bondi-Hoyle-Lyttleton sub-grid accretion recipe (Eq. 1.3) that is widely used in the literature. However, accretion will most likely occur by means of angular momentum transport in a nuclear disk with an effective α-viscosity (e.g., Lin & Pringle 1987). Other models for gas funnelling and accretion onto central MBHs have been recently proposed to account for the shortcomings of the "standard" approach. Power et al. (2010) propose an accretion scheme for angular momentum-dominated gaseous flows in a stationary gravitational background, introducing a delay in the accretion as a free parameter related to viscous timescales; from their simulations, they find that the Bondi prescription *overestimates* the inflow rate across the MBH influence radius. Hopkins & Quataert (2010) model the transport of angular momentum via disk instabilities arising in galaxy mergers, on scales both larger and smaller than those resolved in this work. They describe the inflow rates down to the MBH sphere of influence with $\dot{M} \sim a M_{\rm g} \Omega$, where $M_{\rm g}$ is the available gaseous mass, Ω the angular speed, and a is related to the amplitude of the instabilities. They find that the Bondi accretion recipe systematically *underestimates* (although with large scatter) the actual inflow rate at sub-pc scales, while better predictions are given by an effective α-disk model. It is therefore unclear whether our accretion recipe introduces a bias in the MBH mass growth, and in which direction. In an attempt to investigate the effect of other sub-grid recipes on our results, we computed *a posteriori* accretion rates in our reference simulation with the recent α-disk sub-resolution model of DeBuhr et al. (2009). We find that such model yields higher $\dot{M}$ compared to the Bondi prescription, in agreement with the findings by Hopkins & Quataert (2010); the accretion rates onto the two MBHs are enhanced by roughly the same factor. However, the α-disk prescription relies on the assumption of viscous heating of the gas, a process which is entirely unresolved in our simulations at the relevant scales; therefore, it is unclear whether the physical properties of our gas particles can be employed in the sub-grid recipe in any straightfoward way without introducing additional parameters (see e.g. the model by Hobbs et al. 2011). We would like to emphasize here that, while the absolute values of $\dot{M}$ can depend on the employed numerical prescription, the physical picture concerning the *relative* growth of the two MBHs emerging from our simulations should be robust to changes in sub-grid modelling. Indeed, our findings reflect clear and well-resolved large scale effects, namely how gravitational torques and orbit circularization can enhance MBH sinking while making a larger gaseous mass relative to $M_{\rm BH}$ available for accretion onto the secondary black hole.

The results presented in this chapter are also relevant in the context of MBH gravitational recoils, as briefly touched upon in §2.2.3. Indeed, if a large fraction of unequal-mass galaxy mergers results in mergers between MBHs with nearly equal masses, then the recoil velocity distribution of the MBH population will be different than expected (e.g., Volonteri et al. 2010). However, the actual recoil velocity distribution will also depend on the magnitude and relative orientation of the spins of the MBHs at the final stage of the merger, which is likely driven by gas dynamics at scales well below those resolved in our simulations (Perego et al. 2009; Dotti et al. 2010).

Our findings highlight the fundamental role of tidal stripping and gas-dynamical effects in deciding the formation and properties of close MBH pairs in unequal-mass galaxy mergers. Moreover, our resuls suggest that the efficiency of MBH pair formation may correlate with the final mass ratio of the pair itself, so that MBH pairs with larger mass ratios tend to be produced more effectively and promptly. Gravitational wave detectors will eventually enable the use of gravitational wave signals from MBH coalescences as a new, independent probe of cosmic structure formation. Indeed, gravitational wave-forms can allow the determination of mass, spin, and orbital parameters of the merging MBHs. In principle, this information could be used to infer the masses of the merging host galaxies. However, our results demonstrate that this connection cannot be made by simply applying the observed scaling relations between the masses of MBHs and the properties of their host galaxies, even if these scalings are applicable to galaxies throughout cosmic history. The findings presented here suggest that the mapping between galaxy and MBH mergers depends on various factors, such as the gas content of the merging galaxies and the encounter geometry, and as such might need to be approached in a probabilistic way. Such investigations would require a combination of a series of merger experiments that explore a larger parameter space (van Wassenhove et al., in prep.) with semi-analytical models of the co-evolution between galaxies and MBHs, an effort that is already ongoing (Bonoli et al., in prep.).

3

Formation of Massive Black Holes in gas-rich galaxy mergers

As mentioned in §1.1, observations of distant bright quasars suggest that billion solar mass supermassive black holes were already in place less than a billion years after the Big Bang (Fan 2006), but current models of MBH seed formation still leave many issues unsolved. In this chapter, we discuss simulations showing that high-redshift mergers between massive protogalaxies naturally produce the conditions for direct collapse into a MBH.[1]

3.1 Context

In order to grow to the billion solar mass MBHs that power bright quasars at $z \sim 6$, the hundred solar mass black hole seeds produced by the collapse of primordial metal-free Population III stars at $z > 15$ (Madau & Rees 2001; Omukai et al. 2008; Regan & Haehnelt 2009) need to accrete steadily at or above the Eddington rate (Volonteri & Rees 2006). However, recent hydrodynamical simulations with radiative transfer indicate that such high accretion rates may be impossible to maintain. In fact, the seed is produced inside a gas bubble that has been ionized by the progenitor star; such surrounding gas has very low densities (Johnson & Bromm 2007), with radiative feedback from accretion and radiation pressure exacerbating the problem (Pelupessy et al. 2007; Alvarez et al. 2009; Milosavljević et al. 2009). Other processes occurring throughout the cosmic evolution of these seeds, such as slingshot interactions and the expulsion of a black hole from the host halo due to GW recoil can further suppress their growth and occupation fraction (Volonteri & Rees 2006; Haiman 2004).

---

[1] Results presented here have appeared in Mayer, Kazantzidis, Escala, & Callegari (2010)

In the model of direct collapse (Begelman et al. 2006; Volonteri et al. 2008; Omukai et al. 2008; Regan & Haehnelt 2009; Haehnelt et al. 1998), the outward transport of angular momentum by gravitational torques (Shlosman et al. 1989; Lodato & Natarajan 2006; Levine et al. 2008), gravity-driven turbulence (Escala 2007), or magnetorotational instability (Eisenstein & Loeb 1995) in isolated protogalactic disks (Volonteri et al. 2008; Regan & Haehnelt 2009; Lodato & Natarajan 2006) or primordial halos (Bromm & Loeb 2003; Wise et al. 2008) is quite efficient, and could in principle accumulate enough gas at their centers to directly produce seeds exceeding 10^5 $M_\odot$. Such massive seeds should be able to grow rapidly to a billion solar mass (Volonteri & Rees 2006). However, numerical experiments and analytical arguments show that gas would be converted into stars faster than it is driven to the center (Lodato & Natarajan 2006; Wise et al. 2008). This is because inflow rates due to angular momentum transport in this regime are still low enough, that the inflowing gas could sustain a comparable SF rate. Hence it is necessary to invoke primordial metal-free gas and dissociation of the star-forming molecular gas phase by the cosmic ultraviolet (UV) background in order to suppress cooling, and hence star formation (Volonteri et al. 2008; Regan & Haehnelt 2009; Lodato & Natarajan 2006; Djorgovski et al. 2008), so that the gas reservoir is not depleted. Yet again, recent calculations show that the metals readily produced by the early generations of stars are sufficient to trigger efficient cooling and star formation (Omukai et al. 2008). Therefore, whether or not protogalaxies ever met the conditions required for direct SMBH formation is still a puzzle.

3.2 The reference simulation

Until now, direct collapse scenarios were limited to consider gas inflows in isolated objects, contrary to the accepted picture of hierarchical structure formation protogalaxies grow primarily through rapid and repeated mutual interactions and mergers. In major mergers, tidal torques and shock dissipation are capable of driving most of the gas content of galaxies from kiloparsec scales down to scales of several tens of parsecs at rates as high as 100 $M_\odot$ yr^{-1} despite the concurrent high star formation rates (Kazantzidis et al. 2005; Mayer et al. 2007). If such prodigious gas inflows could continue all the way down to the very center of the merger remnant, they could provide the natural conditions for direct massive black hole formation. Addressing this issue requires a three-dimensional simulation following gasdynamics across an unprecedented range of spatial scales, from tens of kiloparsecs to below a parsec; this has been achieved by performing a large-scale merger simulation and then performing particle splitting in the very last stage of the galaxy collision, as explained in this section.

3.2.1 Set-up

The galaxy merger

The reference simulation discussed here is based on a 1:1 galaxy merger simulation. The equilibrium models of each galaxy are analogous to the $z = 0$ primary galaxy described in §2.2.1. Such a halo mass of 10^{12} $M_\odot$ is consistent with that inferred for the hosts of high-redshift quasars based on their number densities (Volonteri & Rees 2006; Pelupessy et al. 2007; Li et al. 2007). The details of the model are based on our knowledge of present-day disk galaxies simply because there is little information available from observations of galaxy structure at very high redshift. Yet, this modeling strategy should be regarded as conservative for the purpose of this study, since high-z disks are expected to be denser, more gas-rich and more turbulent than present-day galaxies, which should favour the formation of massive nuclear disks. Kiloparsec-scale rotating disks of stars and gas as those that we have assumed in our initial conditions should be already present in halos with masses $> 10^{11}$ $M_\odot$ at $z > 4$ (Levine et al. 2008). While a stellar bulge is always present in the most massive disk galaxies out to $z = 1$ (Sargent et al. 2007) there is still insufficient knowledge of galactic structure at higher redshift to confirm that this is the case also at $z > 6$. However, the presence of the bulge has the effect of stabilizing the galaxy disks against external perturbations (Binney & Tremaine 1987). This implies that, without the bulge, the two disks would undergo even stronger instabilities during the final stage of the merger, with an associated gas inflow that would be even stronger. Hence, including the bulge should be regarded as a conservative assumption for our purposes. Moreover, there is some evidence that the disks of high-z galaxies are more clumpy, turbulent, and more vigorously star forming than present-day galaxies (Genzel et al. 2006; Förster Schreiber et al. 2009). Recent simulations (Agertz et al. 2009b) suggest that rapid accretion of cold gas flows builds up turbulent, clumpy disks with properties resembling those of the observations. These "gravitoturbulent" clumpy disks are very efficient at redistributing their angular momentum, and indeed clump-clump interactions as well as dynamical friction of clumps against the background matter had been previously suggested as a way to produce centrally concentrated components in galaxies, such as bulges (Elmegreen et al. 2008). Therefore a clumpy galaxy should be even more susceptible to mechanisms that remove angular momentum from the gas, funnelling it to the nuclear region (analogously to what shown in Fig. 3.8).

The choice of the orbit is the same as in §2.2.1, as is the number of particles in each component of the models. Using the standard scaling relations (Downes & Solomon 1998) for the merger orbits, $T_{\rm orb} \propto (1+z)^{-3/2}$. Since at $z = 0$ the merging timescale on a typical cosmological orbit is ~ 5 Gyr[8], it follows that, for example, $T_{\rm orb} \sim 0.2$ Gyr at $z = 8$, which is comfortably shorter than a billion year, i.e. the age of the Universe at the time of the high-

z QSOs. From a statistical perspective, in the concordance WMAP5 cosmology 10^{12} $M_\odot$ galaxies would correspond to fairly high density peaks collapsing at $z \sim 7-8$ (Pelupessy et al. 2007), ($\sim 4-5\sigma$, where σ is the variance of the cosmological density field); at $z > 6$, at least one major merger is expected in the history of such a galaxy (Li et al. 2007).

We adopted a gravitational softening of $\epsilon = 0.1$ kpc for both the DM and baryonic particles of the galaxy. The gas fraction is $f_g = 0.1$ of the total disk mass. This is fairly typical for Milky Way-sized galaxies at low redshift but it is, again, a conservative assumption for galaxies at $z > 2$ (Law et al. 2009). Moreover, in previous work it has been shown that the existence of a coherent nuclear disk after a major merger is a general result that does not seem to depend strongly on the details of the initial orbital configuration (Kazantzidis et al. 2005; Mayer et al. 2007). Similarly, gas masses and densities in the nuclear region were found to differ by less than a factor of 2 for runs having the same initial gas mass fraction in the galaxy disks but different initial orbits.

The merging galaxies undergo two close encounters as dynamical friction against their extended halos erodes their orbital energy. Before the final impact, when the two baryonic cores are separated by 6 kpc and begin their last orbit, we perform particle splitting in the gas component within a volume 30 kpc in size.

Particle splitting

We use the same technique of static particle splitting that has been employed before to study the dynamics of MBH binaries evolving in circumnuclear gaseous disks (Mayer et al. 2007; Dotti et al. 2007) as well as during galaxy mergers (Katz 1992), and to study the assembly of galaxies from the cooling flow in a galaxy-sized halo (Kaufmann et al. 2006). A similar technique has been used by others to study the dynamics of binary black holes in spherical gaseous backgrounds (Escala et al. 2004).

In the static splitting performed here, a subvolume is selected for refinement, the splitting is performed, and the simulation is then restarted with increased mass resolution only in the region of interest. By selecting a large enough volume for the refined region one can avoid dealing with spurious effects at the resolution boundary. We select the volume of the high-resolution region large enough to guarantee that the dynamical timescale of the entire low-resolution region is much longer than the dynamical timescale of the refined region. In other words, we make sure that low-resolution gas particles will reach the high-resolution region on a timescale longer than the actual time span probed in this work. This is important because the more massive gas particles from the coarse region can exchange energy with the lower-mass particles of the refined region via two-body encounters, artificially affecting their dynamics and thermodynamics (Steinmetz & White 1997). Hence our choice to split in a volume of 30 kpc in radius, while the two galaxy cores are separated by only 6 kpc. The new particles are randomly distributed according to the SPH smoothing kernel within a volume of size $\sim h_p^3$, where h_p is the smoothing length of the parent particle. The velocities of the child particles are equal to those of their parent particle (ensuring momentum conservation) and so is their temperature, while each child particle is assigned a mass equal to $1/N_{\rm split}$ the mass of the parent particle, where $N_{\rm split}$ is the number of child particles per parent particle.

The mass resolution in the gas component was originally 2×10^4 $M_\odot$ and becomes $\sim$ 3000 $M_\odot$ after splitting, for a total of 1.5 million SPH particles. The star and dark matter particles are not split, to limit the computational burden. The softening of the gas particles is reduced to 0.1 pc. For the new mass resolution, the local Jeans length (see p. 71) is always resolved by 10 or more SPH smoothing kernels (Bate & Burkert 1997; Nelson 2006) in the highest density regions occurring in the simulations. In the refined simulations stars and dark matter particles essentially provide a smooth background potential, while the computation focuses on the gas component which dominates by mass in the nuclear region. By performing numerical tests we have verified that, owing to the fact that gas dominates the mass and dynamics of the nuclear region, the large softening adopted for the dark matter particles does not affect significantly the density profile of the inner dark halo that surrounds the nuclear disk.

Gas thermodynamics

In the refined simulation, we adopt an effective equation of state (EOS) that accounts for the net balance between cooling and heating (Spaans & Silk 2000): each gas particle obeys

$$P = (\gamma - 1)\,\rho\, u\,,$$

where γ is the usual ratio between specific heats. The specific internal energy u evolves with time as a result of $P\mathrm{d}V$ work and shock heating modeled via the standard Monaghan artificial viscosity term. Therefore, the entropy of the system increases as a result of shocks. Including this kind of irreversible heating is important since the two galaxy cores undergo a violent collision. Shocks are generated even later as the nuclear, self-gravitating disk becomes non-axisymmetric, developing strong spiral arms. As a consequence, the highly dynamical regime modeled here is much different from that considered by previous works starting from an equilibrium disk model, which could be evolved using a polytropic equation of state and neglecting shock heating (Dotti et al. 2007, 2006). On the other hand, radiative cooling is not directly included in the refined simulations. Instead, γ is changed in order to mimic different degrees of dissipation in the gas component, thereby turning the equation of state of the gas into an "effective" equation of state (Spaans & Silk 2000; Klessen et al. 2007). It has been shown elsewhere (Mayer et al. 2007) that a proper transition between the radiative cooling regime and the effective equation of state regime does not introduce numerical artifacts in the simulation.

A lower resolution, unrefined simulation (Kazantzidis et al. 2005) shows that, during the final collision, the star formation peaks at $\sim 30\ \mathrm{M}_{\odot}\ \mathrm{yr}^{-1}$ over about 10^8yr. Motivated by this, we choose an EOS appropriate for interstellar gas heated by a major starburst (Klessen et al. 2007) with solar metallicity as suggested by the abundance analysis of the high-redshift QSOs (Walter et al. 2004). Previous works (Klessen et al. 2007) have used a two-dimensional radiative transfer code to study the effective equation of state of interstellar clouds exposed to the intense UV radiation field expected in a starburst. It was found that the gas has a γ in the range $1.1-1.4$ for densities in the range $5\times10^3-10^5$ atoms cm^{-3}, comparable to the volume-weighted mean density in the simulated nuclear disk. Such values of the adiabatic index are expected for quite a range of starburst intensities, from $10\ \mathrm{M}_{\odot}\ \mathrm{yr}^{-1}$ to more than $100\ \mathrm{M}_{\odot}\ \mathrm{yr}^{-1}$, hence encompassing the peak star formation rate in the original low-resolution merger simulations.

We adopt $\gamma = 7/5$ until the first gas inflow is completed in the simulation. The mean properties (mass, density, pressure support contributed by the thermal and turbulent components, rotational velocity) of nuclear disks formed in galaxy mergers (Downes & Solomon 1998) and simulated with such an effective equation of state compare well with the corresponding properties of nuclear disks observed in detailed observations of merger remnants has been already shown in previous work (Mayer et al. 2007). For densities above 10^5 atoms cm^{-3} cooling is more efficient and γ should drop to ~ 1.1 according to the adopted EOS model (Klessen et al. 2007). This condition is verified in the central few parsecs after the first inflow ($\sim 10^4$ yr after the merger), hence $\gamma = 1.1$ is adopted from this time onward.

3.2.2 Formation of the Jeans-unstable massive cloud

The final collision of the two galactic cores produces a massive turbulent rotating nuclear disk with a mass of $\sim 2\times10^9\ \mathrm{M}_{\odot}$ and a size of ~ 80 pc. The disk is born in an unstable configuration, with a prominent two-armed spiral pattern imprinted by the collision and sustained by its own strong self-gravity (Fig. 3.1). The gas has a high turbulent velocity dispersion ($\sigma \sim 100\ \mathrm{km\ s}^{-1}$) maintained by gravitational instability (Escala 2007) and rotates at a speed of several 100 $\mathrm{km\ s}^{-1}$ within 50 pc. The disk is stable against fragmentation but the strong spiral pattern swiftly transports mass inward and angular momentum outward. Only $\sim 10^4$ yr after the merger is completed, more than 20% of the disk mass ($\sim 5\times10^8\ \mathrm{M}_{\odot}$) resides within the central few parsecs (Fig. 3.2), where the inflow rate peaks at $\dot{M} > 10^4\ \mathrm{M}_{\odot}\ \mathrm{yr}^{-1}$, orders of magnitude above the inflow rates found in simulations of

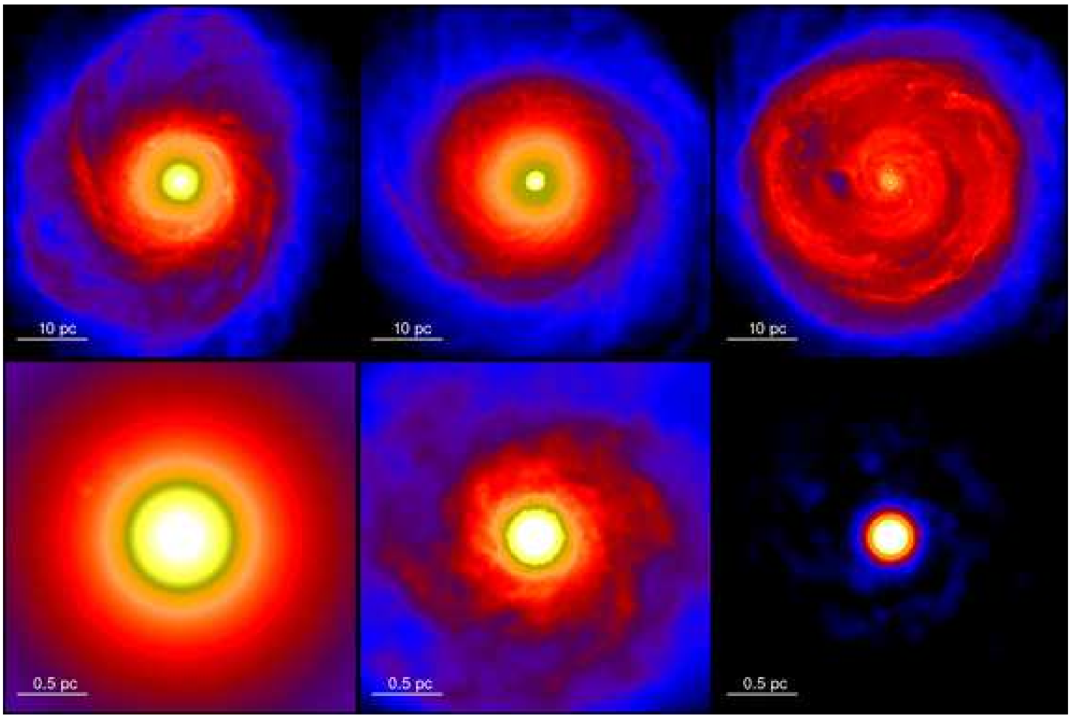

Figure 3.1: Time evolution of the nuclear gas disk from its formation until the onset of central collapse. The surface density maps of the nuclear disk are shown at large scales (*top row*) and small scales (*bottom row*). Density is colour-coded on a logarithmic scale from 2×10^4 to 10^8 $\mathrm{M}_\odot/\mathrm{pc}^2$ (*upper panels*) and from 2×10^6 to $2 \times 10^{1}0$ $\mathrm{M}_\odot/\mathrm{pc}^2$ (*lower panels*). The time of the merger is defined as the time at which the two density peaks associated with the merging galactic cores are no longer distinguishable. For reference, the disk orbital time at ~ 20 pc is 5×10^4 yr, while at 1 pc it is 4×10^3 yr. Global spiral modes, in particular the two-armed spiral initially triggered by the final collision between the two cores, are evident at scales of tens of parsecs (first two top panels) and cause the mass increase in the central parsec region (bottom panels) that allows the collapse into a massive central cloud (third bottom panel).

isolated protogalaxies (Regan & Haehnelt 2009; Lodato & Natarajan 2006; Levine et al. 2008; Wise et al. 2008).

The gas funnelled to the central 2-3 pc region of the nuclear disk settles into a rotating, pressure-supported cloud. The density of the cloud increases steadily due to the ongoing inflow, until the cloud becomes Jeans unstable (Jeans 1929) and collapses down to sub-parsec scales on the local dynamical times, $t_{\mathrm{dyn}} \sim 10^3$ yr. The supermassive cloud now contains $\sim 13\%$ of the disk mass, 2.6×10^8 $\mathrm{M}_\odot$ (red line in Fig. 3.2).

The simulation is stopped once the central cloud has contracted to a size comparable to our force resolution limit, below which self-gravity is unresolved. At this point the cloud is still Jeans unstable: with greater resolution, its collapse should continue since the equation of state would become essentially isothermal at even higher densities (Walter et al. 2004). If we assume that the cloud keeps its steep density profile ($r \sim \rho^{-\gamma}$ with $\gamma \geq 2$)

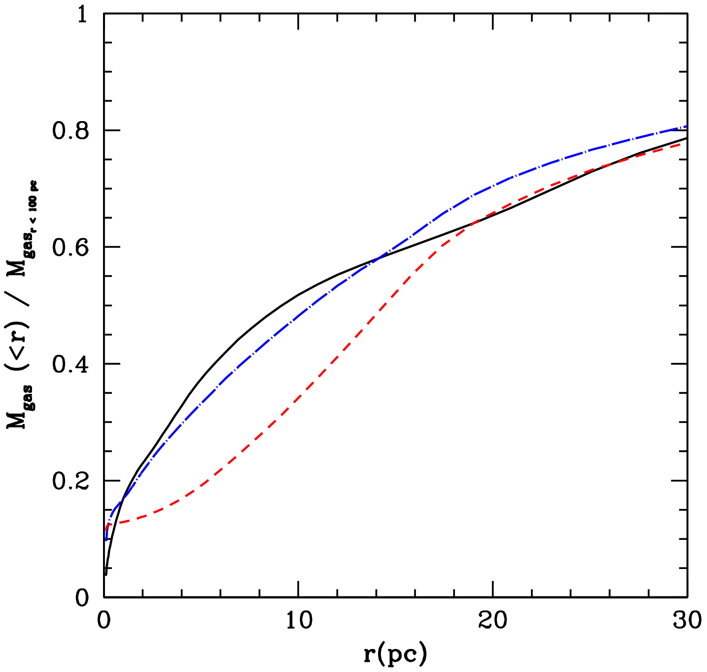

Figure 3.2: Enclosed mass profile for the reference run at three times: 9.1×10^3 yr (black line), 7.49×10^4 yr (blue), 1.04×10^5 yr (red). The accumulation of mass in the inner pc and the outward flow of angular momentum (traced by the flattening of the profile at $r \sim 10$ pc) are visbile.

at scales below our resolution, at a radius of $\sim 10^{-3}$ pc the cloud would be as massive and dense as a quasi-star that can collapse directly into a massive black hole (Omukai et al. 2008). Alternatively, due to its global Jeans instability the cloud could collapse into a supermassive star on its free-fall timescale, which would later produce a black hole of comparable mass (Wise et al. 2008).

The formation of the collapsing cloud occurs only $\sim 10^5$ yr after the completion of the merger, a timescale much shorter than the 10^8 years needed to convert most of the nuclear gas into stars during the starburst. Therefore, the merger-driven gas collapse overcomes the major difficulty of previous direct collapse models in isolated protogalaxies, forced to suppress star formation due to much weaker inflows. The rapid accumulation of more than 10^8 M$_\odot$ of gas in the central parsec is confirmed by a complimentary simulation which incorporates star formation (see below in §3.3.2).

Assuming that the nuclear disk forms stars with a $\sim 30\%$ efficiency, the upper limit deduced from observation and models of star forming molecular clouds (Klessen et al. 2007), a dense gas mass in excess of 10^9 M$_\odot$ is available to feed the black hole on the timescale of the inflow despite the concurrent starburst. Considering Eddington-limited accretion (Eq. 1.4 and 1.5), a seed black hole weighting only $m_{\rm seed} \sim 10^5$ M$_\odot$ (i.e., forming

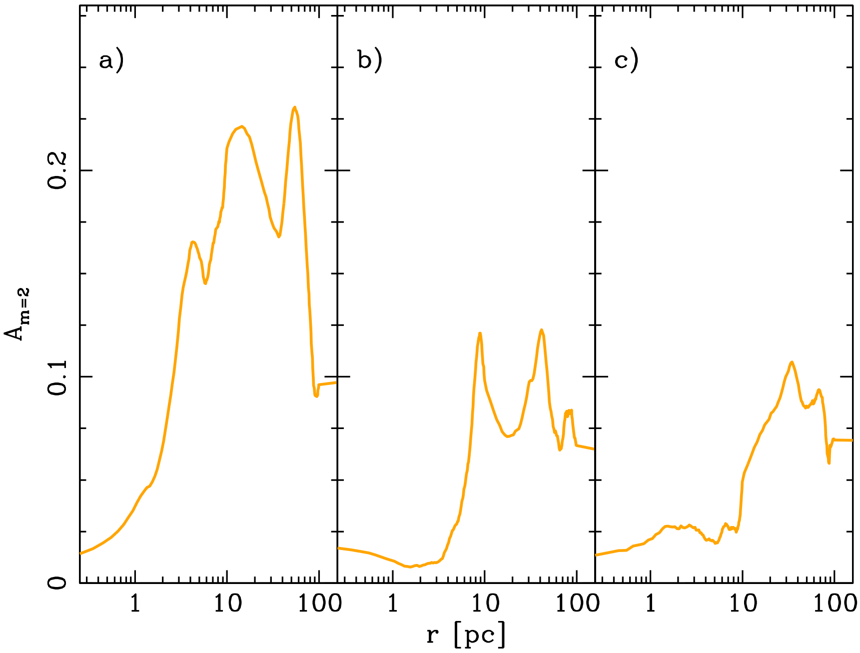

Figure 3.3: Time evolution of the amplitude of the strongest non-axisymmetric mode in the disk ($m = 2$ is the strongest mode at all times). The azimuthally averaged radial profiles are shown, time-averaged over a few outputs around a chosen time t_* to highlight non-transient features. From left to right, we show profiles at $t_* = 9.1 \times 10^3$ yr (a), 7.49×10^4 yr (b) and 1.04×10^5 yr (c) after the merger (as in Fig. 3.1 and 3.2). The time of the first snapshot (a) was indeed chosen near the maximum peak of the $m = 2$ mode, which also corresponds to a maximum inflow rate at scales of $\sim 10-20$ pc (Fig. 3.4). At times (b) and (c), the dominant global $m = 2$ mode has weakened considerably in the center, while in the outer region it causes the disk "expansion" seen in red curve in Fig. 3.2.

out of less than 1% of the supermassive cloud) can grow to $M_{BH} \sim 10^9$ $M_\odot$ in as little as 3.6×10^8 yr, possibly explaining the rapid appearance of bright QSOs if the merger takes place at $z \sim 7-8$ (see below in §3.2.4).

3.2.3 Mass transport and stability of the nuclear region

We have measured the strength of the non-axisymmetric modes in the nuclear disk in the reference simulation using a Fourier decomposition, in order to establish a clear correlation between the regions of the disk at which the maximum inflow occurs in the nuclear disk and the amplitude of the strongest mode, as shown in Figures 3.3 and 3.4. The amplitude A_m of the Fourier mode of order m is defined as

$$A_m(R) = \frac{\left| \int_0^{2\pi} \Sigma(R,\phi) e^{-im\phi} \mathrm{d}\phi \right|}{\Sigma(R)}$$

where $\Sigma(R,\phi)$ is the 2-dimensional surface density, and $\Sigma(R)$ is its azimuthal average.

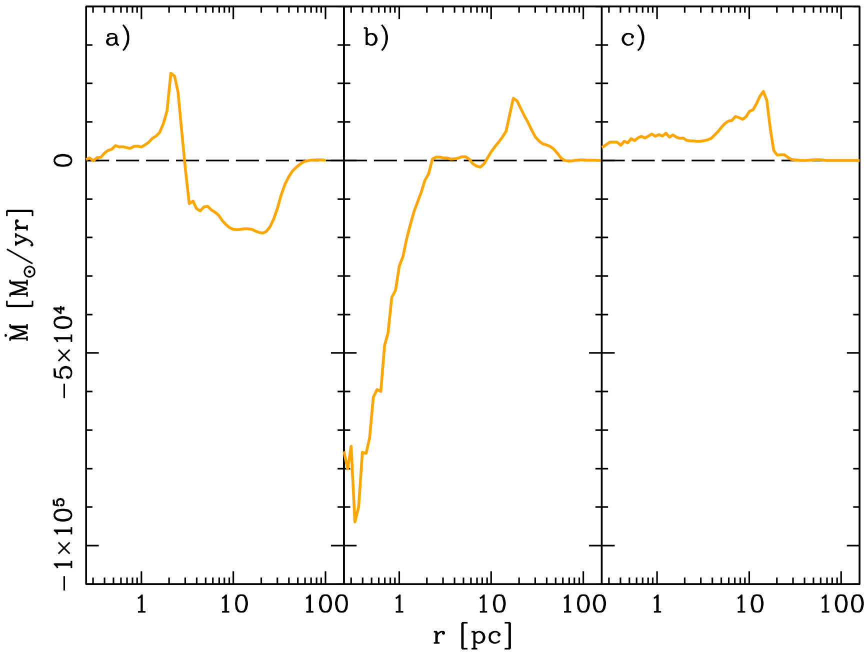

Figure 3.4: Gas inflow rate in the disk at three different times. Spatial and time averages are as in Fig. 3.3. The time of the first snapshot (a), where the $m = 2$ mode peaks, corresponds to the maximum inflow rate at scales of $\sim 10-20$ pc. At time (b) the Jeans collapse has already started at parsec scales, as shown by the very large inflow rate, which is indeed the highest measured throughout the simulation. At larger ($\sim$ 10 pc) scales the inflow has instead decreased because the dominant global $m = 2$ mode has also weakened considerably (Fig. 3.3). At time (c) the inner region is stable (as the force resolution has been reached), while outside the central parsec a net outflow is seen.

The strongest mode in the disk at all times is a two-armed spiral, corresponding to $m = 2$ in the Fourier decomposition, as also evident in Fig. 3.1. Such mode is the imprint of the collision between the two galaxy cores. The inflow rate peaks at $> 10^4$ $M_\odot$ yr^{-1}, which corresponds to radial velocities of $\sim$ 100 km s^{-1}. This is sustained for only a few 10^4 yr, allowing to bring a few 10^8 $M_\odot$ of gas within the inner 10 pc. Note that the large radial velocities are of order of the turbulent velocities seen in nuclear disks residing at the center of merger remnants (Downes & Solomon 1998). In Fig. 3.4 we also show the second, small-scale radial inflow triggered by the onset of the Jeans collapse of the gas within the central parsec. The collapse begins at the parsec scale as soon as the enclosed mass climbs above the local Jeans mass ($\sim 7 \times 10^7$ $M_\odot$ at $r = 1$ pc, note that using the Bonnor-Ebert mass would yield essentially the same result within a factor $\sim$ 2). Gas at parsec scales rotates with a speed $V_{\rm rot} \sim 600$ km s^{-1}, but it is pressure supported as the temperature raises close to 10^8 K owing to adiabatic compression ($c_s \sim 1000$ km s^{-1} $> V_{\rm rot}$). The fact that pressure provides the most important support against gravity justifies our use of the Jeans mass to characterize the phase of collapse, although a more complete description of the process would involve accounting for the effect of rotation and the continued mass flux from the

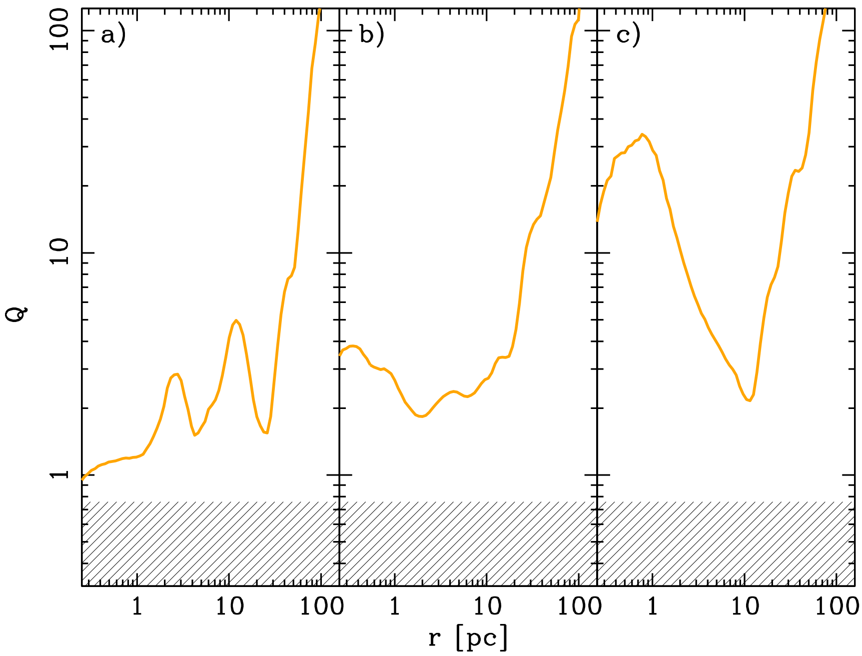

Figure 3.5: Azimuthally averaged Toomre Q profile of the disk at the same times as the panels in Fig. 3.1 (time increasing from left to right). The shaded area corresponds to the instability region marked by $Q \leq 0.67$, this being the stability threshold for disks of finite thickness (Nelson et al. 1998). The Toomre parameter is calculated using the effective sound speed, which includes the contribution of the turbulent (radial) velocity dispersion, $\tilde{v}_s = \sqrt{({c_s}^2 + {\sigma_r}^2)}$, where c_s is the thermal sound speed and σ_r the radial velocity dispersion of the gas. Note that $\sigma_r \sim c_s$ outside the central few parsecs; within the inner few parsecs, especially after the onset of the Jeans collapse (panels b - c) the thermal pressure is dominant as the gas is strongly adiabatically compressed (the high central value of Q seen in panel (c) is associated with the formation of the supermassive hot central cloud).

outer region of the disk.

The right panels of Figures 3.3 and 3.4 show the final expansion of the disk as the spiral arms unwind and transfer angular momentum outward of tens of parsecs, generating a net outflow. At this point, the inner profile has reached stability as further collapse is not possible (the resolution limit has been reached). Expansion of the disk as a result of angular momentum transfer driven by spiral modes is a well-documented phenomenon in both gaseous and stellar disks from galactic to planetary scales (Agertz et al. 2009a; Begelman 2008; Mayer et al. 2004).

In Fig. 3.5, we show the evolution of the Toomre parameter Q (Toomre 1964), defined as

$$Q \equiv \frac{c_s \kappa}{\pi G \Sigma_g}$$

where c_s is the sound speed, κ the epicyclic frequency, and Σ_g the surface density of the gas. The Toomre parameter represents the balance between the self-gravity $G\Sigma$ of the disk and the stabilizing effect of pressure (through c_s) on small scales and shear (κ) on large scales, and stricly speaking it measures the *local* stability of a differentially rotating disk to axisymmetric perturbations. It is important to note that the disk is born out of equilibrium from the collision of the two cores, rather than becoming unstable starting from an equilibrium rotational configuration as assumed in the standard perturbative approach. The disk indeed reaches a near-equilibrium configuration only after the phase of intense inflows. Nevertheless, previous studies on gaseous disks have shown that the Toomre parameter provides a good heuristic measure of the susceptibility of disks to fragmentation, quite independently of how the disk is initially set up, and in this sense also applies to *global* stability to generic, non-axisymmetric perturbations (Durisen et al. 2007). Fig. 3.5 shows that the Toomre parameter remains always in the theoretical regime of stability against fragmentation, although it drops initially to values in the range $1-1.5$ where strong spiral instabilities are expected, and are indeed observed. After the phase of strong non-axisymmetric instability associated with the inflow and subsequent central collapse is terminated (first and second panel of the figure) the disk self-regulates to a more stable state, with a minimum $Q \sim 2$.

The very high inflow rates in Fig. 3.4 seem to be in contrast with the expectations of analytical models that study a thin and self-gravitating isothermal accretion disk in steady state. Through a local stability analysis, recent works argue that there exists a *maximum* inflow rate *above* which fragmentation, and thus star formation, will occur (Lodato & Natarajan 2006). In steady state, such maximum inflow rate can be expressed as

$$\dot{M}_{\rm max} = 2\alpha \frac{{c_s}^3}{G}$$

where $\alpha \sim 0.06$ is the maximum disk viscosity resulting from gravitational stresses and c_s is again the sound speed. Protogalactic disks with temperatures ~ 4000 K ($c_s \sim 5$ km s^{-1}) are typically considered, for which $\dot{M}_{\rm max} = 10^{-2}$ M$_\odot$ yr^{-1}. In our disks the thermal sound speed is much higher, but because the disks are in a gravoturbulent state, it is more sensible to consider the sum of the thermal sound speed and turbulent velocity dispersion, as we have done for Q in Fig. 3.5. This amounts to about $600-700$ km s^{-1} at scales of 25 pc (the scale of the first inflow), which implies an increase of a factor up to $140^3 = 2.7 \times 10^6$, which would yield a maximum inflow rate $\sim 10^4$ M$_\odot$ yr^{-1}, quite in agreement with the numerical results. The second inflow at parsec scales is even stronger and exceed the “maximum” rate possible without fragmenting. However, since this inflow is triggered by the Jeans collapse of the central cloud rather than by transport by spiral waves (as the low $m = 2$ amplitude indicates), the argument based on the maximum viscous stress associated with gravitational instability does not apply anymore: in globally unstable disks, effective α viscosities even larger than unity can easily arise (Krumholz et al. 2007). Dropping the constraint

$\alpha \sim 0.06$, as suggested by the nature of global instability, would allow even higher inflow rates without fragmentation.

3.2.4 Mass growth of the MBH seed

The time $t(M_{\rm BH})$ required for a black hole of initial mass $m_{\rm seed}$ to reach a mass $M_{\rm BH}$, assuming Eddington limited accretion, is given by

$$t(M_{\rm BH}) = \frac{\tau}{f_{\rm edd}} \left(\frac{\epsilon_r}{1-\epsilon_r}\right) \ln(M_{\rm BH}/m_{\rm seed}) \,,$$

where τ is the Salpeter time (see Eq. 1.5 on p. 14) and $f_{\rm edd}$ quantifies at which fraction of the Eddington limit the black hole is accreting. In this case, we can evaluate such time for $M_{\rm BH} = 10^9$ M$_\odot$ and $m_{\rm seed} = 2.6 \times 10^5$ M$_\odot$ (corresponding to 0.1% of the mass of the collapsing central cloud in our simulation). We choose standard parameters $f_{\rm edd} = 1$, $\epsilon_r = 0.1$ and, to compute the characteristic accretion timescale τ, we adopt a molecular weight per electron for a plasma at zero metallicity with cosmic abundance of hydrogen ($X = 0.75$) and helium ($Y = 0.25$), yielding an mean molecular weight per electron $\mu_e = 1/(1 - Y/2) = 1.14$, so that $\tau = 0.395$ Gyr. Note that metallicity effects are marginal in this calculation. With these choices, we obtain $t(M_{\rm BH}) = 0.362$ Gyr. Assuming that the seed black hole can accrete at the Eddington limit ($f_{\rm edd} = 1$) is justified by the fact that the hole would accrete the gas belonging to the nuclear disk, which has very high densities $n_H \sim 10^5 - 10^8$ atoms/cm^2 at scales below 10 pc. Such densities are several orders of magnitude higher than e.g. those of the gas surrounding the small black hole seeds formed by the collapse of Pop III stars, which accrete at sub-Eddington rates (Djorgovski et al. 2008). Therefore, not only our model can lead to seeds that are much more massive relative to those resulting from Pop III stars, but also the subsequent gas accretion occurs in a much more favourable environment.

The accretion timescale is especially sensitive to the radiative efficiency (Shapiro 2005). The value of ϵ_r depends on the spin of the black hole, which in turn depends on the mechanism of formation and accretion. It may be as large as 0.42 for maximally spinning black holes accreting in standard thin disks, in which case $t(M_{\rm BH}) > 1$ Gyr. Values of ϵ_r in the range $0.1 - 0.2$ should be more likely, according to the Soltan argument. In summary, $t(M_{\rm BH}) < 1$ Gyr requires $\epsilon_r \leq 0.2$ and $f_{\rm edd} \geq 0.7$. On the other hand, if the galaxy merger occurs at $z \sim 8$, and the black hole has to grow to its final mass by $z \sim 6$, the time available for accretion is < 0.5 Gyr for the standard WMAP5 cosmology, which is consistent with our standard choice of parameters $f_{\rm edd} = 1$ and $\epsilon_r = 0.1$.

3.3 Companion simulations

In this section, we describe additional simulations that highlight some key aspects of supermassive cloud formation: mass dependence (§3.3.1) and star formation (§3.3.2).

3.3.1 Dependence on the mass of the merging galaxies

In order to assess how our physical picture applies to different regimes, we ran two additional major mergers with all parameters equal to our reference case, but with masses rescaled by a factor of 5 and 40, respectively. The number densities of such halos at $z \sim 8$ are, respectively, 10^{-5} and 10^{-2} per Mpc^3. Mass rescaling of distances and velocities at fixed z is done by keeping constant the virial overdensity of the models and the morphological structure of the galaxies; it follows that $R \propto M^{1/3}$ and $V \propto M^{1/3}$. We adopt the same EOS as in the original simulation. The results are shown in Fig. 3.6, where the final cumulative gas mass profiles in the different runs are shown. We find that the multi-scale gas inflow and the Jeans collapse of the resulting supermassive cloud occur even more vigorously in the run with 5 times lower mass: indeed, a higher fraction of the nuclear disk gas mass is deposited to the center (the total mass of the merger remnant is 4×10^{11} M$_\odot$). Instead the inflow is relatively weaker in the test with 40 times smaller mass (total mass of the merger remnant 5×10^{10} M$_\odot$). Most importantly, in the latter case we do not observe a central gravitational collapse because the mass contained within the inner parsec remains below the local Jeans mass (the density maps in Fig. 3.7 show that there is no central density peak in this case only). Therefore, no SMBH seed formation through this mechanism is expected in the major merger with the lowest-mass galaxies.

The trend of strength of the gas inflow vs. galaxy mass can be understood as a consequence of how the two critical factors determining the stability of the nuclear disk – effective pressure/temperature and disk surface density – scale with galaxy mass. The surface density of the nuclear disk scales roughly as

$$\Sigma \propto M/R^2 \propto M^{1/3} .$$

The disk angular frequency $\Omega \propto V/R$ does not depend on M since $V \propto R$. On the other hand, the thermal and non-thermal (turbulent) energy content of the disk arising from the merger will be determined by the energy injected by the shock (note that, because of the stiff EOS ($\gamma = 7/5$) during the collision, radiative losses are implicitly small). The energy imparted by the shock is

$$E_{\rm shock} \propto M_{\rm vir} {V_{\rm vir}}^2 \propto M^{5/3}$$

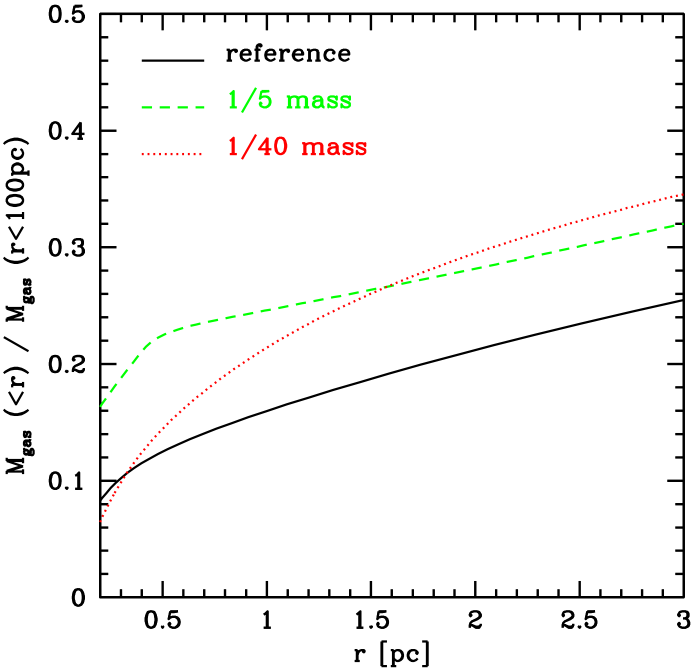

Figure 3.6: Evolution of the cumulative gas mass profile of the nuclear disk in the different mergers. In order to highlight how the inflow efficiency scales with mass, all profiles are normalized to the respective total mass within 100 pc (compare with Fig. 3.9) for the standard run as well as for the runs with lower mass galaxies. Lines are labelled on the figure. The mass profiles are shown at 1.036×10^5 yr after the merger. The time of the merger is defined as the time at which the two density peaks associated with the merging cores of the galaxies are no longer distinguishable.

(where the product of the galaxies' virial mass and virial velocity squared measures the orbital energy of the collision).

Let us first assume that $U \sim E_{shock}$, where U is the internal energy of the gas, including both thermal and turbulent energies. This is equivalent to assuming that shock-heating is the main contribution to the internal energy of the nuclear disk after the collision. The effective sound speed in the nuclear disk is $\tilde{c}_s \propto U^{1/2}$, hence the Toomre parameter of the nuclear disk scales as

$$Q \propto \tilde{c}_s \, \Omega \, \Sigma^{-1} \propto M^{1/2} \, .$$

In other words, nuclear disks in lower-mass galaxies are increasingly more unstable, as the energy imparted by the collision decreases more rapidly than the disk self-gravity. This is the first key result, which explains why the intermediate-mass merger produces a more unstable nuclear disk, and thus a relatively more massive nuclear cloud compared to the reference simulation. It also explains the qualitative features of the supermassive cloud in (Fig. 3.7), which appears to be less pressure-supported (hence more flattened) at

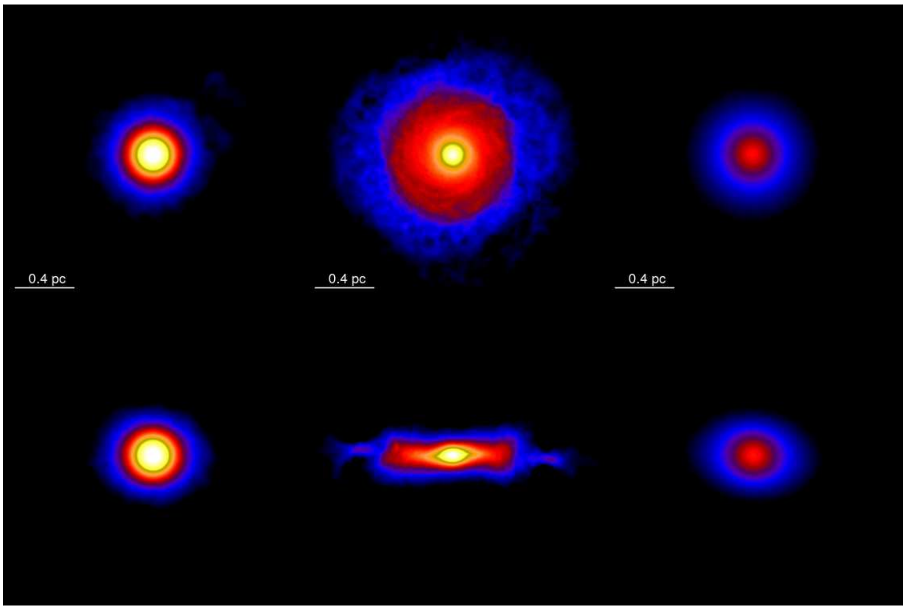

Figure 3.7: Logarithmic surface density maps of the final nuclear gas distribution in the central parsec in runs with different galaxy mass. *Top panels*: face-on view; *bottom panels*: edge-on view. From left to right, the standard, intermediate- and lowest-mass merger remnants are shown, all at 1.036×10^5 yr following the merger. The density limits are as in Fig. 3.1. Note how the lowest mass case does not exhibit the central density peak of the other two, and indeed in this case the central parsec region is stable to Jeans collapse. In the intermediate-mass case there is more residual angular momentum within the central parsec, which thus exhibits a central cloud clearly flattened by rotation.

intermediate masses.

At even lower masses, the energy imparted by the shock (which scales as $M^{5/3}$) will eventually become lower than the initial internal energy of the colliding galaxy cores, which here mimics the "normal" equilibrium conditions between the different phases of the ISM. If $U \gg E_{\rm shock}$, we can assume that $\tilde{c}_s$ does not depend on M anymore, so that

$$Q \propto \Sigma^{-1} \propto M^{-1/3} \, .$$

When the energy imparted by the collision is negligible in the total energy budget of the ISM, lighter disks are more stable as their self-gravity is weaker. This explains the increased stability of the lowest mass merger that we considered, which results in its inability to undergo a central Jeans collapse.

The exact transition mass between the two regimes that we have just described (shock-dominated and gravity-dominated) will depend on the details of radiative heating and cooling, and on other mechanisms, such as heating by supernovae explosions, that can contribute to thermal and non-thermal pressure. Effects that we miss in our simulations, such as supernovae explosions and the cosmic ionizing radiation at high z, can only reinforce our claim that below 10^{11} $M_\odot$ the nuclear region will be stable to pc-scale inflows; for example recent results (Governato et al. 2010) show that for low-mass galaxies supernovae-driven outflows prevail over gas inflows in mergers, in agreement with our proposed scenario.

3.3.2 Star formation

The conversion of gas into stars is not included in the reference simulation, although its radiative feedback on gas thermodynamics is included with the choice of the EOS (§3.2.1). Indeed, the refined calculation is carried out for less than 1% of the starburst duration of 10^8 yr indicated by the companion merger simulation carried out without splitting (Kazantzidis et al. 2005; Mayer et al. 2007), suggesting that the conversion of gas into stars is not important on the timescales of interest for this work. Cautionary remarks regarding this point are however necessary. Had we included SF directly in the refined simulations we would have probably found local gas consumption timescales shorter than the global starburst timescale since particle splitting allows to resolve much higher densities, and the SFR depends on the local gas density.

As for the first issue, we can obtain a rough estimate of how short the star formation timescale can be in the following way. To begin with, in the nuclear disk most of the gas is at densities > 100 atoms cm^{-3} where molecular hydrogen formation is efficient. Let us then make the extreme assumption that all the gas in the disk is molecular and readily available for star formation. Then, let us simply assume that molecular gas will be turned into stars on the local orbital timescale. Star formation in molecular clouds is rather inefficient, and typically ≤ 30% of the dense, molecular gas is converted into stars, possibly because internal turbulence in the clouds prevents them from collapsing altogether (Klessen et al. 2007). Therefore, the SFR can be estimated to be

$$\dot{M}_* = 0.3 \times M_{\mathrm{gas}}/T_{\mathrm{orb}}$$

where $T_{\mathrm{orb}} = 2.5 \times 10^5$ yr is the orbital time at the disk half mass radius (25 pc), and $M_{\mathrm{gas}} = 3 \times 10^9$ $M_\odot$ is the mass of the enclosed mass of the disk at such distance. The resulting upper limit on the star formation rate is 3600 $M_\odot$ yr^{-1}, about 80 times higher than that estimated in the low-res simulations. Nonetheless, even with such high SFR only 10% of the gas within 25-30 pc (this is also the region where the first inflow occurs, Fig. 3.2) would be converted into stars during the time required to form the central supermassive cloud (~ 10^5 years). On the other hand, this high SF rate justifies the use of the EOS valid for a starburst regime even on the short timescales probed by our calculations.

Along with star formation, another astrophysical aspect that we include in a very simplified way is SN feedback. Feedback from SN type II would contribute to both heating

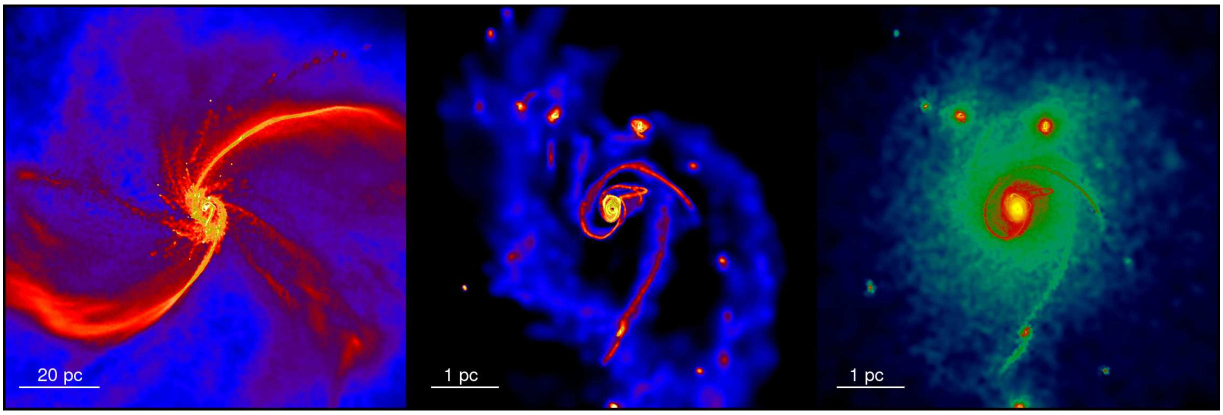

Figure 3.8: Logarithmic surface density maps of the nuclear disk in the run with cooling and star formation. *Left panel*: gas density map at large scales (100 pc). *Middle panel*: gas density at small scales (5 pc). *Right panel*: stellar density at small scales (5 pc). Note that more than 90% of the stellar mass in the inner parsec is in new stars formed during the final collision of the two galaxy cores. The maps are shown at 3×10^4 yr after the end of the merger. The density limits are between 10^4 and 10^8 $M_\odot/pc^2$ in the left panel, between 10^6 and 10^{10} $M_\odot/pc^2$ in the middle panel (note that gas densities are much higher than in standard run shown in Fig. 3.1 as a result of efficient cooling) and between 10^5 and 10^{10} $M_\odot/pc^2$ in the right panel. Fragmentation due to gravitational instability is evident, and stars form predominantly in the clumpy regions. Nevertheless, a strong inflow builds up a supermassive gaseous object in the central parsec (the density peak evident in the middle).

the gas and increasing its turbulence (the timescale of SN type II explosions is sufficiently short to be relevant here), which should go in the direction of decreasing the star formation rate and therefore strengthening our previous argument concerning the role of star formation. It would also tend to stiffen the equation of state even in the central regions of highest density (where we tend to overestimate γ), likely bringing the effective γ in closer agreement to the values adopted here. On the other end, a quick calculation suggests that feedback should not have a major impact on the global energetics of the nuclear disk. In fact, assuming the upper limit on the star formation rate of 3600 $M_\odot$ yr^{-1} and a Miller-Scalo initial stellar mass function, we obtain that supernovae should dump $\leq 2.5 \times 10^{52}$ erg yr^{-1} (7×10^{48} erg per solar mass of stars formed) into the surrounding gas, corresponding to $\leq 2.5 \times 10^{57}$ erg dumped during the MBH formation timescale, $\sim 10^5$ yr. This is at most 20% of the the overall internal energy budget of the gas in the nuclear disk, hence its effects on thermodynamics will be moderate. In addition, most of this energy will be deposited outside the inner few parsecs, where the strong radial inflow proceeds on the shortest timescale. As a result, the dynamics of the gas inflow, that are crucial in our formation model, should not be significantly affected.

We have tested the validity of these general conclusion based on scaling laws, by performing one run that implements radiative cooling and star formation rather than the effective EOS. We use a SF density theshold of 10^4 atoms cm^{-3}, as suggested by observa-

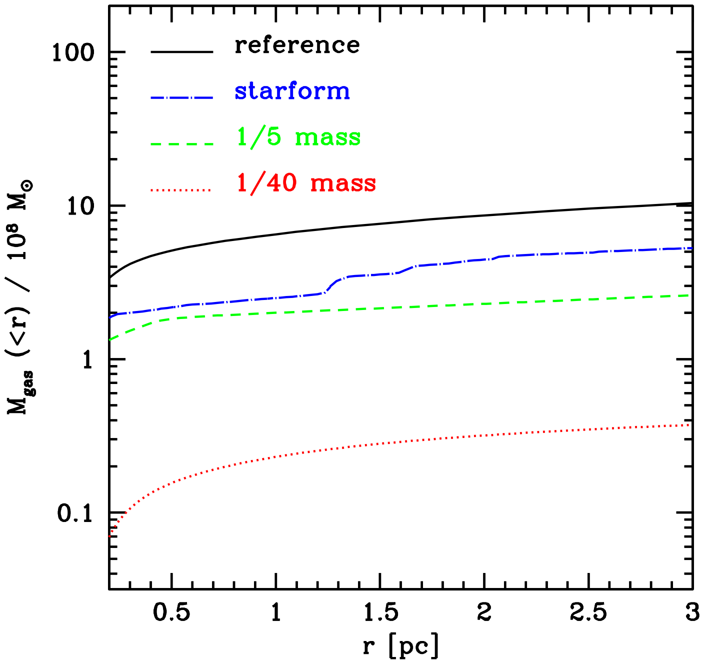

Figure 3.9: Evolution of the cumulative gas mass profile of the nuclear disk in the different mergers. Profiles are normalized to a fixed reference mass of $10^8 M_\odot$ and are shown for the inner 30 pc for the reference run (*black curve*) as well as for the runs with lower mass galaxies (*green and red*) and for the run with star formation (*blue*). The mass profiles are shown at 1.036×10^5 yr after the merger, except in the case of the star formation run, which is shown at an earlier time (at 3×10^4 yr after the merger) because the simulation had to be stopped earlier due to excessive computational burden. In the star formation run, gas accumulation at the center occurs more rapidly than in the other runs because radiative cooling is included, which leads to more effective sinking of the gas following fragmentation.

tions of star formation within pc-scale molecular cloud cores (Evans et al. 2009). This is the highest density threshold that we can afford at our resolution while still resolving the local Jeans length (as discussed on p. 71). The star formation efficiency in gas lumps that satisfy the critical density threshold is set to 10% (Evans et al. 2009). We start the run only about a million years before the galaxy merger is completed (the main star formation burst occurs during the final collision of the galaxy cores in the low-resolution simulation by Kazantzidis et al. 2005). We stop the run a few 10^4 yr after the merger; at this point the gas inflow rate is higher than the peak rate measured in the standard simulation with the fiducial EOS. Due to the short timescale covered by the simulation, supernovae explosions would not kick in to establish a hot, pressure-supported phase co-existing with the cold phase. Hence, rather than including SN feedback directly, we incorporate its effects implicitly by limiting the minimum gas sound speed to 30 km s^{-1}; this maintains a nuclear disk scale height of a few parsecs, consistent with the results of multi-phase models of turbulent circumnuclear disks which evolve the system for many dynamical times including the effect of supernovae explosions (Wada 2001; Wada & Norman 2002). This pressure floor is important to avoid producing an unrealistically thin nuclear disk that would undergo immediately, and artificially, large-scale fragmentation via gravitational instability. Note that this simulation is biased towards favoring fragmentation, since we include optically thin cooling in this simulation and neglect optical depth effects in the high density, optically thick gas, that would act to reduce cooling.

In the densest regions of the nuclear disk the cooling time is shorter than the dynamical time, so that locally fragmentation and vigorous star formation is expected (Lodato & Natarajan 2006), and indeed it occurs. The star formation peaks at 10^4 $M_\odot$ yr^{-1}, and it is on average a few 1000 $M_\odot$ yr^{-1} (the average is in rough agreement with our previous analytical estimate). Peak star formation rates are comparable to those found in cosmological simulations (Li et al. 2007) for the hosts of bright high-z QSOs. At the end of the simulation, nearly half of the gas in the central tens of parsecs has been turned into stars (Fig. 3.9). However, despite its intensity, the SF does not disrupt the multi-scale gas inflow, and $> 10^8$ $M_\odot$ of gas accumulate within the central parsec (Fig. 3.9). The inflow rate peaks at values even higher than in the simulation with no star formation because the gas, which is cooling vigorously, is less pressure-supported, and because gas clumps formed by fragmentation lose quickly orbital angular momentum via dynamical friction (Fig. 3.8). At the final stage most of the gas is in a thin disk only a parsec in height. The rotating disk is bar-unstable at the resolution limit of 0.1 pc, hence would lose angular momentum further and trigger the collapse.

3.4 Remarks

In this chapter, it was shown how a hot, gravoturbulent disk can easily sustain accretion rates orders of magnitude higher than those of cold, non-fragmenting protogalactic disks considered in recent literature, hence allowing naturally the formation of central supermassive objects before gas is consumed by star formation. These particular conditions should arise naturally in the highly perturbed nuclear disks formed in high-z major galaxy mergers, and should indeed be interpreted as a by-product of the starburst itself. Thus, in our model star formation has indeed a positive role in allowing the direct collapse since it provides enough heating to prevent large-scale fragmentation.

One caveat to this model may come from pre-existing MBHs formed by another mechanism, such as collapse of Pop III stars or direct collapse in an unstable protogalaxy, *before* a massive seed is produced via our mechanism in a gas-rich galaxy merger. That a black hole seed might be already present before the first major merger is plausible since in our mechanism should operate at relatively moderate redshifts ($z < 10$), when sufficiently massive disk galaxies would be already in place, while, for example, seed formation from collapse of Pop III seeds would occur much earlier. If the heating resulting from feedback by the accreting Pop III seed can at least double the internal energy content of the gas, it would stabilize the disk further and likely suppress the inflow; this is because the Toomre parameter would reach $Q > 2$, which implies stability to spiral and bar modes (see the plot for the reference simulation in Fig. 3.5). Assuming $f_{\mathrm{Edd}} = 1$, $\epsilon_r = 0.1$ and $\epsilon_{\mathrm{fb}} = 1$, and that accretion onto the seed can be sustained for all the time preceding the merger (~ 0.36 Gyr in our model), we find a minimum pre-existing black hole mass of $\sim 10^6$ $\mathrm{M}_{\odot}$, below which significant heating does not occur. Such mass is too large to have been assembled by accretion onto Pop III seeds in the limited amount of time available before the merger ($<< 1$ Gyr). Therefore, we conclude that the heating from a pre-existing Pop III seed would not interfere with our direct collapse mechanism.

This direct collapse scenario should work down to about 10^{11} $\mathrm{M}_{\odot}$ (§3.3.1). This is naturally consistent with the observational evidence that below such mass scale galaxies do not seem to host massive black holes (at least not black holes consistent with the extrapolation of the $M_{\mathrm{BH}} - M_{\sigma}$ and $M_{\mathrm{H}} - M_{\mathrm{bulge}}$ relations). This of course does not exclude that smaller, intermediate-mass black holes (below a few 10^5 $\mathrm{M}_{\odot}$) may have formed by different mechanisms in relatively low-mass galaxies. At low redshift, our formation mechanism should be suppressed, as MBHs in the two merging galaxies should have already formed. In this case, heating of the surrounding gas by AGN feedback might be strong enough to overcome cooling and produce a stiffer equation of state in the nuclear gas: either a dense nuclear disk will not form at all and no multi-scale scale gas inflows will occur, or the higher pressure support of the gas within the nuclear disk could prevent the secondary inflow and thus the formation of the central supermassive cloud.

These results have an interesting application to the specific case of the MBH of the Milky Way. From cosmological simulations of Milky Way-sized galaxies (chapter 4), we know that the most massive progenitors of such galaxies at $z \sim 6$ are hosted in halos with mass of order 10^{10} $\mathrm{M}_{\odot}$ or smaller, which later undergo a series of mergers. We have argued that mergers at such mass scale would not be conducive to direct collapse into a MBH, while this can happen very efficiently above a few 10^{11} $\mathrm{M}_{\odot}$. Interestingly, the latter mass scale is close to the mass scale of the most massive progenitors of a Milky Way-sized galaxy at much lower redshift, $z \sim 3$. This is also when the stellar spheroid is finally assembled in such simulations (compare with Fig. 4.6 in the extreme case of an early assembly and more quiescent late history). There is thus the possibility that such major merger triggered the formation of the Galactic MBH. Currently there is no constraint on when our MBH came into place. If it formed by our proposed mechanism, then it should have formed quite late, at $z = 2-3$: this is when, in the history of the Milky Way, gas-rich mergers could take place between galaxies massive enough to trigger direct collapse via the central gas inflow. Of course the MBH of the Milky Way, being relatively light, might have formed earlier by the other competing mechanisms, including slower growth of a Pop III seed.

We are already including the MBH seeding mechanism here presented into semianalytical models of galaxy formation, in order to check its predictions against data of the MBH population (Bonoli et al., in prep.). For example, it is not obvious whether the MBH scaling relations in the local Universe can be easily satisfied; large deviations from the local $M_{\rm BH} - \sigma$ relation (Djorgovski et al. 2008) should be expected at high redshift, as the black hole mass grows faster than that of its host galaxy in our scenario. Deeper observations in the rest-frame optical and UV, as well as future gravitational wave experiments, will be able to test the existence of a population of black holes that had a jump-start by probing the distribution of active and merging black holes as a function of redshift.

4

The *Eris* simulations: formation of a late-type disk galaxy

In chapters 2 and 3, the connection between galaxy interactions and MBHs has been explored, with simulations that focused on the intermediate-to-small scale, from ~ 100 kpc down to 1 pc. While the initial conditions of these simulations were tuned to satisfy theoretical expectations about how galaxies evolve in ΛCDM, the complexity of the cosmological context was missing. The next step in this line of research would be to include the information we gained from such studies into a fully cosmological simulation, following the coevolution of MBHs and galaxies across cosmic time. It would be too computationally demanding (if not still technically unfeasible) to simulate an entire galaxy population with enough resolution to capture at least the coarser among the key processes that we presented in the previous chapters. A very important step in this direction would be to follow the history of at least one simulated galaxy that resembles the Milky Way – for which we have by far the largest wealth of observational constraints – where numerical and physical modelling can be tuned and tested.

In this chapter, we describe a series of new cosmological N-body/SPH simulations of extreme dynamic range, in which a close analog of a Milky Way-type galaxy arises. The simulated galaxy was named “Eris” after the Greek goddess of discord and strife.[1] The resolution and the parameters of the sub-grid modelling vary across these simulations, shedding light on the respective roles of astrophysical processes and numerical effects in determining the properties of the final galaxy. Such simulations, valuable on their own, also open the way to the next generation of high-resolution studies of MBH-galaxy coevolution.

---

[1] The Eris simulations are introduced in Guedes, Callegari, Madau, & Mayer (2011).

4.1 Context

Simulations of the formation of late-type spiral galaxies in ΛCDM cosmology have traditionally failed to yield realistic results. Opinions vary as to whether this is simply a problem of the inability of numerical codes to properly model the necessary physics, or if merger-driven galaxy assembly is fundamentally incompatible with the observed number density of dynamically "fragile", rotationally-supported disks (for a most recent paper arguing in this direction, see Kormendy et al. 2010). For this reason, the formation of realistic late-type spirals has been a long-standing problem of galaxy formation in a ΛCDM universe.

Baryons in the Universe can acquire angular momentum through tidal torques from nearby structures, and then condense at the center of the host dark matter halo (Fall & Efstathiou 1980). A centrifugally-supported baryonic disk forms, with a size that depends on the fraction of the original angular momentum that is retained during the contraction. In numerical simulations of this process, however, a fundamental "angular momentum problem" arises, as galaxies are produced with a baryonic component that is quite deficient in angular momentum compared to real spirals: galaxies are produced with substantially more compact disks than in real spirals (Navarro & Benz 1991), with an excess of old stars in the center, and offset from the observed Tully-Fisher relation (Navarro & Steinmetz 2000). Aside from artificial losses of angular momentum caused by insufficient resolution and other numerical effects (Okamoto et al. 2003; Governato et al. 2004; Kaufmann et al. 2007), this failure has traditionally been traced back to the very nature of the hierarchical buildup of structures: dynamical friction transfers the orbital angular momentum of merging substructures to the outer halo, and causes the associated cold baryons to sink to the center of the proto-galaxy and form a spheroid rather than a disk (e.g., Maller & Dekel 2002).

A popular solution to the angular momentum problem envisions energy injection from supernovae (SNe) and evolving stars as a mechanism to prevent efficient gas cooling and condensation, and to remove low angular momentum gas from the centers of galaxies. Modern simulations with improved resolution and more effective recipes for SN feedback (Robertson et al. 2004; Governato et al. 2007; Scannapieco et al. 2009; Stinson et al. 2010; Piontek & Steinmetz 2011; Brooks et al. 2011) have yielded rotationally-supported disks with realistic exponential scale lengths, not only in galaxies formed in relative isolation but also in those that are accreted by massive groups with a dominant central elliptical (Feldmann et al. 2010, 2011). They have also modified the standard picture of gas accretion and cooling onto galaxy disks: for galaxies up to Milky Way masses, gas acquired through filamentary "cold flows" that was never shock-heated to the halo virial temperature is largely responsible for star formation in the disk at all times (Brooks et al. 2009; Kereš et al.

2009; Ceverino et al. 2010). Yet, these simulations typically continue to produce centrally-concentrated systems, with rotation curves that rise steeply close to the center: simulated disk galaxies fall exclusively in the S0 or Sa category, leaving late-type spirals with negligible bulges and large disks with flat rotation curves – such as our own Milky Way – as an unsolved puzzle. Two recent exceptions are the simulations of Agertz et al. (2011) and Governato et al. (2010). In the first, replicas of Sb/Sc galaxies with moderate bulges were obtained with a low efficiency of star formation that may implicitly mimic the bottleneck of the conversion of atomic gas into molecular, at the expense of producing stellar disks that are much more massive than expected at a given halo mass (e.g. Guo et al. 2010). In the second, a realistic bulgeless dwarf galaxy with a shallow central dark-matter profile was formed by resolving the inhomogenous ISM and the process of energy injection from multiple SNe in clustered star forming regions. In this work we extend the latter approach to the scale of more massive galaxies. In this chapter, we present initial results from a series of SPH cosmological simulation of high dynamic range that include radiative cooling, heating from a cosmic UV field, SN feedback, and a varying star formation recipe based different SF efficiencies and gas density thresholds. It is this last feature, we argue, that is key to the formation of a more realistic massive late-type spiral in ΛCDM.

4.2 The simulations

The simulations here discussed are part of a campaign of extreme resolution simulations of the formation of Milky Way-sized galaxies. They were performed with GASOLINE in a WMAP3 cosmology, $\Omega_M = 0.24$, $\Omega_\Lambda = 1-\Omega_M$, $\Omega_b = 0.042$, $H_0 = 73\,\mathrm{km\,s^{-1}\,Mpc^{-1}}$, $n = 0.96$, $\sigma_8 = 0.76$ for $\sim$ 1.5 milion cpu hours each.

We started from a low-resolution (300^3 particles), dark matter-only, periodic box of 90 Mpc on a side. The initial conditions for the low-resolution box are generated using GRAFIC (Bertschinger 2001). Its approach is based on writing the cosmological density field as a convolution:

$$\begin{aligned}\delta(x) &= \int \mathrm{d}^3k\, e^{i\vec{k}\cdot\vec{x}}T(k)\xi(\vec{k}) \\ &= \int \mathrm{d}^3x'\, \xi(x')T(|x-x'|) \\ &= (\xi * T)(x)\end{aligned}$$

where $\delta(x) \equiv \left[\rho(x)-\bar{\rho}\right]/\bar{\rho}$ measures the deviations from the average cosmic density $\bar{\rho}$, $\xi(x)$ is Gaussian white noise, and $T(k)$ is the *transfer function* related to the power spectrum P of $\delta(x)$ by

$$T(k) = [P(k)]^{1/2}\ .$$

In this way, an arbitrary Gaussian random field (in our case, cosmological fluctuations) can be constructed from a discretization of the equation for $\delta(x)$: one only needs to sample white noise in real space, Fourier-transform it and multiply by T in $\vec{k}$ space, and then transform the result back to real space.[2]

The target halo at $z = 0$ was then chosen to have a mass similar to the Milky Way's, and a rather quiet late merging history, i.e. to have had no major mergers (defined as mass ratio $\geq 1:8$) after $z = 3$. Three halos with masses between 6×10^{11} and 8×10^{11} $\mathrm{M}_{\odot}$ satisfied such conditions in the 90^3 Mpc^3 box, and we picked the one which appeared to be most "regular" and isolated.

New initial conditions were then generated with improved mass resolution (by a factor 20^3) on a nested grid in a Lagrangian sub-region of size 1 Mpc, centered around the chosen halo, using a standard "zoom-in" technique to add small-scale perturbations (again following Bertschinger 2001). The technique used to generate the nested grids is analogous to the one outlined above for the unrefined box, with the additional constraint that at each higher refinement level, the white noise has to have the same long-wave properties as the coarser grid. Let $\xi_0(\vec{m})$ be the lower-level noise as a function of the grid integer coordinates $\vec{m}$, and $\xi_1(\vec{m},\vec{n})$ be the uncorrected noise in the refined region (where $\vec{n}$ are the coordinates on the subgrid); then the long-wave constraint is achieved by using the noise resulting from the simple linear correction

$$\xi(\vec{m},\vec{n}) = \xi_1(\vec{m},\vec{n}) + \xi_0(\vec{m}) - \xi_1(\vec{m})$$

to generate the density field. The noise $\xi(\vec{m},\vec{n})$ now has all the desired properties.

High-resolution particles were further split into 13 million dark matter particles and an equal number of gas particles, for a final dark and gas particle mass of $m_{\mathrm{DM}} = 9.8 \times 10^4$ $\mathrm{M}_{\odot}$ and $m_{\mathrm{SPH}} = 2 \times 10^4$ $\mathrm{M}_{\odot}$, respectively. The gravitational softening length, ϵ_G, was fixed to 120 pc for all particle species from $z = 9$ to the present, and evolved as $1/(1+z)$ from $z = 9$ to the starting redshift of $z = 90$. The version of GASOLINE used in this study includes also metallicity-dependent radiative cooling at low temperatures (Mashchenko et al. 2006). A uniform UV background modifies the ionization and excitation state of the gas and is implemented using an updated version of the Haardt & Madau (1996) spectrum. In our reference run, hereafter simply "Eris", star formation occurs when cold ($T_{\mathrm{SF}} < 3 \times 10^4$ K), virialized gas reaches a threshold density $n_{\mathrm{SF}} = 5$ atoms cm^{-3}, and proceeds with an efficiency of $\epsilon_{\mathrm{SF}} = 0.1$. We adopt $\epsilon_{\mathrm{SN}} = 0.8$ (the same value used in previous cosmological simulations, e.g. Governato et al. 2007), while no feedback from an active galactic nucleus was included.

---

[2] Additional subtleties – in particular related to the refinement technique – can be found in the GRAFIC paper by Bertschinger (2001).

The adoption of a density threshold for star formation that is 50 times higher than in many previous lower-resolution studies is possible owing to the high mass and spatial resolution of this run, which resolves the giant cloud complexes where star formation actually occurs in the ISM and the true scale-height of the neutral atomic ISM. A good resolution criterion is to require that the Jeans instability (Jeans 1929) be resolved at $n_{\rm SF}$ with a certain number N_l of softening lengths and a number N_m of SPH particles, so that:

$$c_s \left(\frac{\pi}{G\,\rho_{\rm SF}}\right)^{1/2} \geq N_l\,\epsilon_G$$

and

$$\frac{\pi^{5/2}}{6G^{3/2}}\,\rho_{\rm SF}^{-1/2}\,c_s^3 \geq N_m\,m_{\rm SPH}\,,$$

where $\rho_{\rm SF} = \mu m_p n_{\rm SF}$. Since, for any reasonable choice of ϵ_G, in high density regions the SPH smoothing length is smaller than the softening, these criteria guarantee that both gravity and hydro are resolved correctly. For example, in the Eris $z = 0$ galaxy the minimum smoothing length for gas particles is 5 times smaller than the force softening.

The formulae here above can be used to constrain what SF density threshold can be afforded at a given numerical resolution, or vice-versa. In particular, the local Jeans length corresponding to our density threshold (for $T = 10^3$ K, a lower bound on the typical temperature of the cold gas in the simulations – very little gas inside the virial radius ever cools down below this temperature) is resolved with more than 5 SPH smoothing lengths, thus preventing artificial fragmentation (Bate & Burkert 1997). Analogously, the Jeans mass at threshold density is resolved with 100 $m_{\rm SPH}$. While not as high as the value of $n_{\rm SF} = 100$ atoms cm^{-3} used in Governato et al. (2010) dwarf galaxy simulation, whose particle mass was substantially lower and allowed to resolve the Jeans length of star forming gas at much higher densities, our star formation threshold is still large enough to allow the development of a clumpy, inhomogeneous ISM with more localized energy injection by multiple overlapping SN explosions. This allows galactic pressure-driven outflows to develop and remove low-angular momentum material. To demonstrate the important role of the star formation parameters on the structural properties of simulated massive galaxies, we have run a low-threshold twin simulation (termed “ErisLT") with $n_{\rm SF} = 0.1$ atoms cm^{-3}. We have kept all the other simulation parameters fixed (same mass and spatial resolution and identical feedback scheme) except for the star formation efficiency parameter, $\epsilon_{\rm SF}$, which was lowered from 0.1 (Eris) to 0.05 (ErisLT) to match the observed normalization of the star formation density in local galaxies (see Governato et al. 2010). ErisLT was stopped at redshift 0.7 in order to limit the computational burden. We also ran another twin (“ErisLE”) in which the threshold was kept at 5 atoms cm^{-3}, but we adopted $\epsilon_{\rm SF} = 0.05$. A companion simulation with 8 times lower mass resolution (“ErisLR”) was

Galaxy	$\epsilon_{\rm SF}$	$n_{\rm SF}$	refinement
Eris	0.1	5	20^3
ErisLE	0.05	5	20^3
ErisLT	0.05	0.1	20^3
ErisLR	0.05	0.1	10^3

Table 4.1: Summary of the numerical parameters of the various versions of Eris. The refinement is expressed as mass refinement = (grid refinement)^3 over the base cosmological box.

also run, with the SF parameters $n_{\rm SF} = 0.1$ atoms cm^{-3} and $\epsilon_{\rm SF} = 0.05$ as in the older generation of simulations of this kind. A summary of the parameters that change among the simulations is presented in Tab. 4.1, and the differences among the runs are discussed in §4.3.2 below.

4.3 Results

We first focus on the final $z = 0$ state and properties of the galaxy in the reference simulation "Eris", presenting a detailed comparison with observations appeared in Guedes, Callegari, Madau, & Mayer (2011a). We then present some key differences with the other simulations.

4.3.1 Analysis of Eris

Eris appears to be the first cosmological hydrodynamic simulation in which the galaxy structural properties, the mass budget in the various components, and the scaling relations between mass and luminosity are all consistent with many observational constraints.

Structural parameters

At the present epoch, Eris is a massive, barred, late-type spiral with structural properties consistent with those of Sb/Sbc galaxies, of which our own Milky Way is an example. It has a virial radius of $R_{\rm vir} = 239$ kpc (defined as the radius enclosing a mean density of $93\rho_{\rm crit}$, Bryan & Norman 1998), total mass $M_{\rm vir} = 7.9 \times 10^{11}\,{\rm M}_\odot$ and spin parameter $\lambda = 0.019$ (following Bullock et al. 2001). Within $R_{\rm vir}$, it contains 7.0, 3.0, and 8.6 million dark matter, gas, and star particles, respectively. The total mass enclosed within 60 kpc is $M_{<60} = 3.3 \times 10^{11}\,{\rm M}_\odot$. Its rotation curve

$$V_c(r) \equiv \left[\frac{GM(<r)}{r}\right]^{1/2}$$

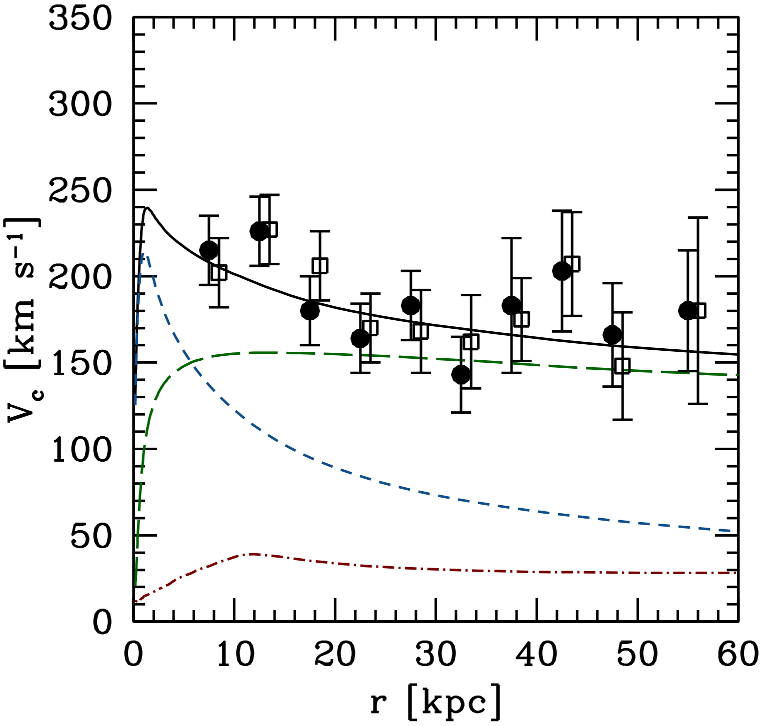

Figure 4.1: The rotation curve of Eris at $z = 0$. The figure shows the contributions to the circular velocity V_c of the various components: dark matter (*long-dashed curve*), stars (*short-dashed curve*), gas (*dot-short dashed curve*), and total (*solid curve*). The data points show two realizations of the rotation curve of the Milky Way from observations of blue horizontal-branch halo stars in the *Sloan Digital Sky Survey* (Xue et al. 2008), and have been offset slightly from each other in radius for clarity.

is shown in Fig. 4.1; it has a peak circular velocity of $V_{\rm peak} = 238\,{\rm km\,s^{-1}}$ reached at $R_{\rm peak} = 1.34$ kpc, and a value of $V_{c,\odot} = 206\,{\rm km\,s^{-1}}$ at 8 kpc. Its overall shape out to 20 kpc is not unlike that of the recent reconstruction of the Milky Way rotation curve by Sofue et al. (2009). The circular velocity decreases gently to distances of 60 kpc from its value at the solar radius, in agreement with observations of blue horizontal-branch halo stars in the *Sloan Digital Sky Survey* (Xue et al. 2008). The measured $V_{c,\odot}$,$M_{<60}$, and $M_{\rm vir}$ agree within the errors with the values of $V_{c,\odot} = 221 \pm 18\,{\rm km\,s^{-1}}$, $M_{<60} = 4.0 \pm 0.7 \times 10^{11}\,{\rm M_\odot}$, and $M_{\rm vir} = 1.0^{+0.3}_{-0.2} \times 10^{12}\,{\rm M_\odot}$ derived recently for the Milky Way using the narrow GD-1 stream of stars (for $V_{c,\odot}$, Koposov et al. 2010) and halo stars as kinematic tracers (for $M_{<60}$ and $M_{\rm vir}$, Xue et al. 2008).

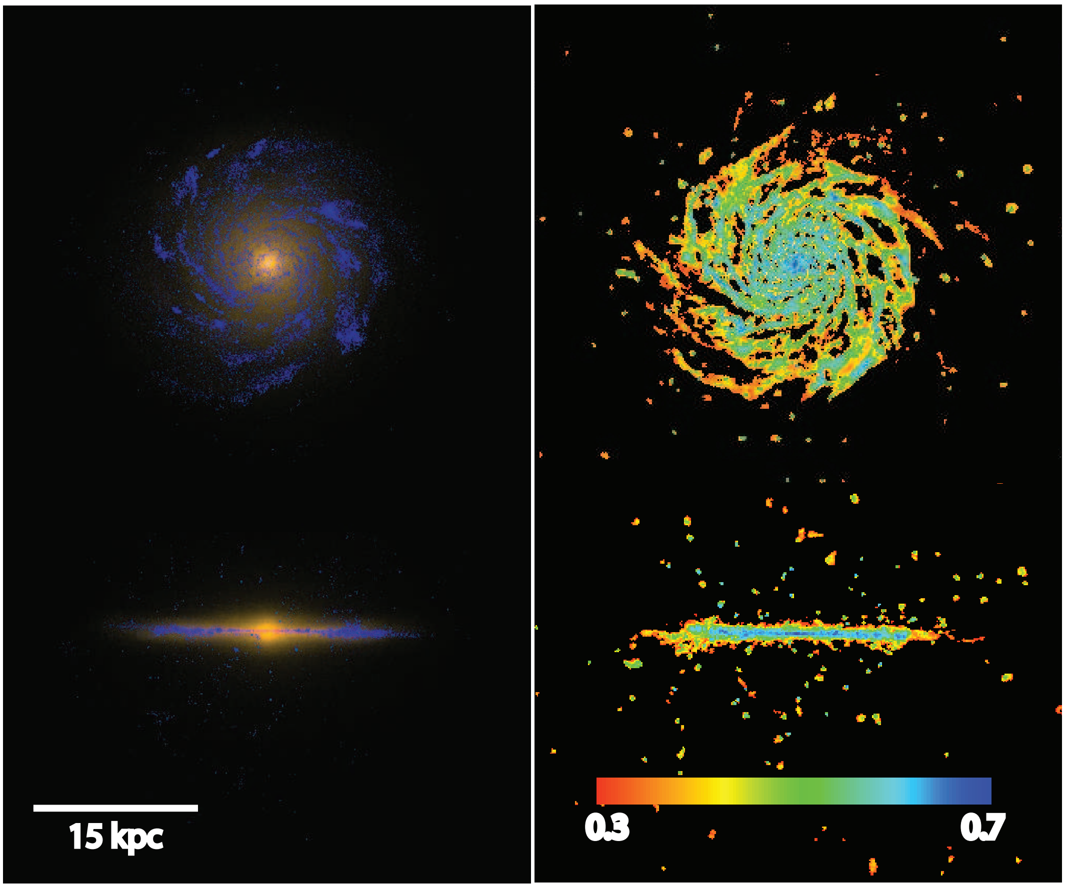

Figure 4.2: *Left panel:* The optical/UV stellar properties of Eris at $z = 0$. The images, created with the radiative transfer code SUNRISE (Jonsson 2006), show an i, V, and FUV stellar composite of the simulated galaxy seen face-on and edge-on. A Kroupa IMF was assumed. *Right panel:* Projected face-on and edge-on surface density maps of Eris's neutral gas at $z = 0$. The color bar shows the neutral gas fraction.

Brightness profile

To correctly compare Eris with observations, artificial images of Eris were created using the radiation transfer code SUNRISE (Jonsson 2006), which produces spectral energy distributions using the age and metallicities of each simulated star particle, and takes into account the three-dimensional effect of dust reprocessing. The results for a Kroupa IMF are shown in Figure 4.2.

A 2D photometric decomposition was performed on the dust-reddened i-band light distribution with the GALFIT program (Peng et al. 2002). At the present epoch, the total i-band magnitude is $M_i = -21.7$, and a stellar disk with a scale length $R_d = 2.5$ kpc dominates the light distribution (Fig. 4.3). The disk scale length is comparable to the value $R_d = 2.3 \pm 0.6$ kpc, adopted for the Milky Way in the compilation by Hammer et al. (2007), and with the scale length of the Milky Way thin disk, 2.6 kpc, as traced by M dwarfs in the solar neighborhood (Jurić et al. 2008). Its value also agrees with the scaling relations

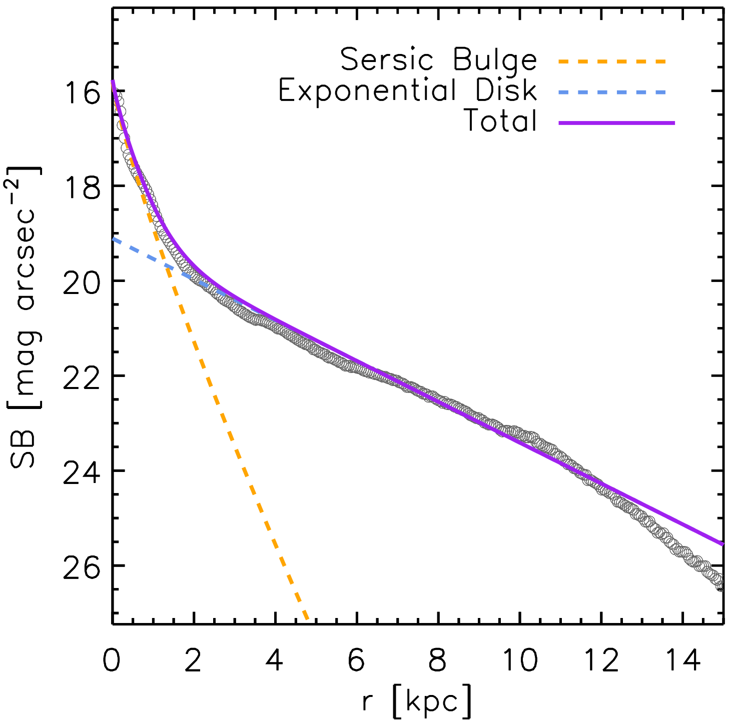

Figure 4.3: The 1D i-band radial surface brightness profile of Eris at $z = 0$. This is well fitted by a Sérsic bulge with index $n_s = 1.4$, an exponential disk with scale length $R_d = 2.5$ kpc, and a bulge-to-disk ratio $B/D = 0.35$. The dust reddened, face-on 2D light distribution created by SUNRISE was analyzed with GALFIT (Peng et al. 2002) following a procedure similar to that detailed in Weinzirl et al. (2009). The "downbending" in the brightness exponential profile at about 5 disk scale length and the surface brightness where the break occurs, 23.5 i-mag arcsec^{-2}, are characteristic of late-type spiral galaxies (Pohlen & Trujillo 2006).

of spiral galaxies (Courteau et al. 2007). The SDSS $u - g = 1.03$ mag and $g - r = 0.49$ mag integrated colors, obtained directly from the SUNRISE images, fall within 1σ of the mean optical colors of late-type galaxies as luminous as Eris (Blanton et al. 2003). As in the sample of truncated late-type spirals of Bakos et al. (2008), there is no break in the stellar surface *mass* density profile of Eris: rather, Eris's stellar age profile shows a "U shape" with a minimum of 6 Gyr at the break radius. The break therefore reflects a radial change in stellar population that, in turn, is likely the result of the stochastic radial migration of young stars from the inner parts of the disk to the outskirts (Roškar et al. 2008).

After a two-component fit to the i-band surface brightness profile, Eris's bulge-to-disk luminosity ratio turns out to be $B/D = 0.35$; this value is typical of Sb spirals, which are characterized by a median (±68/2 per cent) value $\log B/D = -0.53^{+0.27}_{-0.30}$, and of many Sbc galaxies, which have $\log B/D = -0.86^{+0.34}_{-0.40}$ (Graham & Worley 2008). A three-component decomposition (disk+bar+bulge) would lower the B/D ratio further. The bulge Sérsic index,

$n_s = 1.4$, is indicative of a “pseudobulge” rather than a classical one: according to Weinzirl et al. (2009), ∼ 75% of all bright spirals have bulges with $n_s \leq 2$. Eris’s large final disk (disk-to-total ratio $D/T = 0.74$) is not typically found in lower-resolution simulations of Milky Way-sized galaxies that impose no restrictions on merger history: e.g., only one of the eight galaxies simulated by Scannapieco et al. (2010) has a photometric D/T as large as 0.68 (and six have $D/T < 0.5$), and only one out of the six galaxies above $M_{\rm vir} = 10^{11}\,{\rm M}_\odot$ simulated by Brooks et al. (2011) has a disk-to-total ratio comparable to Eris’s (“h239", which is offset, however, from the stellar mass-halo mass relation).

Stellar content

Eris’s total mass in baryons is $M_b = 9.5 \times 10^{10}\,{\rm M}_\odot$, corresponding to a mass fraction $f_b = 0.12$ that is 30% lower than the universal value of 0.175 in the adopted cosmology. Stars (and their remnants) comprise 41% of all baryons within $R_{\rm vir}$: the total stellar mass, $M_* = 3.9 \times 10^{10}\,{\rm M}_\odot$, is comparable to the value estimated for the Milky Way, $4.9 - 5.5 \times 10^{10}\,{\rm M}_\odot$, by Flynn et al. (2006).

To make a bias-free comparison with the stellar mass-halo mass relation derived from the abundance matching technique by Behroozi et al. (2010) we adopt the following procedure. We fit the SDSS u,g,r,i,z broadband colors from the mock SUNRISE images with the flexible stellar population synthesis code of Conroy et al. (2009): the fit assumes a Kroupa IMF and provides a *photometric* stellar mass estimate of $\mathscr{M}_* = 3.2 \times 10^{10}\,{\rm M}_\odot$ (Conroy, private communication), 18% lower than the value directly measured in the simulation. The photometric stellar mass of Eris can now be weighted self-consistently against the Behroozi et al. (2010) average stellar mass-halo relation (which uses a Chabrier 2003 IMF), free of IMF systematics, after offsetting all Behroozi et al. (2010) stellar masses by 0.06 dex (to correct from Chabrier to Kroupa IMF). The comparison, depicted in the right panel of Figure 4.4, demonstrates that Eris’s implied “baryon conversion efficiency", $\eta \equiv (\mathscr{M}_*/M_{\rm vir}) \times (\Omega_M/\Omega_b) = 23\%$, is in excellent agreement with that predicted by the abundance matching technique. This contrasts with the recent analysis of many hydrodynamic simulations of galaxy formation by Guo et al. (2010), who show that the great majority of them form too many stars compared to their total mass, to be viable models for the bulk of the observed galaxy population.

With a circular velocity of $V_{80} = 210\,{\rm km\,s^{-1}}$ at the radius $R_{80} = 6.8$ kpc (containing 80% of the i-band flux), our galaxy lies close to the Tully-Fisher relation of the Pizagno et al. (2007) galaxy sample (see the left panel of Fig. 4.4). As discussed in Pizagno et al. (2007), the Tully-Fisher uses V_{80} as the primary velocity measure rather than $V_{2.2}$, the circular velocity at 2.2 disk scale lengths, since the former is less sensitive to the degeneracies of bulge-disk decomposition. The ratio $V_{2.2}/V_{200} = 214\,{\rm km\,s^{-1}}/129\,{\rm km\,s^{-1}} = 1.66$ in Eris,

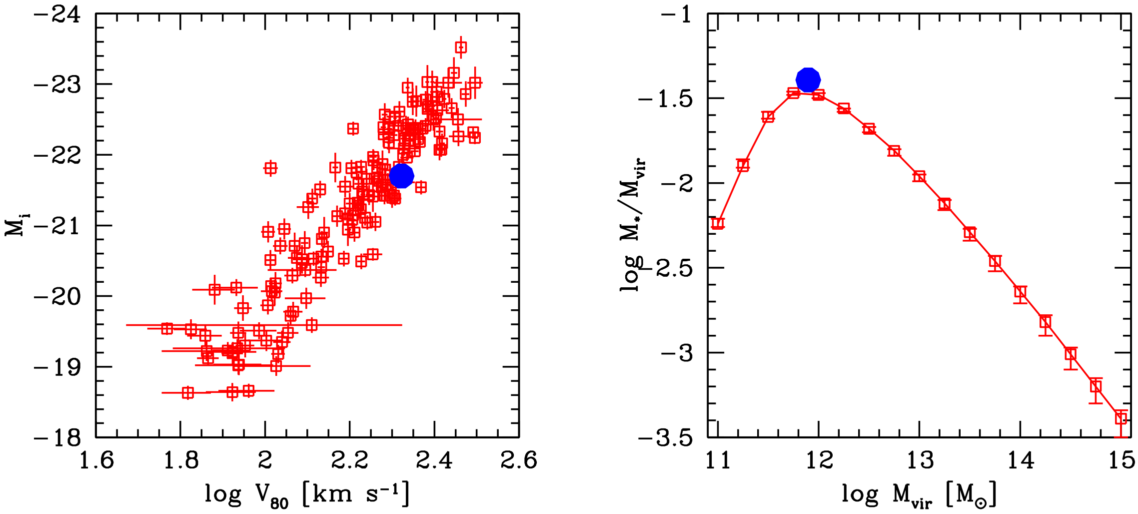

Figure 4.4: *Left panel:* The i-band Tully-Fisher relation for the Pizagno et al. (2007) galaxy sample (*empty squares with error bars*). *Filled circle:* The Eris simulation. Here V_{80} denotes the circular velocity at the radius containing 80% of the i-band flux, as defined by Pizagno et al. (2007). *Right panel:* The stellar mass - halo mass relation at $z = 0.1$ from Behroozi et al. (2010), modified for a Kroupa IMF (*empty squares with error bars*). Errors bars include only statistical uncertainties. *Filled circle:* The Eris simulation with a photometric stellar mass of $\mathscr{M}_* = 3.2\times10^{10}$ M$_\odot$ and a virial mass of $M_{\rm vir} = 7.9\times10^{11}$ M$_\odot$ (see text for details).

where V_{200} is the circular velocity at the radius enclosing a mean overdensity of $200\,\rho_{\rm crit}$ (R_{200} = 177 kpc), is equal to the value suggested by the dynamical model for the Milky Way of Klypin et al. (2002). It is also consistent with the recent measurements of the virial mass of the Milky Way by Smith & Brooks (2007) and Xue et al. (2008), implying $V_{2.2}/V_{200} = 1.48^{+0.25}_{-0.26}$ and $V_{2.2}/V_{200} = 1.67^{+0.31}_{-0.24}$, respectively.[3] Eris is likely ~20% less massive than the Milky Way, and therefore the agreement between simulated and observed kinematic data should be confirmed in future simulations of slightly more massive halos and more active accretion histories. Like the Milky Way, however, Eris is offset relative to determinations using various dark halo mass tracers for late-type disk galaxies by Dutton et al. (2010), who predict for typical dark matter halos with $V_{2.2} = 220\,{\rm km\,s^{-1}}$ the ratio $V_{2.2}/V_{200} = 1.11^{+0.22}_{-0.20}$ (2σ).

---

[3] The $V_{2.2}/V_{200}$ ratios from Smith & Brooks (2007) and Xue et al. (2008), were computed by Dutton et al. (2010) from these data sets after converting different virial mass definitions and for an assumed Milky Way's $V_{2.2} = 220\,{\rm km\,s^{-1}}$.

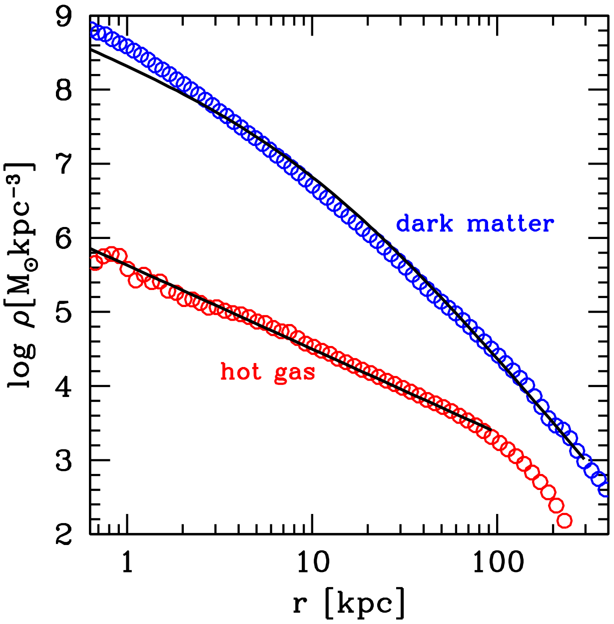

Figure 4.5: The dark matter (*blue empty dots*) and hot ($T > 3 \times 10^5$ K) gas (*red empty dots*) density profiles of Eris at $z = 0$. The solid lines show the best-fit NFW profile for the dark matter (*upper curve*) and the best-fit power-law profile (with slope −1.13) for the hot gas (*lower curve*). The best-fit NFW profile is characterized by a large halo concentration parameter $c \equiv R_{\rm vir}/R_s = 22$ as the dark matter halo contracts in response to the condensation of baryons in its center.

Gas content

Eris's HI (neutral hydrogen) mass is $M_{\rm HI} = 1.9 \times 10^9$ M$_\odot$, comparable to the HI mass estimated for the Milky Way disk by Nakanishi & Sofue (2003), but smaller than the value of $\sim 5 \times 10^9$ M$_\odot$ given by Wolfire et al. (2003). The HI-to-stellar mass ratio, 1.9×10^9 M$_\odot$/3.9×10^{10} M$_\odot$ = 0.049, is equal to the median value observed in the GASS survey (Catinella et al. 2010) for galaxies of comparable stellar mass. Eris's HI disk extends out to about 15 kpc (6 stellar disk scale lengths), similar to the size of the HI disk of the Milky Way (Nakanishi & Sofue 2003). Clustered SN explosions create a large number of holes in the face-on HI distribution of Eris (right panel of Fig. 4.2) due to bubbles of hot gas expanding perpendicular to the disk. These holes are mostly located within the bright optical disk and preferentially in regions of high star formation: they are kpc in size, as observed, e.g., in the nearby low-inclination spiral galaxy NGC 6946 (Boomsma et al. 2008).

About 6.7×10^9 M$_\odot$ of gas are found in a cold phase below $T = 3 \times 10^4$ K. This is comparable to the total mass of the atomic and warm ionized medium inferred for the Milky Way (e.g. Ferrière 2001). The gas mass that is hot ($T > 3 \times 10^5$ K) and thus potentially X-ray luminous is $M_X = 3.6 \times 10^{10}$ M$_\odot$, 63% of the total gas content. For comparison, 12% of the gas is in the cold phase and 25% is in a warm phase with 3×10^4 K $< T < 3 \times 10^5$ K. The fractions of cold, warm, and hot gas within its inner 20 kpc are 83.5%, 1.5%, and 15%, respectively. Hot gas within 20 kpc contains significant amount of angular momentum and is co-rotating with the cold disk. The hot gas baryon fraction, $f_X = M_X/M_{\rm vir} = 0.046$, is 3.8 times smaller than the cosmological baryon fraction. This implies an average density for the hot gas that is 3.8 times smaller than assumed in the standard “cooling flow" halo model à la White et al. (1991), and yields a factor of 14.5 smaller X-ray emission measure. Moreover, contrary to the standard assumption that hot gas follows the radial distribution of the dark matter, the density distribution of hot gas in Eris follows a “flattened" $\rho_X(r) \propto r^{-1.13}$ power-law profile out to 100 kpc (see Fig. 4.5), which would yield an X-ray surface brightness profile that is not as sharply peaked as expected for hot halos with NFW profiles, and therefore satisfying the observational constraints (e.g. Anderson & Bregman 2010). The flattened density profile we find is consistent with the results of much lower-resolution simulations by Crain et al. (2010), who identified the reason for the more extended gas distribution and weaker X-ray coronae in the entropy injection by SNe at $z \sim 1-3$. Only 10% of the gas in Eris is in a very hot phase above $T = 10^6$ K: its density at $R \geq 70$ kpc is $n \leq 6 \times 10^{-5}$ atoms cm^{-3}, which is well within the observational constraints from O VI absorption measurements (Sembach et al. 2003) in the halo of the Milky Way, but still high enough to produce significant ram pressure stripping of dwarf spheroidal satellites (see p. 126 in the Appendix).

Star formation and kinematic decomposition

Left panel of Fig. 4.6 shows the star formation history of all star particles identified within Eris’s virial radius at $z = 0$ (regardless of whether they formed within the main host or in satellites), and of its kinematically-decomposed present-day *disk* and *spheroid*. The decomposition technique follows Scannapieco et al. (2009), and is based on the distribution of orbital circularity parameters j_z/j_c of the simulated stars introduced by Abadi et al. (2003). Here, j_z is the angular momentum of each star in the z-direction (i.e. the direction defined by the total angular momentum of all gas particles within 5 kpc from the host center) and j_c is the angular momentum of a circular orbit at the same radius. Stars belonging to the “spheroid” are defined as those that are not part of the rotationally-supported disk and therefore typically include bulge and stellar halo stars, as well as stellar bars if they are present. The distribution of circularity parameters, shown in the right panel of Fig. 4.6, is characterized by two peaks: one at $j_z/j_c \simeq 1$ that is indicative of the presence of a dominant cold disk in rotational support, and a second one at $j_z/j_c \simeq 0$ corresponding to a modest hot spheroidal component dominated by velocity dispersion.

The vast majority of disk stars in the Milky Way reside in a thin disk component with

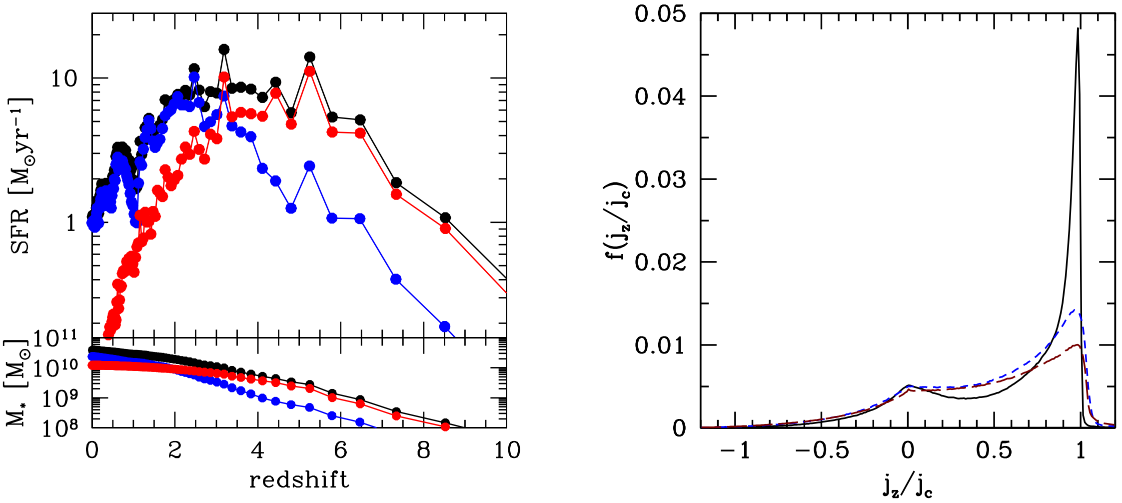

Figure 4.6: *Left panel*: Star formation history of all star particles identified within Eris's virial radius at $z = 0$. Black filled dots: total star formation rate (*top panel*) and stellar mass (*bottom panel*) as a function of redshift. Blue filled dots: same for disk star particles identified at $z = 0$. Red filled dots: same for spheroid star particles identified at $z = 0$. *Right panel*: Stellar mass fraction as a function of the "orbital circularity parameter" j_z/j_c, describing the degree of rotational support of a given stellar particle, for Eris at $z = 0$ (*solid line*) and Eris at $z = 1$ (*short-dashed blue line*). ErisLT at $z = 1$ (*long-dashed red line*) is also shown for comparison (see also Fig. 4.8. The high fraction of stars in a centrifugally-supported thin disk is evident from the sharp peak close to 1.

exponential scale height $h_z = 300 \pm 60$ pc (Jurić et al. 2008). A study of the vertical structure of edge-on spiral galaxies finds that the scale height of their thin disk increases systematically with circular velocity as $z_0 = 610\ (V_c/100\,\mathrm{km\,s^{-1}})^{0.9}$ pc (Yoachim & Dalcanton 2006), where z_0 is the scale height of a sech^2 profile, $z_0 \approx 2h_z$ at large heights above the disk plane. Eris's kinematically-decomposed stellar disk agrees well with the above scaling: by fitting an exponential (sech^2) profile to the simulation data, we derive a scale height of $h_z = 490$ pc ($z_0 = 860$ pc) at a galactocentric distance of 8 kpc.

Today, Eris is forming stars at a rate of SFR = $1.1\,\mathrm{M_\odot\,yr^{-1}}$, comparable to the value of SFR = $0.68 - 1.45\,\mathrm{M_\odot\,yr^{-1}}$, recently inferred for the Milky Way by Robitaille & Whitney (2010) using *Spitzer* data. The star formation rate declines rapidly with redshift from a plateau value of $\sim 10\,\mathrm{M_\odot\,yr^{-1}}$ maintained between $z = 2$ and $z = 5$. SN feedback and photoheating by the ultraviolet radiation background efficiently quench star formation at $z > 5$. The rate of formation of spheroidal stars fades rapidly after redshift 3, while disk stars nearly triple their mass from $z = 2$ to the present.

The star formation rate surface densities Σ_{SFR} and HI gas surface densities Σ_{HI} of Eris's disk are shown in Fig. 4.7. The simulation data were averaged over square patches 750

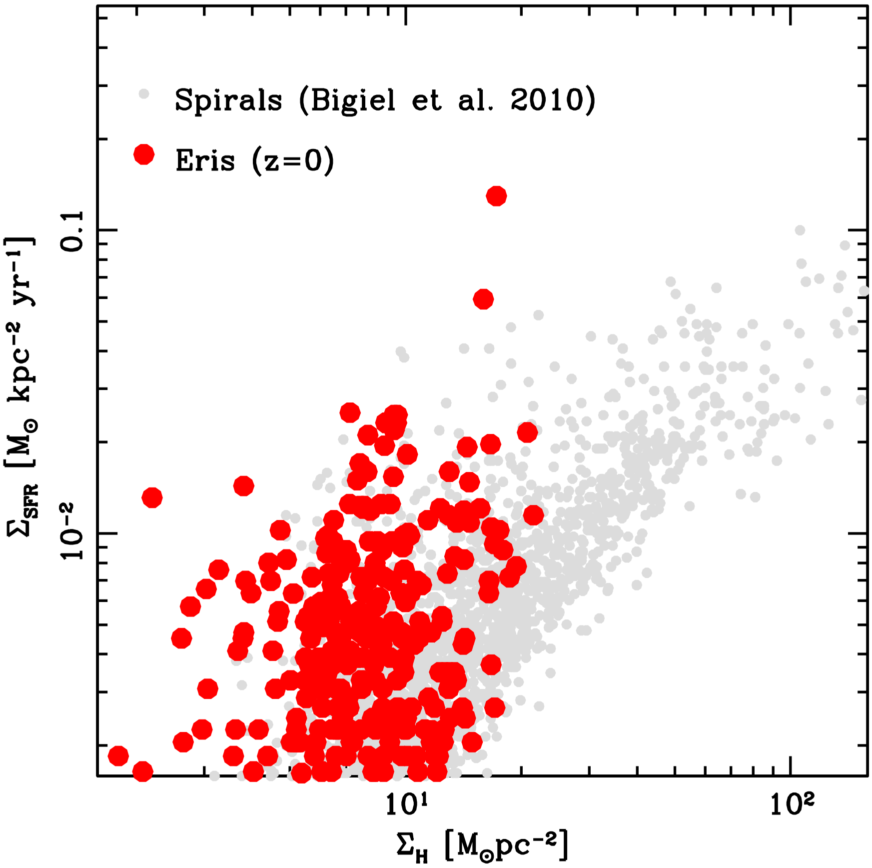

Figure 4.7: Σ_{SFR} vs. Σ_{HI} for Eris's disk at $z = 0$ (*red dots*). The simulation data were averaged over square patches 750 pc on the side: some discreteness effects associated with the limited resolution of the star formation timescale can be seen at low values of Σ_{SFR}. Every dot represents one sampling point. Note that our simulations do not model the formation of H_2. The *grey dots* show the pixel-by-pixel Σ_{SFR} data as a function of Σ_{HI} (at 750 pc resolution) for 7 spiral galaxies from the THINGS survey (Bigiel et al. 2008).

pc on the side for comparison with the pixel-to-pixel observations at 750 pc resolution of 7 spiral galaxies from the THINGS survey (Bigiel et al. 2008). The observed relationship between Σ_{gas} and Σ_{SFR} varies dramatically among and within spiral galaxies, and most galaxies show little or no correlation between Σ_{HI} and Σ_{SFR} (Bigiel et al. 2008). Rather, there is a clear correlation between Σ_{H_2} and Σ_{SFR} (molecular Schmidt law), and gas at densities in excess of $\sim 10\,M_\odot$ pc^{-2} is observed to be fully molecular[4]. While the total mass of cold gas in Eris is comparable to the sum of the atomic and molecular gas mass of Sb galaxies such as the Milky Way, we do not model directly the formation of H_2 molecules. Indeed, as clearly shown in Fig. 4.7, even at Eris's high resolution we do not have kpc-scale regions at gas surface densities $\geq 30\,M_\odot$ pc^{-2}. Furthermore, our gravitational softening is still large compared to the size of typical molecular clouds, which are a few 10 pc in size,

---

[4] At solar metallicities, this density corresponds to the column density of atomic hydrogen required to shield a molecular region against photodissociation (Krumholz et al. 2009).

Galaxy	$M_{\rm vir}$ [10^{11} M$_\odot$]	$V_{\rm peak}$ [km/s]	M_* [10^{10} M$_\odot$]	f_b	$f_{\rm cold}$
Eris ($z = 0$)	7.9	238	3.9	0.121	0.12
ErisLE ($z = 0$)	8.1	214	3.2	0.133	0.09
ErisLR ($z = 0$)	8.4	246	6.9	0.154	0.06
Eris ($z = 1$)	5.4	237	2.9	0.126	0.40
ErisLE ($z = 1$)	5.6	212	2.4	0.127	0.28
ErisLT ($z = 1$)	5.5	308	3.4	0.158	0.18
ErisLR ($z = 1$)	4.5	319	5.0	0.168	0.21

Table 4.2: Physical roperties of Eris in different simulations, at $z = 0$ and $z = 1$: virial mass $M_{\rm vir}$, peak circular velocity $V_{\rm peak}$, total stellar mass M_* within the virial radius, baryon raction f_b, and fraction of cold vs. total gas $F_{\rm cold}$. Simulations indicated in **boldface** are those with a high SF threshold. For ErisLT, only the $z = 1$ data are available as the simulation was stopped around $z = 0.7$.

and our gas density threshold for star formation is still somewhat below the density of real molecular clouds. Both effects contribute to further smooth out the high density tail of the total gas distribution. Yet, the figure shows that our simulated disk is forming stars in the same range of $\Sigma_{\rm SFR} - \Sigma_{\rm HI}$ values observed in spiral galaxies, validating our SF prescription.

The global atomic gas depletion timescale, i.e. the time needed for the present rate of star formation to consume the existing atomic gas reservoir, is $t_{\rm HI} \equiv M_{\rm HI}/{\rm SFR} = 1.9 \times 10^9\,{\rm M}_\odot/1.1\,{\rm M}_\odot\,{\rm yr}^{-1} = 1.7$ Gyr in Eris today. As this is significantly smaller than the Hubble time, star formation rates and gas fractions must be set by the balance between gas accretion from the halo and stellar feedback. The depletion time for atomic gas observed in the COLD GASS survey (Saintonge et al. 2011) is on average 3 Gyr, with a large scatter from one galaxy to another.

4.3.2 Comparison with ErisLT, ErisLE and ErisLR

Tab. 4.2 offers an overview of the differences arising in the Eris galaxy by changing resolution and/or SF parameters.

The most notable case is the ErisLT run, which has the same resolution as Eris but a "traditional" SF recipe with $n_{\rm SF} = 0.1$ atoms cm^{-3} and $\epsilon_{\rm SF} = 0.05$. ErisLT produces a galaxy resembling an early-type Sa spiral with $B/D = 0.42$ (against Eris's $B/D = 0.31$), closer to (but still on the low side of) the typical outcome of previously published cosmological simulations (e.g. Governato et al. 2010; Scannapieco et al. 2010). Accordingly, its rotation curve peaks at 308 km s^{-1} (while Eris has $V_{\rm peak} = 237$ km s^{-1}) and declines steeply within few kpc from the center (left panel of Fig. 4.8).

Remarkably, while ErisLT was run with a star formation efficiency that was half of that

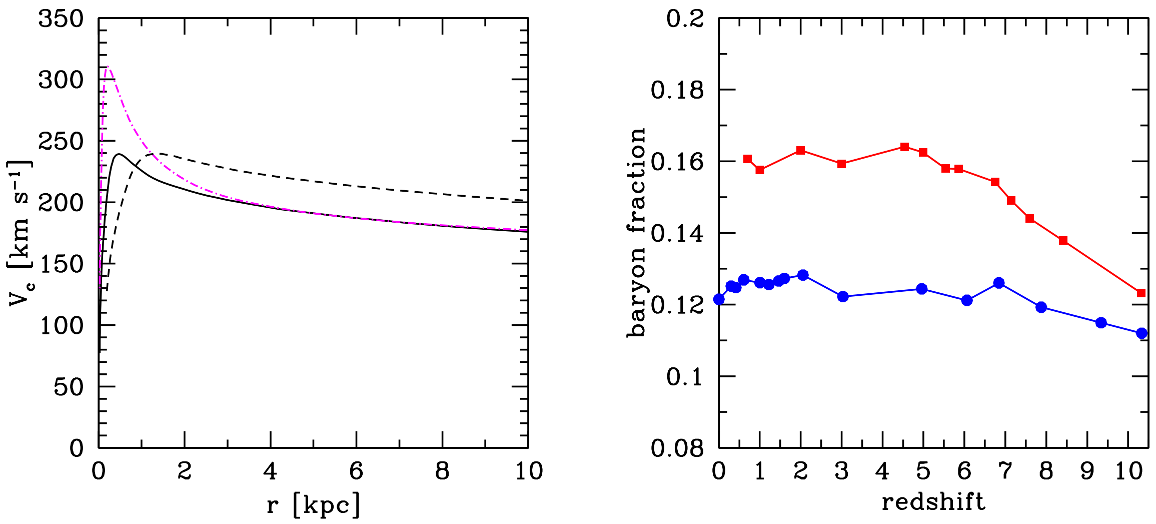

Figure 4.8: Two comparisons between Eris and ErisLT. *Left panel*: rotation curves for Eris at $z = 0$ (*dashed black line*), Eris at $z = 1$, (*solid black line*, and ErisLT at $z = 1$ (*dot-dashed purple line*). *Right panel*: evolution of the baryon fraction for Eris (*blue*) and ErisLT (*red*).

adopted for Eris, its stellar content at $z = 1$ is 20% higher, *showing that the most important parameter in regulating the total star formation is not the efficiency but rather the density threshold*. Such difference translates also into the stark discrepancy in f_b that can be read from Tab. 4.2, where ErisLT is closer in value to ErisLR. The difference in baryonic content between the two simulations is established at very early times (right panel of Fig. 4.8). Since in ErisLT the collapse of baryons is suppressed mostly by the UV background in small protogalaxies, its f_b increases from $z = 10$ to $z = 5$, as its dark matter halo grows from $M_{\rm vir} = 3 \times 10^9\,{\rm M}_\odot$ to $M_{\rm vir} = 6 \times 10^{10}\,{\rm M}_\odot$. Eris, due to the completely different structure of its ISM and the larger impact that feedback can exert in the main halo or in the accreted satellites at all $z < 10$, maintains a relatively low baryon fraction, between 64% and 73% of the cosmic value.

The different density distribution of gas particles in the high-resolution versions of Eris at $z = 1$ is shown in Fig. 4.9 as a more direct example of the effect of changing $n_{\rm SF}$. It can be seen how, though having all the same resolution, Eris and ErisLE develop a double-peaked density distribution with one peak around $n_{\rm SF}$, while ErisLT does not. Such high-density peak in ErisLE is at slightly larger values than Eris, because gas can reach higher densities before turning into stars when $\epsilon_{\rm SF}$ is lower; however, at fixed $\epsilon_{\rm SF}$, as is the case for ErisLE and ErisLT, differences due to changes in threshold are much stronger. With a higher $n_{\rm SF}$, the ISM develops a more inhomogeneous structure, with important consequences on the large-scale pattern of star formation in the galaxy, and, as a byproduct, on the effect of SN feedback (e.g. Governato et al. 2010). SF is now concentrated in smaller, denser clumps

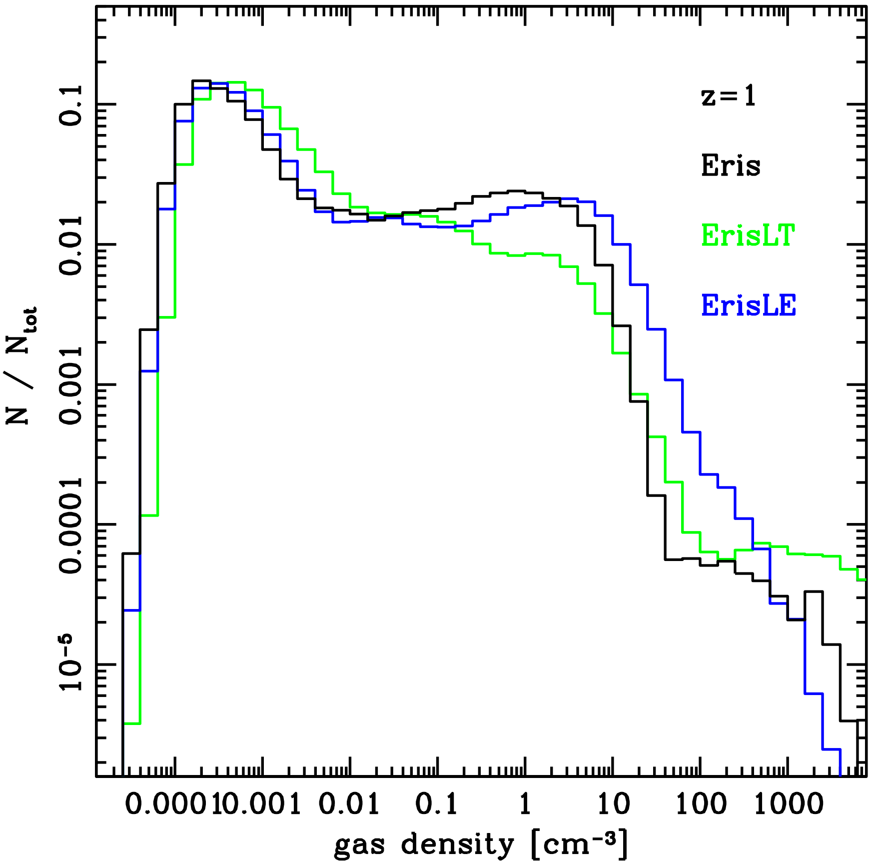

Figure 4.9: Distribution of the gas SPH densities within the virial radius at $z = 1$, for all the high-resolution versions of Eris discussed here. Colors are labelled on the figure.

where the SFR per unit mass is higher (since it is propoprtional to $\rho_{\mathrm{gas}}^{1.5}$); SN feedback energy is thus able to disperse such clumps, and to cause outflows in the form of large hot bubbles, which do not form in the more homogeneous medium of ErisLT.

Another effect of the different threshold is to change *where* in the disk SF occurs. This can be seen from Fig. 4.10, where the radial distribution of SPH densities and temperatures is shown. It can be seen that SF can only occur in Eris's inner densest regions within 10 kpc from the center. By contrast, in ErisLT, SF is spread out over a significant fraction of the host galaxy, extending well beyond the central region. At $z = 3$, when outflows are stronger due the high SF rates triggered by mergers, it is the central cold, low-angular momentum gas that is preferentially removed in Eris, as previously found for dwarf galaxies by Governato et al. (2010). Such outflows are weaker in ErisLT, where star formation is more diffuse and the energy injection from SNe is more evenly deposited in the ISM: cold gas accumulates in the inner regions already at very high redshifts and continues to turn into stars unabated by feedback (see also Ceverino & Klypin 2009; Robertson & Kravtsov 2008). At lower z, ErisLT has now consumed its low-angular momentum cold gas in SF,

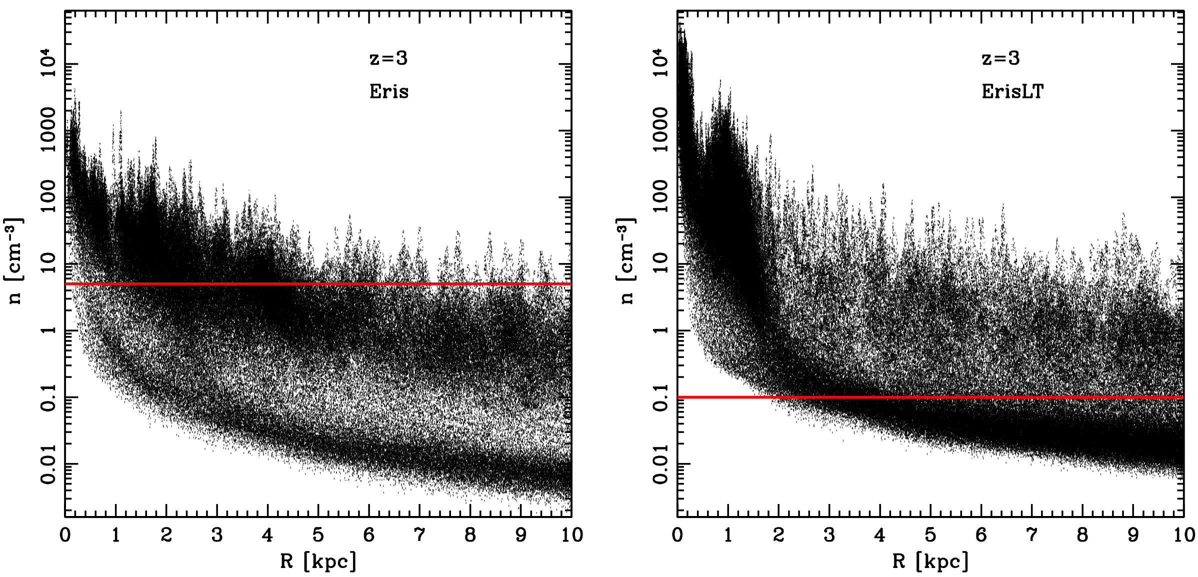

Figure 4.10: Properties of the radial gas distribution for Eris and ErisLT. The SPH gas density of each SPH particle is plotted as a function of its radial distance from the galaxy center for Eris (*left panel*) and ErisLT (*right panel*) at $z = 3$. Horizontal red lines mark the minimum gas density for star formation in each run. Reflecting the bimodal distribution of Eris's gas in Fig. 4.9, the gas in the left panel clearly separates vertically into a cold phase eligible for star formation at higher density, and a hot phase at lower density. Such bimodal distribution at a given radius is absent in the right panel. See also Fig. 7 in Guedes et al. (2011a) for more details.

while Eris has preserved a higher cold gas fraction due to the more effective regulation of SF via feedback. By $z = 1$, both galaxies have formed roughly the same amount of stars, but 90% of the gas within 20 kpc from the center is still cold in Eris, compared to only 57% in ErisLT. The resulting distributions of stellar angular momenta are also different in the two cases (see right panel of Fig. 4.6). Gas being blown out at high redshift has a systematically lower angular momentum than the gas that gets accreted at later times (Brook et al. 2010), and this explains the flatter rotation curve of Eris relative to ErisLT.

Finally, there are some notable differences also between Eris and ErisLE. It can be seen in the left panel of Fig. 4.11 and in Tab. 4.2 that the factor of 2 difference in SF efficiency does *not* translate at all in a proportionately large difference in final stellar mass, or even in SFR as a function of time. In fact, as we have argued in this Section, the density threshold has a much more fundamental role in determining on what state of self-regulation the galaxy will settle. However, the difference in the $V_{\rm circ}$ profiles shown in the right panel of the same Figure is quite striking: $V_{\rm peak}$ in ErisLE is 10% lower, and is located at slightly smaller radii. On the other hand, the final baryon fraction seems to be slightly "worse" with respect to the observational constraints: $f_b = 0.133$. It is not yet clear what the main driver of this difference is: the shift in the density distribution peak seen in Fig. 4.9 may

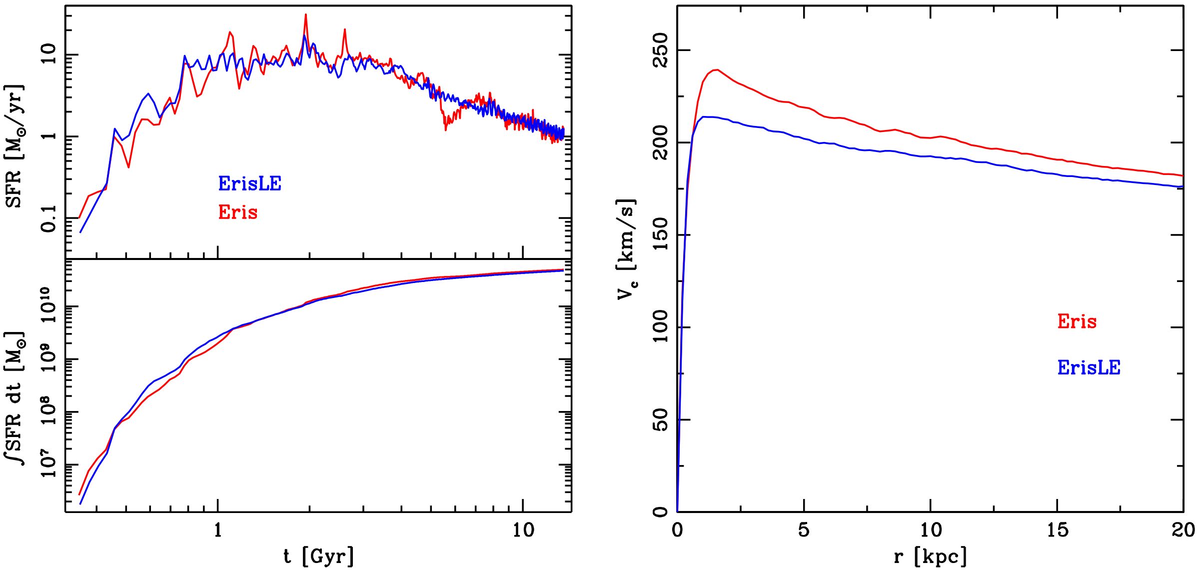

Figure 4.11: Comparison between Eris and ErisLE. *Left figure*: differential (*top*) and integrated (*bottom*) star formation history for Eris in red and ErisLE in blue. *Right figure*: circular velocity profile for the two galaxies at $z = 0$ (colors as in left figure).

play a role in the main galaxy as well as in its satellites, especially at higher z in smaller halos where internal feedback and outflows play a major role. The investigation is still ongoing, and will be presented in forthcoming papers.

4.4 Final remarks

Approximately 70% of bright spirals have $B/T \leq 0.2$ (Weinzirl et al. 2009). Recent attempts to generate such disk-dominated galaxies in cosmological simulations have failed to reproduce simultaneously their observed morphologies as well as their baryonic/stellar content (Scannapieco et al. 2010; Agertz et al. 2011). Since the modelling of accretion onto central MBHs in cosmological simulations usually relies on sub-grid recipes that estimate the accretion flow from ≥ 100 pc scales, it is unclear what effect the poorly modelled large-scale dynamics has on predictions for MBH growth. Similarly, AGN feedback has been traditionally tuned (starting from the seminal work by Springel et al. 2005) to reproduce observational constraints which may depend, e.g., on the relative timescales of accretion vs. SF, such as the $M_{\rm BH} - M_{\rm bulge}$ relation. In a highly non-linear problem as the coevolution of galaxies and MBHs, the systematic effects that this tuning of sub-grid parameters has on the final predictions of the model are still poorly understood.

Our very high-resolution Eris simulation appears to form a close analog of a Milky Way disk galaxy by capturing a realistic inhomogeneous ISM in which SF occurs in high density regions of mass comparable to that of giant cloud complexes. The chosen SF and feedback prescriptions combine to expel a significant amount of baryons from the system; they preferentially remove low angular momentum material and leave plenty of cold gas available for disk SF (e.g., Scannapieco et al. 2009), thus allowing a good fit to the Tully-Fisher relation (e.g., Piontek & Steinmetz 2011) and other constraints. Contrary to the "inefficient star formation" prescription adopted by Agertz et al. (2011), this is achieved with a strong localized SN feedback and a high (10%) Schmidt-law efficiency. We stress that this success stems from a very natural assumption: SF happens in the densest regions of a highly inhomogeneous ISM. However, it must be noted that our SF efficiency is simply phenomenological, and does not have a direct relation to the true SF efficiency within giant molecular clouds, which is the end result of all the processes regulating SF including feedback, and concerns scales (tens of parsecs) and densities (> 1000 atoms cm^{-3}) that are not yet resolved in cosmological simulations.

It is fair to point out that, while the success of our Eris simulation in matching the observations appears to be linked to the ability of correctly following SF in an inhomogenous ISM and regulating it with SN feedback, many avenues remain unexplored and require further investigation. Simulations of even higher resolution, approaching the true gas densities reached in star forming giant molecular cloud complexes (about a factor of 10 higher than adopted here), are needed to test the convergence and robustness of our results, and are in the making. The density threshold should depend on metallicity and therefore on redshift (Gnedin et al. 2009), which may affect the structure of the ISM and SN feedback differently in progenitors at different epochs. The feedback model that we use is still phenomenological, and the actual mechanism of outflow generation may require the combination of more than one effect to support a large-scale blastwave (e.g. Ceverino & Klypin 2009).

As an additional caveat, the simulations presented in this paper neglect cooling by metal lines at temperatures above 10^4 K. At the mass scale considered here, cold flows are mostly responsible for the assembly of the star forming disk even at low redshift, as opposed to the cooling flow of the hot halo mode (Brooks et al. 2009). This suggests that the details of the cooling function for gas above 10^4 K, namely in the hot mode, are not important for the assembly of the disk. Piontek & Steinmetz (2011) find that metal cooling gives origin to a stronger burst of SF at high redshift in the progenitors of Milky-Way sized galaxies and thus to bigger bulges. One may expect that resolving even higher density thresholds than Eris will produce stronger density constrasts in the simulated ISM: heating and outflows from even more localized SN feedback may have an even stronger effect, and offset the impact of increased cooling as suggested by Piontek & Steinmetz (2011). We plan to explore these issues in the next generation of simulations (some of which are already on their way) with increased resolution, a higher SF density threshold, and the inclusion of molecular phase physics and high-temperature metal cooling.

Another aspect that warrants further investigation is the evolution of B/D. Gas inflows and the redistribution of stellar angular momentum from bars and minor interactions with satellites both contribute to the growth of the bulge, while at late times ($z < 0.5$) the bulge grows purely secularly. This effect will be quantified in a forthcoming paper. More typical galaxies undergoing significant mergers at later times may develop smaller bulges due to the more prolonged effect of supernovae outflows, which could explain why 11 out of 19 nearby massive spirals show no evidence for a classical bulge (Kormendy et al. 2010)). If true, the trend would be at odds with the standard picture in which mergers lead to earlier-type galaxies. This would be an important new element in the theory of galaxy formation, perhaps complementary to the finding that gas-rich mergers assist the growth of larger disks (Hopkins et al. 2009; Governato et al. 2009), and could also affect the prevalent picture of merger-fuelled AGN growth, if the mass in bulges is not assembled when the MBHs are accreting (as is the case in Springel et al. 2005; Hopkins et al. 2005).

On a related note, the last major merger in our simulations occurs at $z \sim 3$, and therefore Eris is expected to show some offset from the observed structural parameters of the average spiral galaxy. The same likely applies to the Milky Way itself, which indeed Eris closely resembles. Whether or not the good match with the properties of typical spiral galaxies is related to the fact that we have selected a particularly quiet merging history, in which outflows shut off early as the rate of SF drops after the last major merger, will have to be investigated. In particular, the implications for the apparently under-massive Galactic MBH with respect to predictions of the $M_{\rm BH} - \sigma_*$ relations (as mentioned on p. 65), will also be explored in the next series of Eris simulations, which will include a MBH seeding recipe inspired by our work in chapter 3, and will be able to capture the strong interplay between the large- and small-scale dynamics highlighted in chapter 2, but now in a fully cosmological context.

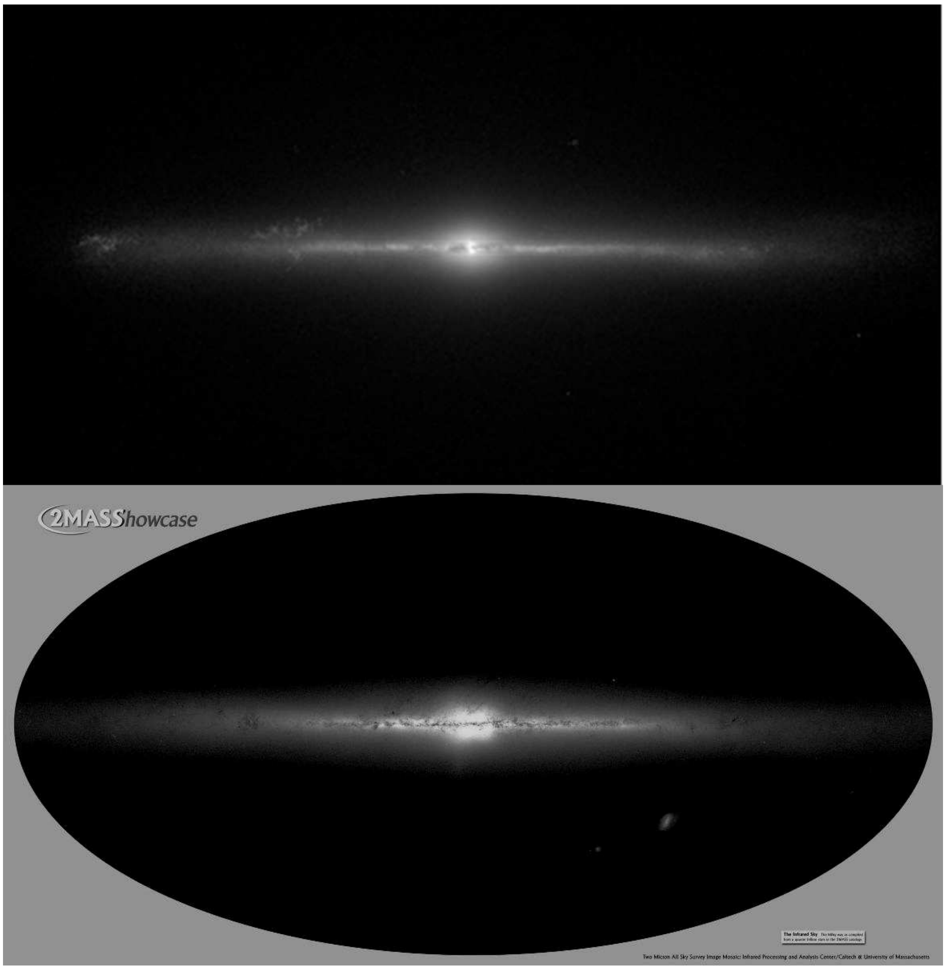

Figure 4.12: I-band edge-on view of Eris (*Upper panel*) produced with Sunrise by J. Guedes, and IR edge-on view of the Milky Way (*Lower panel*) from the 2MASS Showcase (credits: 2MASS/J. Carpenter, T. H. Jarrett, & R. Hurt)

Appendix A

Tidal stirring of dwarf galaxies

Another subject explored during this thesis work was the evolution of dwarf galaxies transformed by *tidal stirring* (Mayer et al. 2001). The main project (described in §A.1 on p. 126) is still in the simulation stage, and was designed around the first realistic dwarf irregular galaxies formed in a cosmological simulation by Governato et al. (2010).

Additional work was done on a large set of collisionless simulations that allowed the exploration of a wide portion of the parameter space; the Kazantzidis, Łokas, Callegari, Mayer, & Moustakas (2011) paper presenting their results is included here below. We are also working on a companion paper which, through yet another set of simulations currently being run, will explore the effects of the inclusion of gas on the relatively simple picture emerging from these next few pages.

THE ASTROPHYSICAL JOURNAL, ACCEPTED
Preprint typeset using LaTeX style emulateapj v. 03/07/07

ON THE EFFICIENCY OF THE TIDAL STIRRING MECHANISM FOR THE ORIGIN OF DWARF SPHEROIDALS: DEPENDENCE ON THE ORBITAL AND STRUCTURAL PARAMETERS OF THE PROGENITOR DISKY DWARFS

STELIOS KAZANTZIDIS[1], EWA L. ŁOKAS[2], SIMONE CALLEGARI[3],
LUCIO MAYER[3,4], AND LEONIDAS A. MOUSTAKAS[5]

The Astrophysical Journal, accepted

ABSTRACT

The tidal stirring model posits the formation of dwarf spheroidal galaxies (dSphs) via the tidal interactions between late-type, rotationally-supported dwarfs and Milky Way-sized host galaxies. Using a comprehensive set of collisionless *N*-body simulations, we investigate the efficiency of the tidal stirring mechanism for the origin of dSphs. In particular, we examine the degree to which the tidal field of the primary galaxy affects the sizes, masses, shapes, and kinematics of the disky dwarfs for a range of dwarf orbital and structural parameters. Our study is the first to employ self-consistent, equilibrium models for the progenitor dwarf galaxies constructed from a composite distribution function and consisting of exponential stellar disks embedded in massive, cosmologically-motivated dark matter halos. Exploring a wide variety of dwarf orbital configurations and initial structures, we demonstrate that in the majority of cases the disky dwarfs experience significant mass loss and their stellar distributions undergo a dramatic morphological, as well as dynamical, transformation. Specifically, the stellar components evolve from disks to bars and finally to pressure-supported, spheroidal systems with kinematic and structural properties akin to those of the classic dSphs in the Local Group (LG) and similar environments. The self-consistency of the adopted dwarf models is crucial for confirming this complex transformation process via tidally-induced dynamical instabilities and impulsive tidal heating of the stellar distribution. Our results suggest that such tidal transformations should be common occurrences within the currently favored cosmological paradigm and highlight the key factor responsible for an effective metamorphosis to be the strength of the tidal shocks at the pericenters of the orbit. We also demonstrate that the combination of short orbital times and small pericentric distances, characteristic of dwarfs being accreted by their hosts at high redshift, induces the strongest and most complete transformations. Our models also indicate that the efficiency of the transformation via tidal stirring is affected significantly by the structure of the progenitor disky dwarfs. While the mass-to-light ratios, M/L, of the dwarf galaxies typically decrease monotonically with time as the extended dark matter halos are efficiently tidally stripped, we identify a few cases where this trend is reversed later in the evolution when stellar mass loss becomes more effective. We also find that the dwarf remnants satisfy the relation $V_{\rm max} = \sqrt{3}\sigma_*$, where σ_* is the one-dimensional, central stellar velocity dispersion and $V_{\rm max}$ is the maximum halo circular velocity, which has intriguing implications for the missing satellites problem. Assuming that the distant dSphs in the LG, such as Leo I, Tucana, and Cetus are the products of tidal stirring, our findings suggest that these galaxies should have only been partially stirred by the tidal field of their hosts. We thus predict that these remote dwarfs should exhibit higher values of $V_{\rm rot}/\sigma_*$, where $V_{\rm rot}$ is the stellar rotational velocity, compared to those of dSphs located closer to the primary galaxies. Overall, we conclude that the action of tidal forces from the hosts constitutes a crucial evolutionary mechanism for shaping the nature of dwarf galaxies in environments such as that of the LG. Environmental processes of this type should thus be included as ingredients in models of dwarf galaxy formation and evolution.

Subject headings: galaxies: dwarfs – galaxies: fundamental parameters – galaxies: kinematics and dynamics – galaxies: Local Group – galaxies: structure – cosmology: dark matter

1. INTRODUCTION

The currently favored cold dark matter (CDM) paradigm of hierarchical structure formation (e.g., White & Rees 1978; Blumenthal et al. 1984) generically predicts that dwarf galaxies comprise the primary building blocks of more massive systems. Observational evidence has recently confirmed this expectation with the discovery of streams and complex stellar structures associated with accreted and tidally disrupted dwarfs in the Milky Way (MW) (e.g., Ibata et al. 1994; Yanny et al. 2000; Ibata et al. 2001b; Newberg et al. 2002; Majewski et al. 2003; Martin et al. 2004; Martínez-Delgado et al. 2005; Grillmair & Dionatos 2006; Belokurov et al. 2006), the Andromeda galaxy (M31) (Ibata et al. 2001a; Ferguson et al. 2002, 2005; Kalirai et al. 2006; Ibata et al. 2007), and beyond the Local Group (LG) (e.g., Malin & Hadley 1997; Shang et al. 1998; Peng et al. 2002; Forbes et al. 2003; Pohlen et al. 2004). Understanding the formation and evolution of dwarf galaxies is crucial for testing the predictions of the CDM theory and gaining insight into the physical processes of structure formation.

In this context, the dwarf spheroidal galaxies (dSphs) of the LG (see Mateo 1998 and Tolstoy et al. 2009 for comprehensive reviews) constitute excellent candidates for constraining the CDM model, as they are believed to be highly dark matter

---

[1] Center for Cosmology and Astro-Particle Physics; and Department of Physics; and Department of Astronomy, The Ohio State University, Columbus, OH 43210, USA; `stelios@mps.ohio-state.edu`

[2] Nicolaus Copernicus Astronomical Center, 00-716 Warsaw, Poland; `lokas@camk.edu.pl`

[3] Institute for Theoretical Physics, University of Zürich, CH-8057 Zürich, Switzerland; `callegar@physik.uzh.ch`

[4] Institute of Astronomy, Department of Physics, ETH Zürich, CH-8093 Zürich, Switzerland; `lucio@phys.ethz.ch`

[5] Jet Propulsion Laboratory, California Institute of Technology, Pasadena, CA 91109, USA; `leonidas@jpl.nasa.gov`

(DM) dominated, with mass-to-light ratios of $M/L_V \sim 10^{1-3}$ (e.g., Mateo 1998; Gilmore et al. 2007; Simon & Geha 2007; Walker et al. 2009) (for alternative explanations of their extreme DM content see, e.g., Kuhn & Miller 1989; Milgrom 1995; Kroupa 1997; Łokas 2001). dSphs are the faintest galaxies known and their stellar components are supported by random motions, with a ratio of rotational velocity to line-of-sight, central velocity dispersion of $V_{\rm rot}/\sigma_* \lesssim 1$ (Mateo 1998). Among the dwarf galaxies in the LG, dSphs are also the most numerous and they tend to be clustered around the massive spirals MW and M31 (though some outliers exist including the distant dwarf Leo I and the isolated dSphs Cetus and Tucana that lie on the outskirts of the LG). This tendency is referred to as the morphology-density relation where rotationally-supported dwarf irregular galaxies (dIrrs) are found in the periphery of the LG (e.g., Mateo 1998; Grebel 1999). Moreover, dSphs are gas poor or completely devoid of gas (e.g., Mateo 1998; Grcevich & Putman 2009) and they exhibit a wide diversity in their star formation histories (e.g., Grebel 2000; Orban et al. 2008). Owing to their proximity, dSphs have been most thoroughly studied in the LG. However, dwarfs with the properties of dSphs have been recently identified in nearby groups and clusters of galaxies (Chiboucas et al. 2009; Penny et al. 2009) suggesting that these intriguing galaxies are not unique to the LG.

While our understanding of dSphs has grown impressively in the past decade, a definitive model for their origin still remains elusive (see Mayer 2010 and Kravtsov 2010 for recent reviews). Two main classes of models have been proposed so far to explain their formation and present-day properties. In the first, dSphs are the result of the interplay between cosmic reonization and stellar feedback suppressing gas accretion and star formation in low-mass galaxies (e.g., Dekel & Silk 1986; Bullock et al. 2000; Susa & Umemura 2004; Ricotti & Gnedin 2005; Tassis et al. 2008; Sawala et al. 2010; Macciò et al. 2010). In the second, the origin of dSphs is intimately linked to various environmental mechanisms, including tidal and ram pressure stripping (e.g., Einasto et al. 1974; Faber & Lin 1983; Mayer et al. 2001a,b; Kravtsov et al. 2004; Mayer et al. 2006, 2007; Klimentowski et al. 2007; Peñarrubia et al. 2008; Klimentowski et al. 2009a) and resonant stripping (D'Onghia et al. 2009).

Using controlled simulations of individual disky dwarf galaxies orbiting inside a MW-sized host, Mayer et al. (2001a,b) demonstrated for the first time that the repeated action of tidal forces from the primary galaxy can transform the dwarfs into pressure-supported stellar systems with the structural and kinematic properties of dSphs (see also Klimentowski et al. 2007, 2009a). This transformation mechanism, termed "tidal stirring", involves a combination of tidally-induced dynamical instabilities in stellar disks (e.g., the bar and buckling instabilities) and impulsive tidal heating of the stellar distribution. In the context of CDM, tidal stirring should be particularly effective since satellites of massive galaxies are affected by strong tidal forces due to their highly eccentric orbits (e.g., Ghigna et al. 1998; Diemand et al. 2007).

Although the tidal stirring model naturally explains the tendency of dSphs to be concentrated near the dominant spiral galaxies, it is only applicable to classic dSphs, namely those that were known before the discovery of the ultra-faint dwarfs by the Sloan Digital Sky Survey (SDSS) (e.g., Simon & Geha 2007). When combined with ram pressure stripping and the effect of radiation fields at high redshift, such as the cosmic ionizing ultraviolet background, the tidal stirring mechanism can also account for both the low gas fraction and the extremely high DM content in some of the classic dSphs such as Draco and Ursa Minor (Mayer et al. 2006, 2007). Recently, the structure and kinematics of the stellar core of the nearby Sagittarius dwarf galaxy have also been successfully modeled within the framework of tidal stirring (Łokas et al. 2010b).

In addition to controlled numerical experiments, significant theoretical effort has been devoted to performing fully cosmological, hydrodynamical simulations of dwarf galaxy formation (e.g., Ricotti & Gnedin 2005; Read et al. 2006a; Tassis et al. 2008; Governato et al. 2010; Sawala et al. 2010). While pressure-supported objects with the properties of LG dSphs have been produced in some cases, (e.g., Ricotti & Gnedin 2005; Sawala et al. 2010), other studies have demonstrated the formation of systems with properties similar to those of the likely progenitors of dSphs according to the tidal stirring model (Governato et al. 2010). Successes notwithstanding and despite the continuing increase in dynamic range, limited resolution prohibits current cosmological simulations with hydrodynamics to address in detail the dynamical and structural evolution of dwarf *satellite* galaxies. In addition, due to numerical loss of angular momentum and overcooling, satellites in cosmological simulations of galaxy formation are too bright and too dense (e.g., Governato et al. 2007).

Given these facts, we are motivated to explore the tidal evolution of individual, rotationally-supported dwarf galaxies inside MW-sized hosts using a large ensemble of controlled N-body simulations. While our work is informed by many past numerical investigations aimed to elucidate the tidal stirring scenario for the origin of dSphs (Mayer et al. 2001a,b, 2002; Klimentowski et al. 2007, 2009a), our numerical experiments extend those of earlier studies in several important respects. For example, unlike previous work, we employ self-consistent, equilibrium numerical models of disky dwarfs for our experiments. These models are derived from three-integral composite distribution functions (DFs) and are thus superior to those constructed from simpler approximate prescriptions that produce models that are initially out of equilibrium (e.g., Hernquist 1993). The transformation via tidal stirring is an intricate process with several distinct stages that depends sensitively on the development of tidally-induced dynamical instabilities (e.g., bars) and the detailed response of the stellar distribution to tidal shocks. For this reason, the self-consistency of the adopted models is crucial.

Moreover, we explore a wide variety of orbital configurations and structural parameters for the progenitor dwarf galaxies, conducting a simulation campaign that allows the investigation of a much larger parameter space than before. Our ultimate goal is to determine the degree to which the evolution of rotationally-supported dwarfs is affected by the strong tidal field of their host galaxies under a broad range of initial conditions, and through this to establish the generic efficiency of the tidal stirring mechanism for the origin of dSphs. Lastly, our numerical experiments are characterized by much higher numerical resolution than that of previous related studies. This fact, in conjunction with the increasing accuracy of current observational data (e.g., Walker et al. 2009), offers unique opportunities for a systematic and quantitative comparison with observations, and we undertake such a task in a companion paper (Łokas et al. 2010, in preparation).

In this study, we focus on the evolution of the intrinsic, global parameters of accreted disky dwarfs orbiting inside a MW-sized primary galaxy. Our results firmly establish that tidal interactions between late-type dwarf galaxies and their hosts can produce objects with kinematic and structural properties akin to those of the *classic* dSphs in the LG and similar environments under a wide variety of initial conditions. We conclude that such tidal transformations should be common occurrences within the currently favored cosmological paradigm. Environmental mechanisms of the type highlighted in the present work should thus constitute important ingredients in models of dwarf galaxy formation and evolution.

The outline of this paper is as follows. In § 2, we introduce the dwarf and host galaxy models. In this section, we also describe the methods adopted and the setup of the numerical experiments performed in the present study. In § 3 and § 4, we investigate the degree to which the orbital parameters and initial structure of the progenitor disky dwarfs can influence their morphological and dynamical transformation into dSphs. Implications and extensions of our findings are presented in § 5, which also includes a discussion of the caveats of the current study and a number of promising directions for future work. Lastly, in § 6 we summarize our main results and conclusions.

2. SIMULATIONS AND METHODS

2.1. *Models of Dwarf Galaxies*

The present investigation utilizes fully self-consistent, equilibrium models of dwarf galaxies for tidal stirring experiments. This aspect of the modeling constitutes one of the major improvements we introduce in this study. As we discussed in the previous section, the nature of the transformation mechanism is such that the self-consistency of the adopted dwarf models is essential. Specifically, we employ the method of Widrow & Dubinski (2005) to construct numerical realizations of dwarf galaxies consisting of exponential stellar disks embedded in cuspy, cosmologically-motivated Navarro et al. (1996, hereafter NFW) DM halos. The Widrow & Dubinski (2005) models are specified by a large number of parameters. They are derived from three-integral, composite DFs and thus represent self-consistent, equilibrium solutions to the coupled Poisson and collisionless Boltzmann equations. The Widrow & Dubinski (2005) method has been recently used in a variety of numerical studies associated with instabilities in disk galaxies, including the dynamics of warps and bars (Dubinski & Chakrabarty 2009; Dubinski et al. 2009) and the heating of galactic disks by halo substructure (Gauthier et al. 2006; Kazantzidis et al. 2008; Purcell et al. 2009; Kazantzidis et al. 2009). We refer the reader to Widrow & Dubinski (2005) for an overview of all relevant parameters and a detailed description of this technique.

The density distributions of the dwarf DM halos are given by

$$\rho_{\rm NFW}(r) = \frac{\rho_s}{\left(r/r_s\right)\left(1+r/r_s\right)^2} , \qquad (1)$$

where ρ_s is a characteristic inner density, and r_s denotes the scale radius of the density profile defined as the distance from the center where the logarithmic slope, ${\rm d}\ln\rho({\rm r})/{\rm d}\ln{\rm r}$, is equal to −2. The NFW density profile is formally infinite in extent with a cumulative mass that diverges as $r \rightarrow \infty$. In order to keep the total mass finite, Widrow & Dubinski (2005) impose a tidal radius in the DM halo, R_h, which represents the outer edge of the system. In our modeling, R_h is chosen in such a way that it becomes roughly equal to the cosmologically-motivated virial radius, $R_h \approx r_{\rm vir}$. As a result of this choice, the total mass of the halo within R_h, which we denote M_h, would be equivalent to the virial mass. We control the shape of the halo density profile via the concentration parameter $c \equiv r_{\rm vir}/r_s \approx R_h/r_s$. Higher values of concentration correspond to a larger fraction of the mass contained in the inner regions of the halo. Lastly, all DM halos were constructed with no net angular momentum.

The surface density profiles of the dwarf disks follow an exponential distribution in cylindrical radius R, while the vertical structure is modeled by constant-thickness, self-gravitating isothermal sheets (Spitzer 1942)

$$\rho_d(R,z) \propto \exp\left(-\frac{R}{R_d}\right) {\rm sech}^2\left(\frac{z}{z_d}\right) , \qquad (2)$$

where R_d and z_d denote the radial scale length and the (sech^2) vertical scale height of the disk, respectively. The phase-space DF of the disk is fully determined once the disk velocity ellipsoid is specified. The radial velocity dispersion, $\sigma_R(R)$, is assumed to be exponential with $\sigma_R^2(R) = \sigma_{R0}^2 \exp\left(-R/R_d\right)$, where σ_{R0} denotes the central radial velocity dispersion. The disk azimuthal dispersion, $\sigma_\phi(R)$, is related to $\sigma_R(R)$ via the epicycle approximation (Binney & Tremaine 2008), while the vertical velocity dispersion, $\sigma_z(R)$, is set by the requirement that the adopted value of the scale height z_d is maintained in the total potential of the galaxy model. Here we parametrize the disk thickness as z_d/R_d and the disk mass as a given fraction, m_d, of the halo mass, M_h. For simplicity, we also assume a constant value of $\sigma_{R0} = 10\ {\rm km\,s^{-1}}$ for all our dwarf models. This choice results in a decreasing ratio of $V_{\rm rot}/\sigma_*$ with decreasing mass, where $V_{\rm rot}$ and σ_* denote the stellar rotational velocity and line-of-sight central velocity dispersion, a trend that is indeed observed in dIrrs of the LG (Mateo 1998).

Our goal is to assess the degree to which the structure of late-type disky dwarfs can influence their tidal evolution inside their host galaxies. For this reason, we generated a number of dwarf galaxy models that differed in a number of important structural parameters, including the disk thickness, mass, and scale length, and the halo mass and concentration parameter. To investigate the impact of all these quantities on the tidal evolution of the dwarfs, we first constructed a "reference" or "default" dwarf galaxy model and subsequently initialized additional models by varying (increasing and decreasing) all relevant parameters in a systematic way, modifying only one at a time. Throughout the paper, we compare the effect of changing a single parameter in three distinct dwarf models, namely the reference one and those with the largest and smallest values of a given parameter. We also stress that we do not attempt any explicit rescaling of our dwarf galaxy models with redshift to account for the cosmic epoch at which the dwarfs were accreted by their hosts, as was done in previous studies (Mayer et al. 2001a,b). On the one hand, this allows us to avoid any uncertainties regarding the applicability of such scalings to dwarf galaxies. On the other hand, our systematic parameter survey aims to address different choices for the basic structural parameters of the progenitors of present-day dSphs. As such, it should account to at least a certain extent for the wide diversity of dwarf galaxy structures expected at various cosmological epochs.

In total, we constructed 11 high-resolution numerical models of rotationally-supported dwarfs, which we denote D1-D11. The initial structural parameters of these models are listed in Table 1 (see § 2.4 for details on how the parameters corresponding to columns (12)-(17) of this table are calculated). Particular emphasis should be placed on column 4 of this table which lists the dimensionless spin parameters of the dwarf DM halos, λ. This parameter is a measure of the to-

TABLE 1
INITIAL STRUCTURAL PARAMETERS OF THE DWARF GALAXY MODELS

Model (1)	z_d/R_d (2)	m_d (M_h) (3)	λ (4)	c (5)	M_h ($10^9 M_\odot$) (6)	r_s (kpc) (7)	R_d (kpc) (8)	Q (9)	$V_{\rm max}$ (km s^{-1}) (10)	$r_{\rm max}$ (kpc) (11)	M/L ($M_\odot/L_\odot$) (12)	$V_{\rm rot}/\sigma_*$ (13)	β (14)	A_2 (15)	b/a (16)	c/a (17)
D1	0.2	0.02	0.040	20	1	1.29	0.41	3.93	19.8	2.07	29.5	2.93	0.15	0	1.00	0.12
D2	**0.1**	0.02	0.040	20	1	1.29	0.41	3.90	19.9	2.12	30.4	3.04	0.29	0	1.00	0.06
D3	**0.3**	0.02	0.040	20	1	1.29	0.41	3.91	19.8	2.19	31.1	2.85	0.02	0	1.00	0.18
D4	0.2	**0.01**	0.040	20	1	1.29	0.41	7.60	19.4	2.44	64.3	2.85	0.21	0	1.00	0.12
D5	0.2	**0.04**	0.040	20	1	1.29	0.41	2.05	21.0	1.69	14.2	3.06	0.03	0	1.00	0.13
D6	0.2	0.02	**0.024**	20	1	1.29	0.25	2.25	19.8	1.99	27.2	2.71	0.05	0	1.00	0.11
D7	0.2	0.02	**0.066**	20	1	1.29	0.66	6.32	19.8	2.32	35.8	3.06	0.27	0	1.00	0.12
D8	0.2	0.02	0.040	**10**	1	2.58	0.41	2.97	16.5	4.54	42.4	2.07	0.27	0	1.00	0.10
D9	0.2	0.02	0.040	**40**	1	0.65	0.41	5.00	24.8	1.19	32.6	3.78	0.13	0	1.00	0.13
D10	0.2	0.02	0.040	20	**0.2**	0.76	0.24	7.95	11.6	1.29	31.2	1.38	0.58	0	1.00	0.12
D11	0.2	0.02	0.040	20	**5**	2.21	0.70	2.14	32.0	3.52	25.9	4.38	-0.51	0	1.00	0.12

NOTES.—The quantities in each column are as follows. Column 1: Dwarf galaxy model. Column 2: Scale height of the disk of the dwarf in units of the disk radial scale length, R_d. Column 3: Mass of the disk of the dwarf in units of the mass of the dwarf halo, M_h. Column 4: Spin parameter of the DM halo of the dwarf used to determine the scale length of the dwarf disk (see text for details). The corresponding disk scale lengths are listed in column 8. Column 5: Concentration parameter of the DM halo of the dwarf. Column 6: Mass of the DM halo of the dwarf in units of $10^9 M_\odot$. This parameter is equivalent to the cosmologically-motivated virial mass. Column 7: Scale radius of the DM halo of the dwarf in kpc. Column 8: Radial scale length of the disk of the dwarf in kpc. Column 9: Toomre stability parameter of the dwarf disk at $R = 2.5R_d$. Column 10: Maximum circular velocity of the dwarf in km s^{-1}. Column 11: Radius at which the maximum circular velocity occurs in kpc. Column 12: Mass-to-light ratio of the dwarf in units of $M_\odot/L_\odot$. Column 13: Ratio of stellar rotational velocity to one-dimensional stellar velocity dispersion of the dwarf. Column 14: Anisotropy parameter of the stellar distribution of the dwarf. Column 15: Amplitude of the $m = 2$ Fourier component of the surface density distribution of the dwarf stars. Column 16: Axis ratio b/a of the stellar component of the dwarf. Column 17: Axis ratio c/a of the stellar component of the dwarf. See § 2.4 for details on how the parameters listed in columns 12-17 are calculated. Note that the entries in these columns are computed within $r_{\rm max}$.

tal energy content of a DM halo stored in rotation and it is defined as $\lambda \equiv J|E|^{1/2}/GM^{5/2}$ (Peebles 1969), where J is the total angular momentum, E is the binding energy, and M is the mass of the halo. Although our halos are non-rotating, we still employ the parameter λ to assign scale lengths to the dwarf disks. This is because the disk scale length is not a free parameter in our modeling, but rather is derived via the semi-analytic model of Mo et al. (1998) for the structure of disk galaxies in the ΛCDM paradigm[6]. According to this model, the baryons settle into a rotationally supported structure whose scale length is determined by the mass, spin parameter and concentration of the DM halo, and the fraction of mass and angular momentum in baryons relative to that of the halo. Assuming that the specific angular momentum of baryons is conserved during their infall and that the halo and baryons start with the same specific angular momentum, R_d is uniquely determined in our models by M_h, λ, c, and m_d. We note that the Widrow & Dubinski (2005) method for building disk galaxies does not explicitly take into account the adiabatic contraction of the halo in response to the slow accumulation of the baryons (e.g., Blumenthal et al. 1986). Therefore, in order to be consistent, we derive the values for the disk scale lengths without considering this effect. In summary, the values of λ that we discuss throughout this study do not reflect the angular momentum content of the DM halos, but rather serve the practical purpose of enabling us to derive the values of R_d in the dwarf disks according to Mo et al. (1998).

Our reference dwarf model D1 is characterized by the following values for the adopted set of parameters: $z_d/R_d = 0.2$, $m_d = 0.02$, $\lambda = 0.04$, $c = 20$, and $M_h = 10^9 M_\odot$. The details of how we varied these values in our simulation campaign are described in each relevant subsection of § 4. In what follows, we motivate the choices for the default values of the various parameters in dwarf model D1. Our choices are mainly guided by studies of the properties of cosmological halos.

Using a constrained simulation of the LG, Klimentowski et al. (2010) studied the distribution of subhalo masses at the time of infall onto the primary as a function of redshift. These authors found that a significant fraction of satellites that were accreted by their hosts since $z \lesssim 2$ and survived until the present time had masses of $\approx 10^9 M_\odot$ (see Figure 8 of Klimentowski et al. 2010). Assuming a concordance ΛCDM model, the median concentration value for a $z = 0$ cosmological halo at this mass scale is $c \approx 20$ (e.g., Bullock et al. 2001b; Macciò et al. 2007). In addition, both observational and theoretical evidence suggests that dwarf galaxies are not formed as thin disks, but rather are born as thick, puffy systems (e.g., Dalcanton et al. 2004; Kaufmann et al. 2007). This is a consequence of the greater importance of feedback processes and turbulent motions in dwarf galaxies. We take this expectation into account by conservatively adopting $z_d/R_d = 0.2$, instead of the typical value $z_d/R_d = 0.1$ employed throughout the literature which would be more appropriate for massive disk galaxies (e.g., Kregel et al. 2002).

As has been established by a large number of studies, the distribution of halo spin parameters in N-body simulations is well described by a log-normal distribution, with median values of $\lambda_{\rm med} \approx 0.04$ and dispersions of $\sigma_\lambda \sim 0.5$ (e.g., Bullock et al. 2001a; Shaw et al. 2006; Macciò et al. 2007; Bett et al. 2007; Macciò et al. 2008). According to Macciò et al. (2007) (see also Bett et al. 2007 and Macciò et al. 2008), the distri-

---

[6] In reality, the Mo et al. (1998) formalism and its assumptions for the formation of galactic disks may be inappropriate at the scales of dwarf galaxies. This is due to the greater importance of thermal over rotational support in such low-mass systems which modify the simple analytic scalings of Mo et al. (1998). Nonetheless, given that our purpose is not to derive exact scale lengths for our dwarf galaxies but simply to determine the degree to which the tidal evolution of disky dwarfs is affected by the sizes of their disks, following Mo et al. (1998) is reasonable and does not bias our results in any way.

bution of halo spins shows no dependence on halo mass. We stress that this conclusion does hold for halos with masses of the order of $\sim 10^9 M_\odot$ that we consider here (A. Macciò 2010, private communication). Lastly, we choose the default value for the disk mass fraction of our dwarfs equal to $m_d = 0.02$. This value is much lower than the universal baryon fraction but quite typical for present-day low surface brightness (LSB) or dIrr galaxies (e.g., Jimenez et al. 2003; Geha et al. 2006; Oh et al. 2008), and is also in agreement with results of hydrodynamical simulations of dwarf galaxy formation (e.g., Tassis et al. 2003; Governato et al. 2010).

For each dwarf galaxy model, we generated an N-body realization containing a total of 2.2 million particles ($N_h = 10^6$ DM particles and $N_d = 1.2 \times 10^6$ disk particles). The gravitational softening was set to $\epsilon_h = 60$ pc and $\epsilon_d = 15$ pc for the particles in the two components, respectively. The process of transforming a disky dwarf into a dSph via tidal stirring is fairly complex and depends on a number of subtle dynamical effects (e.g., Mayer et al. 2001a). It is thus important to establish both the quality and the sufficient resolution of our dwarf galaxy models. For this reason, we evolved all dwarf galaxies in isolation for a period of 10 Gyr. These test simulations revealed that the dwarfs retained their equilibrium configuration within the adopted force resolution over the timescales of the experiments. Therefore, our models should be largely unaffected by both two-body relaxation and artificial numerical heating of the dwarf disk through interactions with the massive particles of the dwarf halo. The same simulations also confirmed the stability of all dwarf galaxy models against bar formation. Thus, any significant bar growth identified in the dwarfs during the course of the numerical experiments should be the result of the tidal field of the host galaxy, rather than a consequence of noise present in the initial conditions. All of these precautions imply that our dwarf galaxy models should indeed be adequate to resolve the generic tidal evolution of late-type disky dwarfs and to elucidate their transformation via tidally-induced dynamical instabilities and impulsive tidal heating.

2.2. *Primary Galaxy Model*

Another improvement we introduce in the present study is the fact that we employ self-gravitating primary galaxies as opposed to static host potentials adopted in the majority of earlier related investigations. The motivation behind this choice is twofold. First and most importantly, live primary galaxies can trigger instabilities in the disks of the dwarfs, that otherwise may not develop, and which could influence the dynamical and morphological evolution of the dwarf galaxies themselves (Weinberg & Blitz 2006). Second, by representing the host galaxies as a distribution of interacting particles, we enable the dwarf galaxies to suffer dynamical friction. As a result of a progressively decaying orbit, the mass loss and tidal stripping experienced by the dwarfs will be enhanced with obvious consequences for their dynamical evolution inside the host.

For simplicity, we assume a single primary galaxy with the present-day structural properties of the MW. In particular, we employ model MWb of Widrow & Dubinski (2005), which satisfies a broad range of observational constraints for the MW galaxy. Specifically, the exponential stellar disk has a mass of $M_D = 3.53 \times 10^{10} M_\odot$, a radial scale length of $R_D = 2.82$ kpc, and a sech^2 scale height of $z_D = 400$ pc. The bulge which follows the Hernquist (1990) density profile has a mass and a scale radius of $M_B = 1.18 \times 10^{10} M_\odot$ and $a_B = 0.88$ kpc, respectively. The DM halo has an NFW profile with a tidal radius of $R_H = 244.5$ kpc, a mass of $M_H = 7.35 \times 10^{11} M_\odot$, and a scale radius of $r_H = 8.82$ kpc.

The simulations reported here use $N_D = 10^6$ particles in the disk, $N_B = 5 \times 10^5$ in the bulge, and $N_H = 2 \times 10^6$ in the DM halo of the host galaxy, and employ a gravitational softening of $\epsilon_D = 50$ pc, $\epsilon_B = 50$ pc, and $\epsilon_H = 2$ kpc, respectively. The choice for the fairly large softening in the DM particles of the primary galaxy was motivated by our desire to minimize discreteness noise in the host potential. Such noise may lead to spurious two-body heating between the excessively massive halo particles of the primary galaxy and those of the dwarf disk, potentially interfering with the interpretation of our results. In order to confirm the adequacy of our choice for ϵ_H, we placed the reference dwarf model D1 at rest at various distances inside the host galaxy and monitored the changes of its basic properties (e.g., surface density, velocity dispersions, thickness) as a function of time. The evolution of the structural parameters within radii of interest (see § 2.4 below) was found to be fairly small, specifically $\lesssim 20\%$, during a period of several Gyr. This indicates that the chosen numerical parameters are indeed appropriate to suppress the effect of two-body heating between the halo particles of the primary galaxy and those of the dwarf disk.

2.3. *Description of Tidal Stirring Simulations*

Our simulation campaign comprised 17 numerical experiments, which we denote R1-R17, of the tidal interactions between rotationally-supported dwarf galaxies and their hosts. Table 2 provides a summary of all simulations we performed in this study. The various dwarf galaxy models are placed on bound orbits inside the primary galaxy. Except for varying the initial structure of the disky dwarf galaxies, we also investigated the degree to which their tidal evolution is affected by the orbital parameters and, in particular, on the sizes and the eccentricities of the dwarf orbits.

The size of the orbit is expected to be crucial for the efficiency of tidal stirring, since the tidal force exerted by the primary galaxy depends strongly on the distance from its center. To explore this effect, we conducted a set of simulations where the default dwarf galaxy model D1 is placed on three orbits with different sizes. Although the orbits of LG dwarfs are currently poorly constrained observationally, their current distances, which give an indication of the apocenters of their orbits, coupled with studies of the orbital properties of cosmological halos, can be used to inform our choices. Indeed, using a cosmological simulation of the LG, Klimentowski et al. (2010) studied the orbital distribution of present-day satellites that were identified inside the virial radius of their hosts and had completed at least one orbit around them. These authors found that a significant fraction of this satellite population had apocentric distances between $r_{\rm apo} \approx 250$ and ≈ 85 kpc, with typical values of $r_{\rm apo} \approx 125$ kpc (see Figure 6 of Klimentowski et al. 2010). Adopting $R_{\rm vir} \approx 250$ kpc as the virial radius of the MW halo at $z = 0$ (e.g., Klypin et al. 2002), the previous numbers would roughly correspond to $R_{\rm vir}$, $R_{\rm vir}/3$, and $R_{\rm vir}/2$. The value $r_{\rm apo} = 125$ kpc also approximately matches the virial radius of the MW halo at $z \sim 1$ (e.g., Wechsler et al. 2002). A critical reader may note that the characteristic orbits of the $z = 0$ subhalo population that we have considered may not be representative of those at the time of satellite infall onto the primary. This is especially true for systems that are accreted at high redshift ($z \gtrsim 1$). Given the complexity of halo formation in a cosmological context, this is a valid concern. While ad-

TABLE 2
SUMMARY OF SIMULATIONS

Simulation (1)	Dwarf Model (2)	$r_{\rm apo}$ (kpc) (3)	$r_{\rm peri}$ (kpc) (4)	$r_{\rm apo}/r_{\rm peri}$ (5)	i (deg) (6)	z_d/R_d (7)	m_d (M_h) (8)	λ (9)	c (10)	M_h $(10^9 M_\odot)$ (11)
R1	D1	125	25	5	45	0.2	0.02	0.040	20	1
R2	D1	**85**	**17**	5	45	0.2	0.02	0.040	20	1
R3	D1	**250**	**50**	5	45	0.2	0.02	0.040	20	1
R4	D1	125	**12.5**	**10**	45	0.2	0.02	0.040	20	1
R5	D1	125	**50**	**2.5**	45	0.2	0.02	0.040	20	1
R6	D1	125	25	5	**0**	0.2	0.02	0.040	20	1
R7	D1	125	25	5	**90**	0.2	0.02	0.040	20	1
R8	D2	125	25	5	45	**0.1**	0.02	0.040	20	1
R9	D3	125	25	5	45	**0.3**	0.02	0.040	20	1
R10	D4	125	25	5	45	0.2	**0.01**	0.040	20	1
R11	D5	125	25	5	45	0.2	**0.04**	0.040	20	1
R12	D6	125	25	5	45	0.2	0.02	**0.024**	20	1
R13	D7	125	25	5	45	0.2	0.02	**0.066**	20	1
R14	D8	125	25	5	45	0.2	0.02	0.040	**10**	1
R15	D9	125	25	5	45	0.2	0.02	0.040	**40**	1
R16	D10	125	25	5	45	0.2	0.02	0.040	20	**0.2**
R17	D11	125	25	5	45	0.2	0.02	0.040	20	**5**

NOTES.—Columns 3-5 refer to the initial orbital parameters of the disky dwarfs. Columns 7-11 list the initial structural parameters of the dwarf galaxy models. The quantities in each column are as follows. Column 1: Abbreviation for the tidal stirring simulations. Column 2: Dwarf galaxy model. Column 3: Apocentric distance of the orbit of the dwarf in kpc. Column 4: Pericentric distance of the orbit of the dwarf in kpc. Column 5: Eccentricity of the orbit of the dwarf. Column 6: Inclination of the disk of the dwarf with respect to the orbital plane in degrees. Column 7: Scale height of the disk of the dwarf in units of the disk radial scale length, R_d. Column 8: Mass of the disk of the dwarf in units of the mass of the dwarf halo, M_h. Column 9: Spin parameter of the DM halo of the dwarf used to determine the scale length of the dwarf disk (see text for details).The corresponding disk scale lengths are listed in column 8 of Table 1. Column 10: Concentration parameter of the DM halo of the dwarf. Column 11: Mass of the DM halo of the dwarf in units of $10^9 M_\odot$. This parameter is equivalent to the cosmologically-motivated virial mass.

dressing this issue is certainly beyond the scope of the present paper, we note that at least dynamical friction should not have a major effect, if any, in altering the orbits of satellites with masses of the order of $\sim 10^9 M_\odot$ that we have adopted here (Colpi et al. 1999).

Motivated by the previous discussion, we adopt $r_{\rm apo} = 125$, 85, and 250 kpc as the apocentric distances of the dwarfs in the experiments with different sizes of orbits. We refer to these simulations as "R1", "R2", and "R3", respectively, and discuss them in § 3.1. Fixing the eccentricity of the orbits will determine the corresponding pericentric distances. Specifically, we adopt an eccentricity of $r_{\rm apo}/r_{\rm peri} = 5$, close to the median ratio of apocentric to pericentric radii found in cosmological N-body simulations (e.g., Ghigna et al. 1998; Diemand et al. 2007). Interestingly, the pericentric distance of the tightest orbit with $r_{\rm peri} = 17$ kpc roughly corresponds to that inferred for the Sagittarius dwarf galaxy (e.g., Law et al. 2005). In addition, the pericentric distance of the most extended orbit with $r_{\rm peri} = 50$ kpc is similar to that of the Large Magellanic Cloud (LMC), provided that the LMC has just crossed the pericenter of its orbit around the MW (Besla et al. 2007). Given the typical parameters associated with experiment R1, throughout this work we refer to it as the "reference" or "default" simulation that we use as the basis for the comparison with other experiments.

Apart from the size of the orbit, we also investigate the impact of the orbital eccentricity on the tidal transformation of the dwarfs. Cosmological simulations (e.g., Ghigna et al. 1998; Diemand et al. 2007; Klimentowski et al. 2010). indicate that satellite orbits range from nearly circular ($r_{\rm apo}/r_{\rm peri} \approx 1$) to highly eccentric ($r_{\rm apo}/r_{\rm peri} \gtrsim 10$). On high-eccentricity orbits, the effective duration of the tidal shock becomes so short that the response of the system is prone to be impulsive rather than adiabatic and, as a result, tidal heating is particularly efficient (e.g., Gnedin et al. 1999). To this end, we considered two additional simulations in which we placed the dwarf galaxy model D1 on a highly and a mildly eccentric orbit, respectively. In particular, we considered orbits with eccentricities that were by a factor of 2 larger ($r_{\rm apo}/r_{\rm peri} = 10$) and smaller ($r_{\rm apo}/r_{\rm peri} = 2.5$) compared to that of R1. We refer to these experiments as "R4" and "R5" (see Table 2) and discuss them in § 3.2. In order to meaningfully compare the results of this set of simulations, we kept the apocentric distance of the reference experiment R1 constant ($r_{\rm apo} = 125$ kpc). The desired value of eccentricity is then achieved by simply varying the pericentric distance, $r_{\rm peri}$. This modeling results in a pericentric distance of $r_{\rm peri} = 12.5$ kpc in simulation R4, which is the smallest in all experiments we performed in the present study.

Initial conditions for the tidal stirring experiments were generated by building models of dwarf galaxies and placing them at the apocenters of their orbits. In the coordinate system chosen to describe the simulations, the orbital plane is the xy plane, and the center of mass of the combined system of dwarf and primary coincides with the coordinate origin. We stress that we did not impose any truncation in the density distribution of the dwarfs (i.e.,, at the corresponding Jacobi tidal radius) to reflect their placement in the host tidal field. In addition, the dwarf galaxies are not grown adiabatically in their orbits, but rather are introduced in the simulations directly. We have explicitly checked that this set of assumptions does not bias our results. Indeed, the initial starting positions of the dwarfs correspond to a rather low density in the host galaxy. This results in a fairly weak tidal perturbation that does not affect the very inner regions of the dwarf, which constitute the primary target of the present study.

According to the LG cosmological simulation of Klimentowski et al. (2010), most satellites that survived until the present time and whose masses at the epoch of infall onto the primary were in the range that we consider here (around $10^9 M_\odot$), entered their hosts at $z \lesssim 2$. Motivated by this finding, we follow the tidal evolution of the dwarfs inside their host galaxies for 10 Gyr. In the great majority of our experiments, the alignments of the internal angular momentum of the dwarf, that of the primary disk and the orbital angular momentum were all mildly prograde and equal to 45°. We discuss the implications of this choice in § 5.6 but emphasize at the outset that our results should not be affected by any strong coupling of angular momenta.

Lastly, all numerical experiments discussed in this work were performed with PKDGRAV, a multistepping, parallel, tree N-body code (Stadel 2001). In all experiments, we set the base time step to be equal to 1% of the dynamical time at the half-mass radius of the dwarf model and allowed the individual particle time steps to be at most a factor of 2^{20} smaller. The time integration was performed with high enough accuracy such that the total energy was conserved to better than 0.5% in all cases, which is adequate for the type of study that we undertake in this paper. As we have already stated, our main goal is to investigate the dynamical evolution of the dwarfs which is driven by the response of their inner regions to the tidal shocks. The total energy contained in the inner parts of our dwarf models is a few percent of that of the entire system, so the accuracy of the energy conservation must be at least comparable to that in order to resolve meaningfully the dynamics of the region of interest.

2.4. *Parameters of Relevance*

In order to illustrate the evolution of the intrinsic, global properties of the dwarf galaxies as they orbit inside their hosts, we calculated a set of parameters as a function of time. Specifically, we examined the degree to which the mass, size, shape, and kinematics of the dwarfs is affected subject to the strong tidal field of the primary galaxy.

For each simulation output, we first constructed the circular velocity profile of the dwarf galaxy, $V_c(r) = [GM(< r)/r]^{1/2}$, where $M(< r)$ is the spherically-averaged total mass profile about its center. As a measure of how the mass of the dwarf is affected at any stage, we employed the maximum circular velocity, $V_{\rm max}$, which reflects the mass distribution in the inner regions and is a commonly adopted quantity throughout the literature. The attractive feature of $V_{\rm max}$ is that it is well defined and allows us to overcome difficulties regarding the determination of the tidal radius (e.g., Read et al. 2006b).

In order to demonstrate how the size of the dwarf galaxy is affected by tides, we investigated the evolution of the radius at which $V_{\rm max}$ occurs, $r_{\rm max}$. Following Klimentowski et al. (2009a), we chose $r_{\rm max}$ as the characteristic scale where we computed the remaining properties of the dwarfs. This radius is large enough to include a significant fraction of the mass of the dwarf at all times, while at the same time is small enough not to be affected by the tidal tails (see Klimentowski et al. 2007, 2009b). Due to the fact that tidal stripping truncates the dwarf galaxies at increasingly smaller physical radii, this characteristic radius decreases with time, from a few kpc initially down to a fraction of a kpc at the end of the evolution.

Because of the copious amounts of DM in dSphs, another quantity of particular interest is the mass-to-light ratio, M/L. Since the bulk of the stellar populations in these galaxies is old ($t \gtrsim 8-10$ Gyr; see, e.g., Grebel 2000), we chose to calculate the M/L ratio by conservatively adopting a fixed stellar mass-to-light ratio of $(M/L)_* = 3M_\odot/L_\odot$ (e.g., Schulz et al. 2002). We note that while such values for $(M/L)_*$ should be appropriate for the present time, they may not be necessarily representative for the whole evolution, as the dwarfs might undergo periodic bursts of star formation triggered by tidal compression at pericentric passages (Mayer et al. 2001a). However, for dwarf galaxies accreted by their hosts as early as 10 Gyr ago, as assumed here, most of the gas should be quickly stripped by ram pressure aided by the cosmic ionizing background radiation (Mayer et al. 2007). As a result, star formation should cease soon after the dwarfs are accreted by the host galaxy. In addition, using the stellar population synthesis models of Bruzual & Charlot (1993), Mayer et al. (2001a) showed that even when a burst of star formation occurs at first pericentric approach, the final $(M/L)_*$ ratio would correspond to that of an old stellar population after 7 – 8 Gyr of evolution inside the primary potential. This is because the effect of the newly-formed population on the $(M/L)_*$ ratio and on the color of the dwarf galaxy diminishes quite rapidly. The above discussion suggests that the assumption of $(M/L)_* = 3M_\odot/L_\odot$ in the present study is fairly reasonable.

Obviously, one of the most representative properties of dSphs is their spheroidal shape. We quantified the shape of the stellar component by calculating the moments of the inertia tensor for all stars within $r_{\rm max}$ and deriving principal axis ratios b/a and c/a, where a, b, and c denote the major, intermediate, and minor axis of the stellar distribution, respectively. Another interesting quantity which can illuminate the dynamical and morphological evolution of the dwarf galaxies inside their hosts, is the amplitude of the $m = 2$ Fourier component of the stellar surface density distribution, A_2, given by

$$A_2 = \frac{1}{N}\left|\sum_{j=1}^{N} e^{2i\phi_j}\right| . \qquad (3)$$

Here ϕ_j denotes the two-dimensional cylindrical polar angle coordinate of particle j projected onto the xy plane (along the shortest axis) and the summation is performed over all stars within $r_{\rm max}$. The motivation behind studying the evolution of A_2 is twofold. First, it can be used as an auxiliary measure of the shape of the stellar component since the triaxiality parameter, $T = (a^2 - b^2)/(a^2 - c^2)$ (Franx et al. 1991), can be very noisy for systems close to spherical symmetry. We note, however, that A_2 can still be ambiguous as its value is close to zero for both nearly spherical and disky shapes. Second, as we discuss below, in the majority of cases we studied, the strong tidal shocks at pericentric passages trigger the formation of bars in the disks of the dwarfs. The parameter A_2 will allow us to determine when a bar forms and to quantify the strength of the bar instability.

For the purposes of the present study, we designate the formation of a bar when the amplitude of the $m = 2$ Fourier component satisfies $A_2 \gtrsim 0.2$ between two consecutive pericentric passages, namely for one full orbital period of the dwarf around its host. These conditions ensure that any tidally-induced bars that we detect in our simulations will be relatively strong (see, e.g., Debattista et al. 2006 for even weaker bars in isolated disk galaxies). They also guarantee that any temporary increase of A_2, when the dwarfs are strongly elongated by tidal forces at the pericenters of the orbit, will not be ascribed to a true bar instability.

dSphs are low-angular momentum systems, as highlighted by their low ratio of rotational velocity to line-of-sight central velocity dispersion, $V_{\rm rot}/\sigma_* \lesssim 1$ (e.g., Mateo 1998). It is thus important to investigate the evolution of the kinematics in the tidally-stirred disky dwarfs. To this end, after determining the directions of the principal axes of the stellar component in each output, we introduced a spherical coordinate system (r, θ, ϕ) so that the z-axis is along the shortest axis of the stellar distribution and the angle ϕ is computed on the xy plane. We measured the kinematics of the dwarfs within $r_{\rm max}$ by calculating the rotational velocity around the shortest axis $V_{\rm rot} = V_\phi$ and the dispersions σ_r, σ_θ and σ_ϕ around the mean values. We combined these dispersions into the one-dimensional stellar velocity dispersion parameter, $\sigma_* \equiv [(\sigma_r^2 + \sigma_\theta^2 + \sigma_\phi^2)/3]^{1/2}$, which we adopted as a measure of the amount of random motions in the stars. We note that throughout this paper we compare the derived values of σ_* with those of observed dSphs. Defining σ_* as an average over three directions makes such comparisons more meaningful, since the observed one-dimensional stellar velocity dispersions depend on the random line-of-sight.

Another illuminating quantity related to stellar kinematics is the anisotropy parameter, $\beta \equiv 1 - \sigma_t^2/2\sigma_r^2$, where σ_r and $\sigma_t = (\sigma_\theta^2 + \sigma_\phi^2)^{1/2}$ denote the radial and tangential velocity dispersion, respectively. This quantity describes the degree of anisotropy of the velocity distribution by indicating the amount of radial ($\beta = 1$) versus circular ($\beta \to -\infty$) orbits in the stellar population. We stress that this parameter cannot be measured directly from observations, but only determined by dynamical modeling (e.g., Łokas 2002). Given that a well established range for the velocity anisotropy of observed dSphs does not yet exist, our simulations can provide useful predictions for the possible values of β in such systems.

2.5. *Classification Criteria*

The goal of the present study is to determine the conditions under which systems with the properties of dSphs can be produced via the tidal interactions between disky dwarfs and their host galaxies. Observed dSphs possess a unique set of kinematic and structural properties that we can utilize in order to perform comparisons with simulated dwarfs. In particular, we imposed two criteria for establishing the formation of a dSph in our simulations.

The first criterion is related to the shape of the stellar component. Specifically, only simulated dwarf galaxies whose final states are characterized by $c/a \gtrsim 0.5$ may be regarded as dSphs. The motivation behind this choice stems from the fact that most classic dSphs (e.g., Fornax, Draco, Leo I, Tucana, Sextans, Carina) have projected ellipticities, $\epsilon \equiv 1 - b/a$, in the range $0.1 \lesssim \epsilon \lesssim 0.5$ (e.g., Mateo 1998; McGaugh & Wolf 2010), or equivalently projected axis ratios $b/a \gtrsim 0.5$, where b and a denote the minor and major axis of the stellar distribution, respectively. Given that an elongated shape cannot appear more elongated in projection, the condition that *intrinsic* $c/a \gtrsim 0.5$ in the simulated dwarfs (n.b. by definition $b/a \geq c/a$) ensures that the *projected* b/a will also satisfy $b/a \gtrsim 0.5$ in any possible projection, in accord with the values inferred for observed dSphs. We note that the intrinsic axis ratios of the dwarf remnants do not vary significantly with radius. Thus, they are appropriate for comparisons with observed ellipticities that are not computed within $r_{\rm max}$, but rather estimated either at the outer parts of the stellar distribution (Mateo 1998) or within some observationally-defined radius (e.g., half-light radius).

The second classification criterion is related to the kinematics of the stellar component. In particular, we classify as dSphs only those systems which, after 10 Gyr of evolution inside the primary galaxy, exhibit $V_{\rm rot}/\sigma_* \lesssim 1$ in accordance with the results of observational studies of classic dSphs (e.g., Mateo 1998). We stress that the values we compute for $V_{\rm rot}$ and σ_* are fairly close to what an observer would measure using line-of-sight velocities, making the comparison with observations reasonable. Indeed, at $r_{\rm max}$ the rotation is close to the maximum value and can be readily measured if the line-of-sight is perpendicular to the rotation axis. Moreover, the velocity dispersion profiles of our remnants do not strongly vary with radius (as well as with line-of-sight) suggesting that our derived values for σ_* should not differ significantly from those of the central velocity dispersion commonly used by observers. As a result of all these facts, the condition $V_{\rm rot}/\sigma_* \lesssim 1$ that we impose here guarantees that $V_{\rm rot}/\sigma_* \lesssim 1$ will also be satisfied for a significant fraction, if not all, of random lines-of-sight.

Overall, for the purposes of the present study, the above classification scheme is adequate to establish the formation of a dSph in our simulations. A more direct comparison between theoretical and observational measurements for the properties of dSphs will be performed in a companion paper (Łokas et al. 2010, in preparation).

3. EFFICIENCY OF TIDAL STIRRING AND ORBITAL PARAMETERS OF THE PROGENITOR DISKY DWARFS

In this section, we gauge the dependence of the efficiency of tidal stirring on the orbital parameters of the progenitor rotationally-supported dwarfs, and in particular, on the size and eccentricity of their orbits.

3.1. *Size of the Orbit*

We first investigate the degree to which the tidal evolution of a disky dwarf is affected by the size of its orbit. The size of the orbit should be crucial for the outcome of tidal stirring since the tidal force depends strongly on the distance of the dwarf from the center of the host galaxy. In order to ascertain this, we considered two additional simulations (R2, R3) in which we placed the dwarf galaxy model D1 on orbits with sizes that were different from that of the reference experiment R1. Specifically, in this set of simulations, we kept the eccentricity constant, but varied the default apocentric and pericentric distance by the same factor, leaving all other simulation parameters unchanged (see Table 2). Figure 1 shows the orbital trajectories of the dwarf galaxies from the respective center of their host as a function of time for experiments R1, R2, and R3. In Figure 2, we present the time evolution of the relevant parameters discussed in § 2.4 ($V_{\rm max}$, $r_{\rm max}$, b/a, c/a, $V_{\rm rot}/\sigma_*$, β, M/L, and A_2) for the same simulations.

In order to highlight some general trends in the evolution of these quantities with time, we first focus on the reference experiment R1. As a result of the continuous action of the host galaxy tidal field, the overall structure of the orbiting dwarf is altered as it experiences a gradual decrease of its mass and physical size. This is reflected in the evolution of $r_{\rm max}$ and $V_{\rm max}$, respectively, which are both reduced systematically as a function of time. The preferential stripping of the mass from the outer, low-density regions of the dwarf galaxy leads to the adjustment of the circular velocity profile in such a way that both $r_{\rm max}$ and $V_{\rm max}$ decrease. The temporary but substantial increase of $r_{\rm max}$ at the first pericentric approach

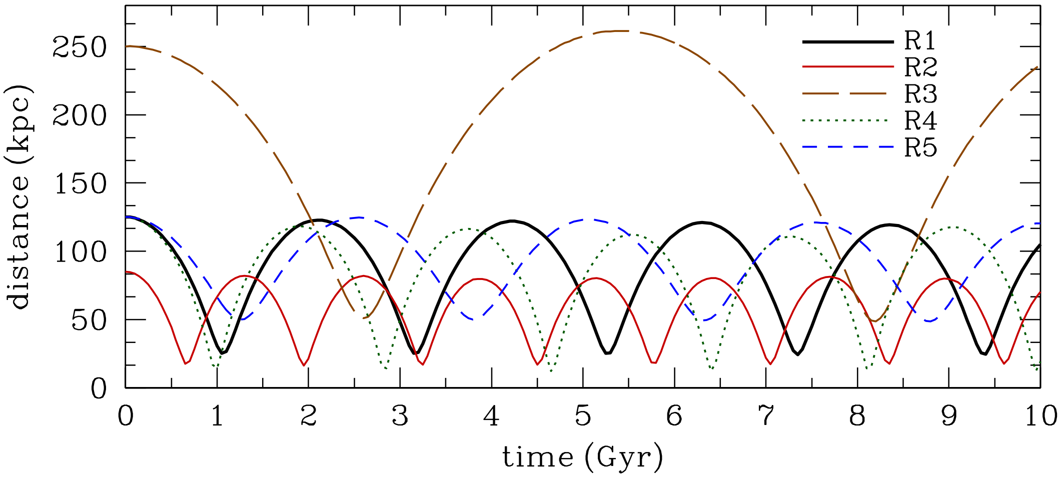

FIG. 1.— Distances of the orbiting dwarf galaxies from the centers of their hosts as a function of time. Results are presented for simulations R1-R5, where the dwarfs are characterized by different orbital parameters.

can be attributed to the fact that the dwarf is being deformed by strong tidal forces for the first time and, as a result, its density distribution becomes very extended. This increase in $r_{\rm max}$ is not observed at subsequent pericentric passages as the dwarf galaxy becomes progressively more compact during its evolution and thus the ability of the tidal field to distort it is reduced. As we show below, in cases where the dwarfs are initially more concentrated (as a result of either being embedded in halos of higher concentration or hosting more compact or massive disks) or are on wider orbits and experience weaker tidal forces, this increase in $r_{\rm max}$ does not occur.

The evolution of $V_{\rm max}$ shows two interesting features. First, $V_{\rm max}$ decreases significantly near the pericenters of the orbit, where the intensity and variation of the time-dependent tidal force is the strongest, and the tidal shocks occur. This drop in $V_{\rm max}$ is associated with mass loss from all regions of the dwarf galaxy. Because tidal shocks act on a very short timescale, even the inner regions of the dwarf, which are characterized by the highest densities and thus the shortest dynamical times, respond impulsively to the external tidal perturbation and mass is tidally stripped directly from regions within $r_{\rm max}$. However, $V_{\rm max}$ also decreases because a fraction of the particles that are removed from larger radii are, in fact, on eccentric orbits with large apocentric distances. Although these particles spend most of their time outside of $r_{\rm max}$, they still contribute to the total mass in the inner regions. These are preferentially DM particles, since stars are confined to the central region of the dwarf by construction. After experiencing the tidal shock, it takes a few hundred million years, i.e., a multiple of the dynamical time of the system, for the dwarf to readjust to a new equilibrium state with a new value of $V_{\rm max}$.

Second, $V_{\rm max}$ remains remarkably constant between pericentric approaches as the dwarf responds adiabatically to the weak intensity and variation of the tidal force. Overall, tides act nearly impulsively at pericentric passages and have little influence on the dwarf galaxy between pericentric passages. This general behavior of $V_{\rm max}$ and $r_{\rm max}$ is observed in all our simulations, and is in agreement with results reported in earlier studies (e.g., Hayashi et al. 2003; Kazantzidis et al. 2004b; Kravtsov et al. 2004; Peñarrubia et al. 2008). We note that, in the reference experiment R1, the dwarf looses $\sim 90\%$ of its initial mass within $r_{\rm max}$ during its orbital evolution but still survives as a bound entity. For such substantial mass loss, $V_{\rm max}$ and $r_{\rm max}$ decreased by a factor of ~ 1.7 and ~ 4, respectively. This finding has interesting implications as it suggests that tidal stripping affects the evolution of the $r_{\rm max} - V_{\rm max}$ relation expected in the ΛCDM cosmological model (see also Kravtsov 2010).

Focusing on the evolution of the M/L ratio, which we also estimate within $r_{\rm max}$, Figure 2 shows that it decreases monotonically as a function of time. This is a consequence of two facts. First, the stellar distributions of the dwarfs are naturally less extended than their DM halos. This implies that, within $r_{\rm max}$, the particles with the smallest binding energies and longest dynamical timescales, namely the particles that are most susceptible to be unbound by the tidal shocks, belong predominantly to the extended DM halos. Second, as discussed above, particles that are stripped from the outer parts of the dwarf but still contribute to the total mass in the inner regions belong preferentially to the DM component. For these reasons, DM is stripped more readily than the stars within $r_{\rm max}$ and this decreases the M/L ratio. In addition to these two processes, during the orbital evolution of the dwarfs, $r_{\rm max}$ decreases monotonically and moves towards the inner, stellar-dominated regions, resulting in a natural increase of the fraction of mass in stars within $r_{\rm max}$.

The evolution of the Fourier component A_2 shows a sudden increase after the first pericentric approach which signifies the formation of a tidally-induced bar. The onset of the bar instability coincides with a drop of $V_{\rm rot}/\sigma_*$, whose value continuously decreases thereafter. Loss of angular momentum caused by the bar and simultaneous increase of the stellar velocity dispersion due to tidal heating lead to a final value of $V_{\rm rot}/\sigma_* \approx 0.55$. As a result of the tidal shocks, the strength of the bar diminishes as a function of time and the dwarf becomes progressively more spherical. After 10 Gyr of evolution inside the host, the initially-disky stellar distribution is transformed into a spheroid with axis ratios of $c/a \approx 0.7$ and $b/a \approx 0.9$.

In what follows, we shall concentrate on comparing the tidal response of the dwarf in the reference simulation R1 with that in experiments R2 and R3. Figure 2 demonstrates that the dependence of the evolution of $r_{\rm max}$, $V_{\rm max}$, and M/L ratio on the size of the orbit is dramatic. As expected, the tighter the orbit is, the stronger and more rapid the decrease in all parameters. Specifically, the dwarf galaxy in simulation R2 with the smallest pericentric distance looses $\sim 99\%$ of its initial mass within $r_{\rm max}$ during its orbital evolution. In this case, $V_{\rm max}$ and $r_{\rm max}$ decreased by a factor of ~ 2.7 and ~ 11.5, respectively.

In addition, Figure 2 illustrates two interesting features in

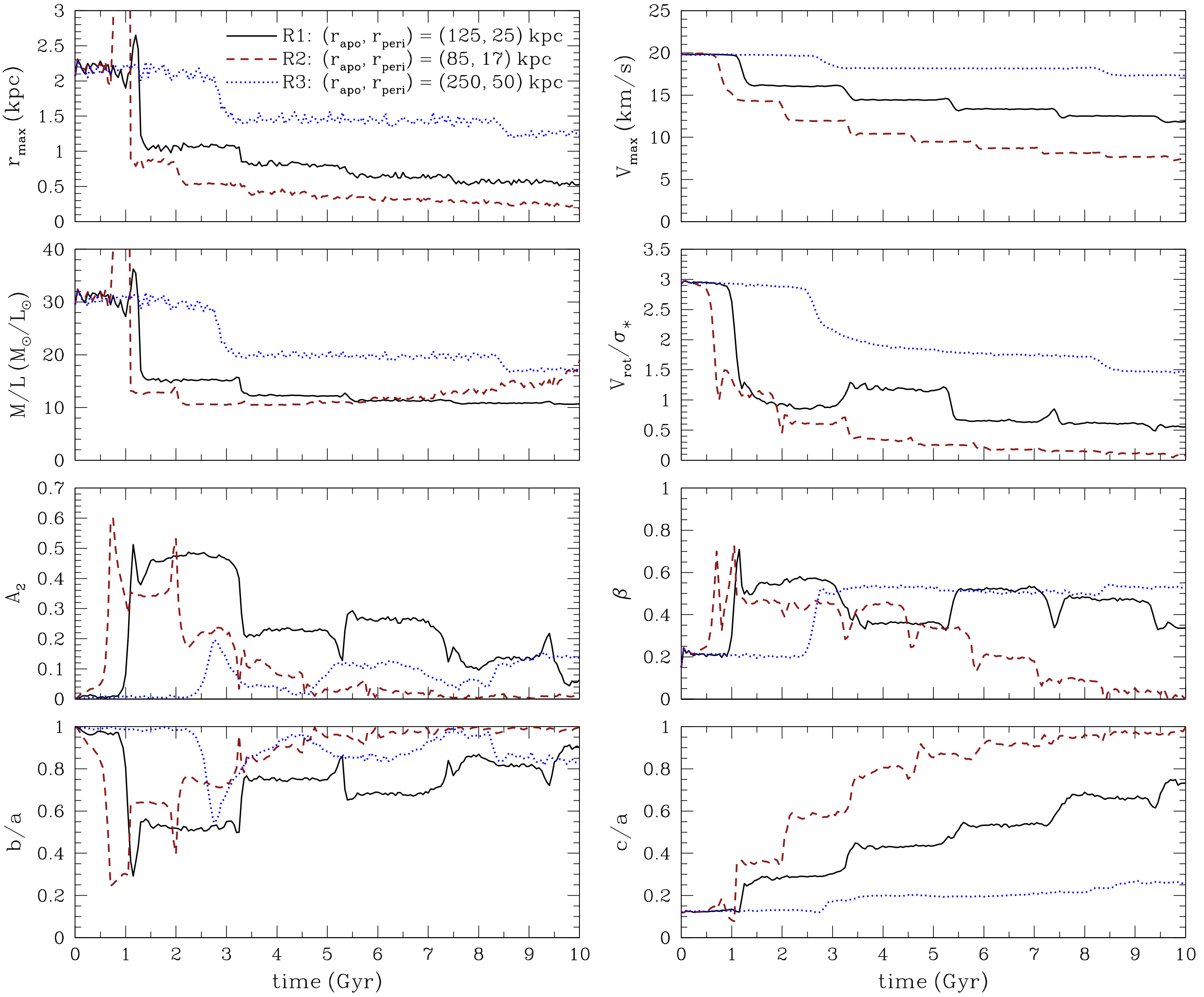

FIG. 2.— Comparison of the evolution of various parameters as a function of time illustrating the dependence of the tidal transformation of disky dwarf galaxies on the sizes of their orbits. Results are presented for the default simulation R1 and for experiments R2 and R3. The description of the simulations is presented in Table 2. For a fixed eccentricity, $r_{\rm apo}/r_{\rm peri}$, rotationally-supported dwarfs on tighter orbits with smaller pericentric distances, $r_{\rm peri}$, exhibit stronger tidal evolution inside their host galaxies and the efficiency of their transformation into dSphs is enhanced considerably.

the behavior of the dwarfs in experiments R1 and R2. First, the monotonic decrease of the M/L ratio is reversed for the tightest orbit in simulation R2 during the late stages of the evolution, indicating that the stars begin to be stripped more effectively compared to the DM. Second, the systematic decrease of $V_{\rm rot}/\sigma_*$ is reversed temporarily for simulation R1 between the second and third pericentric passage. We postpone the investigation of both issues for § 5.

In the case of experiments R1 and R2, the evolution of the anisotropy parameter β reflects the transition to more radial orbits after the first pericentric approach, as the dwarfs change shapes to prolate spheroids. The stellar orbits tend to become more isotropic with time, especially for simulation R2 where the velocity distribution of the dwarf at the end is completely isotropic ($\beta \approx 0$). The velocity anisotropy of the remnant in experiment R1 is mildly radial with $\beta \approx 0.3$.

Interestingly, the most strongly perturbed dwarf in simulation R2 is almost entirely pressure-supported ($V_{\rm rot}/\sigma_* \lesssim 0.1$) and its final shape is also spherically-symmetric ($b/a \approx c/a \approx 1$). Furthermore, while the dwarf in experiment R2 develops a strong bar, its counterpart in simulation R3 does not. The least evolved dwarf in experiment R3 remains oblate for the whole time except for a short period after the first pericentric approach. According to the criteria described in § 2.5, the final dwarfs in simulations R1 and R2 would be classified as dSphs but the remnant in experiment R3 would not as it has a disky shape and it is still dominated by rotation ($V_{\rm rot}/\sigma_* > 1$). It is also important to highlight the strong association between bar formation and the formation of dSphs reported in this set of simulations. Such a connection is observed in all but one of our experiments.

The final structural parameters of the simulated dwarfs after 10 Gyr of evolution inside the primary galaxy are listed in Table 3. Special emphasis should be placed on columns 10 and 11 of this table. Column 10 refers to whether a tidally-induced bar was formed in the stellar distribution of the dwarf galaxy during the course of its evolution inside the host. Column 11 indicates whether a dSph was produced as a result of the tidal interaction between the progenitor disky dwarf and the primary galaxy. The entries in column 6 demonstrate that

TABLE 3
SUMMARY OF RESULTS

Simulation (1)	$V_{\rm max}$ (km s^{-1}) (2)	$r_{\rm max}$ (kpc) (3)	M/L ($M_\odot/L_\odot$) (4)	$V_{\rm rot}/\sigma_*$ (5)	β (6)	A_2 (7)	b/a (8)	c/a (9)	Bar Formation (10)	Classification (11)	$T_{\rm orb}$ (Gyr) (12)
R1	11.9	0.53	10.7	0.55	0.34	0.06	0.90	0.73	yes	dSph	2.09
R2	7.3	0.18	19.2	0.08	0.00	0.00	1.00	1.00	yes	dSph	1.28
R3	17.3	1.22	16.9	1.46	0.52	0.14	0.82	0.26	no	non-dSph	5.40
R4	7.2	0.24	15.3	0.03	0.03	0.03	0.95	0.94	yes	dSph	1.81
R5	16.0	0.98	14.0	1.25	0.54	0.06	0.88	0.36	no	non-dSph	2.50
R6	12.2	0.51	10.3	0.24	0.51	0.04	0.95	0.73	yes	dSph	2.09
R7	12.4	0.55	10.7	0.23	0.48	0.16	0.80	0.74	yes	dSph	2.09
R8	12.7	0.50	10.3	0.74	0.42	0.10	0.86	0.66	yes	dSph	2.09
R9	12.0	0.55	11.8	0.61	0.23	0.04	0.94	0.77	yes	dSph	2.09
R10	10.4	0.55	18.8	0.56	0.19	0.04	0.93	0.80	yes	dSph	2.09
R11	16.0	0.49	6.7	0.40	0.48	0.28	0.67	0.58	yes	dSph	2.09
R12	14.6	0.41	6.7	0.56	0.45	0.29	0.67	0.53	yes	dSph	2.09
R13	10.4	0.56	22.3	0.26	0.13	0.03	0.95	0.91	yes	dSph	2.09
R14	7.3	0.40	6.5	0.31	0.15	0.01	0.98	0.89	yes	dSph	2.10
R15	20.3	0.67	23.3	1.18	0.49	0.07	0.88	0.52	no	non-dSph	2.08
R16	7.1	0.36	11.6	0.62	0.33	0.04	0.94	0.73	no	dSph	2.14
R17	19.0	0.77	9.2	0.70	0.23	0.09	0.87	0.68	yes	dSph	1.88

NOTES.—Columns 2-9 refer to the final structural parameters of the simulated dwarfs. The quantities in each column are as follows. Column 1: Abbreviation for the tidal stirring simulations. Column 2: Maximum circular velocity of the dwarf in km s^{-1}. Column 3: Radius at which the maximum circular velocity occurs in kpc. Column 4: Mass-to-light ratio of the dwarf in units of $M_\odot/L_\odot$. Column 5: Ratio of stellar rotational velocity to one-dimensional stellar velocity dispersion of the dwarf. Column 6: Anisotropy parameter of the stellar distribution of the dwarf. Column 7: Amplitude of the $m = 2$ Fourier component of the surface density distribution of the dwarf stars. Column 8: Axis ratio b/a of the stellar component of the dwarf. Column 9: Axis ratio c/a of the stellar component of the dwarf. Column 10: Formation of a tidally-induced bar during the orbital evolution of the dwarf galaxies according to the criteria discussed in § 2.4. Column 11: Classification of the final systems according to the criteria imposed in § 2.5. Column 12: Orbital time in Gyr defined as the average time elapsed between consecutive apocentric passages. Note that the entries in columns 4-9 are estimated within $r_{\rm max}$.

the values of β in the dSph remnants range from isotropic to mildly radial ($0 \lesssim \beta \lesssim 0.5$). Given that a well established range for the velocity anisotropy of observed dSphs does not yet exist, a direct comparison with observations is not possible. However, we note that the magnitude of the radial velocity anisotropy in our dSphs is rather similar to that observed in the outer parts of CDM halos formed in cosmological simulations (e.g., Cole & Lacey 1996). Lastly, the orbital times listed in the last column of Table 3 are defined as the average time elapsed between consecutive apocentric passages.

Figure 3 shows the surface density maps of the final stellar distributions of the dwarfs in simulations R1, R2, and R3. Results are presented for projections onto the xz, yz, and xy planes and particles are color-coded on a logarithmic scale, with hues ranging from orange to white indicating increasing stellar density. This figure visually confirms the conclusions advanced above regarding the degree of morphological transformation experienced by the dwarfs in in this set of experiments.

3.2. *Eccentricity of the Orbit*

In this section, we explore the extent to which the tidal evolution of a rotationally-supported dwarf is influenced by the eccentricity of its orbit. As we discussed earlier, this effect is worth investigating as the effective duration of the tidal shock, and thus the response of the system to the tidal perturbation, depends on the orbital eccentricity (e.g., Gnedin et al. 1999). To this end, we conducted two additional simulations (R4, R5) in which we placed the dwarf galaxy model D1 on orbits with eccentricities that are larger ($r_{\rm apo}/r_{\rm peri} = 10$) and smaller ($r_{\rm apo}/r_{\rm peri} = 2.5$) by a factor of 2 from that of the reference experiment R1 (see Table 2). Simulations R4 and R5 should be viewed as corresponding to a highly and a mildly eccentric orbit, respectively. Figure 1 shows the orbital trajectories of the dwarf galaxies from the centers of their hosts in these experiments.

Figure 4 shows the main results related to this set of simulations. As expected, this figure demonstrates that for a fixed apocentric distance, higher eccentricity orbits induce a much stronger transformation in the orbiting dwarfs. The evolution of the various parameters in this set of experiments proves to be analogous to the one presented in Figure 2. The dwarf galaxies in simulations R4 and R5 evolve similarly to those in R2 and R3, respectively, and the same strong link between bar formation and the formation of dSphs is reported. Indeed, the disky dwarf in experiment R4 develops a bar and the final product is a nearly spherical ($b/a \approx c/a \gtrsim 0.9$), isotropic ($\beta \approx 0.03$), and non-rotating ($V_{\rm rot}/\sigma_* \approx 0.03$) dSph, with final properties akin to those of the remnant in simulation R2. The evolution of $V_{\rm max}$, $r_{\rm max}$, and mass within $r_{\rm max}$ is also similar in the two cases. This is due to the fact that although the orbital time of the dwarf in experiment R4 is significantly larger, is has a smaller pericentric distance compared to that of R2. On the other hand, the dwarf in experiment R5 does not form a bar and remains oblate, radially anisotropic and rotating, analogous to the one in simulation R3, despite the shorter orbital time and larger number of pericentric passages (see Figure 1).

A last interesting thing to note is that the bar instability that develops in the most strongly perturbed dwarf (R4) is weaker compared to that of the reference simulation, despite the fact that the pericentric distance is much smaller in the former case. The same behavior, although to a lesser degree, is observed in Figure 2. We speculate that this is a consequence of the very strong tidal forces in simulations R2 and R4. The

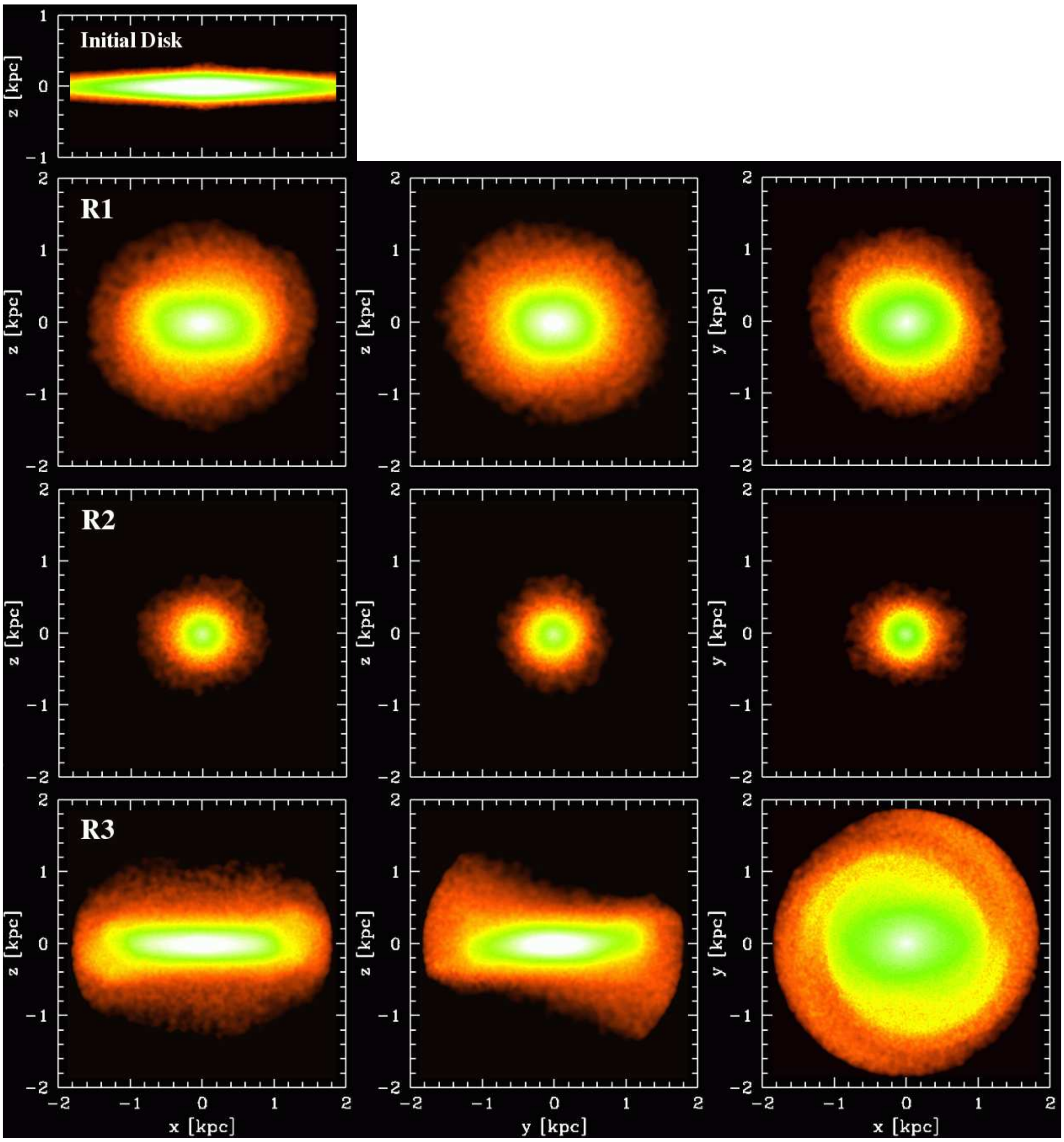

FIG. 3.— Surface density maps of the final stellar distributions of the dwarfs in simulations R1 (upper panels), R2 (middle panels), and R3 (lower panels). In order to aid comparison, the first panel also includes the edge-on view of the initial disk. Particles are color-coded on a logarithmic scale, with hues ranging from orange to white indicating increasing stellar density. Local density is calculated using an SPH smoothing kernel of 32 neighbors. Results are presented for projections onto the xz (left columns), yz (middle columns), and xy planes (right columns), where the x, y, and z axes lie along the major, intermediate, and minor axes of the stellar distribution, respectively. R1 is our reference simulation. Experiment R2 with the shortest orbital time and the second smallest pericentric distance all our experiments ($T_{\rm orb}$ = 1.28 Gyr and $r_{\rm peri}$ = 17 kpc) yields a spherically-symmetric ($b/a \approx c/a \approx 1$) and isotropic ($\beta \approx 0$) stellar system with negligible amounts of rotation ($V_{\rm rot}/\sigma_* \lesssim 0.1$) that would be classified as a dSph. The dwarf in simulation R3, whose orbit is characterized by the longest orbital time and largest pericentric distance ($T_{\rm orb}$ = 5.40 Gyr and $r_{\rm peri}$ = 50 kpc), is not transformed into a dSph and remains disky even after 10 Gyr of tidal evolution inside the host galaxy.

tidal shocks may heat the newly formed bar so substantially that they actually cause the instability to rapidly dissipate.

To summarize, the results of this and the previous section highlight that the effectiveness of the transformation into a dSph via tidal stirring depends crucially on the orbital parameters of the progenitor disky dwarfs. The relative importance of the orbital time and the pericentric distance in this process will be addressed in § 5.

4. EFFICIENCY OF TIDAL STIRRING AND STRUCTURAL PARAMETERS OF THE PROGENITOR DISKY DWARFS

In this section, we explore how the initial structure of the progenitor disky dwarfs could influence the outcome of their tidal evolution inside the gravitational field of their host galaxies. We begin by focusing on the parameters of the dwarf disk and discuss in turn the effect of the disk inclination, thickness, mass, and scale length. In § 4.2, we turn our attention to the properties of the DM halo of the dwarf and investigate the extent to which the effectiveness of tidal stirring is affected by the halo concentration parameter and mass.

4.1. *Varying the Parameters of the Disk*

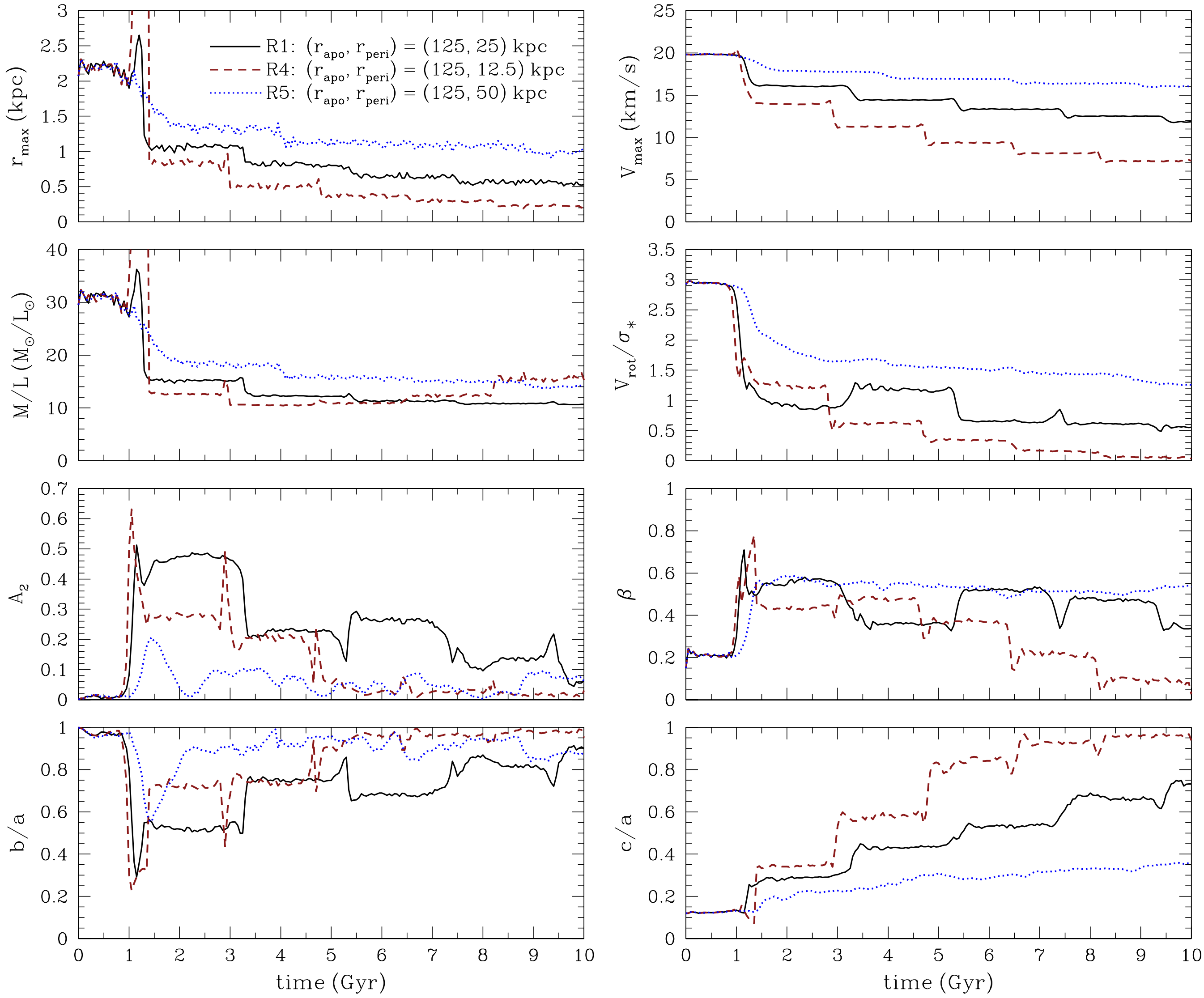

FIG. 4.— Comparison of the evolution of various parameters as a function of time illustrating the dependence of the tidal transformation of disky dwarf galaxies on the eccentricities of their orbits. Results are presented for the default simulation R1 and for experiments R4 and R5. The description of the simulations is presented in Table 2. For a fixed apocentric distance, $r_{\rm apo}$, rotationally-supported dwarfs on orbits with higher eccentricities, $r_{\rm apo}/r_{\rm peri}$, and thus smaller pericentric distances, $r_{\rm peri}$, display stronger tidal evolution inside their host galaxies and the efficiency of their transformation into dSphs is increased substantially.

4.1.1. *Disk Inclination*

We first investigate the extent to which the tidal evolution of a late-type disky dwarf is affected by the initial inclination of its disk with respect to the orbital plane. This is worth exploring as stronger alignments between the orbital angular momentum of the dwarf and the internal angular momentum of its disk can result in more effective stripping (e.g., Read et al. 2006b). For this purpose, we performed two additional simulations in which we placed the dwarf galaxy model D1 on the same orbit as in simulation R1 after changing the default inclination from $i = 45°$ to $i = 0°$ and to $i = 90°$ (see Table 2). Figure 5 contains the results pertaining to this set of simulations.

Although the initial inclination of the dwarf disk is very different, the size (in terms of $r_{\rm max}$), the mass (in terms of $V_{\rm max}$), and the M/L ratio evolve fairly similarly. This is a consequence of two facts. First, DM halos were constructed with no net angular momentum. Thus, their stripping should be independent of such considerations and proceed in exactly the same way. Second, the dwarfs are not stripped down to such small scales that the alignment between the stellar angular momentum and the orbital angular momenta would have an important effect on the stripping of the stars (e.g., Read et al. 2006b). Indeed, we find the decrease in mass within $r_{\rm max}$ for both stars and DM to be independent of the initial disk inclination.

It is important to note that Klimentowski et al. (2009a) reported that disk inclination has a significant effect on the evolution of $V_{\rm max}$ in similar tidal stirring experiments. Specifically, they found that $V_{\rm max}$ decreased much more strongly in the $i = 0°$ case compared to the $i = 45°$ and $i = 90°$ cases (see Figure 10 of Klimentowski et al. 2009a). This was because the DM halos in the Klimentowski et al. (2009a) experiments were constructed with net angular momentum which was aligned with the angular momentum of the dwarf disk. Moreover, the stellar disks were much more extended compared to those of the present study and, as a result, the stripping of the dwarfs down to the smallest scales of stars did occur at some point during the evolution. In fact, the mass

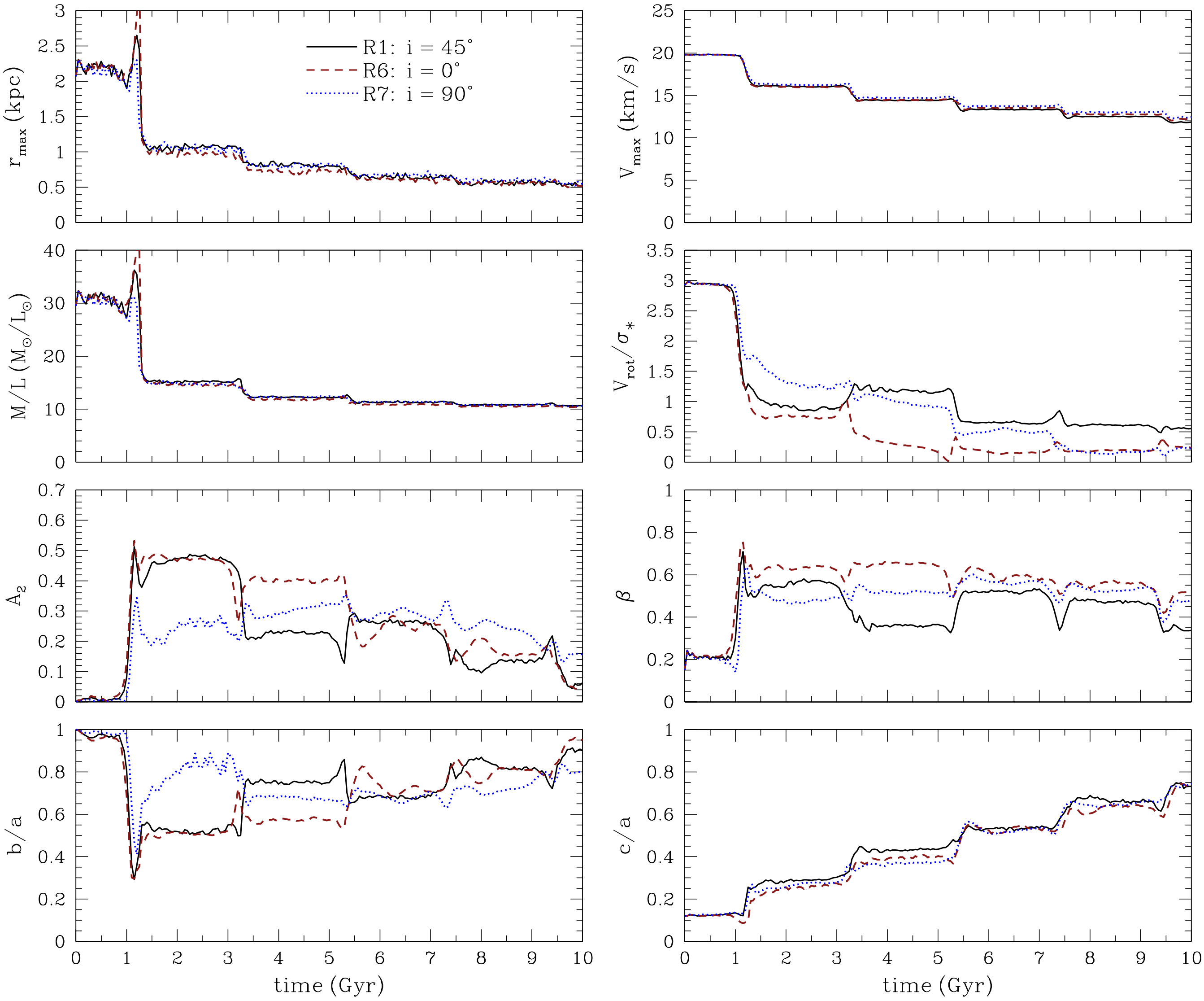

FIG. 5.— Comparison of the evolution of various parameters as a function of time illustrating the dependence of the tidal transformation of disky dwarf galaxies on the inclinations of their disks with respect to the orbital plane, *i*. Results are presented for simulations R1, R6, and R7. For the specific choices of *i* in this set of experiments, the tidal evolution of the rotationally-supported dwarfs inside their host galaxies and the efficiency of their transformation into dSphs depend very weakly on the disk inclination.

within $r_{\rm max}$ of both stars and DM in the Klimentowski et al. (2009a) experiments decreased more in the $i=0°$ case lending support to the previous arguments.

The behavior of the bar strength amplitude A_2 in Figure 5, demonstrates that all dwarfs possess a tidally-induced bar after the first pericentric passage. However, the bar appears to be much weaker in simulation R7, indicating that the tidal forces acting on the dwarf disk were smaller in this case. During subsequent pericentric passages the situation becomes progressively more complex as strong variations in the values of A_2 are observed among the three simulations. At the end of the evolution, the tidally-induced bars are diminished in all cases. Investigating the reasons for the very different evolution of the bars in this set of experiments is clearly beyond the scope of the present paper. However, it is interesting to note that recent targeted numerical experiments have highlighted the importance of stochasticity in the evolution of *isolated* disk galaxies leading to macroscopic differences in the evolution of bars (Sellwood & Debattista 2009). Among the causes for this stochastic evolution, Sellwood & Debattista (2009) identified interference between multiple disk modes, amplification of noise, bending modes, dynamical friction between the bar and the halo, and intrinsic chaos. Obviously, further analysis would be required to determine whether the observed behavior of the bars in this set of simulations can also be attributed to stochasticity and/or possibly to other considerations such as the different initial disk inclinations and resonances.

The final systems in simulations R6 and R7 are characterized by $c/a \approx 0.7$ and $V_{\rm rot}/\sigma_* \approx 0.2$ (see Table 3) and, therefore, would be classified as dSphs according to the criteria described in § 2.5. While the evolution of kinematics and shape is, in broad terms, fairly similar among the three experiments, there are some interesting differences that are worth mentioning. For example, the rotation is lost more quickly in simulation R6 ($i=0°$), where $V_{\rm rot}/\sigma_*$ drops almost to zero at ~ 5 Gyr and remains constant thereafter. The substantial and rapid decrease of $V_{\rm rot}/\sigma_*$ in this experiment is explained by the presence of a very strong bar instability between ~ 1 and ~ 5 Gyr. We also note that in experiment R7 the axis ratio b/a

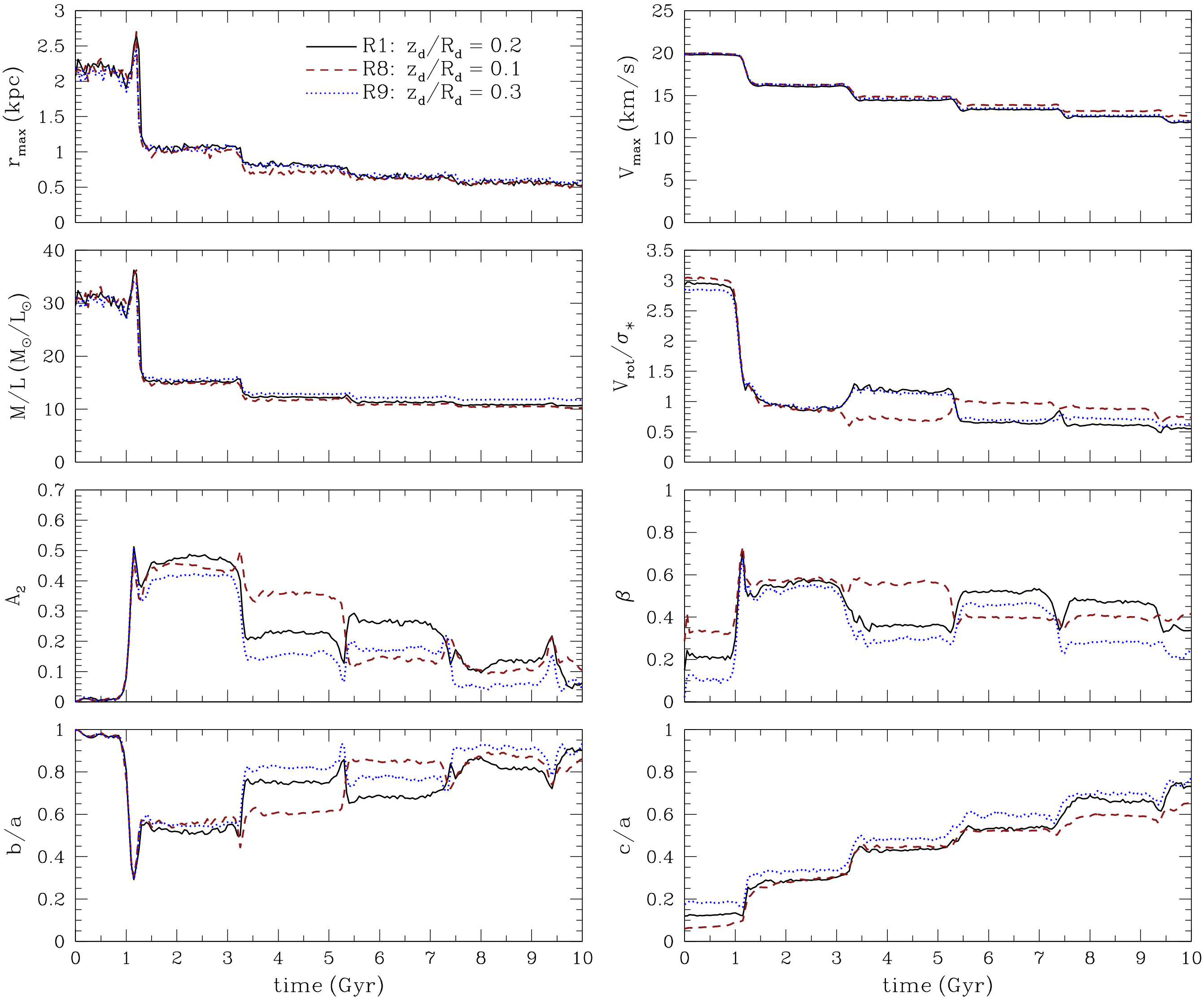

FIG. 6.— Comparison of the evolution of various parameters as a function of time illustrating the dependence of the tidal transformation of disky dwarf galaxies on the thicknesses of their disks. Disk thicknesses are parametrized as z_d/R_d and results are presented for simulations R1, R8, and R9. For the specific choices of z_d/R_d in this set of experiments, the tidal evolution of the rotationally-supported dwarfs inside their host galaxies and the efficiency of their transformation into dSphs are essentially independent of the disk thickness.

remains almost constant with time and significantly different from unity, so that the stellar component is triaxial rather than prolate at early times.

4.1.2. *Disk Thickness*

In this section, we investigate the dependence of the tidal evolution of a disky dwarf on the thickness of its disk. Such an investigation is important for two reasons. First, feedback mechanisms and turbulent motions in dwarf galaxies should be effective in producing thicker systems. Second, the efficiency of tidal heating and the strength of bar instabilities that are both vital for tidal stirring should be different in thicker stellar distributions (e.g., Kazantzidis et al. 2009). To this end, we generated two additional dwarf galaxy models that were identical to D1 except for their scale height, which was chosen equal to $z_d/R_d = 0.1$ and $z_d/R_d = 0.3$. We refer to these models as "D2" and "D3", respectively (see Table 1). The choice for the larger thickness in model D2 reflects the greater importance of pressure support in low-mass galaxies and was motivated by both observations as well as results of recent numerical simulations of the formation of isolated galaxies (Kaufmann et al. 2007), including systems with $V_{max} \approx 20$ km s^{-1} as our default dwarf model. On the other hand, model D3 with the thinner disk was constructed mainly for completeness. After building these two new dwarf models, we placed them on the same orbit as in simulation R1 and followed their tidal evolution inside the host galaxy. We refer to these experiments as "R8" and "R9" (see Table 2) and present the relevant results in Figure 6.

Overall, for the specific choices of initial thickness in this set of experiments, no significant difference in the evolution of the dwarfs can be discerned. Had we adopted thicker and/or thinner disks, such differences may have been more pronounced. The final properties of the systems in simulations R8 and R9 indicate that the remnants can be classified as dSphs (see Table 3).

Figure 6 demonstrates that r_{max}, V_{max}, and the M/L ratio evolve almost identically in the three experiments. A similarly strong bar is induced in all dwarfs after the first pericentric approach. While the thicker disk is initially more isotropic by construction, all three dwarfs exhibit nearly identical values of β between the first and second pericentric approach. At later times, the evolution is somewhat different, but generally the the stellar component of the thicker disk (R9) has a more spherical shape and is characterized by more isotropic orbits. All dwarfs end up mildly triaxial and very similar to the remnant in simulation R1, but their paths to this state are slightly different. Occasionally, departures from the typical trend of decreasing rotational velocity occur (see Figure 11) but they happen at different pericentric passages for different experiments. We come back to this issue in § 5.

4.1.3. *Disk Mass*

In this section, we investigate the degree to which the tidal evolution of a rotationally-supported dwarf is affected by the mass of its disk. In order to ascertain this, we generated two additional dwarf galaxy models that were identical to D1 except for their disk mass, which differed by a factor of 2: $m_d = 0.01$ and $m_d = 0.04$[7]. We refer to these models as "D4" and "D5", respectively (see Table 1). This range of m_d values is consistent with that inferred from exquisite measurements of the mass distribution of nearby dwarfs combining high resolution gas kinematics in the THINGS survey and deep Spitzer photometry (Oh et al. 2010, in preparation). It is also in agreement with results of hydrodynamical simulations of dwarf galaxy formation (e.g., Tassis et al. 2003; Governato et al. 2010). After building these two new dwarf models, we placed them inside the host galaxy on the same orbit as in simulation R1 and followed their tidal evolution. We refer to these experiments as "R10" and "R11" (see Table 2) and present their results in Figure 7.

This figure demonstrates that the mass of their disk has a substantial effect on the tidal evolution of the disky dwarfs. Interestingly, although the initial values of $r_{\rm max}$ are different and smaller for the more massive disks due to the more concentrated mass distribution, at the end of the evolution they converge to nearly the same values. The opposite is true for the mass, as quantified by $V_{\rm max}$. Indeed, the least massive disk increases the susceptibility of the dwarf to tidal effects and the mass loss within $r_{\rm max}$ is larger in this case. Overall, the results presented in Figure 7 indicate that the masses of the dwarfs are differentiated as a result of the tidal evolution.

The M/L ratios, which differed significantly in the beginning, evolve in a fairly different way. The most massive disk, which had the smallest value of M/L initially, is affected most weakly and its M/L ratio decreases only slightly. The weak evolution of the M/L ratio in this case can be attributed to the fact that the initial $r_{\rm max}$ is very small (and remains so until the end of the evolution). As a result, $r_{\rm max}$ probes the central regions of the dwarf, where the reasons that we have indicated in § 3.1 for the preferential stripping of DM over stars do not apply. Indeed, DM particles within this inner region are very unlikely to be on orbits of high enough eccentricity to have apocenters larger than the tidal radius and be stripped. Moreover, the slopes of the density profiles of stars and DM are similar below ~ 1 kpc, implying that the average binding energies of DM and stars do not differ significantly in this region. Interestingly, despite the different evolution, the hierarchy of M/L is preserved; the dwarf which has the highest M/L ratio initially also exhibits the highest M/L ratio in the end.

The mass of the disk affects the evolution of the stellar shape substantially, and to some degree also influences that of the stellar kinematics. Owing to its higher self-gravity, the most massive disk (R11) develops the strongest tidally-induced bar after the first pericentric approach, leading to a pronounced decrease in $V_{\rm rot}/\sigma_*$. We note that the values of A_2 remain the largest in this case until the end of the evolution ($t = 10$ Gyr). As a result, the dwarf galaxy in simulation R11 retains a strongly prolate shape with final values of $c/a \approx 0.6$ and $b/a \approx 0.7$. On the other hand, the dwarf with the least massive disk (R10) remains triaxial rather than prolate for most of the time. Due to the significantly lower disk self-gravity in this case, the tidal shocks heat the disk much more effectively, producing a quite spherical stellar component in the end ($c/a \approx 0.8, b/a \approx 0.9$).

However, the interpretation of the evolution of kinematics is less obvious. While the least massive disk loses its rotation monotonically (see Figure 11), the evolution of its most massive counterpart is more chaotic with occasional strong increases of the rotational velocity, even after two consecutive pericentric passages (third and fourth). We note that this behavior is observed in only one more simulation (R12; see next section) but is not as strong as reported here. Overall, the values of c/a, in conjunction with the fact that $V_{\rm rot}/\sigma_* \lesssim 0.6$, indicate that the final systems in simulations R10 and R11 would be classified as dSphs (see Table 3).

4.1.4. *Disk Scale Length*

This section addresses the extent to which the tidal evolution of a disky dwarf is influenced by the radial scale length of its disk, R_d. For this purpose, we generated two additional dwarf galaxy models that were identical to D1 except for the scale lengths of their disks. We reiterate that the disk scale length is not a free parameter in our simulations, but rather is derived via the semi-analytic galaxy formation model of Mo et al. (1998). Because of this choice our method requires us to assign values to the halo spin parameter λ in order to derive the scale length of the dwarf disk, despite the fact that the halos of our dwarfs are constructed with no net angular momentum.

Recall that we chose $\lambda = 0.04$ for our reference dwarf model D1, close to the median value of halo spins found in cosmological N-body simulations (e.g., Bullock et al. 2001a; Shaw et al. 2006; Macciò et al. 2007; Bett et al. 2007). To investigate the effect of the disk scale length, we initialized two additional dwarf models with $\lambda = 0.024$ and $\lambda = 0.066$. These values correspond to the 1σ deviations from the median λ, assuming a log-normal distribution with $\lambda_{\rm med} = 0.04$ and $\sigma_\lambda = 0.5$, in agreement with the previous cosmological studies. We refer to these dwarf models as "D6" and "D7", respectively, and list their disk scale lengths in Table 1. In the corresponding experiments "R12" and "R13", we placed these dwarfs on the same orbit as in simulation R1 and followed their tidal evolution inside the host galaxy. Note that for consistency we have kept the thickness z_d/R_d in this set of experiments constant. As a result, the disk becomes larger (smaller) in both the radial and vertical direction when λ is increased (decreased). The relevant results are presented in Figure 8 which demonstrates that the remnant dwarfs in this

---

[7] We note that formally, according to the model of Mo et al. (1998), varying the disk mass and keeping the other relevant parameters (M_h, λ, and c) constant would result in different scale lengths for the dwarf disk. However, for consistency and in order to isolate the effect of a single parameter on the tidal evolution of the dwarfs, we adopt identical disk scale lengths in this set of experiments. The same convention applies to the simulations described in § 4.2.1 in which we construct dwarf models with different halo concentration parameters.

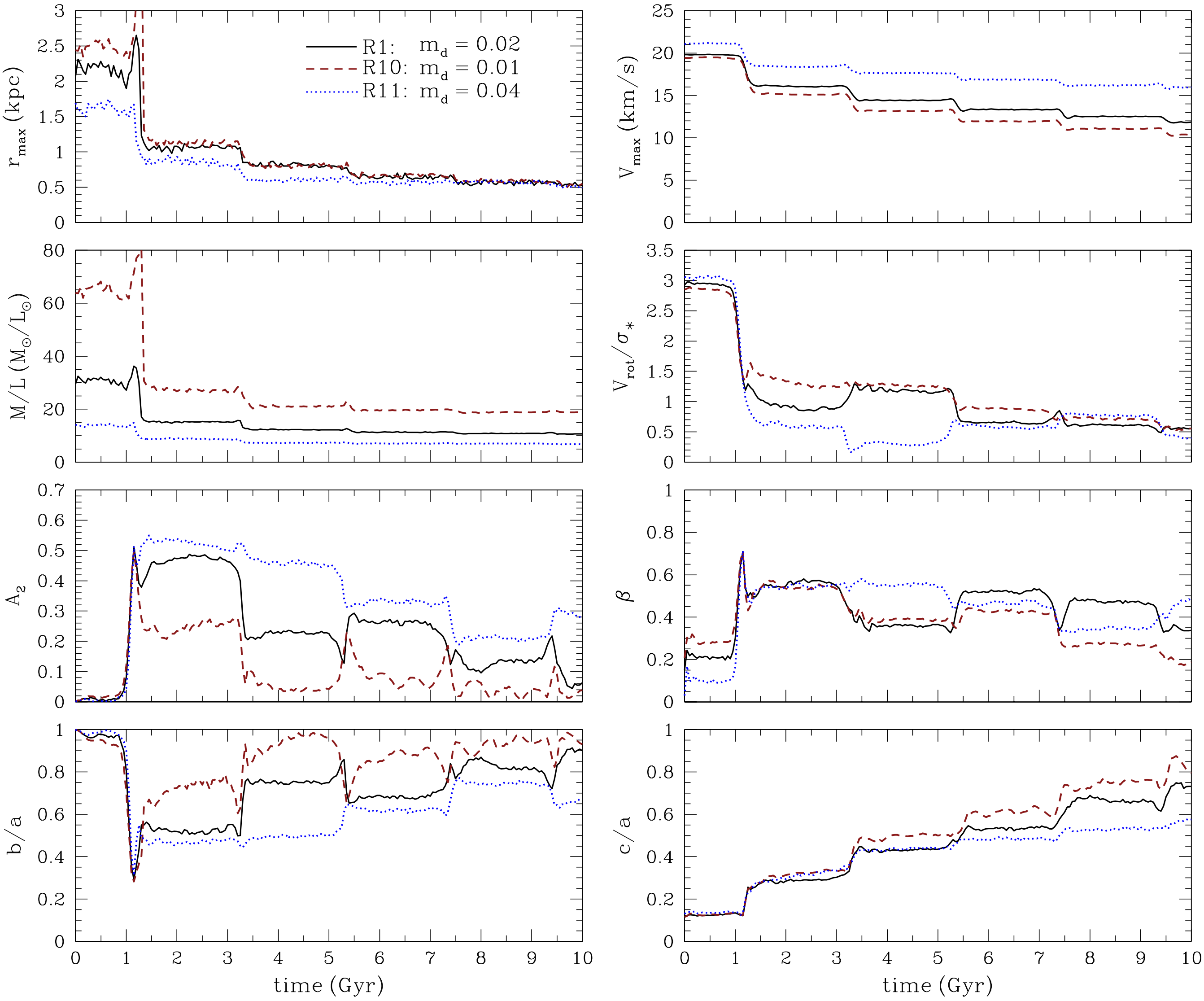

FIG. 7.— Comparison of the evolution of various parameters as a function of time illustrating the dependence of the tidal transformation of disky dwarf galaxies on the masses of their disks. Disk masses are parametrized as a given fraction, m_d, of the halo mass, M_h, and results are presented for simulations R1, R10, and R11. Rotationally-supported dwarfs with less massive disks exhibit stronger tidal evolution inside their host galaxies and the efficiency of their transformation into dSphs is augmented significantly.

set of simulations would be classified as dSphs (see Table 3).

This figure shows that the scale length of the dwarf disk is a parameter that affects significantly the tidal evolution of the disky dwarfs. The initial value of $r_{\max}$ is smaller for the more compact disk in simulation R12 and it remains so until the end of the evolution. This experiment does not show the characteristic temporary increase of $r_{\max}$ at the first pericentric approach observed in the reference simulation R1. This is because the more compact disk diminishes the ability of the host tidal field to distort the inner regions of the dwarf galaxy. As expected, the mass loss within $r_{\max}$ measured by the decreasing value of $V_{\max}$ is more pronounced for the more extended disks with a larger value of λ. This is simply a consequence of the fact that larger disk scale lengths make the potential well of the dwarf shallower and decrease the total binding energy in the inner parts.

As expected, the dwarf with the most extended disk (R13) has a larger initial value of the M/L ratio within $r_{\max}$. Due to the dissimilar values of R_d, the stripping of the stars proceeds differently in this set of experiments and, as expected, is much more effective in the case of the most extended disk. This differential stripping of the stars manifests itself in the evolution of the M/L ratio. Although the initial values of the M/L ratios are not very different, the final value of M/L is much larger in simulation R13. Interestingly, the M/L ratio in this experiment starts to increase during the intermediate stages of the evolution ($t \sim 5$ Gyr). Such a behavior is similar to that reported in § 3 for experiments R2 and R4, even though this transition occurred earlier there and the final M/L values obtained were slightly lower. We discuss this issue in § 5. Overall, Figure 8 indicates that the M/L ratios are differentiated as a result of the tidal evolution.

Evidently, the size of the disk affects substantially the evolution of the stellar shape, and to some degree also influences that of the stellar kinematics. The behavior of the Fourier component A_2 after the first pericentric passage is slightly misleading. Indeed, both lower and larger λ cases show similar values of this parameter, but for different reasons. While the most compact disk (R12) retains an oblate shape, the most extended one (R13) is triaxial, but neither shows such

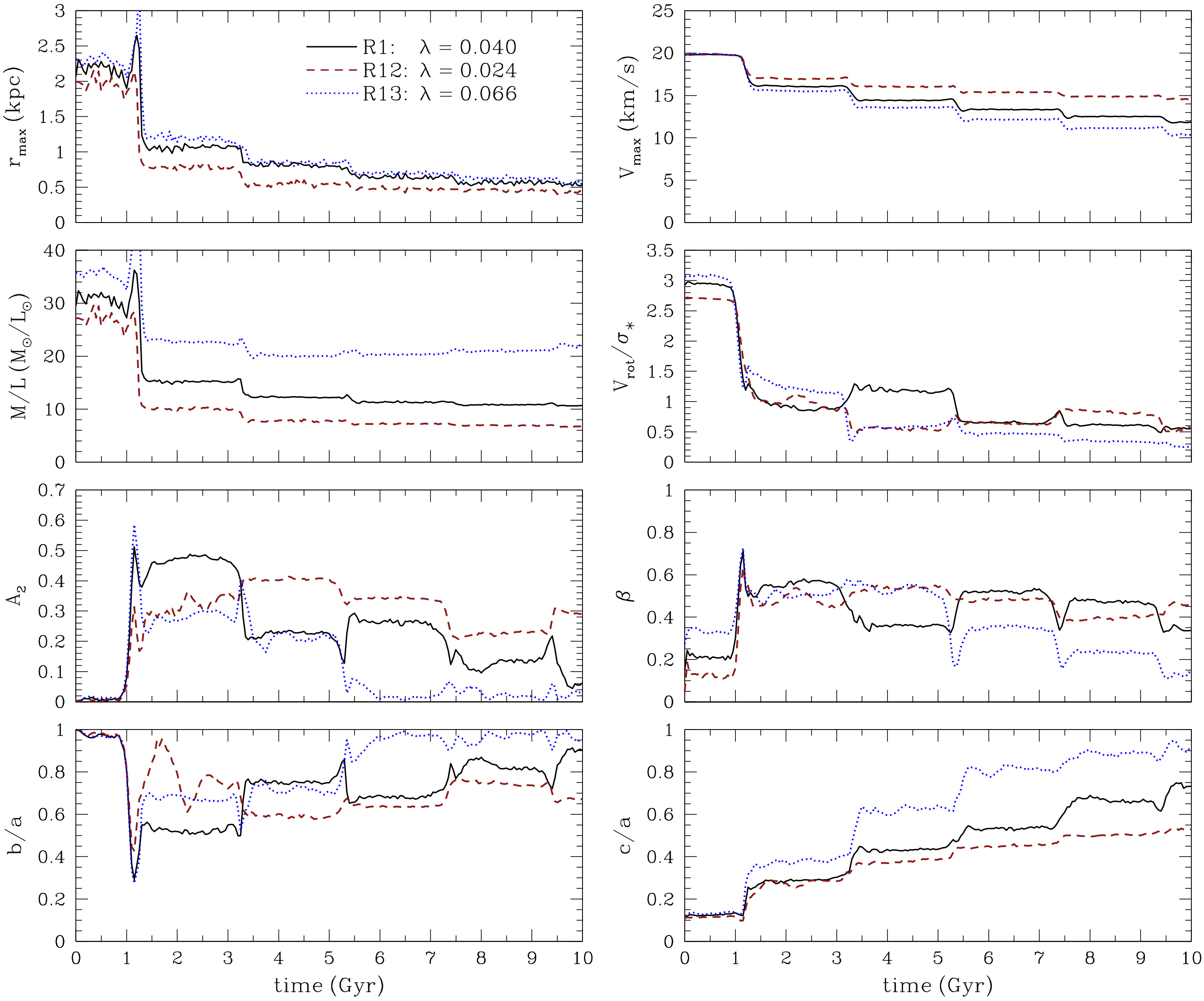

FIG. 8.— Comparison of the evolution of various parameters as a function of time illustrating the dependence of the tidal transformation of disky dwarf galaxies on the radial scale lengths of their disks, R_d. Results are presented for simulations R1, R12, and R13. The spin parameters of the dwarf DM halos, λ, used to determine the disk scale lengths in this set of experiments are indicated in the labels (see text for details). The corresponding values of R_d for the three different choices of λ are equal to $R_d = (0.41, 0.25, 0.66)$ kpc, respectively (see Table 1). Rotationally-supported dwarfs with more extended disks experience stronger tidal evolution inside their host galaxies and the efficiency of their transformation into dSphs is enhanced substantially.

a strong bar mode as our reference experiment R1. The situation changes radically after the second pericentric passage. On the one hand, owing to its higher self-gravity, the low-λ dwarf forms a fairly strong bar and remains prolate until the end of the evolution with final values of $c/a \approx 0.5$ and $b/a \approx 0.7$. In fact, the remnant in this experiment exhibits the least spheroidal shape of all our classified dSphs, highlighting the resilience of the most compact disk to tidal heating. This system could be the analogue of the most elongated dSphs in the LG such as Ursa Minor (Irwin & Hatzidimitriou 1995). On the other hand, tidal effects are quite efficient in the case of the high-λ disk with the lowest self-gravity and cause its rapid transformation into a nearly isotropic ($\beta \approx 0.1$) and spherical stellar component ($b/a \approx c/a \gtrsim 0.9$) that retains little rotation ($V_{\rm rot}/\sigma_* \lesssim 0.3$).

4.2. *Varying the Parameters of the Halo*

4.2.1. *Halo Concentration*

In this section, we investigate the degree to which the tidal evolution of a disky dwarf is affected by the concentration parameter of its DM halo, c. To this end, we constructed two additional dwarf galaxy models that were identical to D1 except for the halo concentration parameters. Recall that we chose $c = 20$ for our reference model D1, close to the median concentration value for $z = 0$ cosmological halos of mass $\sim 10^9 M_\odot$ (e.g., Bullock et al. 2001b; Macciò et al. 2007). To investigate the effect of the halo concentration on our results, we constructed two additional dwarf models with $c = 10$ and $c = 40$. These values roughly correspond to the 2σ deviations from the median $c = 20$, in accordance with the previous cosmological studies[8]. We refer to these dwarf models as “D8” and “D9”, respectively, and list their structural parameters in

---

[8] We note that $c = 40$ is markedly incompatible with results of the distribution of DM in present-day LSB and dIrr galaxies through the modeling of rotation curves (see the recent review of de Blok 2010 for a discussion on this issue). Nevertheless, even though it is clearly inconsistent with observations, we decided to consider this limiting case simply for completeness.

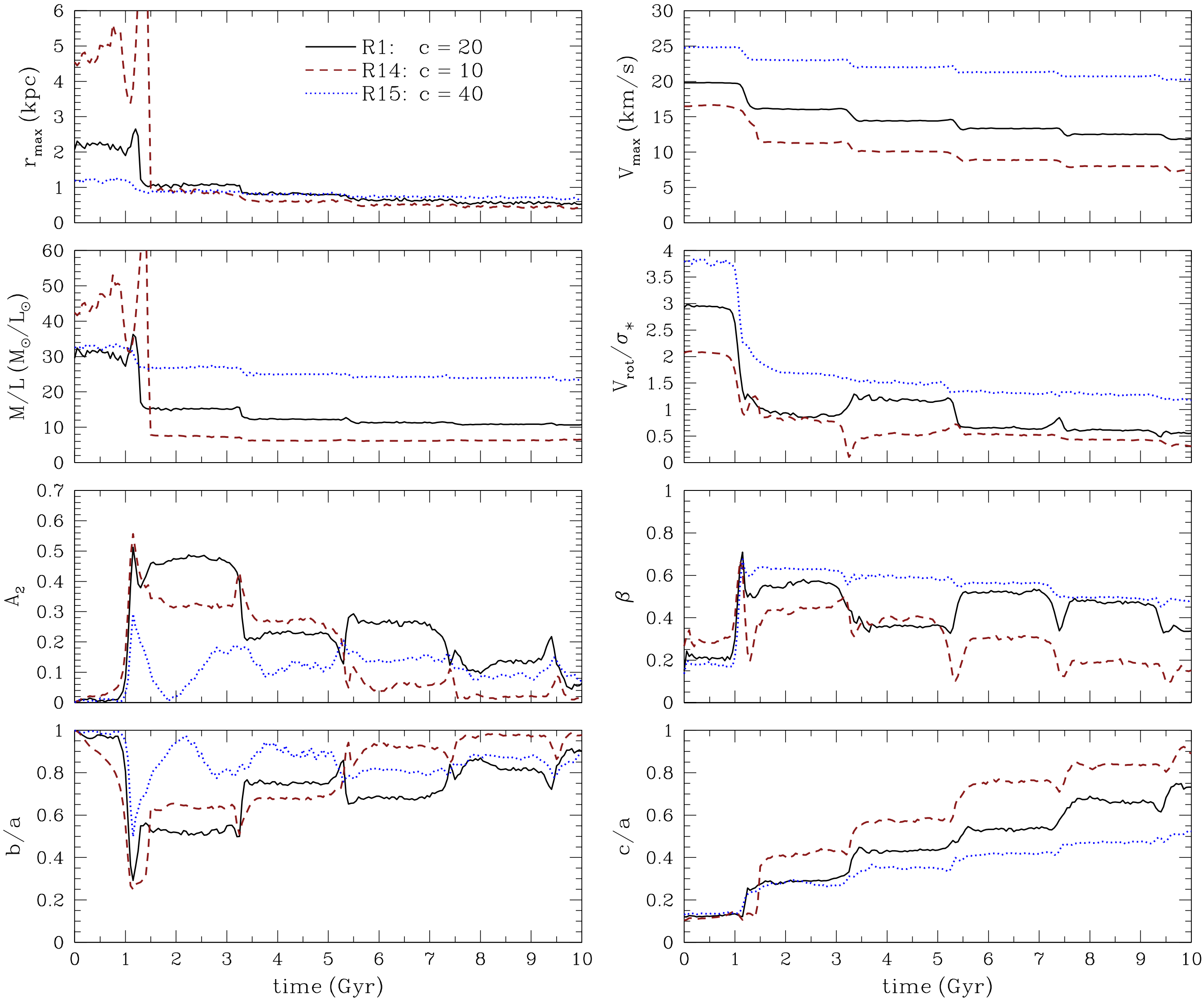

FIG. 9.— Comparison of the evolution of various parameters as a function of time illustrating the dependence of the tidal transformation of disky dwarf galaxies on the concentration parameters of their DM halos, c. Results are presented for simulations R1, R14, and R15. Rotationally-supported dwarfs embedded in less concentrated DM halos exhibit stronger tidal evolution inside their host galaxies and the efficiency of their transformation into dSphs is increased considerably.

Table 1. In the corresponding experiments "R14" and "R15", we placed these dwarfs on the same orbit as in simulation R1 and followed their tidal evolution inside the host galaxy. Figure 9 contains the results of these simulations.

As expected, the less concentrated dwarf is characterized by a larger initial $r_{\rm max}$. As in the case of the experiments with different disk masses (R10, R11), after the first pericentric approach the values of $r_{\rm max}$ converge. Interestingly, at late times the hierarchy is even reversed (the dwarf with the most concentrated halo exhibits the largest $r_{\rm max}$) but the differences are not significant. As demonstrated by the weakest decrease in the value of $V_{\rm max}$, the most concentrated halo increases the resilience of the dwarf galaxy to tides and mass loss. Since the higher concentration makes the potential well of the dwarf deeper, this effect is similar to that of the larger disk mass discussed in § 4.1.3. The effect on the M/L ratio is, however, the opposite; although the M/L ratio within $r_{\rm max}$ was initially larger for the $c = 10$ case it soon becomes the smallest. This is because the DM particles are much more weakly bound in this case and, as a result, are stripped fairly efficiently. After a period of $t = 10$ Gyr inside the host galaxy, the M/L ratios of the dwarfs with the most and the least concentrated halo differ by a factor of ~ 4. The weak evolution of the M/L ratio in simulation R15 is of similar origin to that of the experiment with the most massive disk (R11).

The susceptibility to tides of the low-concentration dwarf in experiment R14 also manifests itself in the evolution of the shape and kinematics. The stellar component in this experiment evolves rapidly and becomes nearly spherical rather quickly with a final $c/a \approx 0.9$. The stronger effect of the tidal shocks in this case reflects the fact that the dwarf responds more impulsively to the tidal perturbation owing to its lower characteristic densities and, correspondingly, longer internal dynamical times. After the first pericentric passage, a strong bar develops in the dwarf disk ($A_2 \gtrsim 0.3$) and the $V_{\rm rot}/\sigma_*$ ratio starts to decrease, reaching a final value of $V_{\rm rot}/\sigma_* \approx 0.3$. The structure of the remnant in this case would resemble that of observed dSphs.

On the other hand, the stellar component of the high-concentration dwarf retains its disky shape, since it is less affected by tides. This is similar to the cases of simulations R3 and R5 where the dwarf galaxies experienced weaker tidal forces due to the larger pericentric distances. In experiment R15, the final axis ratio is higher ($c/a \approx 0.5$) but still the stellar component remains oblate. Most importantly, as demonstrated by the very low values of A_2 throughout the evolution, a bar does not form in this case. As a result, the angular momentum content of the dwarf does not decrease efficiently and the $V_{\rm rot}/\sigma_*$ ratio remains larger than unity until the end of the simulation. The absence of the bar in this case is consistent with results of numerical experiments showing that high values of halo concentration suppress the formation of bars in isolated disk galaxies embedded in CDM halos (Mayer & Wadsley 2004). To summarize, experiment R15 constitutes the only case where a rotationally-supported dwarf is placed on the reference orbit of simulation R1 and neither develops a bar nor yields a dSph. This lends further support to the fact that bar formation and the formation of dSphs are intimately linked in the context of the tidal stirring model.

4.2.2. *Halo Mass*

In this section, we explore the degree to which the tidal evolution of a disky dwarf depends on the mass of its DM halo, M_h. Such a dependence may be expected as various effects, including the strength of tidal shocks as well as dynamical friction, will be affected by the halo mass. For this purpose, we generated two additional dwarf galaxy models that were identical to D1 except for the masses of their halos, which differed by a factor of 5: $M_h = 0.2 \times 10^9 M_\odot$ and $M_h = 5 \times 10^9 M_\odot$. This mass range roughly corresponds to the range of initial subhalo masses that were accreted since $z \lesssim 2$ and survived until the present time in the LG simulation of Klimentowski et al. (2010). We refer to these models as "D10" and "D11", respectively (see Table 1). The motivation behind using the same values for m_d, z_d/R_d, c, and λ in these models as in the reference one (D1) was imposed mainly by simplicity. However, we do note that our choices are reasonable given the scatter in m_d (e.g., Jimenez et al. 2003; Tassis et al. 2003), z_d/R_d (e.g., Dalcanton et al. 2004; Kaufmann et al. 2007), and c (e.g., Bullock et al. 2001b; Macciò et al. 2007) for galaxies in this mass range, and the fact that the distribution of halo spins shows no dependence on halo mass (e.g., Macciò et al. 2007). In the corresponding experiments "R16" and "R17", we placed dwarf models D10 and D11 on the same orbit as in simulation R1 and followed their tidal evolution inside the host galaxy. Figure 10 presents the results of these simulations.

As a result of our choices for the initial structural parameters of the dwarf galaxies in this set of experiments, $r_{\rm max}$ is larger for the dwarf with the most massive halo (R17). This is simply because $r_{\rm max} \approx 2.16 R_h/c$ for the NFW profile, where R_h in our modeling corresponds to the cosmologically motivated virial radius of the system ($R_h \approx r_{\rm vir}$). Figure 10 shows that $r_{\rm max}$ remains larger for the most massive dwarf until the end of the evolution. We emphasize that the pericentric passages which are marked by sudden drops in $V_{\rm max}$ do not occur at the same time for all three dwarfs, despite the fact that the orbital parameters were initially identical. Specifically, the orbit of the most massive dwarf becomes progressively much tighter with continuously reduced apocentric distances, leading to a shorter orbital time (see Table 3). This is due to the effect of dynamical friction, whose strength depends strongly on the mass of the moving body.

Interestingly, after 10 Gyr of evolution inside the host, all three dwarf galaxies lose approximately the same fraction of their initial mass within $r_{\rm max}$ ($\sim 90\%$) and their $V_{\rm max}$ decreases by approximately the same factor of ~ 1.7. This is intriguing given that mass loss is generically affected, among other things, by the depth of the potential well of the dwarf and the details of the dwarf orbit (e.g., the pericentric distance) around the primary galaxy. We note that by construction the three dwarfs have approximately equal average densities within $r_{\rm max}$, and therefore comparable dynamical times at $r_{\rm max}$. Using this fact coupled with some order-of-magnitude calculations it is possible to gain qualitative insight as to the relative evolution of $V_{\rm max}$ and mass within $r_{\rm max}$ is similar in simulations R1, R16, and R17.

According to the tidal approximation of the impulse (which should be valid in our simulations for the purposes of dimensional analysis), the energy injected at each pericentric passage is given by $\Delta E \propto M_{\rm host}^2 M R^2 V_{\rm rel}^{-2}$, where $M_{\rm host}$ is the mass of the host, M denotes the mass of the dwarf, R is a characteristic radius of the dwarf (related to $r_{\rm max}$), and $V_{\rm rel}$ is the relative velocity between the two galaxies at the pericenter of the orbit (Spitzer 1958; Binney & Tremaine 2008). Since, as noted above, the average density within $r_{\rm max}$ is roughly constant among the dwarfs, we have $R \propto M^{1/3}$ in the three different models. Given that $M_{\rm host}$ is the same and $V_{\rm rel}$ is fairly similar in the three experiments considered here, it follows that $\Delta E \propto M^{5/3}$. By virtue of the virial theorem, the energy content of the dwarf should scale as $E \propto GM^2/R \propto M^{5/3}$, and also $E \propto MV^2$, where V is a characteristic velocity of particles within the dwarf (related to $V_{\rm max}$). Hence, the fractional increase in energy caused by the tidal shocks, $\Delta E/E$, is roughly constant, explaining why the $V_{\rm max}$ and $M_{\rm max}$ of the dwarfs in simulations R1, R16, and R17 evolve in a fairly similar way. We stress that similar conclusions would be reached had we used extensions of the standard impulse approximation appropriate for perturbers with extended mass distributions as well as for satellites that move on either straight-path or eccentric orbits (Gnedin et al. 1999). This is because such extensions are characterized by analogous scalings of the relevant variables in our calculations above.

The M/L ratios are similar in all cases and decrease monotonically with time reaching a value of $\sim 10 M_\odot/L_\odot$ in the end of the evolution. The behavior of kinematics shows an interesting feature. While the values of $V_{\rm rot}/\sigma_*$ and β were quite different for the three models initially, they become very similar after the first pericentris passage and remain so until the end of the evolution. The evolution of the shape shows a more clear trend with mass. After the first pericentric approach, the bar is stronger in the most massive dwarf compared to that of the default case and it remains so until the end of the evolution. This simply reflects the higher self-gravity of the disk in simulation R17. On the other hand, while the least massive dwarf remains disky during the entire evolution, its axis ratio c/a increases significantly with a final value of $c/a \approx 0.75$. The dwarf remnants in simulations R16 and R17 are characterized by $c/a \approx 0.7$ and $V_{\rm rot}/\sigma_* \lesssim 0.7$ (see Table 3) and hence would be classified as dSphs.

A last point of interest is that simulation R16 constitutes the only case where the formation of a dSph is not associated with the presence of a tidally-induced bar. Indeed, the increase of the bar amplitude, A_2, in this case is only temporary and occurs at the first pericentric passage when the dwarf is strongly elongated by tidal forces. The absence of a bar is consistent with the fact that the disk of this dwarf ex-

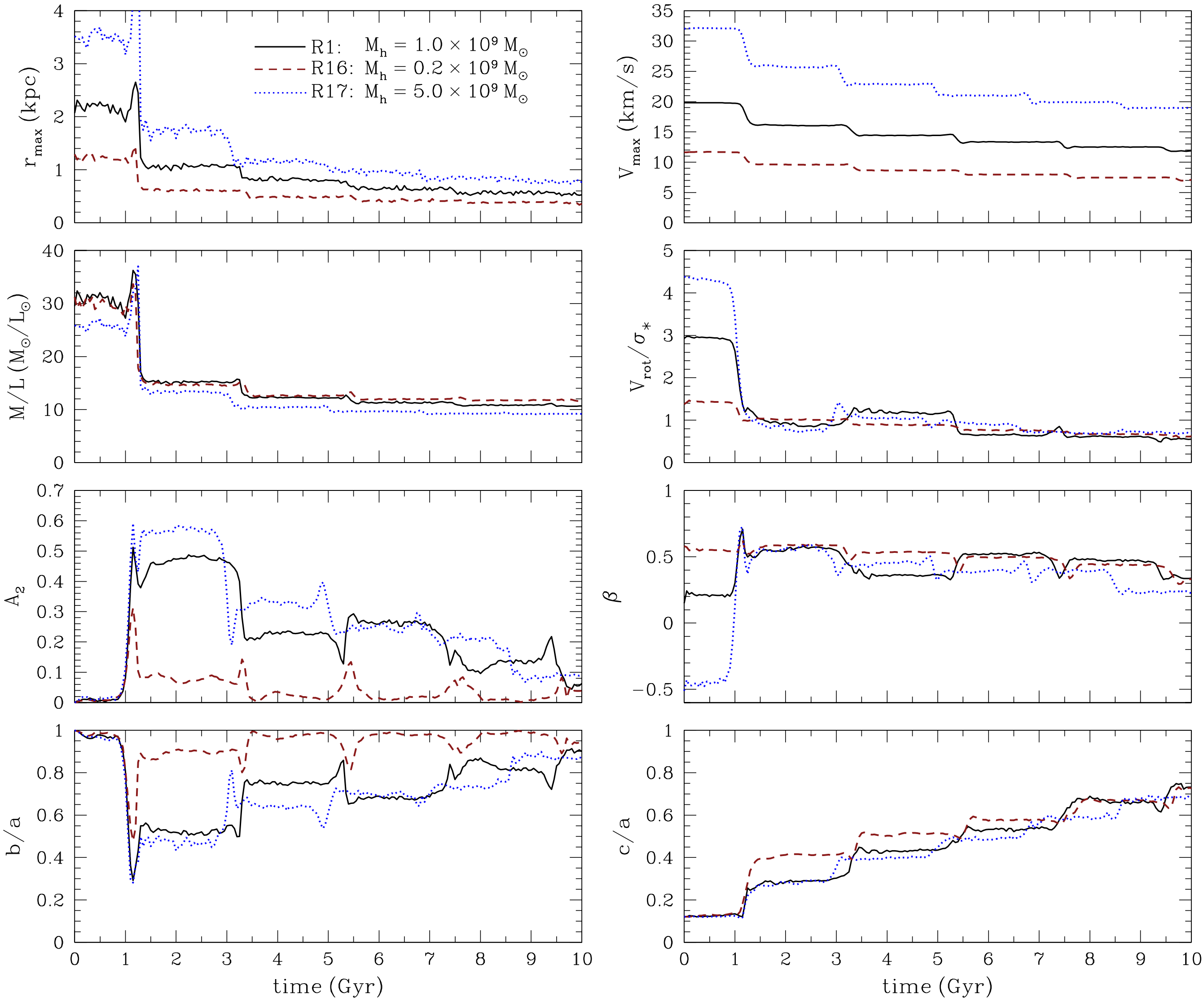

FIG. 10.— Comparison of the evolution of various parameters as a function of time illustrating the dependence of the tidal transformation of disky dwarf galaxies on the masses of their DM halos, M_h. Results are presented for simulations R1, R16, and R17. Owing to the interplay between the effects of dynamical friction and the depth of the potential well, rotationally-supported dwarfs embedded in DM halos of substantially different mass display similar tidal evolution inside their host galaxies and the efficiency of their transformation into dSphs is of comparable magnitude.

hibits the highest value of the Toomre stability parameter (see Table 1). Bar formation causes rotational motion to be transformed into radial motion and thus, in conjunction with tidal heating which also increases the velocity dispersion, is intimately linked to the decrease of V_{rot}/σ_* required for the transformation to a pressure-supported dSph (Mayer et al. 2001a; Debattista et al. 2006). In the case of the least massive dwarf, the initial V_{rot}/σ_* within r_{max} is rather low ($V_{rot}/\sigma_* \lesssim 1.5$) and therefore the bar stage is not necessary to decrease it considerably to levels that are appropriate for dSphs ($V_{rot}/\sigma_* \lesssim 1$). The decrease of V_{rot}/σ_* in the dwarf of experiment R16 occurs almost exclusively at pericentric approaches and is driven by the decrease in V_{rot} (see Figure 11). The decrease in rotational velocity within r_{max} is simply caused by tidal heating which perturbs the circular orbits of the disk stars converting part of the rotation (ordered motions) in the disk to random motions. It is worth noting that in the reference simulation R1, for example, the combination of tidal heating and the tidally-induced bar lead to a decrease in the V_{rot}/σ_* of the dwarf by approximately a factor of 5, illustrating the importance of bar formation in reducing the initial high values of V_{rot}/σ_* appropriate for disky dwarfs to those characteristic of dSphs.

5. DISCUSSION

We begin this section by investigating the $V_{max} - \sigma_*$ relation in our simulations, which is of particular interest for the missing satellites problem. In § 5.2 and § 5.3, we explore the reasons for the increasing rotational velocity and the increasing M/L ratio, respectively, observed in some of our experiments. In § 5.4, we elucidate the fundamental orbital parameter that influences the transformation of disky dwarfs into dSphs and thus the efficiency of the tidal stirring mechanism. In § 5.5, we discuss some additional implications related to the findings of this work. Lastly, in § 5.6 we conclude with a few words of caution and a discussion of promising directions for future work that may lead to more conclusive statements about the role of environmental processes in shaping the nature of dwarf galaxies in environments such as that of the LG.

5.1. $V_{max} - \sigma_*$ *Relation*

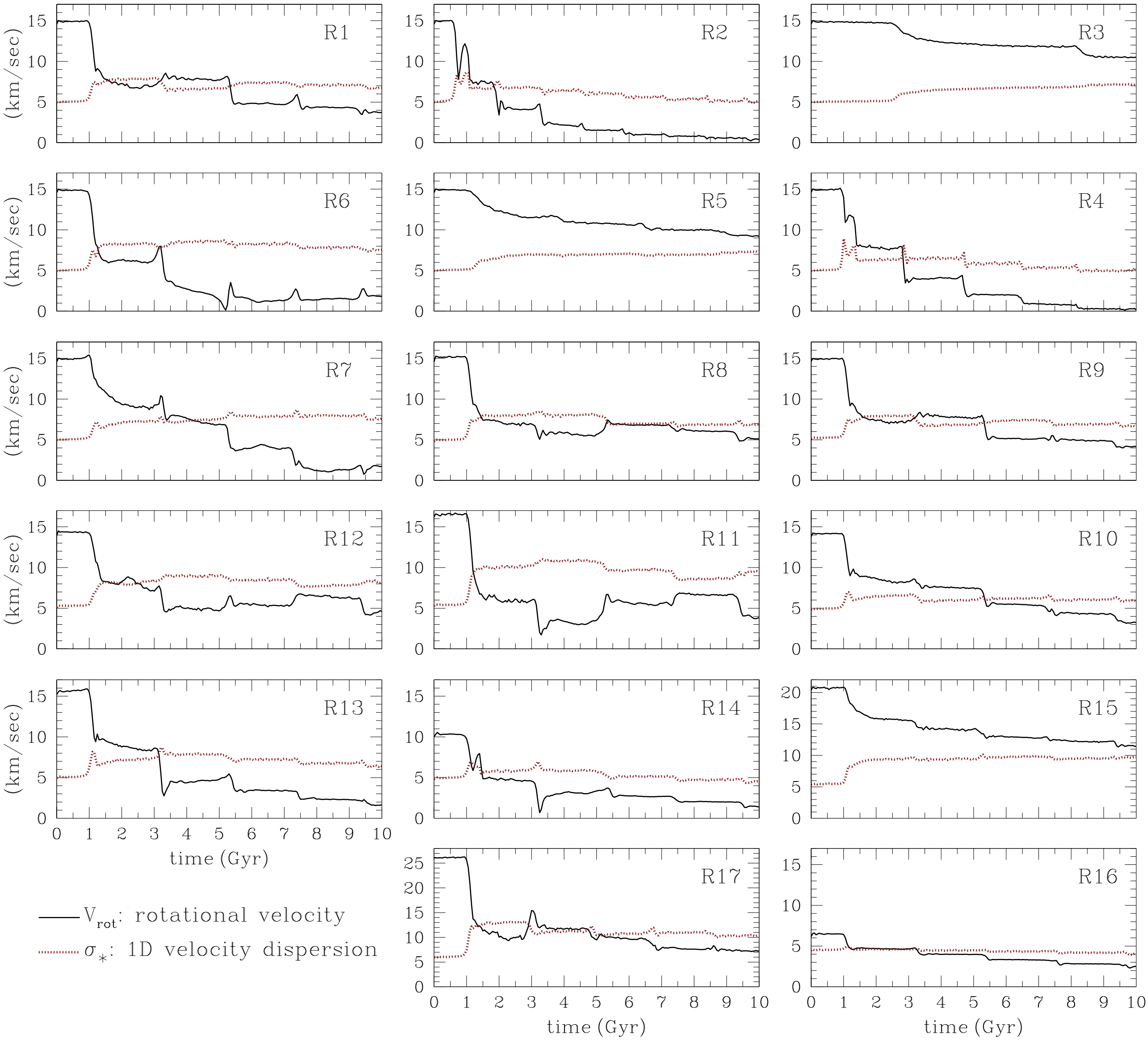

FIG. 11.— Evolution of the stellar rotational velocity, $V_{\rm rot}$, (solid lines) and the one-dimensional stellar velocity dispersion, σ_*, (dotted lines) of the dwarfs in simulations R1-R17. Parameters $V_{\rm rot}$ and σ_* are computed within $r_{\rm max}$. The repeated action of tidal forces exerted by the host galaxy decreases the ratio of $V_{\rm rot}/\sigma_*$, gradually transforming the initially rotationally-supported disky dwarfs to pressure-supported stellar systems dominated by random motions.

Here we investigate the relation between the one-dimensional, central stellar velocity dispersion, σ_*, and the maximum circular velocity, $V_{\rm max}$, in our simulated dwarf galaxies. The knowledge of this relation is crucial, particularly in the context of the missing satellite problem (Moore et al. 1999; Klypin et al. 1999), as it reflects the link between observable properties and dark halo properties in dwarf galaxies. One of the main difficulties intrinsic to this problem lies in the fact that the mapping between $V_{\rm max}$ and σ_*, the latter being a directly observable quantity, depends sensitively on the assumed density structure of the DM halo of the dwarf. For example, adopting an isothermal halo model with a flat circular velocity profile to estimate $V_{\rm max}$ would yield $V_{\rm max} \sim \sqrt{2}\sigma_*$ (e.g., Moore et al. 1999), while assuming an isotropic stellar velocity dispersion tensor would result in $V_{\rm max} \sim \sqrt{3}\sigma_*$ (e.g., Klypin et al. 1999). Given the uncertainties regarding the conversion of σ_* to $V_{\rm max}$ (see Kravtsov 2010 for a thorough discussion on this issue), it is interesting to check the general validity of these assumptions directly in our simulations. The relevant analysis is presented in Figure 12.

The left panel of this figure shows the relation between the one-dimensional stellar velocity dispersion and the maximum circular velocity $V_{\rm max}$ in the final stages of all simulated dwarfs (t = 10 Gyr). We remind the reader that the velocity dispersion profiles of our remnants do not strongly vary with radius and thus our dispersion measurements are close to the central values commonly used by observers. For the purposes of this presentation, we have also replaced σ_* used throughout the paper by $\sigma'_* \equiv [(\sigma_r^2 + \sigma_\theta^2 + \sigma_\phi'^2)/3]^{1/2}$, where $\sigma_\phi'^2 = \sigma_\phi^2 + V_{\rm rot}^2$. This is because rotation was found to be important in some of the remnants, specifically those of simulations R3, R5, and R15 which do not produce dSphs, and thus

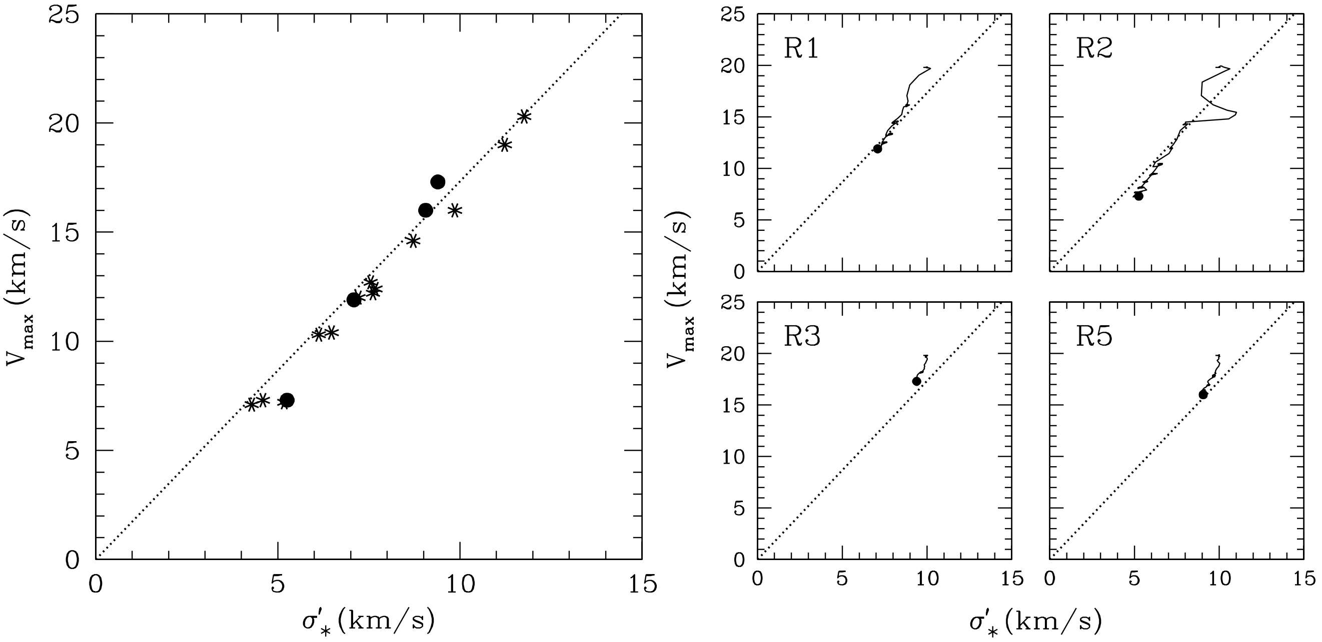

FIG. 12.— Relation between the maximum circular velocity, $V_{\rm max}$, and the one-dimensional, central stellar velocity dispersion, σ'_*, of the dwarfs in our simulations. The latter quantity corresponds to the line-of-sight central velocity dispersion measured in the observations and includes the contribution of rotation (see text for details). Left: The data points indicate the values calculated in the final stages of the dwarfs (t = 10 Gyr) in experiments R1-R17, and the dotted line is intended to identify a slope of $\sqrt{3}$ and is not a fit to the data. The formal best-fit slope differs by less than $\sim$ 4% from $\sqrt{3}$. Circles show results for specific experiments R1, R2, R3, and R5 discussed in the right panel. The relation $V_{\rm max} = \sqrt{3}\sigma_*$, adopted by Klypin et al. (1999) to map the observed central stellar velocity dispersion of dSphs to the maximum circular velocities of their halos, is well justified within the context of the tidal stirring model. Right: Four examples of the evolution of individual dwarf galaxies on the $V_{\rm max} - \sigma'_*$ plane (solid lines). Results are shown for representative simulations R1, R2, R3, and R5, where the same dwarf model (D1) was placed on different obits. R1 is our reference experiment. R2 produces one of the most strongly evolved dwarfs in our simulations, while R3 and R5 correspond to the least tidally-transformed systems in our experiments. In all panels, the filled circles mark the end of the evolution inside the host (t = 10 Gyr). As in the left panel, dotted lines correspond to slopes of $\sqrt{3}$. The dwarf galaxies exhibit fairly different types of trajectories depending on their orbital parameters and can move substantially on the $V_{\rm max} - \sigma'_*$ plane over the course of their evolution inside their hosts.

it had to be included in the calculation of their velocity dispersion. We stress that this modification is not necessary in the majority of cases where dSphs with minimal intrinsic rotation are formed.

The panel demonstrates a strong correlation between σ'_* and $V_{\rm max}$ in all dwarf remnants regardless of their morphology and kinematics. This is not entirely unexpected as both of these quantities are measures of the depth of the potential of the dwarfs. Interestingly, the relation $V_{\rm max} = \sqrt{3}\sigma_*$, formally valid for a tracer stellar population with an isotropic velocity dispersion tensor, reproduces the results of the simulations remarkably well (see also Klimentowski et al. 2009a). Indeed, the formal best-fit slope of the $V_{\rm max} - \sigma'_*$ relation in our simulations differs by less than $\sim$ 4% from $\sqrt{3}$. Given the wide range of orbital and structural parameters that we adopted for the progenitor disky dwarfs in our experiments, this finding is particularly noteworthy. We stress that the relation between σ_* and $V_{\rm max}$ is derived by directly probing the stellar kinematics of the simulated dwarfs. It may thus be reliably used to map the observed central stellar velocity dispersions to halo maximum circular velocities in dwarf galaxies when addressing the missing satellites problem.

Overall, we conclude that moderate conversion factors between σ_* and $V_{\rm max}$ such as those originally adopted by Moore et al. (1999) and Klypin et al. (1999) to formulate the missing satellites problem were reasonable. Recently, using controlled simulations of subhalo evolution, Peñarrubia et al. (2008) have argued in favor of much larger conversion factors in observed MW satellites ($\approx 2-3$; see, however, Kravtsov 2010 for a discussion of possible caveats in the approach of Peñarrubia et al. 2008). We stress that our results should at least hold for dwarf galaxies that have moderate M/L ratios as our final systems (e.g., Leo I or Fornax). Dwarfs that are much more DM dominated (e.g., Draco or Ursa Minor) may, in principle, exhibit a different relation between σ_* and $V_{\rm max}$ owing to their (possibly) different formation and evolutionary histories (e.g., Mayer et al. 2007).

Furthermore, the relation between $V_{\rm max}$ and σ_* reported here is valid for dwarfs that were originally embedded in cuspy NFW-like DM halos, like the ones employed in the present study, and would likely be different with other halo density structures. Indeed, if the halo density profiles in the progenitor disky dwarfs were shallower than NFW in the inner regions that are probed by the stars (e.g., Governato et al. 2010), the resulting circular velocity profiles will still be slowly rising within the luminous radius, and the conversion factor between σ_* and $V_{\rm max}$ can be substantially larger ($\gtrsim 2-4$; see, e.g., Stoehr et al. 2002).

Our findings are corroborated by a number of studies. For example, applying Jeans modeling and varying the anisotropy in the velocity distribution of stars, Kazantzidis et al. (2004b) found that the stellar kinematics of Fornax ($\sigma_* \sim 11 - 13\,{\rm km\,s^{-1}}$) and Draco ($\sigma_* \sim 8 - 10\,{\rm km\,s^{-1}}$), can be reproduced in halos with $V_{\rm max} \sim 20-30\,{\rm km\,s^{-1}}$, which would imply $\sigma_*/V_{\rm max} \sim 0.3-0.65$. Similar results were obtained by Zentner & Bullock (2003) and this range of $V_{\rm max}$ was also confirmed by Madau et al. (2008) using the cosmological Via Lactea simulation of the formation of a MW-sized halo. Another investigation of Draco by Łokas et al. (2005), which considered the contamination of the stars by tidal tails and included the fourth velocity moment in the analysis, found

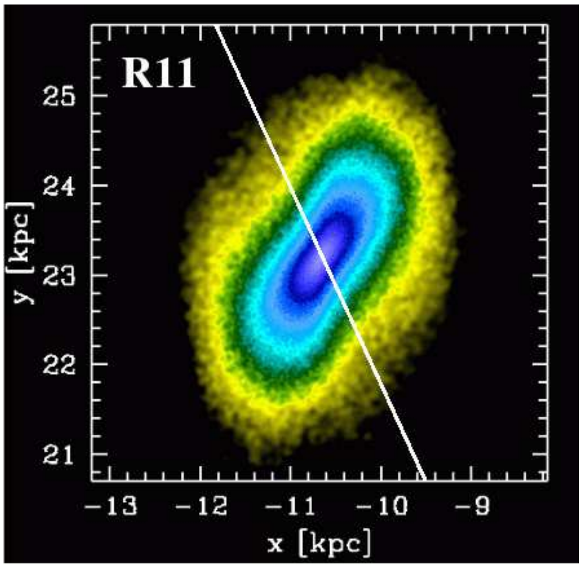

FIG. 13.— Surface density map of the stellar distribution of the dwarf in simulation R11. Particles are color-coded on a logarithmic scale, with hues ranging from yellow to blue indicating increasing stellar density. Local density is calculated using an SPH smoothing kernel of 32 neighbors. The distribution of stars is projected onto the orbital plane and is visualized at the third pericentric approach ($t = 5.25$ Gyr from the start of the simulation). The solid line indicates the direction towards the center of the host galaxy, located at $(x,y) = (0,0)$. A bar is evident in the stellar component and the rotational velocity of the stars, $V_{\rm rot}$, is anticlockwise in this image. The tidal forces point in the same direction as the rotational velocity vectors of the stars in the dwarf, resulting in an increase of $V_{\rm rot}$.

$\sigma_* \sim 8$ km s^{-1} and $V_{\rm max} \sim 16$ km s^{-1}, again in agreement with our results. Lastly, Walker et al. (2009) have recently analyzed the observed velocity dispersion profiles of a number of classic dSphs. Treating the anisotropy of the stellar velocity distribution as a free parameter, these authors estimated the $V_{\rm max}$ of the host halos in the range $\sim 10-25$ km s^{-1}, similar to those that would be obtained assuming the relation between $V_{\rm max}$ and σ_* reported here.

The right panel of Figure 12 illustrates four examples of the *evolution* of individual dwarfs on the $V_{\rm max} - \sigma'_*$ plane. Results are presented for representative experiments R1, R2, R3, and R5, where the same dwarf galaxy (D1) was placed on different obits, but the general trends are confirmed in all simulations. The combination of tidal stripping and loss of angular momentum dominating over tidal heating dictates the characteristic evolution toward lower values of $V_{\rm max}$ and σ'_* seen in all cases. The panel also shows that the dwarf galaxies exhibit different trajectories depending on their orbital parameters and can move substantially on the $V_{\rm max} - \sigma'_*$ plane during the course of their evolution inside their hosts. Both facts imply that the final $V_{\rm max} - \sigma'_*$ relation in our simulations is not a consequence of the initial conditions.

5.2. *Increasing Rotational Velocity*

In the majority of cases we studied, the rotational velocity of the stars within $r_{\rm max}$, $V_{\rm rot}$, decreased systematically with time leading from the initial rotationally-supported dwarfs to pressure-supported stellar systems dominated by random motions. There are instances in the evolution, however, where $V_{\rm rot}$ increases at pericentric passages. As seen in Figure 11, this occurs in simulations R1, R9, and R17 (after the second pericentric approach), R8 (after the third pericentric approach), and R11 and R12 (after the third and fourth pericentric passage).

Investigating for the reason behind the temporary increases of the rotational velocity we checked the orientation of the elongated stellar component at the pericentric approaches at which such increases occur. We found that the typical orientation of the bar is similar to that illustrated in Figure 13 where we see the stellar component of simulation R11 at the third pericentric approach projected onto the orbital plane. The rotational velocity of the stars is anticlockwise in this plot. Therefore, the tidal forces which act along the direction towards the host galaxy (solid line) point in the same direction as the rotational velocity vectors of the stars in the dwarf, effectively speeding up the rotation. Note that the case shown in Figure 13 is the only instance in the entire evolution of the whole suite of 17 experiments where the total angular momentum of the stars within $r_{\rm max}$ increases significantly. In all other cases of increasing $V_{\rm rot}$ the angular momentum does not increase because it is controlled not only by the rotational velocities of the stars but also by $r_{\rm max}$, which decreases at each pericentric passage.

Lastly, we note that the observed increases in $V_{\rm rot}$ are always associated with changes in the shape of the stellar component from a more prolate to a more triaxial configuration, or equivalently with an increase of the difference between the axis ratios b/a and c/a. This is most evident in experiment R11, where the prolate shape with $b/a \approx c/a \approx 0.4$ at the third pericentric passage transforms into a triaxial one (with $b/a > c/a$). A similar phenomenon occurs at the subsequent (fourth) pericentric approach. These changes are also accompanied by changes in other parameters. As verified in Figure 2 and Figures 3–10, when the rotational velocity (or $V_{\rm rot}/\sigma_*$) increases, there is always a drop in the anisotropy parameter β and the bar strength amplitude A_2. This means that at these instances the shape of the stellar component becomes less prolate and the orbital structure of the stellar distribution changes as the stellar orbits become less radial.

5.3. *Increasing M/L Ratio*

In most of our simulations, the M/L ratio computed within $r_{\rm max}$ decreases monotonically as a function of time for the reasons we discussed in § 3.1. In three of our 17 experiments, however, the M/L ratio starts to increase at some point during the evolution. This happens most prominently in simulations R2 and R4, which are characterized by the smallest pericentric distances and produce the most strongly tidally stirred dwarfs. Although much smaller, such an increase in the M/L ratio is also observed in experiment R13 where the stellar disk is more extended due to the larger initial value of the radial scale length, R_d, adopted in this case. We stress at the outset that these increases of the M/L ratio are rather moderate and thus cannot account for the exceptional DM content in some of the classic dSphs such as Draco and Ursa Minor. This implies that the very high values of M/L inferred for some dSph galaxies may not be a consequence of tidal evolution, but could be the result of either the formation process of their progenitors or other mechanisms that affected the baryonic mass fraction of dSphs. For example, the presence and subsequent removal of gas by the combination of tides and ram pressure has been shown to be vital in producing systems with extreme DM content (Mayer et al. 2006, 2007).

Figure 14 investigates the reason behind the increasing M/L ratio. This figure shows the relative mass loss, $|\Delta M|/M$, of stars and DM separately in simulations R2, R4, and R13. For comparison, we also present the same quantities in our reference experiment R1. To avoid noise in the data, the values of

$|\Delta M|/M$ were assigned at pericenters by taking the masses within $r_{\rm max}$ at the following and preceding apocenter, namely $|\Delta M|/M = |M_{i+1} - M_i|/M_i$, where i is the apocenter number. Figure 14 demonstrates that in all four simulations the relative mass loss of the DM component is initially much larger than that of the stars, and that the former always dominates in experiment R1. In simulations R2, R4, and R13, however, the stars begin to be stripped more effectively at some point during the late stages of the evolution, leading to the increase of the M/L ratios reported in Figures 2, 4, and 8.

The reason for this behavior can be attributed to the fact that in these three cases the dwarf galaxies are stripped down to the scales where the alignment between the angular momenta of the stars and the orbital angular momenta of the dwarfs start to have an important effect on stellar stripping. In experiments R2 and R4, with the smallest pericentric distances, this is due to the very strong tidal forces. In simulation R13, the disk is much more extended and, consequently, the dwarf galaxy is stripped down to the stellar scales faster than, for example, in the reference experiment R1. Because in all experiments the stars retain a certain amount of angular momentum (while the DM halos were non-rotating by construction) and the orientation of the angular momentum vector does not strongly vary with time, the stars begin to get stripped more efficiently compared to the DM as their angular momenta are (on average) more strongly aligned with the orbital angular momentum of the dwarf (e.g., Read et al. 2006b). It is important to emphasize, however, that the details of how the M/L ratio would evolve depends, among other things, on the initial angular momentum content of the DM halos, the amount of angular momentum retained by the stars in the late stages of the evolution, and the degree of alignment between the angular momenta of stars and DM and the orbital angular momentum.

5.4. *Orbital Time or Pericentric Distance?*

In this section, we discuss the role of different orbital parameters in influencing the transformation of disky dwarfs into dSphs and thus the efficiency of the tidal stirring mechanism. Specifically, we focus on the relative importance of the orbital time, $T_{\rm orb}$, and the pericentric distance, $r_{\rm peri}$, which determine the number and the strength of the tidal shocks, respectively. The relevant analysis is presented in Figure 15. This figure shows, as a function of $r_{\rm peri}$ and $T_{\rm orb}$, the final values for some of the parameters that we used throughout this study to describe the global evolution of the dwarf galaxies inside the tidal field of their hosts. In particular, we consider the parameters $r_{\rm max}$, $V_{\rm max}$, b/a, c/a, $V_{\rm rot}/\sigma_*$, and β.

The filled symbols in Figure 15 present results for simulations R1-R5 which have been discussed in § 3 (see also Table 3). Open symbols correspond to two additional experiments, which were designed to complement the existing simulations R1-R5. In this new set of experiments, we placed the dwarf galaxy model D1 used in experiments R1-R5 on the following orbits: (i) a short orbital time-large pericentric distance orbit with $r_{\rm peri} = 50$ kpc, $r_{\rm apo} = 80$ kpc, and $T_{\rm orb} \sim 1.7$ Gyr and (ii) a long orbital time-small pericentric distance orbit with $r_{\rm peri} = 12.5$ kpc, $r_{\rm apo} = 250$ kpc, and $T_{\rm orb} \sim 4.6$ Gyr. This choice of parameters ensures that the pericentric distances and orbital times in these new simulations are not related in the same way as in experiments R1-R5, a fact that would be important for the interpretation of the results.

Figure 15 confirms that the final properties of the dwarfs vary dramatically depending on the parameters of the orbit. Although the behavior of the various quantities clearly shows that the final outcome of the transformation depends on both $T_{\rm orb}$ and $r_{\rm peri}$, a closer inspection of the results in this figure illuminates the more crucial role of the pericentric distance compared to that of the orbital time in shaping dSphs via tidal stirring.

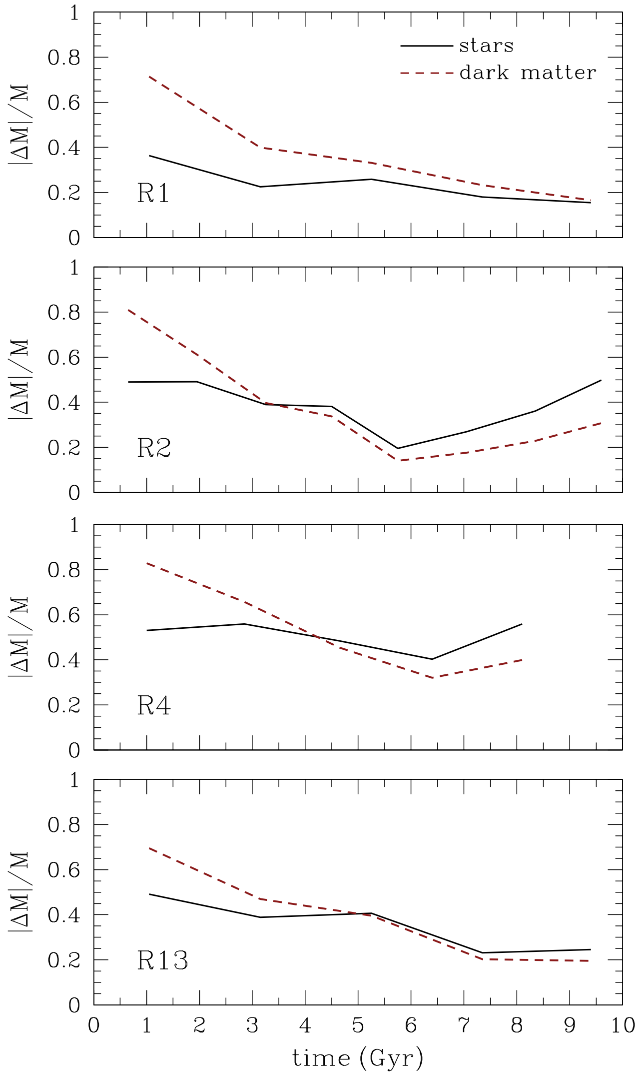

FIG. 14.— Relative mass loss, $|\Delta M|/M$, of the stellar (solid lines) and DM component (dashed lines) in simulations R1, R2, R4, and R13. The values of $\Delta M/M$ are assigned at pericenters and are computed as $|\Delta M|/M \equiv |(M_{i+1} - M_i)|/M_i$, where M_{i+i} and M_i are the masses within $r_{\rm max}$ at the following and preceding apocenter, and i denotes the apocenter number. The relative mass loss of the DM initially exceeds that of the stars in all cases, reflecting the more efficient tidal stripping of the extended DM halos of the dwarfs. While the mass loss in DM dominates at all times in the reference experiment R1, in simulations R2, R4 and R13 the stars begin to be stripped more effectively at some point during the evolution. This preferential stripping of the stars leads to the increase of the M/L ratio reported at intermediate and late times in Figures 2, 4 and 8.

Let us first consider the filled symbols in Figure 15. Dwarf galaxies with the same pericentric distances but with orbital times that differ by approximately a factor of 2 (triangle and pentagon) end up with a similar set of final properties. On the other hand, dwarfs with comparable orbital times but with pericentric distances that differ by a factor of 2 (pentagon, circle, and star) display a wide range of final properties, a fact which reflects the difference in pericentric distances.

Focusing now on the open symbols which correspond to the new experiments, Figure 15 shows that the dwarf galaxy on the long orbital time-small pericentric distance orbit (circle) is characterized by $c/a \gtrsim 0.5$ and $V_{\rm rot}/\sigma_* \lesssim 1$ and hence would be classified as a dSph. We note that this dwarf has experienced only 2 pericentric passages. On the contrary, although it has suffered a much larger number of tidal shocks, the dwarf on the short orbital time-large pericentric distance orbit (square) has $c/a \approx 0.4$ and $V_{\rm rot}/\sigma_* > 1$ and thus did not undergo a transformation into a dSph.

Overall, the results in Figure 15 lead to the following set of conclusions. First, the degree of the tidal transformation depends strongly on the combination of pericentric distance and orbital time. As expected, small pericentric distances and short orbital times, corresponding to orbits associated with a large number of strong tidal shocks and also characteristic of dwarfs being accreted by their hosts at high redshift, produce the most substantial tidal evolution. Furthermore, the larger the number of strong tidal shocks a disky dwarf suffers, the stronger and thus more complete is its transformation.

Second, in order to simply transform a disky dwarf into a dSph (according to the criteria of § 2.5) without necessarily inducing the strongest transformation, the pericentric distance is a more salient parameter than the orbital time. We stress that this conclusion depends on the condition that $T_{\rm orb}$ is short enough to allow the disky dwarfs to conclude at least two pericentric passages[9]. Such a requirement should be generally satisfied in the LG environment, as a significant fraction of LG dwarfs have likely had enough time to complete at least two orbits inside their hosts. Indeed, in the context of the CDM cosmogony, galaxy-sized halos form early and, in particular, the MW halo was probably already in place at $z \sim 2$ (e.g., Governato et al. 2007, 2009). In addition, structure formation in hierarchical models indicates that satellites which are found closer to the center of the primary system at $z = 0$ are typically those that fell into the host potential earlier (e.g., Diemand et al. 2007). According to this, the present distances of most dSphs would suggest that their progenitors should have been accreted by their hosts at relatively early epochs. Assuming a MW-type host potential and the range of orbital parameters of LG satellites that survived until the present time (Klimentowski et al. 2010), results in a typical orbital time of $T_{\rm orb} \sim 2$ Gyr. Combining this value with a conservative redshift of accretion of $z \sim 1$ suggests that dwarf galaxies in the LG should have been able to complete 3 or even 4 passages inside their hosts. This line of reasoning establishes the pericentric distance, and not the orbital time, as the fundamental factor that controls the tidal transformation of disky dwarfs into dSphs in the LG and similar environments.

5.5. *Implications*

In the present study we have established that the strong tidal field of a MW-sized host galaxy can transform late-type, rotationally-supported dwarfs into stellar systems with the kinematic and structural properties of the classic dSphs in the LG and similar environments. Of course, tidal stirring does not constitute the only *environmentally-driven* mechanism proposed for the origin of dSphs. An alternative promising model incorporates direct gravitational interactions between dwarf galaxies. Indeed, cosmological simulations of struc-

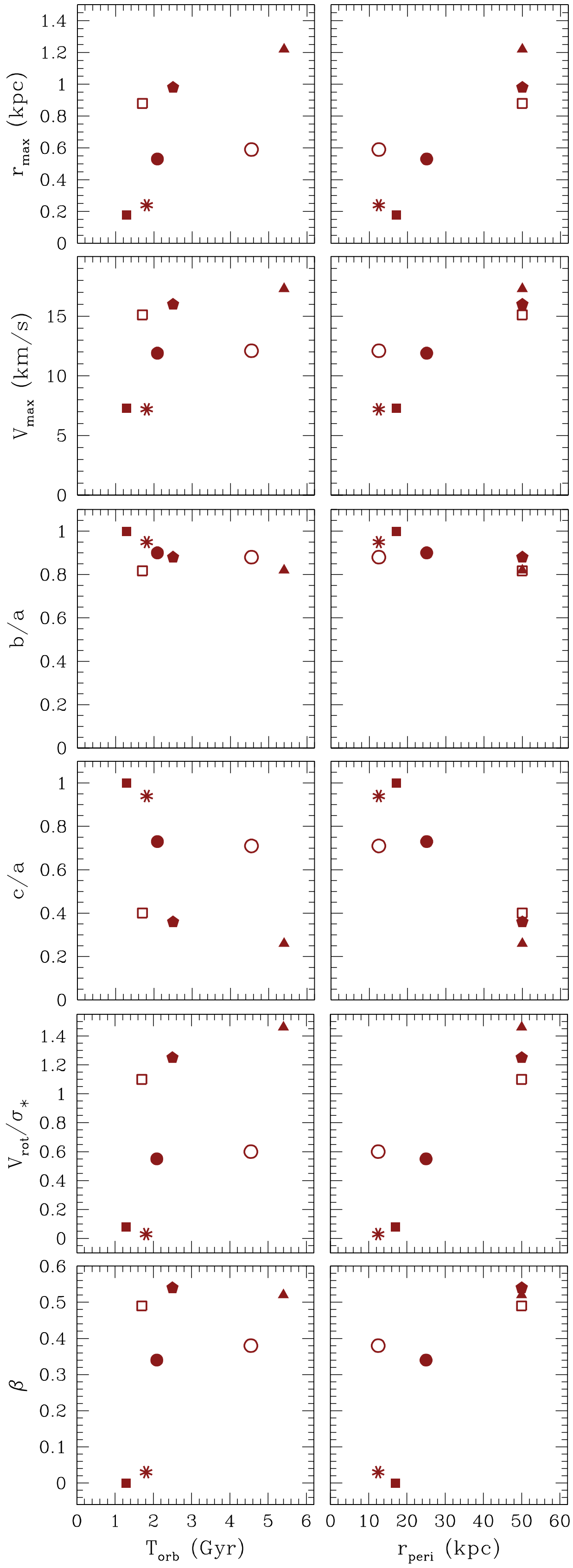

FIG. 15.— Final parameters of the simulated dwarfs as a function of orbital time (left column) and pericentric distance (right column). Filled symbols show results for simulations R1-R5 (see Table 2). Open symbols correspond to experiments where the dwarf galaxy model D1 used in simulations R1-R5 was placed on two additional orbits inside the host galaxy (see text for details). The pericentric distance which determines the strength of the tidal shocks constitutes the key factor responsible for the effective metamorphosis of a disky dwarf into a dSph. The combination of short orbital times and small pericentric distances, characteristic of dwarfs being accreted by their hosts at high redshift, induces the strongest and most complete transformations.

---

[9] As discussed in Mayer et al. (2001a), disky dwarfs which due to their very long orbital times experience just one tidal shock during their orbital evolution would not be transformed, even if their pericentric distances are fairly small (except maybe in cases of very rare, nearly radial orbits). In such circumstances, the orbital time will play the key role in determining the dynamical evolution of infalling dwarfs.

ture formation have indicated that some dwarfs may have entered their Galaxy-sized hosts as members of infalling groups (Kravtsov et al. 2004; D'Onghia & Lake 2008). It is thus plausible that these dwarfs could have experienced significant tidal perturbations before being accreted by the primary galaxies. Kravtsov et al. (2004) did demonstrate this possibility in their ΛCDM cosmological simulations of MW-sized halos.

Using controlled N-body experiments, D'Onghia et al. (2009) have recently shown how the interaction between a pair of disky dwarfs with mass ratios ranging from 1:10 to 1:100 can result in the rapid formation of a dSph. As the less massive member of the pair plunges close to the disk of the more massive companion, its stellar component can experience substantial mass loss and can be tidally heated into a spheroidal configuration, even after only one close pericentric passage. This mechanism, termed "resonant stripping", is effective when the spin angular frequency of the dwarf disk and the angular frequency of the orbit of the dwarf around the more massive system are comparable in magnitude, and the spin and orbital angular momenta are nearly aligned (that is, in a nearly prograde encounter). Such individual, close encounters between dwarf galaxies may have been more common during the assembly process of the host halos from accreting groups (Kravtsov et al. 2004; D'Onghia & Lake 2008). Given that the typical velocity dispersions in such groups should have been quite low (with a dominant group member of the size of the LMC), it is also possible that some of these interactions may have resulted in actual mergers between the dwarf galaxies.

While all these different tidal mechanisms which rely on *pre-processing* the dwarfs before they are accreted by the primary galaxy may play a role at some level, they must also be consistent with the morphology-density relation, a crucial constraint that the tidal stirring model can naturally satisfy. At present, there is no definitive observational or theoretical evidence to rule out any of the scenarios for the origin of dSphs. This also includes models that advocate the *ab initio* formation of dSphs from cosmological initial conditions (e.g., Ricotti & Gnedin 2005; Sawala et al. 2010). In all likelihood, all mechanisms do operate simultaneously to differing degrees in producing the population of dSphs in the LG and similar environments.

Our investigation of the role of different pericentric distances and orbital times on the efficiency of tidal stirring has interesting implications for the expected properties of dSphs. Our results show that in order to transform a disky dwarf with an orbital apocenter in excess of 200 kpc into a dSph, an orbit with an eccentricity that is substantially larger than the median expected eccentricity is required (see Figures 2 and 15). Given that the current distances of dwarf galaxies in the LG are suggestive of their orbital apocenters, the distant dSph Leo I (currently at a distance of ~ 250 kpc from the MW; e.g., Caputo et al. 1999) should be on a very wide, nearly radial orbit, assuming that it is the product of tidal stirring. Furthermore, even on such eccentric orbits the remnants possess some residual rotation at the level of $V_{\rm rot}/\sigma_* \approx 0.5$ (see open circle in Figure 15). We thus predict that Leo I should have a higher $V_{\rm rot}/\sigma_*$ compared to the dSphs located closer to the primaries. Interestingly, albeit inconclusive, there are signatures of intrinsic rotation in Leo I (Sohn et al. 2007; Mateo et al. 2008). We note that such rotation has been shown to explain the observed kinematics of this dwarf (Łokas et al. 2008).

Our prediction that in the context of tidal stirring wider orbits should be associated with less evolved dSphs, and thus with higher values of $V_{\rm rot}/\sigma_*$, should apply, even more so, to the oddly isolated galaxies Cetus and Tucana, which are located in the outskirts of the LG at more than 500 kpc from M31 and the MW, respectively. Although measurements of kinematics are extremely challenging due to the very large distances involved, recent spectroscopic studies have presented tentative evidence for rotation in Cetus (Lewis et al. 2007) and Tucana (Fraternali et al. 2009) with $V_{\rm rot}/\sigma_*$ values in the range of $0.5 \lesssim V_{\rm rot}/\sigma_* \lesssim 1$. If confirmed by future observations, detection of rotation at such levels would be consistent with the predictions of the present study.

Furthermore, at distances in the range $\sim 300-600$ kpc from the MW and M31, we find the dwarf galaxies Phoenix and LGS3, which are classified as "transition-type" dwarfs (Mateo 1998). While these objects exhibit structural properties consistent with those of dSphs, they are associated with some residual gas (see, e.g., Grcevich & Putman 2009 and references therein). On the other hand, these transition-type dwarfs exhibit negligible or no ongoing star formation (no detection of H_{II} regions has been reported), a fact that differentiates them from standard gas-rich, star-forming dIrrs (e.g., Grebel 1999; Skillman 2005). Being at intermediate distances between dSphs and dIrrs and combining properties of both classes of objects, these transition-type dwarfs can provide valuable tests for the predictions of tidal stirring regarding the different stages of the transformation process.

One possibility for their origin is that their progenitors were disky satellites that were accreted only recently by their hosts on wide, fairly radial orbits, and are still in the process of being transformed into dSphs by tidal stirring. It is then plausible that these transition-type dwarfs have only concluded one pericentric passage (or they are on the way to their first pericentric approach), having lost most of their gas by ram pressure stripping. This is a reasonable assumption given that gas removal by the combination of tides and ram pressure proceeds faster than the morphological transformation of the stellar component (Mayer et al. 2006). If the scenario proposed here is correct and their transformation has only been partial, transition-type dwarfs should possess significant rotation in their stellar component (as in the case of the remote dSphs Leo I, Tucana, and Cetus discussed above). Verifying observationally this basic theoretical prediction would be important – unfortunately, the stellar kinematics of these systems is poorly known. Moreover, provided that they are at the intermediate stages of their transformation, our results suggest that they should also show signs of bar-like distortions. Definitive conclusions on all of these issues would require a synergy between detailed photometric and kinematic measurements as well as exhaustive comparisons with theoretical models. To this end, extending the search for evidence of tidal stirring in systems with more recent assembly histories than the LG may reveal a population of satellites in the process of being transformed, and thus offer unique opportunities to constrain the tidal stirring model. Interestingly, recent studies using the SDSS database have uncovered a population of dwarf galaxies in the Virgo cluster that exhibit disk-like features and bars, appearing to be in a transitional stage between a disk and a spheroid (Lisker et al. 2007). The existence of this class of objects is, in broad terms, consistent with the predictions of tidal stirring for the different stages of the transformation.

Several alternative scenarios to tidal stirring exist for explaining the nature of the spheroidal morphology of the distant LG dwarfs. For example, as a result of three-body interactions, satellites can acquire extremely energetic orbits with apocenters beyond the virial radius of the primary and be ejected to large distances (Sales et al. 2007). In this model, ejected subhalos are typically the less massive members of a pair of satellites that is tidally disrupted during the first approach onto the host. Such ejections can also occur during the tidal disruption of a bound system of *multiple* subhalos that is accreted as a single unit by the primary galaxy (Ludlow et al. 2009). In both of these scenarios, strong tidal interactions with the more massive companions can took place before the satellites are accreted by their hosts. Such encounters may eventually transform the dwarfs into dSphs, either via resonant stripping (D'Onghia et al. 2009) or other gravitational processes such as mergers. Interestingly, Kravtsov et al. (2004) reported in their cosmological simulations the existence of a few satellite systems at distances of ~ 1000 kpc from their MW-sized hosts. Based on their final $V_{\rm rot}/\sigma_*$ values, these objects would be classified as dSphs and could plausibly represent the counterparts of Cetus and Tucana in the context of the LG. The tidal heating of these systems did occur in small groups that were accreted by the primary halo at the present epoch. As the tidal forces unbind these accreting groups, energy redistribution can increase the orbital energy and apocentric distance for some of the satellites, providing an explanation for the presence of isolated dSphs in the periphery of the host galaxy. The extreme radial velocity of Leo I (e.g., Mateo et al. 2008) and the relatively high recession velocity of Tucana (Fraternali et al. 2009) may already suggest that these systems have been propelled into their highly energetic orbits through the type of interactions suggested by Sales et al. (2007) and Ludlow et al. (2009).

Binary mergers between individual satellite galaxies taking place outside of infalling groups may offer another alternative explanation for the puzzling presence of the isolated dSphs in the LG. Indeed, it has already been demonstrated that interactions and direct mergers of subhalos can lead to their very strong evolution (e.g., Knebe et al. 2004, 2006; Klimentowski et al. 2010). For example, Klimentowski et al. (2010) found in their constrained simulation of the LG that $\sim 10\%$ of all surviving subhalos in the MW and M31 have undergone a major encounter with another subhalo in the past. Most of these events occurred at very early times, between $z \sim 1$ and $z \sim 3$, while the interacting subhalos have not yet become satellites and are still outside their hosts. Whether binary mergers between dwarfs can explain the existence of dSphs orbiting far from the primary galaxies, such as Tucana and Cetus, is currently under investigation via a combination of cosmological simulations and controlled numerical experiments (Kazantzidis et al., 2010a, in preparation). Ongoing investigations aimed at studying in detail the stellar components of these isolated dSphs (e.g., Bernard et al. 2009; Monelli et al. 2010a), including their star formation histories (e.g., Monelli et al. 2010b), may soon provide useful constraints on the various competing models that have been proposed so far for their origin.

In this paper, we have investigated the tidal evolution of dwarf galaxies comprising exponential stellar disks. Recent cosmological simulations do support the idea that isolated dwarfs are rotating disks (Governato et al. 2010; see, however, Sawala et al. 2010). The morphological and dynamical transformation of such disky dwarf galaxies into dSphs under the action of tidal forces is a rather rich process which involves several stages and is characterized by different events. Consequently, numerical simulations where a spheroidal stellar system is postulated from the beginning (e.g., Muñoz et al. 2008; Peñarrubia et al. 2008) may be inadequate to describe how dSphs have evolved to the present time subject to the tidal field of their hosts. Indeed, if the picture presented here is correct, dSph galaxies should have formed relatively late in most cases and only after concluding a number of pericentric passages inside the primary galaxies.

More specifically, Peñarrubia et al. (2008) performed a series of N-body simulations to study the dynamical evolution of dSphs in a host potential assuming a spherical King model for the stellar component embedded within an NFW halo. These authors reported that tidal effects lead to an increase in the M/L ratio in most cases, in contrast to the findings of the present study. This discrepancy is possibly due to the fact that the stellar distribution in the Peñarrubia et al. (2008) dwarfs followed the King profile which is characterized by a density core. As a result, the stars were loosely bound within the potential of the dwarf galaxy and the stellar component was much more heavily stripped compared to what is typically found here. In our experiments, the formation of tidally-induced bars, which is obviously missing from the Peñarrubia et al. (2008) models, is crucial. This is because bar formation enhances the resilience of the dwarf galaxies to mass loss and tidal stripping by increasing the stellar density and, correspondingly, the depth of the potential well.

Given the existence of a number of qualitatively different scenarios for the formation and evolution of dSphs, it is critical to be able to test these scenarios and discriminate among them. The growing kinematic data sets for dSph galaxies can already facilitate detailed comparisons with theoretical models (e.g., Walker et al. 2009). For example, the level of residual stellar rotation in the remnants can be used to constrain the competing models. Indeed, according to the results presented in Figure 11 and detailed analysis of similar simulations (see Łokas et al. 2010a), if the present-day dSph galaxies originated from disky dwarfs they should, at least in some cases, show signatures of intrinsic rotation. Interestingly, in addition to the cases of the isolated dSphs Leo I (Sohn et al. 2007; Mateo et al. 2008), Cetus (Lewis et al. 2007), and Tucana (Fraternali et al. 2009) mentioned already, detection of rotation at different levels of significance has also been claimed for Ursa Minor (Hargreaves et al. 1994; Armandroff et al. 1995) and Sculptor (Battaglia et al. 2008). It is important to stress, however, that intrinsic rotation may be difficult to distinguish from the velocity gradients induced either by the presence of tidal tails or, for nearby systems, caused by transverse motions (the so-called "perspective rotation"; see Walker et al. 2008). Due to such complications, Leo I seems to be the most promising candidate for detection of intrinsic rotation (see discussion in Łokas et al. 2008). In addition, as discussed above, our simulations predict a positive correlation between the magnitude of stellar rotation in dSphs and their distances from the center of the host galaxy (or equivalently the time of infall of the progenitor dwarf onto the primary). Such a correlation would be difficult to establish, for example, in models that propose the *ab initio* formation of isolated dSphs from cosmological initial conditions (e.g., Ricotti & Gnedin 2005; Sawala et al. 2010). Indeed, in this case the amount of rotation in the stellar components of dSphs should depend on the specifics of the formation process and the intrinsic properties of these systems (e.g., the initial spin parameter of the DM halo of the dwarf) and thus be uncorrelated with the distance from the center of the host galaxy.

In the context of specific observational signatures of the tidal stirring model, bars play a prominent role. According to our results, bar-like structures should be relatively common in dSphs as the bar phase is one of the longest stages in the transformation process. In fact, some of the less evolved dSphs in the LG may still be in the bar stage and show signs of bar-like distortions. One irrefutable example of a LG dwarf that contains a bar is the LMC. Orbital evolution models using three-dimensional velocities constrained by recent proper motion measurements (Kallivayalil et al. 2006) suggest that the LMC may currently be on the first passage having just crossed the pericenter of its orbit around the MW (Besla et al. 2007). Confirming that the LMC is on a such extended orbit with a pericentric distance of $r_{\rm peri} \sim 50$ kpc would be in line with our findings, as we expect its stellar component to be less evolved and thus in some early, transitory stage of the transformation between a disk and a spheroid.

Except for the LMC, however, the overall number of detections of bar-like structures among the dSphs in the LG is relatively low[10]. Indeed, markedly elongated isophotes that could be attributed to a residual bar-like component are observed in only a few cases, including Ursa Minor (Irwin & Hatzidimitriou 1995) and the newly discovered Hercules dSph (Coleman et al. 2007). Recently, the strongly non-spherical shape of the core of the disrupting nearby Sagittarius dSph has also been ascribed to a pre-existing bar (Łokas et al. 2010b). Interestingly, the recently discovered ultra-faint MW satellites also exhibit substantial degrees of flattening (e.g., Martin et al. 2008). Of course, the high elongation of the stellar component in some of the dSphs can also be caused by other effects, including the triaxiality of the surrounding DM halos (Kazantzidis et al. 2010) or tidal deformation in the gravitational field of the MW. Regarding the latter, Martin & Jin (2010) have recently proposed that Hercules dSph is in fact a stellar stream in formation, thus suggesting tidal disruption as the most valid scenario for the extreme shape of this system. Deeper observations to track evidence of such tidal interactions would be able to settle these issues.

The findings of the present study also indicate that the formation of tidally-induced bars is strongly linked with the transformation of rotationally-supported dwarfs to dSphs (for similar conclusions, see Mayer et al. 2001a and Klimentowski et al. 2009a). Indeed, as shown in Table 3, in only one of the 14 simulations that produced dSphs in the end, specifically experiment R16, a bar did not form at some point during the evolution of the progenitor disky dwarf inside the host galaxy. The following sequence of events is typically observed in our simulations. First, the strong tidal forces at the initial pericentric approach trigger a bar instability in the disk of the dwarf. The tidally-induced bar transports angular momentum outwards to the outer regions of the disk and to the DM halo. As tidal stripping removes the outer parts of the dwarf, the entire angular momentum content gradually decreases and the ability of the dwarf galaxy to be supported by rotation progressively diminishes. Second, subsequent tidal shocks destroy the centrophilic stellar orbits which support the bar and increase the stellar velocity dispersion. As a result, the bar continuously loses its elongation and is tidally heated into a more isotropic, diffuse spheroid. The ultimate outcome of these two physical processes is the formation of pressure-supported stellar systems with values of $V_{\rm rot}/\sigma_* \lesssim 1$ that are appropriate for dSphs.

We stress that the above discussion describes only one channel for the transformation of a disky dwarf into a dSph via tidal stirring. An alternative mechanism involves the buckling of the bar due to the amplification of vertical $m = 2$ (bending) modes (Mayer et al. 2001a,b). While the loss of angular momentum occurs in exactly the same way as previously described, the buckling of the bar now becomes the main process that leads to the significant vertical heating and the increase of the velocity dispersion of the system (see, e.g., Debattista et al. 2006 for a detailed description of these processes). In this picture, the spheroidal shape of the stellar distribution constitutes the end result of the instability and is not driven by tidal heating as in the simulations of the present study. Because the buckling instability requires a fairly strong bar to develop, this transformation mechanism is relevant to relatively massive systems with high surface densities. Indeed, none of the bars in our low surface density dwarfs showed any signs of buckling.

To summarize, it seems that there are at least two channels for the formation of the spheroidal component in the tidal stirring scenario: prolonged impulsive tidal heating and the bar buckling instability. The former is favored in low mass, low surface density disky dwarfs for which heating is particularly efficient. This mechanism likely applies to the progenitors of the faintest classic dSphs such as Draco, Sculptor or Leo I. On the other hand, bar buckling requires strongly self-gravitating systems with higher surface densities. This channel plausibly operates on the progenitors of the brightest dSphs such as Fornax and Sagittarius, and even more so on those of the bright dwarf elliptical satellites of M31, such as NGC185 and NGC167. This mechanism was also found to be applicable to the transformation of relatively massive and bright spiral galaxies in galaxy clusters (Mastropietro et al. 2005).

Our simulations also suggest that the amount of mass loss that the dwarf galaxies experience can be considerable. Indeed, in the reference experiment R1, the dwarf lost $\sim 90\%$ of its initial mass within $r_{\rm max}$ and still survived as a bound entity (the amount of mass loss for the most heavily stripped dwarfs in simulations R2 and R4 reached $\sim 99\%$). Typically, the maximum circular velocities, $V_{\rm max}$, decreased by a factor of ~ 2 during the orbital evolution in the cases where dSphs were produced (this factor increased to ~ 3 in experiments R2 and R4). Such substantial evolution in $V_{\rm max}$ occurred despite the presence of the baryons which tend to moderate the effect of tidal shocks by making the potential well deeper, especially after bar formation. These findings are in agreement with those of Klimentowski et al. (2009a) as well as with results of other studies. For example, Kravtsov et al. (2004), using fully cosmological DM-only simulations, reported that the $V_{\rm max}$ of their most evolved subhalos decreased by a factor of $1.5-2$ on average during 10 Gyr of tidal evolution. More recently, Diemand et al. (2007) and Madau et al. (2008) found that satellites in the Via Lactea simulation lost between ~ 30 and $\sim 99\%$ of their pre-infall mass, and that $V_{\rm max}$ typically decreased by a factor of $\sim 2-3$.

The previous discussion suggests that for subhalos which have been accreted by their hosts at early cosmic epochs and have completed several orbits with fairly small pericenters, $V_{\rm max}$ is expected to have evolved significantly. Therefore, the DM halos of present-day dSphs may have had considerably

---

[10] We note that there are a number of reasons as to why bars in dwarf galaxies may escape detection in the LG. First, bars are oriented randomly with respect to the observer, so some bar-like structures may appear as only slightly flattened. Second, the smoothing procedures usually applied when measuring the surface density distributions of stars in dwarf galaxies can decrease the detectability of bars in these systems (for a thorough discussion pertaining to the difficulties in identifying bars in dSphs, see Klimentowski et al. 2009a).

larger masses and circular velocities when they entered the halo of the MW (see, e.g., Kravtsov et al. 2004 and Madau et al. 2008). This has important implications for galaxy formation models. Indeed, the substantial observational work during the past few years suggests that the present-day classic dSphs of the MW and M31 have central stellar velocity dispersions in the range $\sigma_* \sim 7-13\,\mathrm{km\,s^{-1}}$ (see, e.g., Walker et al. 2009 and references therein). Assuming that $V_{\max} \sim \sqrt{3}\sigma_*$, in accordance with the results of § 5.1, implies current values of $V_{\max}$ in the range $V_{\max} \sim 12-22\,\mathrm{km\,s^{-1}}$ and initial $V_{\max}$ values, namely before infall and tidal mass loss, in the range $V_{\max} \sim 24-44\,\mathrm{km\,s^{-1}}$. These numbers are quite important. Indeed, with such relatively high values of initial halo $V_{\max}$, photoevaporation of the gas by the cosmic ultraviolet background after reionization as well as supernovae feedback could not be the factors that shaped the baryonic content and nature of these dSphs. In fact, according to the radiative transfer simulations of Susa & Umemura (2004), photoevaporation would be effective and remove most of the gas only for $V_{\max} \lesssim 20\,\mathrm{km\,s^{-1}}$. This is consistent with the lack of a clear signature of the reionization epoch in the star formation histories of dSphs (Grebel & Gallagher 2004; Orban et al. 2008).

In this paper, we have also demonstrated how the orbital parameters and initial structures of the progenitor late-type disky dwarfs determine the final properties of the dSphs. Therefore, the fact that Fornax and Draco have roughly similar masses at present, as inferred from the $V_{\max}$ of their halos (e.g., Kazantzidis et al. 2004b), but differ by about an order of magnitude in luminosity and M/L ratio, can be explained in two ways. One possibility is that the progenitors of these two dwarfs began with very different relative amounts of DM and baryons, for reasons related to their formation history and not to the environment. Alternatively, Fornax and Draco originated from systems that had comparable DM and baryonic masses, but experienced dissimilar tidal evolutions because they entered the primary galaxy at different epochs and/or on different orbits.

Regarding the latter, according to the hydrodynamical simulations of Mayer et al. (2007), gas-rich disky satellites that were accreted by their hosts when the intensity of the cosmic ultraviolet background was much higher than today ($z \sim 2$), can be completely stripped of their gas by ram pressure in one or two pericentric passsages. In this case, the final systems would correspond to dSphs with truncated star formation histories such as Draco (e.g., Orban et al. 2008). While the baryonic content of the progenitor dwarfs decreased significantly as a result of gas stripping, the initial DM mass in the central regions around the surviving baryonic core is largely preserved. This is because DM is affected only by tides and not by ram pressure. As a result, exceptional M/L values, of the order of 100, similar to those inferred for Draco and Ursa Minor, can arise. On the other hand, disky dwarfs that were accreted by their hosts at $z \lesssim 1$, when the intensity of the cosmic ultraviolet radiation dropped by more than an order of magnitude compared to $z \sim 2$, were able to retain some gas because tides and ram pressure could not strip it completely. Under these conditions, the infalling dwarf galaxies can undergo tidally-triggered bursts of star formation associated with bar-driven gas inflows at pericentric approaches. Such a model would be applicable to dSphs with extended star formation histories such as Fornax, Carina, and Leo I. This mechanism can produce dSphs that are brighter for a given halo mass (or central stellar velocity dispersion) compared to the ones that were accreted earlier. While this generic scenario seem to explain the differences in the properties of Fornax and Draco despite their similar masses, it would be important to revisit it in future work with models capable of capturing the multiphase structure of the ISM in dwarf galaxies.

Lastly, it has long been debated whether the inferred high M/L ratios of dSphs indeed signify exceptional DM content or are simply a reflection of strong tidal effects and of the fact that these systems are in reality on the verge of disruption. The findings of the present study have intriguing implications for earlier attempts to model dSph galaxies as unbound systems without DM (e.g., Kroupa 1997; Klessen & Kroupa 1998). Indeed, the tidal stirring model demonstrates how mass loss and the formation of tidal tails can be consistent with the presence of a bound stellar component embedded in a relatively massive CDM halo, even after several Gyr of tidal evolution inside the host. Our results indicate that substantial mass loss and the existence of a gravitationally bound dSph galaxy with a relatively high M/L ratio are not mutually exclusive, confirming earlier claims based on a smaller set of lower resolution simulations (Mayer et al. 2002). The findings of the present study also suggest that the claimed detection of extra-tidal stars in a number of dSphs, including Ursa Minor (Martínez-Delgado et al. 2001), Fornax (Coleman et al. 2005), Carina (Muñoz et al. 2006), and Leo I (Sohn et al. 2007) is consistent with satellite accretion in CDM models. We note in passing that the number of such detections may be low due to the intrinsic difficulties associated with separating the tidal tails from the bound core of the dwarfs (see, e.g., Klimentowski et al. 2009b). Furthermore, in the context of tidal stirring, dSphs embedded in CDM halos exhibit stellar distributions that are adequately fit by exponential or King profiles in agreement with observed dSphs (see review by Mayer 2010). Stellar profiles of this type are difficult to accommodate within models that represent dSphs as systems devoid of DM. Indeed, such models predict nearly flat profiles as expected for objects close to complete disruption (e.g., Kroupa 1997).

5.6. *Caveats and Future Directions*

Certainly the approach presented in this paper is not without caveats. A first limitation is related to the fact that we have adopted a single primary galaxy with the present-day structural properties of the MW. In general, at the time when the dwarfs are accreted by the primary galaxy at high redshift, the DM and baryonic masses of the host would be different compared to those of the present time Our methodology thus neglects the cosmological evolution of the host galaxy structure via mergers and smooth accretion during the interactions with the dwarfs. However, this simplification may be justified to a certain degree by recent ΛCDM galaxy formation simulations, which have shown that MW-sized disk galaxies assemble most of the mass in their inner regions between $\sim 8-10$ Gyr ago (e.g., Governato et al. 2007, 2009). This is indeed the timescale that we follow in our simulations. Nonetheless, a more complete investigation would have to include the ongoing formation of the host galaxy. In addition, we have assumed a host DM halo that is spherical (except in the very inner regions that are dominated by the potential of the disk), instead of triaxial as postulated by CDM models (e.g., Frenk et al. 1988). Halo triaxiality and the complexity of halo formation in a realistic cosmological context, with continuous mergers, accretion, and rapidly changing potential wells can have an impact on the orbital evolution of infalling satellites (e.g., Kravtsov et al. 2004), with consequences for the efficiency of their transformation. It will be important to explore these issues in future investigations of tidal stirring.

A second shortcoming of our work is related to the fact that we have focused on experiments where the alignments between the internal angular momenta of the dwarfs, those of the primary disks and the orbital angular momenta were all prograde (45° in most cases; see Table 2). Prograde alignments between the orbital angular momenta of the dwarfs and the spins of the primary disks, or between the angular momenta of the two disks, are expected to be important mainly for orbits with pericentic distances smaller than a characteristic radius containing a non-negligible fraction of the mass of the primary disks. In this case, the tidal effects of the host disks would be enhanced and the orbits of the dwarfs would quickly decay due to the additional dynamical friction provided by the disks of the primary galaxies (e.g., Quinn & Goodman 1986). As our typical pericentric distances are $r_{\rm peri} \gtrsim 15$ kpc, we expect the efficiency of the transformation reported here to be weakly affected by such effects.

On the other hand, the orientation between the orbital angular momenta of the dwarfs and the internal angular momenta of their disks is particularly relevant for our experiments. For retrograde alignments between these two angular momenta, tidal stripping is considerably reduced (e.g., Read et al. 2006b) and both bar formation and the efficiency of transformation via the tidal stirring mechanism are also suppressed (Mayer et al. 2001a). These facts highlight the importance of coupling between orbital and internal motions. Determining the statistics of alignments between internal and orbital angular momenta would require a series of fully cosmological studies, focusing on the accretion of satellites within halos of disk galaxies, and is therefore beyond the scope of this paper. We stress, however, that the orbital parameters adopted in the present study correspond to only moderate alignments, and therefore our results should not be biased by any strong coupling of angular momenta. Unless there is some yet unknown cosmological bias *against* the mildly prograde alignments that we have adopted here, our findings should be able to illuminate at least some of the details of the typical transformation experienced by infalling disky dwarfs in the LG and similar environments.

Lastly, the most evident limitation of this study is that we have addressed the efficiency of the tidal stirring mechanism only in the collisionless regime. Our results should therefore be viewed as preliminary. A more complete treatment including hydrodynamics is required to illuminate one of the most distinct properties of dSphs, namely their low gas content (see, e.g., Grcevich & Putman 2009 and references therein) and fully refine the conclusions presented here. The present-day structure of dwarf galaxies originates from a complex interplay of effects and a full explanation requires detailed knowledge of their star formation histories and chemical evolution, amongst others. Adding star formation as a further ingredient will offer the possibility to determine the magnitude of starbursts induced in the dwarfs at pericentric passages, while gaining a deeper understanding of the wide diversity in their star formation histories (e.g., Grebel 2000; Orban et al. 2008). Furthermore, specific predictions for the metallicity of the remnants formed by tidal stirring, let alone comparisons with the luminosity-metallicity relation for nearby dwarf galaxies (Tolstoy et al. 2009), are not currently available. We plan to extend the present investigation in these directions in due course.

Mayer et al. (2007) have also demonstrated how the efficiency of tidal stirring is affected by the presence of a dissipative component, and how it varies depending on the balance between heating and cooling in the gas. This is especially relevant for disk-like progenitors that are able to overcome ram pressure and retain their gas for a longer period of time. Satellites infalling at $z \lesssim 1$ when the intensity of the cosmic ultraviolet background is weaker and the gas can settle in a colder and denser configuration within the potential of the dwarf would fall in this category. In this case, the tidal heating of the bar into a spheroid becomes less efficient. This is because the bar instability causes the gas to flow towards the central region of the dwarf, increasing its central density and causing a more adiabatic response of the system to the external tidal perturbation.

Despite the aforementioned limitations, several facts do suggest that our results for the efficiency of tidal stirring should be regarded as conservative. First, as we discussed above, some of the progenitors of present-day dSphs might have suffered significant tidal perturbations before being accreted by their hosts (e.g., Kravtsov et al. 2004). Therefore, it is plausible that these systems might have entered their primary galaxies already partially transformed. Such a condition would facilitate their complete transformation inside the tidal field of the primary galaxy. Second, if the progenitor disky dwarfs had either very low halo concentration parameters or core-like density profiles, as it is indeed suggested by both the modeling of rotation curves of present-day LSB and dIrr galaxies (e.g., de Blok 2010) and recent cosmological simulations of dwarf galaxy formation (Governato et al. 2010), our conclusions regarding the effectiveness of the transformation would be reinforced. Indeed, in such circumstances the response of the dwarfs to the tidal shocks would be much more impulsive compared to the cases of steep NFW-like profiles like the ones that we used in our experiments. This would give rise to augmented tidal mass loss (e.g., Kazantzidis et al. 2004a) and to a more effective transformation into a dSph. Lastly, none of the disky dwarfs in our experiments passed through the disk of the host galaxy. This is important as it has been recently shown that disk shocking, namely tidal shocks induced by passages through the disk, can affect significantly the evolution of satellites having masses $\lesssim 10^9 M_{\odot}$ and pericentic distances $\lesssim 30$ kpc, and even cause the disruption of a fraction of them (D'Onghia et al. 2010).

As a final remark, we reiterate that accumulating observational and theoretical evidence suggests that dwarf galaxies are not formed as thin disks, but rather are born as thick, puffy systems (e.g., Dalcanton et al. 2004; Kaufmann et al. 2007). The effect of thermal support, as opposed to rotation, ought to be thoroughly investigated in forthcoming studies of tidal stirring. Indeed, a thicker, more diffuse stellar component suggests a stronger effect of direct tidal heating (Spitzer 1958), but the bar instability, an essential element of tidal stirring, is associated with thin stellar configurations. Moreover, gas stripping by ram pressure should be enhanced in an initially thicker, more diffuse stellar system owing to the reduced gravitational restoring force of the gas. The interplay between all these aspects of the modeling will be assessed with future work where realistic gas-rich dIrrs will be evolved inside MW-sized hosts with recipes of radiative cooling, star formation, and supernovae feedback (Kazantzidis et al., 2010b, in preparation). These dwarfs have been formed self-consistently in cosmological hydrodynamical simulations (Governato et al. 2010) and are characterized by a turbulent and multi-phase realistic ISM.

6. SUMMARY

Using a suite of collisionless N-body simulations we have investigated the efficiency of the tidal stirring mechanism for the origin of dSphs. Specifically, we have examined the degree to which the sizes, masses, shapes, and kinematics of late-type, rotationally-supported dwarfs are affected by the gravitational field of MW-sized host galaxies for a range of dwarf orbital and structural parameters. Unlike previous work on the subject, we have employed equilibrium numerical models of dwarf galaxies constructed from composite DFs and consisting of exponential stellar disks embedded in cosmologically-motivated DM halos. The self-consistency of the adopted models is crucial for confirming the complex transformation process of a disky dwarf into a dSph. This aspect of the modeling constitutes the major improvement that we introduce in the present study. Furthermore, we have extended earlier contributions on the subject by conducting a simulation campaign which is carefully designed to allow an investigation of a much larger parameter space than before. Lastly, the fairly high numerical resolution of our experiments combined with the growing observational data sets for dSph galaxies provide unique opportunities for systematic and quantitative comparisons between the theoretical models and the data, and we undertake such a task in a companion paper (Łokas et al. 2010, in preparation).

Our main results and conclusions can be summarized as follows.

1. Tidal interactions between rotationally-supported dwarf galaxies and MW-sized hosts can lead to the formation of pressure-supported, spheroidal stellar systems with kinematic and structural properties akin to those of the classic dSphs in the LG and similar environments. Our exploration of a wide variety of initial conditions for the progenitor disky dwarfs suggests that such tidal transformations are fairly efficient and should thus be common occurrences within the currently favored cosmological paradigm. Due to the fact that satellite accretion is a generic feature of hierarchical models of structure formation, the transformation process described in this study should be applicable to at least some of the dSph galaxies in the universe.

2. The transformation mechanism is complex and involves a combination of tidally-induced bar instabilities in stellar disks and impulsive tidal heating of the stellar distribution. Given the self-consistency of our dwarf galaxy models, we can safely conclude that the formation of dSphs can be entirely attributed to tidal perturbations, rather than being a consequence of the initial conditions. In the context of the tidal stirring model, bar formation is intimately linked to the formation of dSphs (see Table 3). Loss of angular momentum caused by the bar instability and simultaneous increase of the stellar velocity dispersion due to tidal heating lead to low values of $V_{\rm rot}/\sigma_*$ in the simulated remnants comparable to those of observed dSphs ($V_{\rm rot}/\sigma_* \lesssim 1$). Heating via tidal shocks at pericentric passages decreases continuously the elongation of the bar and causes the initially disky stellar distributions to transform into spheroids with projected axis ratios of $c/a \gtrsim 0.5$.

3. Bar formation constitutes a sufficient but not necessary condition for the formation of dSphs via the tidal stirring of rotationally-supported dwarfs. In cases where bar instabilities are not triggered by the tidal interactions with the host galaxies, spheroidal stellar systems with negligible amounts of rotation can still be produced solely via the action of impulsive tidal heating (R16; see § 4.2.2).

4. The effectiveness of the transformation into a dSph depends crucially on the orbital parameters of the progenitor disky dwarfs (§ 3). For a fixed eccentricity, $r_{\rm apo}/r_{\rm peri}$, tighter orbits which are characterized by shorter orbital times, $T_{\rm orb}$, and smaller apocentric, $r_{\rm apo}$, and pericentric distances, $r_{\rm peri}$, lead to more rapid and complete transformations. For a fixed apocentric distance, orbits with higher eccentricities also induce stronger transformations. Under the right combination of orbital parameters, tidal stirring can yield spherically-symmetric ($b/a \approx c/a \gtrsim 0.95$) and isotropic ($\beta \approx 0$) stellar systems with negligible amounts of rotation ($V_{\rm rot}/\sigma_* \lesssim 0.1$) (R2 and R4; see Table 3).

5. The degree of the tidal transformation depends on both the number and the strength of the tidal shocks, which are determined by the orbital time, $T_{\rm orb}$, and the pericentric distance, $r_{\rm peri}$, respectively. Small pericentric distances and short orbital times, corresponding to orbits associated with a large number of strong tidal shocks, produce the strongest and most complete transformations. However, in order to simply transform a disky dwarf galaxy into a dSph without necessarily inducing the strongest transformation, $r_{\rm peri}$ is the more salient orbital parameter. The last conclusion holds provided that $T_{\rm orb}$ is short enough to allow the dwarfs to complete at least two pericentric passages inside their hosts. Such a condition is likely satisfied for a significant fraction of dwarf galaxies in the LG (see § 5.4).

6. The efficiency of the transformation via tidal stirring is notably affected by the structure of the progenitor disky dwarfs. Specifically, it is enhanced considerably for those with less massive and more extended disks, as well as for dwarfs embedded in halos of lower concentration (see § 4). These properties are akin to those of LSB, gas-rich dIrr galaxies which reside in the outskirts of the LG, a fact that highlights tidal stirring as a plausible causal mechanism for the origin of the morphology-density relation.

7. The robustness of dwarf galaxies to tides and mass loss is increased significantly for those with more massive and more compact disks, as well as for dwarfs embedded in halos of higher concentration (see § 4). This enhanced resilience to tidal effects has important consequences for the missing satellites problem as well as for determining the radial distribution of satellites inside host halos (e.g., Diemand et al. 2004).

8. The products of tidal stirring satisfy the relation $V_{\rm max} = \sqrt{3}\sigma_*$, where σ_* is the one-dimensional, central stellar velocity dispersion and $V_{\rm max}$ is the maximum halo circular velocity (see § 5.1). Such a small conversion factor between σ_* and $V_{\rm max}$, formally valid for a tracer

stellar population with an isotropic velocity dispersion tensor, is in agreement with those originally adopted to formulate the missing satellites problem (Moore et al. 1999; Klypin et al. 1999).

9. The mass-to-light ratios, M/L, of the orbiting disky dwarfs galaxies decrease monotonically with time as the extended DM halos are preferentially tidally stripped. In some cases, however, the M/L ratios start to increase later in the evolution when stellar mass loss becomes more effective (see § 5.3). These cases are associated with either enhanced tidal mass loss (R2 and R4) or more extended initial stellar distributions (R13) and demand that the dwarfs are stripped down to the scales where the alignment between the angular momenta of the stars and the orbital angular momenta of the dwarfs has an important effect on stellar stripping. This mechanism causes only a moderate increase of the M/L ratio and it may thus not be able to account for the extreme DM content in some of the classic dSphs (e.g., Draco or Ursa Minor). Producing such systems likely requires hydrodynamical processes.
10. Distant dSphs in the LG, such as Leo I, Tucana, and Cetus, which are likely moving on very wide orbits, should have only been partially stirred by their hosts, assuming that their properties originate from tidal stirring. As a result, these remote dwarfs should exhibit higher values of $V_{\rm rot}/\sigma_*$ compared to those of dSphs located closer to the primary galaxies. Future conclusive measurements of rotation in these systems will serve to validate (or falsify) this prediction.

The authors acknowledge useful discussions with James Bullock, Mandeep Gill, Andrey Kravtsov, Andrea Macciò, Chiara Mastropietro, Mario Mateo, Chris Orban, Michael Stamatikos, Justin Read, and David Weinberg. S.K. would like to thank Victor Debattista for valuable conversations on bar instabilities and related issues which significantly informed this work. S.K. also acknowledges the hospitality of the Nicolaus Copernicus Astronomical Center during a visit when the final stages of this work were completed. S.K. is funded by the Center for Cosmology and Astro-Particle Physics (CCAPP) at The Ohio State University. E.L.Ł. is grateful for the hospitality of CCAPP during her visit. This research was partially supported by the Polish Ministry of Science and Higher Education under grant NN203025333. The work of L.A.M. was carried out at the Jet Propulsion Laboratory (JPL), California Institute of Technology, under a contract with NASA. L.A.M. acknowledges support from the NASA ATFP program. The numerical simulations were performed on the Cosmos cluster at JPL. Cosmos was provided by funding from the JPL Office of the Chief Information Officer. This work was also supported by an allocation of computing time from the Ohio Supercomputer Center (http://www.osc.edu).

REFERENCES

Armandroff, T. E., Olszewski, E. W., & Pryor, C. 1995, AJ, 110, 2131
Battaglia, G., Helmi, A., Tolstoy, E., Irwin, M., Hill, V., & Jablonka, P. 2008, ApJ, 681, L13
Belokurov, V. et al. 2006, ApJ, 642, L137
Bernard, E. J. et al. 2009, ApJ, 699, 1742
Besla, G., Kallivayalil, N., Hernquist, L., Robertson, B., Cox, T. J., van der Marel, R. P., & Alcock, C. 2007, ApJ, 668, 949
Bett, P., Eke, V., Frenk, C. S., Jenkins, A., Helly, J., & Navarro, J. 2007, MNRAS, 376, 215
Binney, J. & Tremaine, S. 2008, Galactic Dynamics: Second Edition (Princeton University Press)
Blumenthal, G. R., Faber, S. M., Flores, R., & Primack, J. R. 1986, ApJ, 301, 27
Blumenthal, G. R., Faber, S. M., Primack, J. R., & Rees, M. J. 1984, Nature, 311, 517
Bruzual, A. G. & Charlot, S. 1993, ApJ, 405, 538
Bullock, J. S., Dekel, A., Kolatt, T. S., Kravtsov, A. V., Klypin, A. A., Porciani, C., & Primack, J. R. 2001a, ApJ, 555, 240
Bullock, J. S., Kravtsov, A. V., & Weinberg, D. H. 2000, ApJ, 539, 517
Bullock, J. S. et al. 2001b, MNRAS, 321, 559
Caputo, F., Cassisi, S., Castellani, M., Marconi, G., & Santolamazza, P. 1999, AJ, 117, 2199
Chiboucas, K., Karachentsev, I. D., & Tully, R. B. 2009, AJ, 137, 3009
Cole, S. & Lacey, C. 1996, MNRAS, 281, 716
Coleman, M. G., Da Costa, G. S., Bland-Hawthorn, J., & Freeman, K. C. 2005, AJ, 129, 1443
Coleman, M. G. et al. 2007, ApJ, 668, L43
Colpi, M., Mayer, L., & Governato, F. 1999, ApJ, 525, 720
Dalcanton, J. J., Yoachim, P., & Bernstein, R. A. 2004, ApJ, 608, 189
de Blok, W. J. G. 2010, Advances in Astronomy, vol. 2010, Article ID 789293 (astro-ph/0910.3538), 1
Debattista, V. P., Mayer, L., Carollo, C. M., Moore, B., Wadsley, J., & Quinn, T. 2006, ApJ, 645, 209
Dekel, A. & Silk, J. 1986, ApJ, 303, 39
Diemand, J., Kuhlen, M., & Madau, P. 2007, ApJ, 667, 859
Diemand, J., Moore, B., & Stadel, J. 2004, MNRAS, 352, 535
D'Onghia, E., Besla, G., Cox, T. J., & Hernquist, L. 2009, Nature, 460, 605
D'Onghia, E. & Lake, G. 2008, ApJ, 686, L61
D'Onghia, E., Springel, V., Hernquist, L., & Keres, D. 2010, ApJ, 709, 1138
Dubinski, J., Berentzen, I., & Shlosman, I. 2009, ApJ, 697, 293
Dubinski, J. & Chakrabarty, D. 2009, ApJ, 703, 2068
Einasto, J., Saar, E., Kaasik, A., & Chernin, A. D. 1974, Nature, 252, 111
Faber, S. M. & Lin, D. N. C. 1983, ApJ, 266, L17
Ferguson, A. M. N., Irwin, M. J., Ibata, R. A., Lewis, G. F., & Tanvir, N. R. 2002, AJ, 124, 1452
Ferguson, A. M. N. et al. 2005, ApJ, 622, L109
Forbes, D. A., Beasley, M. A., Bekki, K., Brodie, J. P., & Strader, J. 2003, Science, 301, 1217
Franx, M., Illingworth, G., & de Zeeuw, T. 1991, ApJ, 383, 112
Fraternali, F., Tolstoy, E., Irwin, M. J., & Cole, A. A. 2009, A&A, 499, 121
Frenk, C. S., White, S. D. M., Davis, M., & Efstathiou, G. 1988, ApJ, 327, 507
Gauthier, J.-R., Dubinski, J., & Widrow, L. M. 2006, ApJ, 653, 1180
Geha, M., Blanton, M. R., Masjedi, M., & West, A. A. 2006, ApJ, 653, 240
Ghigna, S., Moore, B., Governato, F., Lake, G., Quinn, T., & Stadel, J. 1998, MNRAS, 300, 146
Gilmore, G., Wilkinson, M. I., Wyse, R. F. G., Kleyna, J. T., Koch, A., Evans, N. W., & Grebel, E. K. 2007, ApJ, 663, 948
Gnedin, O. Y., Hernquist, L., & Ostriker, J. P. 1999, ApJ, 514, 109
Governato, F. et al. 2007, MNRAS, 374, 1479
—. 2009, MNRAS, 398, 312
—. 2010, Nature, 463, 203
Grcevich, J. & Putman, M. E. 2009, ApJ, 696, 385
Grebel, E. K. 1999, in IAU Symposium, Vol. 192, The Stellar Content of Local Group Galaxies, ed. P. Whitelock & R. Cannon, 17
Grebel, E. K. 2000, in ESA Special Publication, Vol. 445, Star Formation from the Small to the Large Scale, ed. F. Favata, A. Kaas, & A. Wilson, 87
Grebel, E. K. & Gallagher, III, J. S. 2004, ApJ, 610, L89
Grillmair, C. J. & Dionatos, O. 2006, ApJ, 643, L17
Hargreaves, J. C., Gilmore, G., Irwin, M. J., & Carter, D. 1994, MNRAS, 271, 693
Hayashi, E., Navarro, J. F., Taylor, J. E., Stadel, J., & Quinn, T. 2003, ApJ, 584, 541
Hernquist, L. 1990, ApJ, 356, 359
—. 1993, ApJS, 86, 389
Ibata, R., Irwin, M., Lewis, G., Ferguson, A. M. N., & Tanvir, N. 2001a, Nature, 412, 49
Ibata, R., Lewis, G. F., Irwin, M., Totten, E., & Quinn, T. 2001b, ApJ, 551, 294
Ibata, R., Martin, N. F., Irwin, M., Chapman, S., Ferguson, A. M. N., Lewis, G. F., & McConnachie, A. W. 2007, ApJ, 671, 1591
Ibata, R. A., Gilmore, G., & Irwin, M. J. 1994, Nature, 370, 194
Irwin, M. & Hatzidimitriou, D. 1995, MNRAS, 277, 1354
Jimenez, R., Verde, L., & Oh, S. P. 2003, MNRAS, 339, 243

Kalirai, J. S., Guhathakurta, P., Gilbert, K. M., Reitzel, D. B., Majewski, S. R., Rich, R. M., & Cooper, M. C. 2006, ApJ, 641, 268

Kallivayalil, N., van der Marel, R. P., Alcock, C., Axelrod, T., Cook, K. H., Drake, A. J., & Geha, M. 2006, ApJ, 638, 772

Kaufmann, T., Wheeler, C., & Bullock, J. S. 2007, MNRAS, 382, 1187

Kazantzidis, S., Abadi, M. G., & Navarro, J. F. 2010, ApJ, 720, L62

Kazantzidis, S., Bullock, J. S., Zentner, A. R., Kravtsov, A. V., & Moustakas, L. A. 2008, ApJ, 688, 254

Kazantzidis, S., Magorrian, J., & Moore, B. 2004a, ApJ, 601, 37

Kazantzidis, S., Mayer, L., Mastropietro, C., Diemand, J., Stadel, J., & Moore, B. 2004b, ApJ, 608, 663

Kazantzidis, S., Zentner, A. R., Kravtsov, A. V., Bullock, J. S., & Debattista, V. P. 2009, ApJ, 700, 1896

Klessen, R. S. & Kroupa, P. 1998, ApJ, 498, 143

Klimentowski, J., Łokas, E. L., Kazantzidis, S., Mayer, L., & Mamon, G. A. 2009a, MNRAS, 397, 2015

Klimentowski, J., Łokas, E. L., Kazantzidis, S., Mayer, L., Mamon, G. A., & Prada, F. 2009b, MNRAS, 400, 2162

Klimentowski, J., Łokas, E. L., Kazantzidis, S., Prada, F., Mayer, L., & Mamon, G. A. 2007, MNRAS, 378, 353

Klimentowski, J., Łokas, E. L., Knebe, A., Gottlöber, S., Martinez-Vaquero, L. A., Yepes, G., & Hoffman, Y. 2010, MNRAS, 402, 1899

Klypin, A., Kravtsov, A. V., Valenzuela, O., & Prada, F. 1999, ApJ, 522, 82

Klypin, A., Zhao, H., & Somerville, R. S. 2002, ApJ, 573, 597

Knebe, A., Gill, S. P. D., & Gibson, B. K. 2004, PASA, 21, 216

Knebe, A., Power, C., Gill, S. P. D., & Gibson, B. K. 2006, MNRAS, 368, 741

Kravtsov, A. 2010, Advances in Astronomy, vol. 2010, Article ID 281913 (astro-ph/0906.3295), 1

Kravtsov, A. V., Gnedin, O. Y., & Klypin, A. A. 2004, ApJ, 609, 482

Kregel, M., van der Kruit, P. C., & de Grijs, R. 2002, MNRAS, 334, 646

Kroupa, P. 1997, New Astronomy, 2, 139

Kuhn, J. R. & Miller, R. H. 1989, ApJ, 341, L41

Law, D. R., Johnston, K. V., & Majewski, S. R. 2005, ApJ, 619, 807

Lewis, G. F., Ibata, R. A., Chapman, S. C., McConnachie, A., Irwin, M. J., Tolstoy, E., & Tanvir, N. R. 2007, MNRAS, 375, 1364

Lisker, T., Grebel, E. K., Binggeli, B., & Glatt, K. 2007, ApJ, 660, 1186

Łokas, E. L. 2001, MNRAS, 327, L21

—. 2002, MNRAS, 333, 697

Łokas, E. L., Kazantzidis, S., Klimentowski, J., Mayer, L., & Callegari, S. 2010a, ApJ, 708, 1032

Łokas, E. L., Kazantzidis, S., Majewski, S. R., Law, D. R., Mayer, L., & Frinchaboy, P. M. 2010b, ApJ submitted (astro-ph/1008.3464)

Łokas, E. L., Klimentowski, J., Kazantzidis, S., & Mayer, L. 2008, MNRAS, 390, 625

Łokas, E. L., Mamon, G. A., & Prada, F. 2005, MNRAS, 363, 918

Ludlow, A. D., Navarro, J. F., Springel, V., Jenkins, A., Frenk, C. S., & Helmi, A. 2009, ApJ, 692, 931

Macciò, A. V., Dutton, A. A., & van den Bosch, F. C. 2008, MNRAS, 391, 1940

Macciò, A. V., Dutton, A. A., van den Bosch, F. C., Moore, B., Potter, D., & Stadel, J. 2007, MNRAS, 378, 55

Macciò, A. V., Kang, X., Fontanot, F., Somerville, R. S., Koposov, S., & Monaco, P. 2010, MNRAS, 402, 1995

Madau, P., Diemand, J., & Kuhlen, M. 2008, ApJ, 679, 1260

Majewski, S. R., Skrutskie, M. F., Weinberg, M. D., & Ostheimer, J. C. 2003, ApJ, 599, 1082

Malin, D. & Hadley, B. 1997, Publications of the Astronomical Society of Australia, 14, 52

Martin, N. F., de Jong, J. T. A., & Rix, H. 2008, ApJ, 684, 1075

Martin, N. F., Ibata, R. A., Bellazzini, M., Irwin, M. J., Lewis, G. F., & Dehnen, W. 2004, MNRAS, 348, 12

Martin, N. F. & Jin, S. 2010, ApJ accepted (astro-ph/1008.0014)

Martínez-Delgado, D., Alonso-García, J., Aparicio, A., & Gómez-Flechoso, M. A. 2001, ApJ, 549, L63

Martínez-Delgado, D., Butler, D. J., Rix, H.-W., Franco, V. I., Peñarrubia, J., Alfaro, E. J., & Dinescu, D. I. 2005, ApJ, 633, 205

Mastropietro, C., Moore, B., Mayer, L., Debattista, V. P., Piffaretti, R., & Stadel, J. 2005, MNRAS, 364, 607

Mateo, M., Olszewski, E. W., & Walker, M. G. 2008, ApJ, 675, 201

Mateo, M. L. 1998, ARA&A, 36, 435

Mayer, L. 2010, Advances in Astronomy, vol. 2010, Article ID 278434 (astro-ph/0909.4075), 1

Mayer, L., Governato, F., Colpi, M., Moore, B., Quinn, T., Wadsley, J., Stadel, J., & Lake, G. 2001a, ApJ, 559, 754

—. 2001b, ApJ, 547, L123

Mayer, L., Kazantzidis, S., Mastropietro, C., & Wadsley, J. 2007, Nature, 445, 738

Mayer, L., Mastropietro, C., Wadsley, J., Stadel, J., & Moore, B. 2006, MNRAS, 369, 1021

Mayer, L., Moore, B., Quinn, T., Governato, F., & Stadel, J. 2002, MNRAS, 336, 119

Mayer, L. & Wadsley, J. 2004, MNRAS, 347, 277

McGaugh, S. S. & Wolf, J. 2010, ApJ submitted (astro-ph/1003.3448)

Milgrom, M. 1995, ApJ, 455, 439

Mo, H. J., Mao, S., & White, S. D. M. 1998, MNRAS, 295, 319

Monelli, M., Cassisi, S., Bernard, E. J., Hidalgo, S. L., Aparicio, A., Gallart, C., & Skillman, E. D. 2010a, ApJ, 718, 707

Monelli, M. et al. 2010b, ApJ, 720, 1225

Moore, B., Ghigna, S., Governato, F., Lake, G., Quinn, T., Stadel, J., & Tozzi, P. 1999, ApJ, 524, L19

Muñoz, R. R., Majewski, S. R., & Johnston, K. V. 2008, ApJ, 679, 346

Muñoz, R. R. et al. 2006, ApJ, 649, 201

Navarro, J. F., Frenk, C. S., & White, S. D. M. 1996, ApJ, 462, 563

Newberg, H. J. et al. 2002, ApJ, 569, 245

Oh, S., de Blok, W. J. G., Walter, F., Brinks, E., & Kennicutt, R. C. 2008, AJ, 136, 2761

Orban, C., Gnedin, O. Y., Weisz, D. R., Skillman, E. D., Dolphin, A. E., & Holtzman, J. A. 2008, ApJ, 686, 1030

Peñarrubia, J., Navarro, J. F., & McConnachie, A. W. 2008, ApJ, 673, 226

Peebles, P. J. E. 1969, ApJ, 155, 393

Peng, E. W., Ford, H. C., Freeman, K. C., & White, R. L. 2002, AJ, 124, 3144

Penny, S. J., Conselice, C. J., de Rijcke, S., & Held, E. V. 2009, MNRAS, 393, 1054

Pohlen, M., Martínez-Delgado, D., Majewski, S., Palma, C., Prada, F., & Balcells, M. 2004, in Astronomical Society of the Pacific Conference Series, Vol. 327, Satellites and Tidal Streams, ed. F. Prada, D. Martinez Delgado, & T. J. Mahoney, 288

Purcell, C. W., Kazantzidis, S., & Bullock, J. S. 2009, ApJ, 694, L98

Quinn, P. J. & Goodman, J. 1986, ApJ, 309, 472

Read, J. I., Pontzen, A. P., & Viel, M. 2006a, MNRAS, 371, 885

Read, J. I., Wilkinson, M. I., Evans, N. W., Gilmore, G., & Kleyna, J. T. 2006b, MNRAS, 366, 429

Ricotti, M. & Gnedin, N. Y. 2005, ApJ, 629, 259

Sales, L. V., Navarro, J. F., Abadi, M. G., & Steinmetz, M. 2007, MNRAS, 379, 1475

Sawala, T., Scannapieco, C., Maio, U., & White, S. 2010, MNRAS, 402, 1599

Schulz, J., Fritze-v. Alvensleben, U., Möller, C. S., & Fricke, K. J. 2002, A&A, 392, 1

Sellwood, J. A. & Debattista, V. P. 2009, MNRAS, 398, 1279

Shang, E. et al. 1998, ApJ, 504, L23

Shaw, L. D., Weller, J., Ostriker, J. P., & Bode, P. 2006, ApJ, 646, 815

Simon, J. D. & Geha, M. 2007, ApJ, 670, 313

Skillman, E. D. 2005, New Astronomy Review, 49, 453

Sohn, S. T. et al. 2007, ApJ, 663, 960

Spitzer, Jr., L. 1958, ApJ, 127, 17

Spitzer, L. J. 1942, ApJ, 95, 329

Stadel, J. G. 2001, Ph.D. Thesis, Univ. of Washington

Stoehr, F., White, S. D. M., Tormen, G., & Springel, V. 2002, MNRAS, 335, L84

Susa, H. & Umemura, M. 2004, ApJ, 610, L5

Tassis, K., Abel, T., Bryan, G. L., & Norman, M. L. 2003, ApJ, 587, 13

Tassis, K., Kravtsov, A. V., & Gnedin, N. Y. 2008, ApJ, 672, 888

Tolstoy, E., Hill, V., & Tosi, M. 2009, ARA&A, 47, 371

Walker, M. G., Mateo, M., & Olszewski, E. W. 2008, ApJ, 688, L75

Walker, M. G., Mateo, M., Olszewski, E. W., Peñarrubia, J., Wyn Evans, N., & Gilmore, G. 2009, ApJ, 704, 1274

Wechsler, R. H., Bullock, J. S., Primack, J. R., Kravtsov, A. V., & Dekel, A. 2002, ApJ, 568, 52

Weinberg, M. D. & Blitz, L. 2006, ApJ, 641, L33

White, S. D. M. & Rees, M. J. 1978, MNRAS, 183, 341

Widrow, L. M. & Dubinski, J. 2005, ApJ, 631, 838

Yanny, B. et al. 2000, ApJ, 540, 825

Zentner, A. R. & Bullock, J. S. 2003, ApJ, 598, 49

A.1 Tidal stirring of thick, turbulent disky dwarfs formed in cosmological simulations

As mentioned in chapter 4, Governato et al. (2010) presented the results of the first cosmological simulations modelling the formation of realistic dwarf galaxies. They produced galaxies whose mass distribution closely resembles that of dwarf irregulars (dIrrs) and late-type dwarfs of the THINGS sample (Oh et al. 2011), with faint low surface brightness disks and slowly rising rotation curves. The shape of the rotation curve, which closely matches observed ones, is the result of three key factors: 1) a realistic baryonic disk with a baryon fraction well below universal and a low central density; 2) the absence of a bulge component; 3) the fact that the dark halo is not cuspy, but rather has a shallow inner power-law density profile. Of these properties, only the first two are satisfied by construction in the initial conditions normally used in tidal stirring works, such as those presented in the Kazantzidis et al. (2011) paper.

At $z = 0$, the galaxy has a peak circular velocity in the range 50-60 km s^{-1}, only slightly larger to that used in, e.g., Mayer et al. 2007. Low-mass galaxies with circular velocities in this range (or lower) are expected to be thick as a natural result of the balance between thermal energy, gravitational binding energy and rotational energy for standard halo spin parameters (Kaufmann et al. 2007). In fact, simlarly to real dIrrs (as found by Sánchez-Janssen, Méndez-Abreu, & Aguerri 2010), the dwarfs by Governato et al. (2010) have thick stellar and gaseous disks (aspect ratio close to 3:1), a consequence of the turbulent motions triggered by supernovae winds and outflows in the gas and then inherited by the newly-born stars. This is inevitable in a scenario in which supernovae outflows are strong enough to eject more than half of the baryons, and alter the slope of the dark matter distribution. On the contrary, model galaxies for tidal stirring employ thin disks for both the stellar and gaseous component. While the gaseous component of the disks can become much thicker as a result of the heating by the cosmic UV background (Mayer et al. 2006), with aspect ratios even as low as 3:1, but the inital stellar disk can only be thickened by tides, i.e. only after the interaction with the main galaxy has begun. At comparable mass of the disk and halo, which determine the depth of the potential well and hence the strength of the gravitational restoring force, a thicker disk will have a higher vertical stellar velocity dispersion. As a result, it will have a lower self-gravity. In this case, perturbations of the stellar surface density field, such as bar-like modes, should grow less efficiently.

Here we show preliminary results of new tidal stirring simulations that employ directly

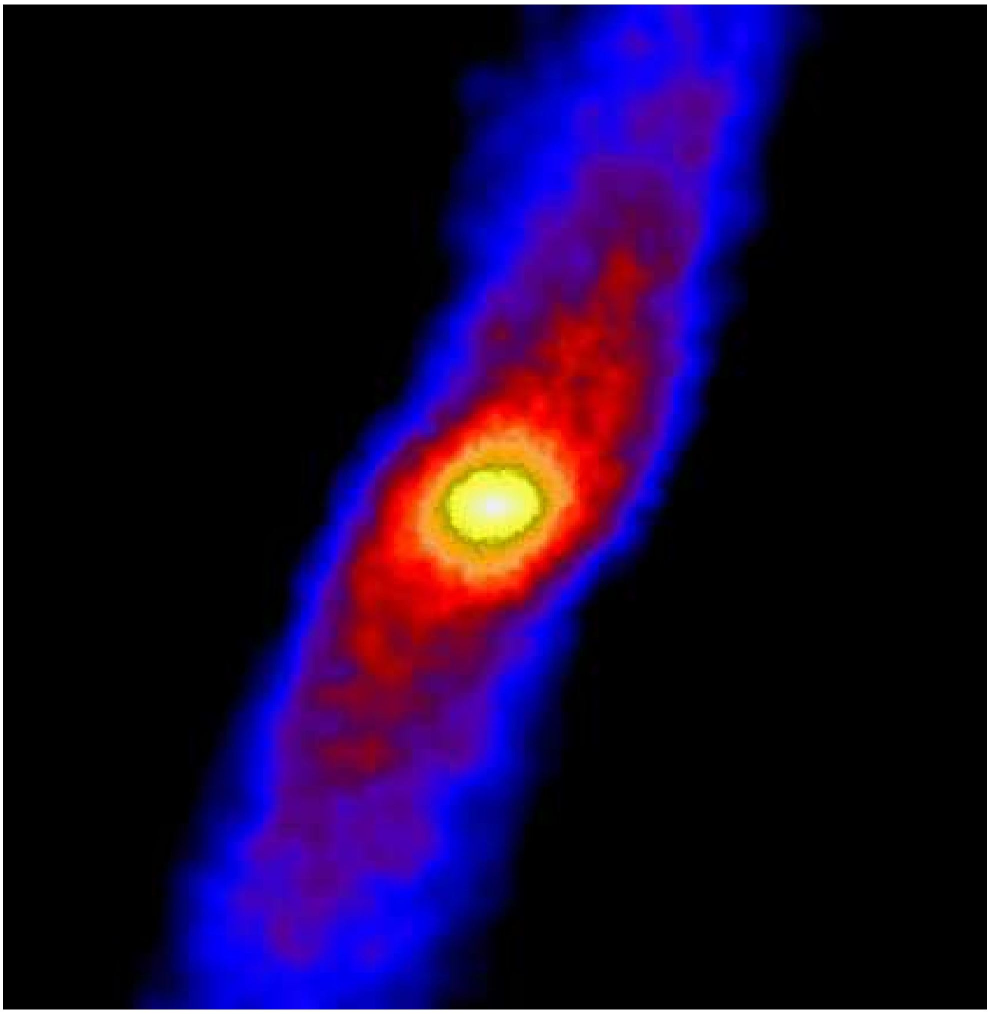

Figure A.1: Evolved state of the cosmological dwarf DG1 (Governato et al. 2010) extracted at z=1 and placed on orbit inside a live Milky Way model. The color-coded density map of the stars seen face-on (perpendicular to the angular momentum vector) is shown. The dwarf is displayed after first pericenter passage. The tidal distorion is evident but there is no sign of a strong bar.

the cosmological dwarfs in the Governato et al. (2010) paper. These are the first hydrodynamical simulations that explore tidal interactions using an hybrid approach, namely combining the very high resolution proper of idealized binary interaction experiments with cosmological initial conditions for one of the two galaxies (the dwarf satellite in this case). The DG1 and DG2 dwarfs are both extracted from the cosmological box at two different cosmic epochs ($z = 2$ and $z = 1$), and then placed on orbit inside the same multi-component model of the Milky Way used in the experiments of Mayer et al. (2006, 2007), which includes a hot gaseous corona.

The two different extraction epochs correspond effectively to two different dwarf models; not only the dwarf grows in mass from $z = 2$ to $z = 1$, but also changes in structure, becoming more rotationally-supported owing to accretion of higher angular momentum material, acquiring a shallower halo density profile, yet maintaining a fairly high thickness. Fig. A.1 shows the first results of the simulation adopting DG2 extracted at $z = 1$, just after the first pericenter passage. At this time the dwarf has $V_{\rm peak} = 45$ km s^{-1}, is gas-dominated and has already a slope shallower than NFW. Ram pressure stripping has already removed the outer gas disk. As shown in the Figure, the disk is tidally distorted but there is no sign of the strong bar-like mode ubiquitous in previous tidal stirring runs at the same stage (compare with Fig. 2.2 in chapter 2). Yet the disk has been heated into a spheroid, and $V/\sigma < 0.5$ near the end of the second orbit, almost a factor of 4 lower compared to the initial state. It appears that direct tidal heating is the culprit behind the transformation, rather than tidally induced non-axisymmetric instabilities. This confirms what reported above in the Kazantzidis et al. (2011) paper, where disk thickness is shown to have little effect on the transformation. However, in that work, a bar formed also in the thick disk case, although the amplitude of the bar mode decreased faster after the first orbit. The thick disk case had an aspect ratio not far from the Governato et al. (2010) cosmological dwarf. Therefore, the reason why the bar does not form in the cosmological dwarf cannot be simply that the disk is thicker; other structural properties might play a role as well. One important difference is that the cosmological dwarf has a disk which is gas dominated rather than purely stellar as in Kazantzidis et al. (2011). Mayer et al. (2007) considered gas dominated dwarfs but with initially thin stellar disks (aspect ratio ~ 0.1); the bar was forming at first pericenter but was dissolving soon afterwards, and direct tidal heating was then taking over. It is thus possible that a disk that is both gas dominated and thick the response is so weak that the bar does not arise at all. A detailed analysis of the evolution of the Toomre and swing amplification parameters will shed light on this. It will be performed in a a forthcoming paper. Therefore, we expect this new work to show that non-axisymmetric instabilities are not as crucial as previously found in driving the transformation. Even more importantly, it will support the much-speculated idea that having a dIrr or dSph morphology may depend exclusively on external processes – such as the infall into a larger halo, which cuts off the dwarf from cosmological accretion and starts the tidal stirring mechanism.

Bibliography

Abadi, M. G., Navarro, J. F., Steinmetz, M., & Eke, V. R. 2003, ApJ, 597, 21

Agertz, O., Lake, G., Teyssier, R., Moore, B., Mayer, L., & Romeo, A. B. 2009a, MNRAS, 392, 294

Agertz, O., Teyssier, R., & Moore, B. 2009b, MNRAS, 397, L64

—. 2011, MNRAS, 410, 1391

Alvarez, M. A., Wise, J. H., & Abel, T. 2009, ApJ, 701, L133

Anderson, M. E. & Bregman, J. N. 2010, ApJ, 714, 320

Baker, J. G., Boggs, W. D., Centrella, J., Kelly, B. J., McWilliams, S. T., Miller, M. C., & van Meter, J. R. 2008, ApJ, 682, L29

Baker, J. G., Centrella, J., Choi, D.-I., Koppitz, M., & van Meter, J. 2006, Physical Review Letters, 96, 111102

Bakos, J., Trujillo, I., & Pohlen, M. 2008, ApJ, 683, L103

Balsara, D. S. 1995, Journal of Computational Physics, 121, 357

Barnes, J. & Hut, P. 1986, Nature, 324, 446

Barnes, J. E. 1988, ApJ, 331, 699

Barnes, J. E. & Hernquist, L. 1996, ApJ, 471, 115

Barnes, J. E. & Hernquist, L. E. 1991, ApJ, 370, L65

Barth, A. J., Bentz, M. C., Greene, J. E., & Ho, L. C. 2008, ApJL in press

Bate, M. R. & Burkert, A. 1997, MNRAS, 288, 1060

Begelman, M. C. 2008, in American Institute of Physics Conference Series, Vol. 990, First Stars III, ed. B. W. O'Shea & A. Heger, 489–493

Begelman, M. C., Blandford, R. D., & Rees, M. J. 1980, Nature, 287, 307

Begelman, M. C., Volonteri, M., & Rees, M. J. 2006, MNRAS, 370, 289

Behroozi, P. S., Conroy, C., & Wechsler, R. H. 2010, ApJ, 717, 379

Bekenstein, J. D. 1973, ApJ, 183, 657

Bennert, N., Canalizo, G., Jungwiert, B., Stockton, A., Schweizer, F., Peng, C. Y., & Lacy, M. 2008, ApJ, 677, 846

Benson, A. J. 2005, MNRAS, 358, 551

Bertschinger, E. 2001, ApJS, 137, 1

Bianchi, S., Chiaberge, M., Piconcelli, E., Guainazzi, M., & Matt, G. 2008, MNRAS, 386, 105

Bigiel, F., Leroy, A., Walter, F., Brinks, E., de Blok, W. J. G., Madore, B., & Thornley, M. D. 2008, AJ, 136, 2846

Binney, J. & Tremaine, S. 1987, Galactic dynamics (Princeton, NJ, Princeton University Press, 1987, 747 p.)

Blandford, R. D. & McKee, C. F. 1982, ApJ, 255, 419

Blanton, M. R., Hogg, D. W., Bahcall, N. A., Baldry, I. K., Brinkmann, J., Csabai, I., Eisenstein, D., Fukugita, M., Gunn, J. E., Ivezić, Ž., Lamb, D. Q., Lupton, R. H., Loveday, J., Munn, J. A., Nichol, R. C., Okamura, S., Schlegel, D. J., Shimasaku, K., Strauss, M. A., Vogeley, M. S., & Weinberg, D. H. 2003, ApJ, 594, 186

Blumenthal, G. R., Faber, S. M., Flores, R., & Primack, J. R. 1986, ApJ, 301, 27

Bondi, H. 1952, MNRAS, 112, 195

Bonoli, S., Marulli, F., Springel, V., White, S. D. M., Branchini, E., & Moscardini, L. 2009, MNRAS, 396, 423

Boomsma, R., Oosterloo, T. A., Fraternali, F., van der Hulst, J. M., & Sancisi, R. 2008, A&A, 490, 555

Boylan-Kolchin, M. & Ma, C.-P. 2007, MNRAS, 374, 1227

Bromm, V. & Loeb, A. 2003, ApJ, 596, 34

Brook, C., Governato, F., Roškar, R., Brooks, A., Mayer, L., Quinn, T., & Wadsley, J. 2010, in American Institute of Physics Conference Series, Vol. 1240, American Institute of Physics Conference Series, ed. V. P. Debattista & C. C. Popescu, 203–206

Brooks, A. M., Governato, F., Quinn, T., Brook, C. B., & Wadsley, J. 2009, ApJ, 694, 396

Brooks, A. M., Solomon, A. R., Governato, F., McCleary, J., MacArthur, L. A., Brook, C. B. A., Jonsson, P., Quinn, T. R., & Wadsley, J. 2011, ApJ, 728, 51

Bryan, G. L. & Norman, M. L. 1998, ApJ, 495, 80

Bullock, J. S., Kolatt, T. S., Sigad, Y., Somerville, R. S., Kravtsov, A. V., Klypin, A. A., Primack, J. R., & Dekel, A. 2001, MNRAS, 321, 559

Callegari, S., Kazantzidis, S., Mayer, L., Colpi, M., Bellovary, J. M., Quinn, T., & Wadsley, J. 2011, ApJ, 729, 85

Callegari, S., Mayer, L., Kazantzidis, S., Colpi, M., Governato, F., Quinn, T., & Wadsley, J. 2009, ApJ, 696, L89

Campanelli, M., Lousto, C. O., Marronetti, P., & Zlochower, Y. 2006, Physical Review Letters, 96, 111101

Campanelli, M., Lousto, C. O., Zlochower, Y., & Merritt, D. 2007, Physical Review Letters, 98, 231102

Catinella, B., Schiminovich, D., Kauffmann, G., Fabello, S., Wang, J., Hummels, C., Lemonias, J., Moran, S. M., Wu, R., Giovanelli, R., Haynes, M. P., Heckman, T. M., Basu-Zych, A. R., Blanton, M. R., Brinchmann, J., Budavári, T., Gonçalves, T., Johnson, B. D., Kennicutt, R. C., Madore, B. F., Martin, C. D., Rich, M. R., Tacconi, L. J., Thilker, D. A., Wild, V., & Wyder, T. K. 2010, MNRAS, 403, 683

Ceverino, D., Dekel, A., & Bournaud, F. 2010, MNRAS, 404, 2151

Ceverino, D. & Klypin, A. 2009, ApJ, 695, 292

Chabrier, G. 2003, ApJ, 586, L133

Chandrasekhar, S. 1943, ApJ, 97, 255

Ciotti, L. & Ostriker, J. P. 2007, ApJ, 665, 1038

Colpi, M. & Dotti, M. 2009, ArXiv e-prints

Colpi, M., Mayer, L., & Governato, F. 1999, ApJ, 525, 720

Conroy, C., Gunn, J. E., & White, M. 2009, ApJ, 699, 486

Courteau, S., Dutton, A. A., van den Bosch, F. C., MacArthur, L. A., Dekel, A., McIntosh, D. H., & Dale, D. A. 2007, ApJ, 671, 203

Crain, R. A., McCarthy, I. G., Frenk, C. S., Theuns, T., & Schaye, J. 2010, MNRAS, 407, 1403

Croom, S. M., Richards, G. T., Shanks, T., Boyle, B. J., Strauss, M. A., Myers, A. D., Nichol, R. C., Pimbblet, K. A., Ross, N. P., Schneider, D. P., Sharp, R. G., & Wake, D. A. 2009, MNRAS, 399, 1755

Cuadra, J., Armitage, P. J., Alexander, R. D., & Begelman, M. C. 2009, MNRAS, 393, 1423

de Vaucouleurs, G. 1948, Annales d'Astrophysique, 11, 247

DeBuhr, J., Quataert, E., Ma, C., & Hopkins, P. 2009, ArXiv e-prints

Decarli, R., Falomo, R., Treves, A., Labita, M., Kotilainen, J. K., & Scarpa, R. 2010, MNRAS, 402, 2453

Di Matteo, T., Springel, V., & Hernquist, L. 2005, Nature, 433, 604

Djorgovski, S. G., Volonteri, M., Springel, V., Bromm, V., & Meylan, G. 2008, in The Eleventh Marcel Grossmann Meeting On Recent Developments in Theoretical and Experimental General Relativity, Gravitation and Relativistic Field Theories, ed. H. Kleinert, R. T. Jantzen, & R. Ruffini, 340–367

Dotti, M., Colpi, M., & Haardt, F. 2006, MNRAS, 367, 103

Dotti, M., Colpi, M., Haardt, F., & Mayer, L. 2007, MNRAS, 379, 956

Dotti, M., Ruszkowski, M., Paredi, L., Colpi, M., Volonteri, M., & Haardt, F. 2009, MNRAS, 396, 1640

Dotti, M., Volonteri, M., Perego, A., Colpi, M., Ruszkowski, M., & Haardt, F. 2010, MNRAS, 402, 682

Downes, D. & Solomon, P. M. 1998, ApJ, 507, 615

Durisen, R. H., Boss, A. P., Mayer, L., Nelson, A. F., Quinn, T., & Rice, W. K. M. 2007, Protostars and Planets V, 607

Dutton, A. A., Conroy, C., van den Bosch, F. C., Prada, F., & More, S. 2010, MNRAS, 407, 2

Eddington, A. S. 1916, MNRAS, 77, 16

Eisenstein, D. J. & Loeb, A. 1995, ApJ, 443, 11

Elmegreen, B. G., Bournaud, F., & Elmegreen, D. M. 2008, ApJ, 688, 67

Escala, A. 2007, ApJ, 671, 1264

Escala, A., Larson, R. B., Coppi, P. S., & Mardones, D. 2004, ApJ, 607, 765

—. 2005, ApJ, 630, 152

Evans, II, N. J., Dunham, M. M., Jørgensen, J. K., Enoch, M. L., Merín, B., van Dishoeck, E. F., Alcalá, J. M., Myers, P. C., Stapelfeldt, K. R., Huard, T. L., Allen, L. E., Harvey, P. M., van Kempen, T., Blake, G. A., Koerner, D. W., Mundy, L. G., Padgett, D. L., & Sargent, A. I. 2009, ApJS, 181, 321

Fakhouri, O. & Ma, C.-P. 2008, MNRAS, 386, 577

Fall, S. M. & Efstathiou, G. 1980, MNRAS, 193, 189

Fan, X. 2006, New Astronomy Reviews, 50, 665

Fan, X., Strauss, M. A., Schneider, D. P., Becker, R. H., White, R. L., Haiman, Z., Gregg, M., Pentericci, L., Grebel, E. K., Narayanan, V. K., Loh, Y.-S., Richards, G. T., Gunn, J. E., Lupton, R. H., Knapp, G. R., Ivezić, Ž., Brandt, W. N., Collinge, M., Hao, L., Harbeck, D., Prada, F., Schaye, J., Strateva, I., Zakamska, N., Anderson, S., Brinkmann, J., Bahcall, N. A., Lamb, D. Q., Okamura, S., Szalay, A., & York, D. G. 2003, AJ, 125, 1649

Feldmann, R., Carollo, C. M., & Mayer, L. 2011, ApJ, 736, 88

Feldmann, R., Carollo, C. M., Mayer, L., Renzini, A., Lake, G., Quinn, T., Stinson, G. S., & Yepes, G. 2010, ApJ, 709, 218

Ferrarese, L. 2002, ApJ, 578, 90

Ferrarese, L., Côté, P., Dalla Bontà, E., Peng, E. W., Merritt, D., Jordán, A., Blakeslee, J. P., Haşegan, M., Mei, S., Piatek, S., Tonry, J. L., & West, M. J. 2006, ApJ, 644, L21

Ferrarese, L. & Merritt, D. 2000, ApJ, 539, L9

Ferrière, K. M. 2001, Reviews of Modern Physics, 73, 1031

Fitchett, M. J. & Detweiler, S. 1984, MNRAS, 211, 933

Flynn, C., Holmberg, J., Portinari, L., Fuchs, B., & Jahreiß, H. 2006, MNRAS, 372, 1149

Förster Schreiber, N. M., Genzel, R., Bouché, N., Cresci, G., Davies, R., Buschkamp, P., Shapiro, K., Tacconi, L. J., Hicks, E. K. S., Genel, S., Shapley, A. E., Erb, D. K., Steidel, C. C., Lutz, D., Eisenhauer, F., Gillessen, S., Sternberg, A., Renzini, A., Cimatti, A., Daddi, E., Kurk, J., Lilly, S., Kong, X., Lehnert, M. D., Nesvadba, N., Verma, A., McCracken, H., Arimoto, N., Mignoli, M., & Onodera, M. 2009, ApJ, 706, 1364

Franx, M., van Dokkum, P. G., Schreiber, N. M. F., Wuyts, S., Labbé, I., & Toft, S. 2008, ApJ, 688, 770

Gebhardt, K. & al. 2000, ApJ, 539, L13

Genzel, R., Eckart, A., Ott, T., & Eisenhauer, F. 1997, MNRAS, 291, 219

Genzel, R. & Karas, V. 2007, in IAU Symposium, Vol. 238, IAU Symposium, ed. V. Karas & G. Matt, 173–180

Genzel, R., Pichon, C., Eckart, A., Gerhard, O. E., & Ott, T. 2000, MNRAS, 317, 348

Genzel, R., Tacconi, L. J., Eisenhauer, F., Förster Schreiber, N. M., Cimatti, A., Daddi, E., Bouché, N., Davies, R., Lehnert, M. D., Lutz, D., Nesvadba, N., Verma, A., Abuter, R., Shapiro, K., Sternberg, A., Renzini, A., Kong, X., Arimoto, N., & Mignoli, M. 2006, Nature, 442, 786

Georgakakis, A., Coil, A. L., Laird, E. S., Griffith, R. L., Nandra, K., Lotz, J. M., Pierce, C. M., Cooper, M. C., Newman, J. A., & Koekemoer, A. M. 2009, MNRAS, 397, 623

Ghez, A. M., Salim, S., Hornstein, S. D., Tanner, A., Lu, J. R., Morris, M., Becklin, E. E., & Duchêne, G. 2005, ApJ, 620, 744

Gingold, R. A. & Monaghan, J. J. 1977, MNRAS, 181, 375

Gnedin, N. Y., Tassis, K., & Kravtsov, A. V. 2009, ApJ, 697, 55

Gnedin, O. Y., Hernquist, L., & Ostriker, J. P. 1999, ApJ, 514, 109

González, J. A., Sperhake, U., Brügmann, B., Hannam, M., & Husa, S. 2007, Physical Review Letters, 98, 091101

Gould, A. & Rix, H.-W. 2000, ApJ, 532, L29

Governato, F., Brook, C., Mayer, L., Brooks, A., Rhee, G., Wadsley, J., Jonsson, P., Willman, B., Stinson, G., Quinn, T., & Madau, P. 2010, Nature, 463, 203

Governato, F., Brook, C. B., Brooks, A. M., Mayer, L., Willman, B., Jonsson, P., Stilp, A. M., Pope, L., Christensen, C., Wadsley, J., & Quinn, T. 2009, MNRAS, 398, 312

Governato, F., Colpi, M., & Maraschi, L. 1994, MNRAS, 271, 317

Governato, F., Mayer, L., Wadsley, J., Gardner, J. P., Willman, B., Hayashi, E., Quinn, T., Stadel, J., & Lake, G. 2004, ApJ, 607, 688

Governato, F., Willman, B., Mayer, L., Brooks, A., Stinson, G., Valenzuela, O., Wadsley, J., & Quinn, T. 2007, MNRAS, 374, 1479

Graham, A. W. & Driver, S. P. 2007, MNRAS, 380, L15

Graham, A. W., Erwin, P., Caon, N., & Trujillo, I. 2001, ApJ, 563, L11

Graham, A. W. & Worley, C. C. 2008, MNRAS, 388, 1708

Granato, G. L., De Zotti, G., Silva, L., Bressan, A., & Danese, L. 2004, ApJ, 600, 580

Guedes, J., Callegari, S., Madau, P., & Mayer, L. 2011a, ArXiv e-prints

Guedes, J., Madau, P., Mayer, L., & Callegari, S. 2011b, ApJ, 729, 125

Gültekin, K., Richstone, D. O., Gebhardt, K., Lauer, T. R., Tremaine, S., Aller, M. C., Bender, R., Dressler, A., Faber, S. M., Filippenko, A. V., Green, R., Ho, L. C., Kormendy, J., Magorrian, J., Pinkney, J., & Siopis, C. 2009, ApJ, 698, 198

Guo, Q., White, S., Li, C., & Boylan-Kolchin, M. 2010, MNRAS, 404, 1111

Haardt, F. & Madau, P. 1996, ApJ, 461, 20

Haehnelt, M. G., Natarajan, P., & Rees, M. J. 1998, MNRAS, 300, 817

Haehnelt, M. G. & Rees, M. J. 1993, MNRAS, 263, 168

Haiman, Z. 2004, ApJ, 613, 36

Hammer, F., Puech, M., Chemin, L., Flores, H., & Lehnert, M. D. 2007, ApJ, 662, 322

Häring, N. & Rix, H.-W. 2004, ApJ, 604, L89

Hasinger, G., Miyaji, T., & Schmidt, M. 2005, A&A, 441, 417

Hernquist, L. 1990, ApJ, 356, 359

—. 1992, ApJ, 400, 460

—. 1993, ApJS, 86, 389

Hernquist, L. & Katz, N. 1989, ApJS, 70, 419

Herrmann, F., Hinder, I., Shoemaker, D. M., Laguna, P., & Matzner, R. A. 2007, Phys. Rev. D, 76, 084032

Hobbs, A., Nayakshin, S., Power, C., & King, A. 2011, MNRAS, 413, 2633

Hopkins, P. F., Cox, T. J., Younger, J. D., & Hernquist, L. 2009, ApJ, 691, 1168

Hopkins, P. F., Hernquist, L., Cox, T. J., Di Matteo, T., Martini, P., Robertson, B., & Springel, V. 2005, ApJ, 630, 705

Hopkins, P. F. & Quataert, E. 2010, MNRAS, 407, 1529

Hudson, D. S., Reiprich, T. H., Clarke, T. E., & Sarazin, C. L. 2006, A&A, 453, 433

Jahnke, K., Kuhlbrodt, B., & Wisotzki, L. 2004, MNRAS, 352, 399

Jeans, S. 1929, Astronomy and cosmogony

Jogee, S. 2006, in Lecture Notes in Physics, Berlin Springer Verlag, Vol. 693, Physics of Active Galactic Nuclei at all Scales, ed. D. Alloin, 143–+

Johansson, P. H., Naab, T., & Burkert, A. 2009, ApJ, 690, 802

Johnson, J. L. & Bromm, V. 2007, MNRAS, 374, 1557

Jonsson, P. 2006, MNRAS, 372, 2

Jurić, M., Ivezić, Ž., Brooks, A., Lupton, R. H., Schlegel, D., Finkbeiner, D., Padmanabhan, N., Bond, N., Sesar, B., Rockosi, C. M., Knapp, G. R., Gunn, J. E., Sumi, T., Schneider, D. P., Barentine, J. C., Brewington, H. J., Brinkmann, J., Fukugita, M., Harvanek, M., Kleinman, S. J., Krzesinski, J., Long, D., Neilsen, Jr., E. H., Nitta, A., Snedden, S. A., & York, D. G. 2008, ApJ, 673, 864

Kaspi, S., Smith, P. S., Netzer, H., Maoz, D., Jannuzi, B. T., & Giveon, U. 2000, ApJ, 533, 631

Katz, N. 1992, ApJ, 391, 502

Kauffmann, G. & Haehnelt, M. 2000, MNRAS, 311, 576

Kauffmann, G., Heckman, T. M., Tremonti, C., Brinchmann, J., Charlot, S., White, S. D. M., Ridgway, S. E., Brinkmann, J., Fukugita, M., Hall, P. B., Ivezić, Ž., Richards, G. T., & Schneider, D. P. 2003, MNRAS, 346, 1055

Kaufmann, T., Mayer, L., Wadsley, J., Stadel, J., & Moore, B. 2006, MNRAS, 370, 1612

—. 2007, MNRAS, 375, 53

Kazantzidis, S., Łokas, E. L., Callegari, S., Mayer, L., & Moustakas, L. A. 2011, ApJ, 726, 98

Kazantzidis, S., Mayer, L., Colpi, M., Madau, P., Debattista, V. P., Wadsley, J., Stadel, J., Quinn, T., & Moore, B. 2005, ApJ, 623, L67

Kazantzidis, S., Mayer, L., Mastropietro, C., Diemand, J., Stadel, J., & Moore, B. 2004, ApJ, 608, 663

Kennicutt, Jr., R. C. 1998, ApJ, 498, 541

Kereš, D., Katz, N., Fardal, M., Davé, R., & Weinberg, D. H. 2009, MNRAS, 395, 160

Klessen, R. S., Spaans, M., & Jappsen, A.-K. 2007, MNRAS, 374, L29

Klypin, A., Zhao, H., & Somerville, R. S. 2002, ApJ, 573, 597

Komossa, S., Burwitz, V., Hasinger, G., Predehl, P., Kaastra, J. S., & Ikebe, Y. 2003, ApJ, 582, L15

Koposov, S. E., Rix, H.-W., & Hogg, D. W. 2010, ApJ, 712, 260

Kormendy, J. 2004, Coevolution of Black Holes and Galaxies, 1

Kormendy, J., Drory, N., Bender, R., & Cornell, M. E. 2010, ApJ, 723, 54

Koushiappas, S. M., Bullock, J. S., & Dekel, A. 2004, MNRAS, 354, 292

Kroupa, P. 2001, MNRAS, 322, 231

Krumholz, M. R., Klein, R. I., & McKee, C. F. 2007, ApJ, 656, 959

Krumholz, M. R., McKee, C. F., & Tumlinson, J. 2009, ApJ, 693, 216

Lacey, C. & Cole, S. 1993, MNRAS, 262, 627

Law, D. R., Steidel, C. C., Erb, D. K., Larkin, J. E., Pettini, M., Shapley, A. E., & Wright, S. A. 2009, ApJ, 697, 2057

Levine, R., Gnedin, N. Y., Hamilton, A. J. S., & Kravtsov, A. V. 2008, ApJ, 678, 154

Li, Y., Mo, H. J., van den Bosch, F. C., & Lin, W. P. 2007, MNRAS, 379, 689

Lin, D. N. C. & Pringle, J. E. 1987, MNRAS, 225, 607

Lodato, G. & Natarajan, P. 2006, MNRAS, 371, 1813

Lodato, G., Nayakshin, S., King, A. R., & Pringle, J. E. 2009, MNRAS, 398, 1392

Loeb, A. & Rasio, F. A. 1994, ApJ, 432, 52

Lynden-Bell, D. 1969, Nature, 223, 690

Madau, P. & Rees, M. J. 2001, ApJ, 551, L27

Magorrian, J. & al. 1998, AJ, 115, 2285

Maller, A. H. & Dekel, A. 2002, MNRAS, 335, 487

Marcolini, A., Brighenti, F., & D'Ercole, A. 2003, MNRAS, 345, 1329

Marconi, A. & Hunt, L. K. 2003, ApJ, 589, L21

Mashchenko, S., Couchman, H. M. P., & Wadsley, J. 2006, Nature, 442, 539

Mayer, L., Governato, F., Colpi, M., Moore, B., Quinn, T., Wadsley, J., Stadel, J., & Lake, G. 2001, ApJ, 547, L123

Mayer, L., Kazantzidis, S., Escala, A., & Callegari, S. 2010, Nature, 466, 1082

Mayer, L., Kazantzidis, S., Madau, P., Colpi, M., Quinn, T., & Wadsley, J. 2007, Science, 316, 1874

Mayer, L., Mastropietro, C., Wadsley, J., Stadel, J., & Moore, B. 2006, MNRAS, 369, 1021

Mayer, L., Quinn, T., Wadsley, J., & Stadel, J. 2004, ApJ, 609, 1045

Merloni, A., Rudnick, G., & Di Matteo, T. 2004, MNRAS, 354, L37

Merritt, D. & Milosavljević, M. 2005, Living Reviews in Relativity, 8, 8

Mihos, J. C. & Hernquist, L. 1996, ApJ, 464, 641

Milosavljević, M., Couch, S. M., & Bromm, V. 2009, ApJ, 696, L146

Milosavljević, M. & Merritt, D. 2001, ApJ, 563, 34

—. 2003, ApJ, 596, 860

Mo, H. J., Mao, S., & White, S. D. M. 1998, MNRAS, 295, 319

Monaghan, J. J. 1992, ARA&A, 30, 543

Mortlock, D. J., Warren, S. J., Venemans, B. P., Patel, M., Hewett, P. C., McMahon, R. G., Simpson, C., Theuns, T., Gonzáles-Solares, E. A., Adamson, A., Dye, S., Hambly, N. C., Hirst, P., Irwin, M. J., Kuiper, E., Lawrence, A., & Röttgering, H. J. A. 2011, Nature, 474, 616

Nagamine, K., Ostriker, J. P., Fukugita, M., & Cen, R. 2006, ApJ, 653, 881

Nakanishi, H. & Sofue, Y. 2003, PASJ, 55, 191

Navarro, J. F. & Benz, W. 1991, ApJ, 380, 320

Navarro, J. F., Frenk, C. S., & White, S. D. M. 1996, ApJ, 462, 563

Navarro, J. F. & Steinmetz, M. 2000, ApJ, 538, 477

Negroponte, J. & White, S. D. M. 1983, MNRAS, 205, 1009

Nelson, A. F. 2006, MNRAS, 373, 1039

Nelson, A. F., Benz, W., Adams, F. C., & Arnett, D. 1998, ApJ, 502, 342

Oh, S.-H., Brook, C., Governato, F., Brinks, E., Mayer, L., de Blok, W. J. G., Brooks, A., & Walter, F. 2011, AJ, 142, 24

Okamoto, T., Jenkins, A., Eke, V. R., Quilis, V., & Frenk, C. S. 2003, MNRAS, 345, 429

Omukai, K., Schneider, R., & Haiman, Z. 2008, ApJ, 686, 801

Ostriker, E. C. 1999, ApJ, 513, 252

Pelupessy, F. I., Di Matteo, T., & Ciardi, B. 2007, ApJ, 665, 107

Peng, E. W., Ford, H. C., Freeman, K. C., & White, R. L. 2002, AJ, 124, 3144

Perego, A., Dotti, M., Colpi, M., & Volonteri, M. 2009, MNRAS, 399, 2249

Peres, A. 1962, Physical Review, 128, 2471

Peters, P. C. 1964, Phys. Rev., 136, B1224, [Phys.Rev.136:1224-1232,1964]

Piontek, F. & Steinmetz, M. 2011, MNRAS, 410, 2625

Pizagno, J., Prada, F., Weinberg, D. H., Rix, H.-W., Pogge, R. W., Grebel, E. K., Harbeck, D., Blanton, M., Brinkmann, J., & Gunn, J. E. 2007, AJ, 134, 945

Pohlen, M. & Trujillo, I. 2006, A&A, 454, 759

Power, C., Baugh, C. M., & Lacey, C. G. 2010, MNRAS, 406, 43

Pretorius, F. 2005, Physical Review Letters, 95, 121101

Price, D. J. & Monaghan, J. J. 2004, MNRAS, 348, 123

Quilis, V., Ibáñez, J. M., & Sáez, D. 2000, A&A, 353, 435

Quinn, P. J. & Goodman, J. 1986, ApJ, 309, 472

Regan, J. A. & Haehnelt, M. G. 2009, MNRAS, 396, 343

Renaud, F., Boily, C. M., Naab, T., & Theis, C. 2009, ApJ, 706, 67

Robertson, B., Yoshida, N., Springel, V., & Hernquist, L. 2004, ApJ, 606, 32

Robertson, B. E. & Kravtsov, A. V. 2008, ApJ, 680, 1083

Robitaille, T. P. & Whitney, B. A. 2010, ApJ, 710, L11

Roškar, R., Debattista, V. P., Stinson, G. S., Quinn, T. R., Kaufmann, T., & Wadsley, J. 2008, ApJ, 675, L65

Saintonge, A., Kauffmann, G., Wang, J., Kramer, C., Tacconi, L. J., Buchbender, C., Catinella, B., Graciá-Carpio, J., Cortese, L., Fabello, S., Fu, J., Genzel, R., Giovanelli, R., Guo, Q., Haynes, M. P., Heckman, T. M., Krumholz, M. R., Lemonias, J., Li, C., Moran, S., Rodriguez-Fernandez, N., Schiminovich, D., Schuster, K., & Sievers, A. 2011, MNRAS, 415, 61

Salpeter, E. E. 1964, ApJ, 140, 796

Sánchez, S. F., Jahnke, K., Wisotzki, L., McIntosh, D. H., Bell, E. F., Barden, M., Beckwith, S. V. W., Borch, A., Caldwell, J. A. R., Häussler, B., Jogee, S., Meisenheimer, K., Peng, C. Y., Rix, H.-W., Somerville, R. S., & Wolf, C. 2004, ApJ, 614, 586

Sánchez-Janssen, R., Méndez-Abreu, J., & Aguerri, J. A. L. 2010, MNRAS, 406, L65

Sanders, D. B., Soifer, B. T., Elias, J. H., Madore, B. F., Matthews, K., Neugebauer, G., & Scoville, N. Z. 1988, ApJ, 325, 74

Sargent, M. T., Carollo, C. M., Lilly, S. J., Scarlata, C., Feldmann, R., Kampczyk, P., Koekemoer, A. M., Scoville, N., Kneib, J.-P., Leauthaud, A., Massey, R., Rhodes, J., Tasca, L. A. M., Capak, P., McCracken, H. J., Porciani, C., Renzini, A., Taniguchi, Y., Thompson, D. J., & Sheth, K. 2007, ApJS, 172, 434

Scannapieco, C., Gadotti, D. A., Jonsson, P., & White, S. D. M. 2010, MNRAS, 407, L41

Scannapieco, C., White, S. D. M., Springel, V., & Tissera, P. B. 2009, MNRAS, 396, 696

Schmidt, M. 1959, ApJ, 129, 243

—. 1963, Nature, 197, 1040

Sembach, K. R., Wakker, B. P., Savage, B. D., Richter, P., Meade, M., Shull, J. M., Jenkins, E. B., Sonneborn, G., & Moos, H. W. 2003, ApJS, 146, 165

Sersic, J. L. 1968, Atlas de galaxias australes

Sesana, A., Haardt, F., Madau, P., & Volonteri, M. 2005, ApJ, 623, 23

Seyfert, C. K. 1943, ApJ, 97, 28

Shankar, F. 2009, New Astronomy Reviews, 53, 57

Shankar, F., Salucci, P., Granato, G. L., De Zotti, G., & Danese, L. 2004, MNRAS, 354, 1020

Shapiro, S. L. 2005, ApJ, 620, 59

Shlosman, I., Begelman, M. C., & Frank, J. 1990, Nature, 345, 679

Shlosman, I., Frank, J., & Begelman, M. C. 1989, Nature, 338, 45

Silk, J. & Rees, M. J. 1998, A&A, 331, L1

Silverman, J. D., Mainieri, V., Lehmer, B. D., Alexander, D. M., Bauer, F. E., Bergeron, J., Brandt, W. N., Gilli, R., Hasinger, G., Schneider, D. P., Tozzi, P., Vignali, C., Koekemoer, A. M., Miyaji, T., Popesso, P., Rosati, P., & Szokoly, G. 2008, ApJ, 675, 1025

Smith, N. & Brooks, K. J. 2007, MNRAS, 379, 1279

Sofue, Y., Honma, M., & Omodaka, T. 2009, PASJ, 61, 227

Soltan, A. 1982, MNRAS, 200, 115

Spaans, M. & Silk, J. 2000, ApJ, 538, 115

Springel, V., Di Matteo, T., & Hernquist, L. 2005, MNRAS, 361, 776

Springel, V. & Hernquist, L. 2002, MNRAS, 333, 649

—. 2005, ApJ, 622, L9

Steinmetz, M. & White, S. D. M. 1997, MNRAS, 288, 545

Stinson, G., Seth, A., Katz, N., Wadsley, J., Governato, F., & Quinn, T. 2006, MNRAS, 373, 1074

Stinson, G. S., Bailin, J., Couchman, H., Wadsley, J., Shen, S., Nickerson, S., Brook, C., & Quinn, T. 2010, MNRAS, 408, 812

Strand, N. E., Brunner, R. J., & Myers, A. D. 2008, ApJ, 688, 180

Taffoni, G., Mayer, L., Colpi, M., & Governato, F. 2003, MNRAS, 341, 434

Toomre, A. 1964, ApJ, 139, 1217

Tremaine, S., Gebhardt, K., Bender, R., Bower, G., Dressler, A., Faber, S. M., Filippenko, A. V., Green, R., Grillmair, C., Ho, L. C., Kormendy, J., Lauer, T. R., Magorrian, J., Pinkney, J., & Richstone, D. 2002, ApJ, 574, 740

Umemura, M., Loeb, A., & Turner, E. L. 1993, ApJ, 419, 459

Valtonen, M. J., Lehto, H. J., Nilsson, K., Heidt, J., Takalo, L. O., Sillanpää, A., Villforth, C., Kidger, M., Poyner, G., Pursimo, T., Zola, S., Wu, J.-H., Zhou, X., Sadakane, K., Drozdz, M., Koziel, D., Marchev, D., Ogloza, W., Porowski, C., Siwak, M., Stachowski, G., Winiarski, M., Hentunen, V.-P., Nissinen, M., Liakos, A., & Dogru, S. 2008, Nature, 452, 851

Vecchio, A. 2004, Phys. Rev. D, 70, 042001

Vestergaard, M. 2002, ApJ, 571, 733

Vitvitska, M., Klypin, A. A., Kravtsov, A. V., Wechsler, R. H., Primack, J. R., & Bullock, J. S. 2002, ApJ, 581, 799

Volonteri, M., Gultekin, K., & Dotti, M. 2010, ArXiv e-prints

Volonteri, M., Haardt, F., & Madau, P. 2003, ApJ, 582, 559

Volonteri, M., Lodato, G., & Natarajan, P. 2008, MNRAS, 383, 1079

Volonteri, M. & Rees, M. J. 2005, ApJ, 633, 624

—. 2006, ApJ, 650, 669

Wada, K. 2001, ApJ, 559, L41

Wada, K. & Norman, C. A. 2002, ApJ, 566, L21

Wadsley, J. W., Stadel, J., & Quinn, T. 2004, New Astronomy, 9, 137

Walter, F., Carilli, C., Bertoldi, F., Menten, K., Cox, P., Lo, K. Y., Fan, X., & Strauss, M. A. 2004, ApJ, 615, L17

Wehner, E. H. & Harris, W. E. 2006, ApJ, 644, L17

Weinzirl, T., Jogee, S., Khochfar, S., Burkert, A., & Kormendy, J. 2009, ApJ, 696, 411

White, D. A., Fabian, A. C., Forman, W., Jones, C., & Stern, C. 1991, ApJ, 375, 35

White, S. D. M. & Rees, M. J. 1978, MNRAS, 183, 341

Wise, J. H., Turk, M. J., & Abel, T. 2008, ApJ, 682, 745

Wolfire, M. G., McKee, C. F., Hollenbach, D., & Tielens, A. G. G. M. 2003, ApJ, 587, 278

Wyithe, J. S. B. & Loeb, A. 2002, ApJ, 581, 886

Xue, X. X., Rix, H. W., Zhao, G., Re Fiorentin, P., Naab, T., Steinmetz, M., van den Bosch, F. C., Beers, T. C., Lee, Y. S., Bell, E. F., Rockosi, C., Yanny, B., Newberg, H., Wilhelm, R., Kang, X., Smith, M. C., & Schneider, D. P. 2008, ApJ, 684, 1143

Yoachim, P. & Dalcanton, J. J. 2006, AJ, 131, 226

Younger, J. D., Hopkins, P. F., Cox, T. J., & Hernquist, L. 2008, ApJ, 686, 815

Yu, Q. & Tremaine, S. 2002, MNRAS, 335, 965

Zel'Dovich, Y. B. 1964, Soviet Physics Doklady, 9, 195

Acknowledgements

I wish to thank first of all my advisor, Lucio Mayer. He taught me a lot, involving me in each new project with enthusiasm, great ideas and trust in my work, and I deeply enjoyed our conversations about astrophysics and beyond. I've been very lucky to work with you.

I'd like to thank Stelios Kazantzidis for all the productive hours spent thinking through projects in the office or at *Starbucks*; for all his "philosophical" questions; and even for bombarding me with emails! I did enjoy working together.

My gratitude goes also to Monica Colpi. She has been an inspiring presence through all these years. I owe her so much of how I see the Universe.

Javiera Guedes (*Javieraaa!*): you are great, and Eris would not have been such a goddess if not for your hard work and passion. Thanks to you and to Piero Madau.

Thank you Marta Volonteri: for many astro-related things, and even more for simply being a great person to talk with. Thank you Massimo Dotti for the scientific insights, and for bravely driving me from Ann Arbor to Columbus the day I missed the plane.

There are many colleagues with whom I didn't write papers, but of whom I very much enjoyed the company and friendship (and scientific advice). They know who they are!

My deepest thanks, as always, to my parents, family, long-time friends, and Lea.

This is Ground Control to Major Tom, you've really made the grade
And the papers want to know whose shirts you wear
Now it's time to leave the capsule if you dare.

This is Major Tom to Ground Control, I'm stepping through the door
And I'm floating in a most peculiar way
And the stars look very different today.

Curriculum vitæ

CALLEGARI
Simone

Born on June 18th, 1981
Nationality: Italian

High school: Liceo Classico B. Zucchi (2000), *Diploma di Maturità Classica*.

B. Sc.: Università degli Studi di Milano–Bicocca (2003), *Laurea triennale* in Physics.
Thesis: *The effects of interstellar reddening on optical afterglows of Gamma-Ray Bursts and the determination of their photometric redshifts*.

M. Sc.: Università degli Studi di Milano Bicocca (2006), *Laurea Specialistica* in Astrophysics and Space Physics.
Thesis: *Interactions between galaxies hosting supermassive black holes*.

Employed as PhD student at the University of Zurich since October 2006.

Refereed publications

Guedes, J.; **Callegari, S.**; Madau, P.; Mayer, L., *Forming Realistic Late-Type Spirals in a LCDM Universe: The Eris Simulation*, ApJ in press.

Guedes J., Madau P., Mayer L., **Callegari S.**, *Recoiling massive black holes in gas-rich galaxy mergers*, ApJ 729, 129 (2011)

Callegari S., Kazantzidis S., Mayer L., Colpi M., Bellovary J. M., Quinn T., Wadsley J., *Growing massive black hole pairs in minor mergers of disk galaxies*, ApJ 729, 85 (2011)

Kazantzidis S., Lokas E. L., **Callegari S.**, Mayer L., Moustakas L. A., *On the efficiency of the tidal stirring mechanism for the origin of dwarf spheroidals*, ApJ 726, 98 (2011)

Mayer L., Kazantzidis S., Escala A., **Callegari S.**, *Direct formation of supermassive black holes via multi-scale gas inflows in galaxy mergers*, Nature 466, 1082 (2010)

Lokas E. W., Kazantzidis S., Klimentowski J., Mayer L., **Callegari S.**, *The stellar structure and kinematics of dwarf spheroidal galaxies formed by tidal stirring*, ApJ 708, 1032 (2010)

Colpi M., **Callegari S.**, Dotti M., Mayer L., *Massive black hole binary evolution in gas-rich mergers*, CQGra 26, 4029 (2009)

Callegari S., Mayer L., Kazantzidis S., Colpi M., Governato F., Quinn T., Wadsley J., *Pairing of supermassive black holes in unequal-mass galaxy mergers*, ApJL 696, 89 (2009)

Mapelli M., Moore B., Giordano L., Mayer L., Colpi M., Ripamonti E., **Callegari S.**, *Intermediate-mass black holes and ultraluminous X-ray sources in the Cartwheel ring galaxy*, MNRAS 383, 230 (2008)

Talks

Formation of massive black hole pairs through galaxy mergers, Università di Milano-Bicocca, Workshop “Bridging electromagnetic astrophysics and cosmology with gravitational waves”, Mar 29 2011.

Massive black hole pairs in minor galaxy mergers, Universität Zürich, Workshop “LISA Massive Black Hole binaries in the cosmic landscape”, Feb 11 2010.

Pairing of supermassive black holes in galaxy mergers, CCAPP seminar at the Center for Cosmology and Astroparticle Physics, Ohio State University, Oct 6 2009.

Coalescence of massive black holes in equal- and unequal-mass galaxy mergers with gas: ultra-high resolution simulations and prospects for LISA, UC Irvine Center for Cosmology Workshop “Intermediate-Mass black holes: from first light to galactic nuclei”, Apr 2 2009.

HPC proposals

Connecting mergers of supermassive black holes and their formation in hierarchical galaxy assembly - II : cosmological simulations with realistic host galaxies (2011), PI: Lucio Mayer, awarded 2,200,000 CPU hours on Cray XT5 Monte Rosa at CSCS (Switzerland).

Connecting mergers of supermassive black holes and their formation during hierarchical galaxy assembly (2010), PI: Lucio Mayer, awarded 2,000,000 CPU hours on Cray XT5 Monte Rosa at CSCS (Switzerland).

Coevolution of galaxies and supermassive black holes (2009), PI: Lucio Mayer; awarded 1,800,000 CPU hours per three-month period on Cray XT5 Monte Rosa at CSCS (Switzerland).

The formation of disk galaxies in a cold dark matter universe (2008), PI: Lucio Mayer; awarded 500,000 CPU hours on Cray XT3 Palu at CSCS (Switzerland).

Teaching

Teaching Assistant for Thermodynamics (prof. G. M. Graf), winter semester 06–07.
Teaching Assistant for Astrophysics and Cosmology (prof. Ph. Jetzer), spring semester 07.
Teaching assistant for Theoretical Astrophysics (prof. L. Mayer), winter semester 07–08.
Teaching assistant for Theoretical Astrophysics (prof. L. Mayer), winter semester 08–09.
Teaching assistant for Astrophysical Dynamics (prof. L. Mayer and prof. J. Diemand), winter semester 09–10.
Teaching assistant for Astrophysical Dynamics (prof. L. Mayer), winter semester 10 – 11.